Spring 5-15-2020

Thermophysical Properties and Phase Transformations in Metallic Liquids and Silicate Glasses

Daniel Christian Van Hoesen
Washington University in St. Louis

Recommended Citation

Van Hoesen, Daniel Christian, "Thermophysical Properties and Phase Transformations in Metallic Liquids and Silicate Glasses" (2020). *Arts & Sciences Electronic Theses and Dissertations*. 2248.
https://openscholarship.wustl.edu/art_sci_etds/2248

WASHINGTON UNIVERSITY IN ST. LOUIS

Department of Physics

Dissertation Examination Committee:
Kenneth F. Kelton, Chair
Katharine Flores
Erik Henriksen
Zohar Nussinov
Li Yang

Thermophysical Properties and Phase Transformations in Metallic Liquids and Silicate Glasses

by

Daniel Christian Van Hoesen

A dissertation presented to
The Graduate School
of Washington University in
partial fulfillment of the
requirements for the degree
of Doctor of Philosophy

May 2020
St. Louis, Missouri

Table of Contents

List of Figures

List of Tables

Acknowledgments

I would first like to thank my advisor, Professor Ken Kelton, for his guidance and support during my time as a graduate student. You were always willing to answer questions and give research advice and career planning advice. I look forward to staying in touch after graduate school.

I would like to thank Dr. Chris Pueblo and Dr. Robert Ashcraft without whom beginning research would have been impossible. Their guidance as senior graduate students when I first joined the Kelton lab was invaluable, and it allowed me to be a productive member of the lab. A special thanks is given to Mark Sellers, Xinsheng Xia, and Rongrong Dai for their support and kindness in the everyday workings of the Kelton lab. I could always ask each of you for help. Thank you for allowing me to discuss ideas, experiments, and life with you. I would also like to thank Jared Lalmansingh for his kindness and help throughout graduate school. His willingness to help in a variety of activities including physics outreach, machine learning club, and for fun side projects continues to be awe inspiring. I look forward to staying connected after graduate school.

I would like to thank Dr. Anup Gangopadhyay for his help with experiments, for his critical review of work, and for training me to be scientist. A special thanks is also given to Dr. Matthew McKenzie for his guidance during a Corning Inc. internship and his collaboration on the barium disilicate glass project.

A special thanks is given to the Washington University in St. Louis Department of Physics staff. Without the help of those in the department office I would have struggled through graduate school. The staff in the machine shop also made it possible for me to perform the experiments that make up my dissertation. I am grateful for your help.

I would like to thank my funding sources. My work on the thermophysical properties of metallic liquids was primarily funded by the National Aeronautics and Space Administration under grant NNX10AU19G. The National Science Foundation under grant DMR 12-06707 and Corning Incorporated funded my work on nucleation and growth in silicate glasses.

Finally, my family has given my unwavering support and encouragement throughout the past few years. In particular, I would like to thank my wife, Katie, for her support in and out of graduate school. Without you, this would not have been possible. I am grateful that you are in my life.

Daniel Christian Van Hoesen

Washington University in St. Louis

May 2020

Abstract of the Dissertation

Thermophysical Properties and Phase Transformations in Metallic Liquids and Silicate Glasses

by

Daniel Christian Van Hoesen

Doctor of Philosophy in Physics

Washington University in St. Louis, 2020

Professor Kenneth F. Kelton, Chair

The first quantitative measurements of the electrical resistivity in binary metallic liquids, used to probe local order in the liquid, are reported in this dissertation. The electrical resistivity is very sensitive to short and medium range ordering because the electron mean free path is approximately the same length scale as the atomic spacing. Particular attention is given to the resistivity value at a crossover temperature that, based on molecular dynamics (MD) simulations, is the onset of cooperative motion in liquid alloys. Experimental evidence for the crossover is found in measurements of the shear viscosity, a dynamical property. An indication of the crossover temperature in the electrical resistivity would support the MD prediction of a direct connection between liquid dynamics and structure. Thermophysical properties of supercooled metallic liquids are difficult to measure due to crystallization induced by heterogeneous nucleation and reactions with container walls that occur with many reactive metals. Electrostatic and electromagnetic containerless processing techniques are used to minimize heterogeneous nucleation and to allow for measurements of the electrical resistivity and the shear viscosity in the equilibrium and supercooled liquid. This dissertation reports the results of electrical resistivity measurements of two binary liquids, made on the International Space Station (ISS) using an electromagnetic levitator. The shear viscosity is measured using the ground-based Beamline Electrostatic Levitation facility located at Washington University in St. Louis. It is found that the electrical resistivity as a function of temperature saturates above the onset of cooperative motion in the liquid, likely due to the ineffectiveness of electron-phonon scattering at high temperatures. These measurements give clear evidence that the liquid structure and the dynamics are strongly related.

In a different project, $BaO \cdot 2SiO_2$ and $5BaO \cdot 8SiO_2$ glasses are numerically modeled using the classical nucleation theory and the diffuse interface theory. Fortran computer code is developed to numerically solve the rate equations of the classical theory to probe the transient and steady-state nucleation and crystal growth in these glasses. A differential thermal analysis technique is simulated to determine the temperature range of significant nucleation. It is found that the numerical technique reproduces the experimental results when the diffusion coefficient is calculated from the measured induction time and the measured growth velocity. It is also shown that changing the scanning rate during the simulations does not obscure the measured region of significant nucleation, indicating that the differential thermal analysis technique is robust.

This dissertation also includes measurements of the specific heat of NASA ISS batch 1, 2, and 3 equilibrium and supercooled metallic liquid alloys. The specific heat is measured with the electromagnetic levitator aboard the ISS using the modulation calorimetry technique. It is also measured with the ground-based electrostatic levitator at Washington University in St. Louis, in which the external heat transport time constant is determined and combined with emissivity data. The dissertation concludes with calculations of the X-ray absorption and multiple scattering corrections for a cylindrical geometry, where the beam is in general off-center from the axis of the cylinder. These precise corrections are needed to search for subtle changes in scattering during the nucleation processes in glasses.

Chapter 1: Introduction

It is common knowledge that the continuous cooling of a liquid leads to a solid that does not freely flow. What are the properties of this material? In particular, how do the structure and dynamics of the material compare to other materials? Clearly the composition plays an important role. However, it may be somewhat surprising that the cooling rate also plays a dramatic role. With a quick enough cooling rate, starting from the equilibrium liquid the phase transition to a crystal solid can be bypassed, taking the liquid into the supercooled liquid (i.e. below the liquidus temperature, T_l) without crystallization and finally into a glass phase, where the dynamics have slowed beyond laboratory time scales. The structure of the glass phase remains similar to that of the liquid but the dynamics are slow, giving it some similarity to a crystalline material. Glass formation occurs with slow cooling rates in some materials, like silicate oxides, but requires very high cooling rates in other materials such as liquid metallic alloys.

The liquid and the glass phases of matter remain poorly understood. For example, is the glass transition purely dynamical or is it a true thermodynamic transition, and what are the correlation lengths associated with the glass phase? These questions require additional study[1].

1.1 Glasses and the Glass Transition

The structure provides a good starting place to investigate the glass transition. Crystalline materials contain periodic long-range order whereas glasses and liquids contain only short and medium-range order. Figure 1.1 shows a two-dimensional representation of a crystal, a network forming glass (such as a silicate glass) and a metallic glass (such as Vitreloy 106). The temperature dependence of the liquid's structure varies nearly linearly with temperature; however, when the crystal forms and grows in the liquid, the structure changes rapidly and is vastly different than that of the liquid. As a liquid cools the ordering decreases smoothly into the glass phase as long as crystallization is bypassed.

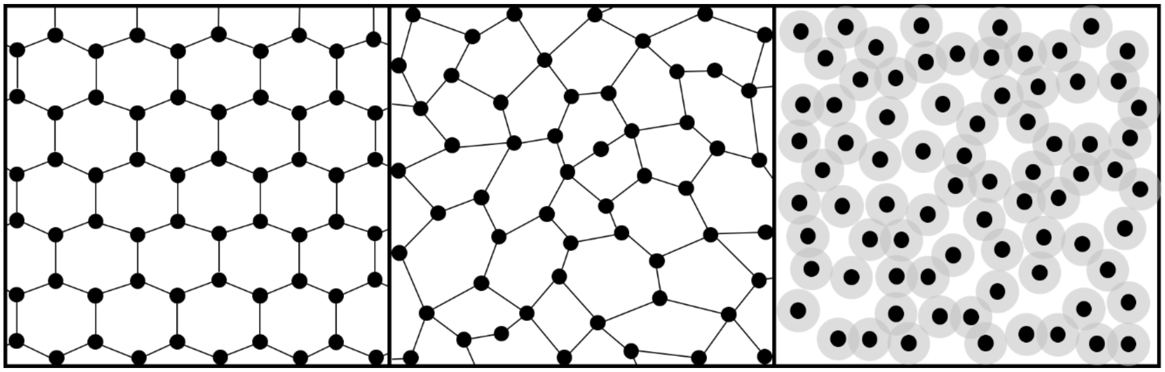

Figure 1.1 – Schematic representations of a two-dimensional crystal (left), network forming glass (center), and a metallic glass (right) adapted from fig. 1.1 in Matthew Blodgett's dissertation[2] with permission.

Scattering experiments provide a convenient way to measure the structure of a material. The pair correlation function describes the amount of ordering by giving the probability of finding an atom (or formula unit) a specific distance away from another atom (or formula unit). It is defined as

$$g(r) = \frac{1}{4\pi N n_0 r^2} \sum_i \sum_{i \neq j} \delta\left(r - r_{ij}\right), \tag{1.1}$$

where r_{ij} is the distance from atom i to atom j, δ is the Dirac delta function, N is the total number of atoms, and n_0 is the number density. It should be noted that $g(r)$ is not measured directly in scattering experiments; instead, the structure factor, $S(q)$, is measured. The structure factor provides the same structural information as the pair correlation function but is expressed in momentum space. For amorphous materials, the structure factor is given by the spherically symmetric Fourier Transform of the pair correlation function,

$$S(q) = 4\pi n_0 \int (g(r) - 1)\frac{\sin(qr)}{qr} r^2 dr\,. \tag{1.2}$$

From $S(q)$ or $g(r)$ it is easy to see that the changes in the structure from the supercooled liquid to the glass are subtle, as is shown in fig. 1.2 and fig. 1.3 for the Vit106 ($Zr_{57}Cu_{15.4}Ni_{12.6}Al_{10}Nb_5$) metallic alloy.

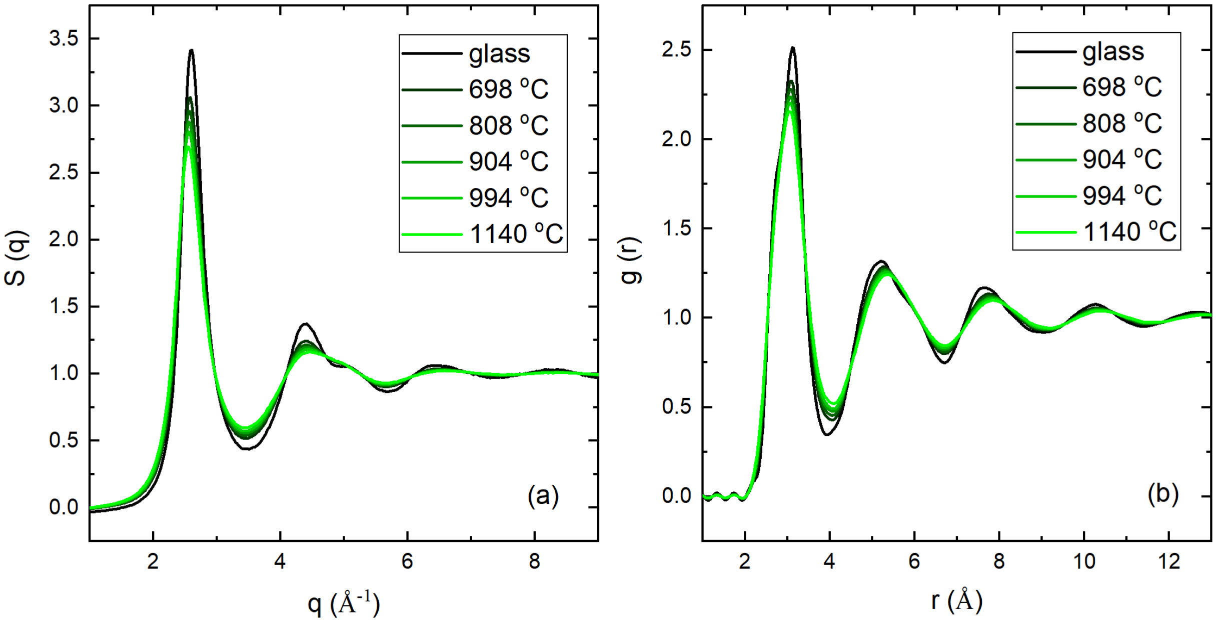

Figure 1.2 – The X-ray structure factor (a) and the X-ray pair correlation function (b) for the Vit106 metallic alloy. These data were taken at the Argonne National Lab Advanced Photon Source on beamline 6-ID-D using the Washington University Beamline Electrostatic Levitator.

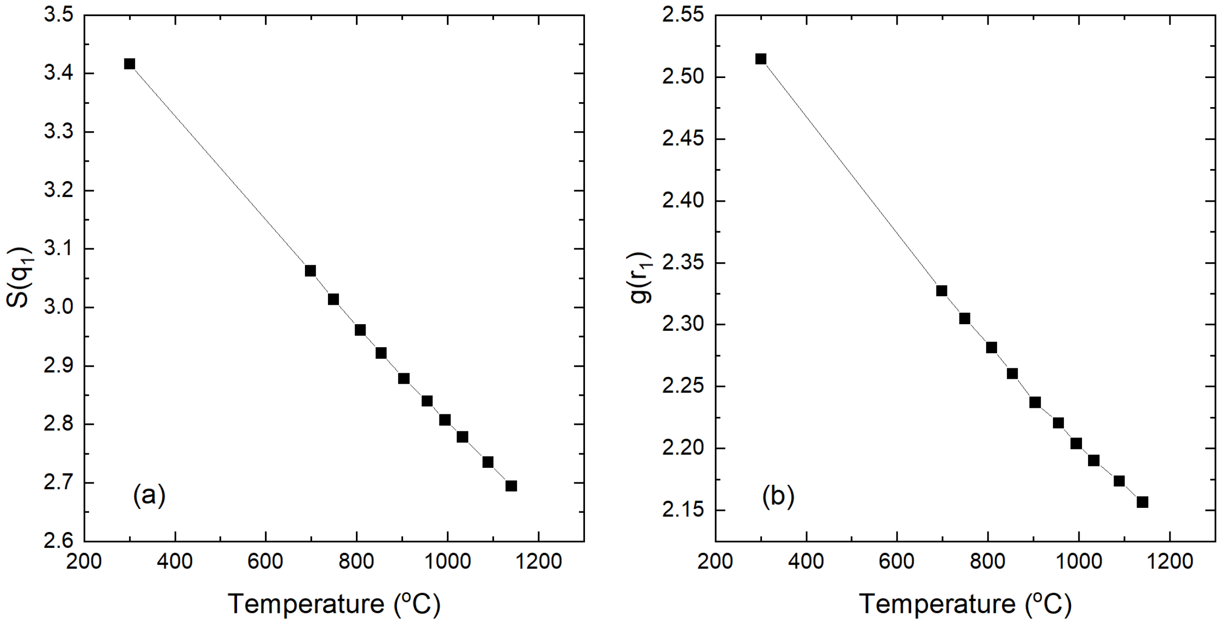

Figure 1.3 – The first peak heights for the X-ray structure factor (a) and the X-ray pair correlation function (b) for the Vit106 metallic alloy. The glass structure (lowest temperature data point) is a continuation of the supercooled liquid structure. These data were taken at the Argonne National Lab Advanced Photon Source on beamline 6-ID-D.

The first peak heights in the X-ray scattering structure factors and pair correlation functions (quantities used to measure the amount of structural change) are not illuminating in terms of discovering the fundamental changes occurring during the transition from the supercooled liquid to the glass. For example, as a liquid continues to cool through the glass transition, the structure factor varies smoothly[3], unlike the behavior for crystallization. Although local structural changes measured by electron scattering experiments (*i.e.* electrical resistivity or electrical conductivity), may be more enlightening (see chapter 3 for measurements of the electrical resistivity of liquid binary alloys).

The glass transition was originally defined as a dynamical transition, where dynamics are arrested at temperatures lower than the glass transition temperature. The dynamics can be described by the shear relaxation time. A material acted upon by an oscillatory disturbance with a frequency that is slower than the relaxation time responds like a solid. Conversely, a material acted upon by a process slower than the relaxation time will respond like a liquid. In this sense equilibrium and supercooled liquids can behave mechanically similar to solids on short timescales. Because liquids can flow, stresses are relieved by atomic rearrangement. The shear relaxation time, τ_R, is expressed in terms of the shear modulus,

$$G(t) = G_\infty \exp\left(-\frac{t}{\tau_R}\right), \tag{1.3}$$

where G_∞ is the infinite frequency shear modulus and t is time. The shear relaxation time is strongly temperature dependent in the supercooled liquid, changing by many orders of magnitude in a short temperature range near the glass transition temperature. The glass transition is defined as the temperature at which the shear relaxation time for the supercooled liquid exceeds laboratory timescales. In the equilibrium liquid ($T > T_l$), τ_R is small ($\sim 10^{-13}\ s$), but in the deeply supercooled liquid it is much larger ($10 - 100\ s$). The glass transition is defined by the temperature at which τ_R exceeds $10 - 100\ s$. For Maxwell liquids (*i.e.* liquids that can be described by an elastic spring and a viscous damper connected in series) where the viscosity, η, is proportional to the shear relaxation time, $\eta = G_\infty \tau_R$, this corresponds to a viscosity of $10^{12}\ Pa \cdot s$. Is the glass transition simply a convenient definition because experiments taking longer than laboratory timescales are time consuming? Dynamic and thermodynamic differences between the glass and the supercooled liquid states suggest that this is not the case.

The calorimetric glass transition can be seen in differential thermal analysis (DTA) or differential scanning calorimetry (DSC) measurements, where an amorphous sample is heated slowly until reaching the glass transition, at which point there is a change in the heat flow. As the sample temperature continues to increase devitrification (*i.e.* glass crystallization) occurs, releasing the heat of fusion. Figure 1.4 shows a DTA curve for a $Cu_{47}Zr_{47}Al_6$ glass sample with the glass transition and crystallization indicated.

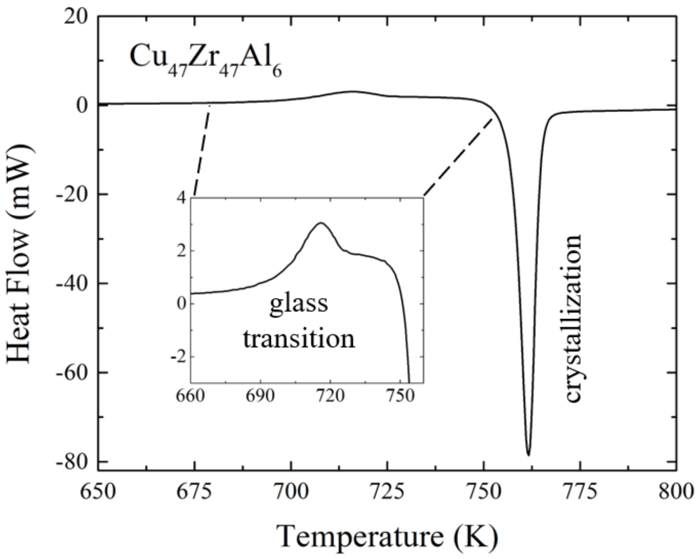

Figure 1.4 – A differential thermal analysis curve showing the heat flow with temperature for a $Cu_{47}Zr_{47}Al_6$ glass sample indicating the glass transition and crystallization.

An indication that the glass transition is in fact a thermodynamic transition comes from a consideration of the entropy of the liquid and the entropy of the crystal phase. The specific heat can be written as $c_p = T\left(\frac{\partial S}{\partial T}\right)_p$, where T is the temperature and S is the entropy. If the specific heat is known, then integrating $(c_p/T)dT$ gives the entropy as a function of temperature. Figure 1.5 (a) shows the specific heat of ethylbenzene in the equilibrium liquid, supercooled liquid, and glass phases. The thermodynamic glass transition temperature, T_g, is visible at the temperature associated with the large decrease in specific heat (~118 K). Degrees of freedom in the liquid "freeze out" at T_g and as a result, the specific heat rapidly drops and the slope of the entropy changes. Figure 1.5 (b) shows the entropy as a function of temperature for ethylbenzene. If we assume that the supercooled liquid bypasses crystallization and continues cooling below the glass transition temperature, then at the Kauzmann temperature, T_K, the entropy of the liquid is equal to the entropy of the crystal. If the trend continued, below T_K the entropy of the liquid would be lower than the entropy of the crystal, violating the third law of thermodynamics if at absolute zero the entropy of the glass phase remains lower than the perfect crystal phase. Kauzmann[4] first described this paradox, suggesting that spontaneous freezing always prevents the liquid from equilibrating near T_K. However, it has been shown that some polymers do not have a crystalline phase[5] and that in some cases the freezing time is much faster than the equilibration time of the liquid[6]. Kauzmann's solution to the paradox is therefore incomplete. Simulations of the supercooled liquid suggest that the glass phase must be the outcome of continued cooling of the liquid if crystallization is bypassed[7]. A discussion of the Kauzmann paradox in ethylbenzene is discussed by Speedy[7].

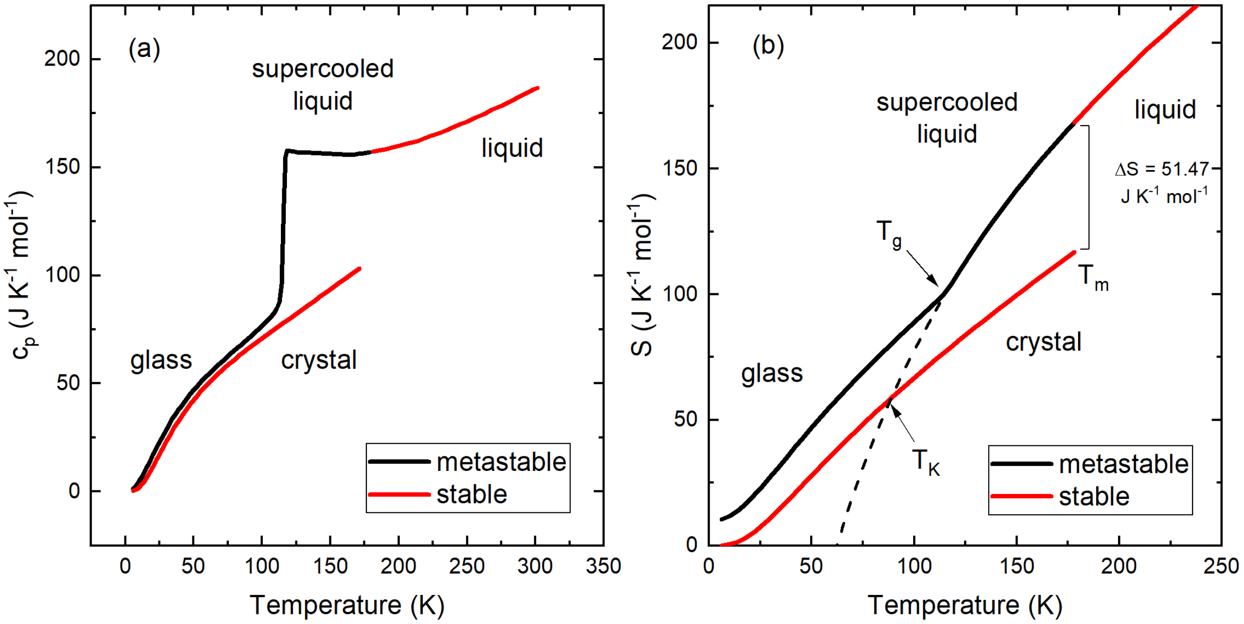

Figure 1.5 – The specific heat (a) and the entropy (b) as a function of temperature for ethylbenzene in the crystal, liquid, supercooled liquid, and glass. The extrapolated entropy from the supercooled liquid phase (dashed black line) intersects the crystal entropy at the Kauzmann temperature, T_K. Specific heat data are taken from Yamamuro et al. 1998 and integrated to find the entropy[8].

1.2 Glass Forming Ability

The processes required to create a glass are not completely understood. There is a significant difference in the ease of forming a glass across materials. For example, some metallic liquids require a cooling rate of 10^6 K/s to bypass crystallization and form a glass while network forming silicates readily form a glass by radiative and convective cooling in ambient conditions. Figure 1.6 shows a schematic of a time-temperature-transformation (TTT) curve, indicating the slowest cooling rate required to bypass nucleation and growth in order to form a glass, which is known as the critical cooling rate. Remaining to the left of the crystal phase curve during cooling ensures that the material remains liquid and forms a glass. Determining the critical cooling rate is complicated, however, and requires significant experimental work. To complicate the issue further, specific applications may require a glass of large dimensions. However, even though small amounts of liquid can be cooled quickly in controlled experimental setups, a bulk liquid cannot be cooled at such high rates. Despite our limited understanding of glass formation, significant progress has been made in determining the criteria for this. The formation of bulk metallic glasses (BMGs) was particularly expensive and difficult until Inoue[9] set the stage for Peker and Johnson to discover the first Zr-based BMG[10]. Inoue later suggested three empirical criteria for creating a BMG, formally known as the Inoue Criteria[11]. To begin with, alloys should contain more than three elements. Secondly, there should be a large mismatch between the sizes of the elements used in the material. Finally, the elements should have a large negative heat of mixing. Several theories of the glass transition (discussed later) give justification for these criteria.

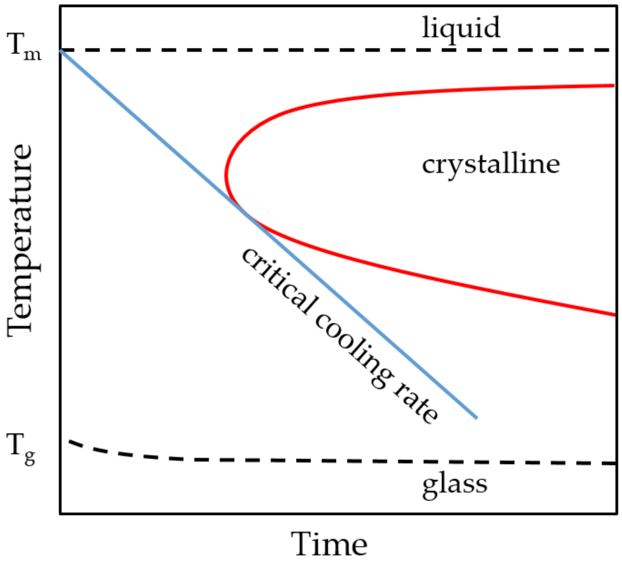

Figure 1.6 – A schematic of a time temperature-transformation-curve showing the critical cooling rate required to bypass nucleation and growth to form a glass. Adapted from fig. 1.3 in M. Blodgett's dissertation[2] with permission.

There are various measures for determining how well a liquid forms a glass. Two of the most obvious include the maximum thickness that the glass can be made, known as the critical casting thickness, and the critical cooling rate necessary for the liquid to form a glass. The critical casting thickness is related to the critical cooling rate as well as to the thermodynamic properties of the liquid controlling heat flow. For a bulk liquid to be cooled completely to a glass, the minimum cooling rate for all parts of the sample must be greater than the critical cooling rate. The critical casting thickness is often used as a proxy for glass forming ability. A significant amount of work has been done to predict the glass forming ability from experimentally measured properties. Angell first plotted the viscosity as a function of T_g/T, known as an Angell plot. He defined strong liquids as those with an Arrhenius behavior over a large temperature range, and he defined fragile liquids as those with a highly non-Arrhenius behavior[12,13]. The fragility of a material is then defined by the temperature dependence of the viscosity. Figure 1.7 is a schematic Angell diagram showing strong and fragile systems. Network forming glasses such as silicates tend to be strong whereas metallic alloys tend to be between strong and fragile. The kinetic fragility parameter, m, is defined from the Angell plot as the slope of the derivative of the viscosity, η, with respect to T_g/T at the glass transition temperature,

$$m = \left.\frac{dlog_{10}(\eta)}{d\left(T_g/T\right)}\right|_{T=T_g} . \qquad 1.4$$

The kinetic fragility parameter as well as the reduced glass transition temperature, $T_{rg} = T_g/T_l$, are believed to correlate with glass forming ability (GFA)[14–18]. Smaller m and larger values of T_{rg} are related to better GFA. This is clear in T_{rg} because the difference in the melting temperature and the temperature of the supercooled liquid is proportional to the driving free energy encouraging nucleation. Therefore, a larger value of T_{rg} means that the driving energy is smaller when crystallization becomes kinetically arrested. A recent study shows that a linear combination of the reduced glass transition temperature and the kinetic fragility parameter gives a good prediction for the critical casting thickness[18–20].

It is rarely possible to extract the kinetic fragility parameter from experimental results because it is difficult to measure the viscosity near the glass transition temperature. Several methods now exist to extract the fragility from high temperature viscosity data[21–23]. Taking this a step further, the fragility can be determined simply from properties of the liquid[24,25]. It is also possible to get a measure of the fragility from the first peak in the X-ray structure factor. The structures of strong glasses vary smoothly with cooling into the glass, while fragile liquids exhibit a jump in the first peak of the structure factor with cooling into the glass[26].

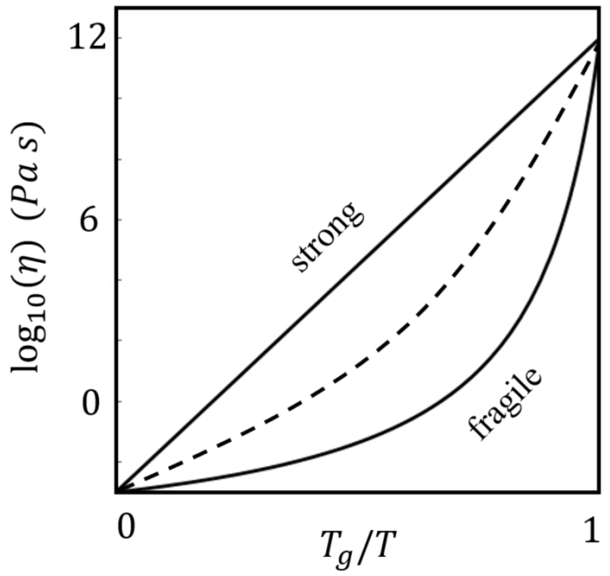

Figure 1.7 – A schematic Angell plot showing the difference in viscosity for strong and fragile systems. The dashed line shows where the majority of metallic alloys exist on the plot. This figure is adapted from fig. 1.7 in Matthew Blodgett's dissertation[2] with permission.

1.3 Theories of the Glass Transition

This section is not a comprehensive review of all the theories of the glass transition. Instead, provided here is an overview of several important glass transition theories. The free volume, energy landscape, mode coupling, AGDM, and avoided critical point / frustrated limited domains theories are briefly discussed.

1.3.1 Free Volume Model

The first developments in the free volume model were made by Eyring in the 1930s where it was predicted that communally shared volume gives rise to the entropy of vaporization and the entropy of fusion[27,28]. In 1951, Fox and Flory proposed that the glass transition occurs because of a decrease in the free volume of liquids as temperature decreases below a critical temperature[29]. At the time, the glass transition was seen as a second order phase transition. Doolittle[30] and Cohen[31] separately derived a diffusion coefficient from the free volume,

$$D \propto \exp\left(-\frac{\gamma v^*}{v_F}\right), \qquad 1.5$$

where v_F is the free volume, γ is the overlap factor, and v^* is a cutoff volume that controls when molecular transport occurs. From here, Cohen and Turnbull formalized the free volume model to explain the glass transition[32]. Cohen and Grest then extended the model using concepts from percolation theory to include thermodynamic behavior and to incorporate a formalized temperature dependence of the free volume, giving rise to a free volume viscosity equation[33],

$$\eta = \eta_0 \exp\left(\frac{B}{(T-T_o)\sqrt{(T-T_0)^2+CT}}\right), \qquad 1.6$$

where T_o, B, and C are fitting parameters.

Cohen, Turnbull, and Grest made four assumptions in their free volume model: (1) each atom is in a cell or cage surrounded by its neighboring atoms making it possible to associate a local volume to each atom; (2) volume beyond that of a critical volume is considered free volume; (3) atomic transport can occur when voids have a volume greater than a critical volume, nearly equal to the molecular volume, that forms due to rearrangement of free volume; and (4) there is no energy required to rearrange free volume. The glass transition temperature is the temperature at which the amount of free volume goes to zero. As such, explaining the glass transition within the model is equivalent to explaining the temperature dependence of the free volume. In the model, the glass transition is a characteristic of all liquids and must occur as long as crystallization is bypassed.

The theory explains the stability of the amorphous phase through the redistribution of free volume. The free energy in the liquid or glass state is minimized when the free volume is distributed randomly. Because a random distribution cannot occur in the crystalline phase, the free energy is lower in an amorphous phase than in a crystalline phase of the same volume. The authors of the theory point out several limiting assumptions including the free energy approximation, the lack of thermally activated motion at low temperatures, and the time dependence of the solid-like and liquid-like regions.

1.3.2 Energy Landscape Model

In 1968 Goldstein published his energy landscape model to help construct a better theory of viscous flow and the glass transition[34]. He describes the energy landscape in phase space where the ground state energy minimum is the crystal phase and other local minima are the amorphous phases. These local minima exist because the atoms in the glass phase, similar to those in the crystalline phase, experience restoring forces when they are displaced by a small distance. The extent of these restoring forces determines the barrier heights. The glass phase, similar to the crystalline phase, is therefore mechanically stable. It is well known that thermodynamic glass properties such as the entropy, volume, and specific heat depend on the thermal history[35,36]. The glass phase data in fig. 1.5 therefore depends on the thermal history of the ethylbenzene sample whereas the crystalline data represents the lowest energy minima in the energy landscape model and has one possible value. This suggests that the number of local minima representing the possible amorphous phases in the energy landscape is large and that the local minima vary in depth. Figure 1.8 is a schematic two-dimensional energy landscape. The system traverses this landscape via thermally activated jumps between minima where groups of atoms rearrange. At sufficiently high temperatures when the thermal energy becomes an appreciable size of the landscape barrier heights, the model breaks down. This occurs at a temperature, T_x, between the melting temperature and the glass transition temperature. Although the energy landscape model paints a physically intuitive picture of the crystal, glass, and liquid phases the theory is limited in predictive power because the phase space landscape is unknown and complicated.

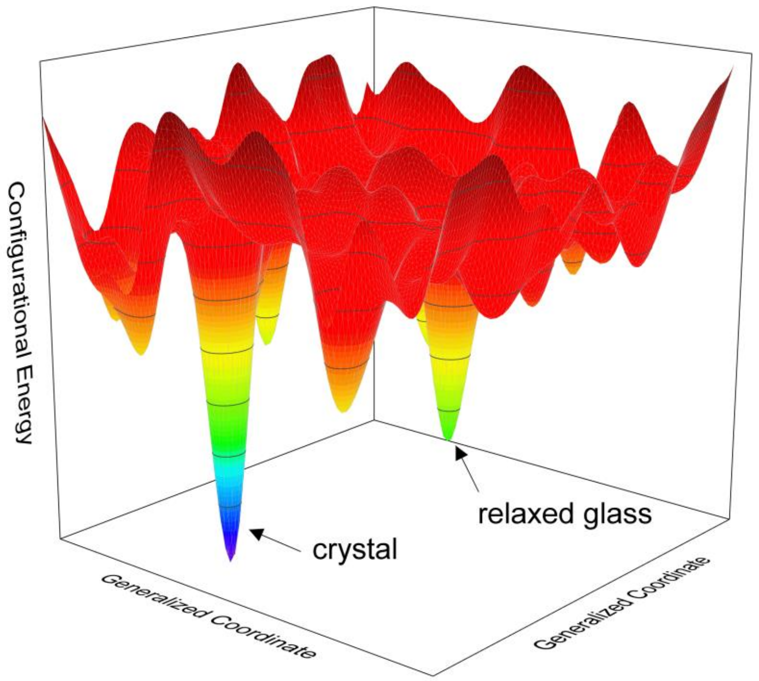

Figure 1.8 – A schematic two-dimensional energy landscape showing the lowest energy crystal minimum and the relaxed glass local minimum.

1.3.3 Mode Coupling Theory

It is well known that supercooled liquids experience a two-step process during relaxation[1,37–39]. In the fast β-relaxation process, an atom collides with another atom and the pair remains correlated for a short time. However, as the temperature decreases, the atoms remain correlated for a longer time because each atom is trapped inside a cage formed by neighboring atoms. The correlation with its neighbors localizes the atom and this localization causes a plateau to develop in the intermediate scattering function and the shear stress autocorrelation function. The length of the plateau is equal to the slow α-relaxation time after which the atom is free from its neighboring atoms and can continue to diffuse. It is interesting to note that the caging effect begins in the ergodic supercooled liquid state in which the system is free to explore all possible states because α-relaxation occurs. The two-step process is therefore seen as a precursor to the nonergodic glassy state.

The Mode Coupling Theory (MCT), originally developed in 1984[40,41] as a model for exploring the dynamics in supercooled liquids is dissimilar to the energy landscape model. In the MCT, dynamics are accounted for without regard for thermal activation. The two models are therefore complementary and work in separate temperature ranges. In fact, evidence suggests that the high temperature cutoff for the validity of the energy landscape model, T_x, is the same as the low temperature cutoff for the validity of the MCT[42,43]. Dynamics dominate atomic rearrangement at high temperatures whereas thermal activation controls atomic rearrangement at low temperatures closer to the glass transition.

The MCT uses the static structure factor, $S(q)$, as an input to self-consistent nonlinear equations of motion acting on the density autocorrelation function. The coupled equations predict an ideal glass transition (dynamical divergence) where the supercooled liquid goes from an ergodic state to a nonergodic glassy state. The theory correctly predicts the two-step relaxation process in supercooled liquids. However, it fails to accurately describe the viscosity at temperatures approaching the mode coupling temperature, T_c, which is higher than the glass transition temperature, T_g. As the temperature approaches T_c, the timescale associated with the α-relaxation process, τ_α, diverges causing the viscosity to diverge[1]. In reality, the structural relaxation time near the calorimetric glass transition temperature is 10 - 100 seconds. The divergence likely occurs because the MCT does not account for thermal activation at low temperatures[1].

1.3.4 Adam, Gibbs, and Di Marzio Theory

The Adam, Gibbs, and Di Marzio theory (AGDM) was originally developed for polymeric systems[44] and was later studied more generally[45]. The authors of the AGDM theory sought a solution to the Kauzmann paradox based on cooperative relaxation. In the theory, larger and larger regions relax together at lower and lower temperatures. The size of the rearranging regions is controlled by the configurational entropy, which is more restricted as temperature decreases. The AGDM theory resolves the Kauzmann entropy paradox by suggesting that there exists a kink in the entropy at T_K so that the entropy of the liquid is never below the crystal entropy. The kink is the result of a second order thermodynamic phase transition. Within the theory, the configurational entropy, S_c, is connected to the viscosity,

$$\eta = \eta_0 \exp\left(\frac{C}{TS_c}\right), \tag{1.7}$$

where η_0 is the infinite temperature viscosity and C is a constant. The AGDM produces a viscosity (or equivalently, a relaxation time) in the form of the Vogel-Fulcher-Tammann equation

$$\eta = \eta_0 \exp\left(\frac{D^* T_0}{T - T_0}\right), \tag{1.8}$$

where η_0, D^*, and T_0 are typically seen as fit parameters. However, within AGDM theory, the temperature T_0 is a fundamental temperature equivalent to the Kauzmann temperature. Gibbs and Adam found that the ratio of the thermodynamic glass transition temperature and the second order phase transition temperature is approximately 1.30[45]. The divergence of the viscosity and the relaxation time at T_0 is the result of the second order transition. The fit parameter D^* is a fragility parameter, where large values correspond to strong liquids. Relating eq. 1.7 and eq. 1.8 shows that D^* and S_c are inversely related. Strong liquids, therefore, undergo a small change in configurational entropy as they cool towards the glass transition, while fragile liquids undergo a large configurational entropy change near T_g.

The authors of the AGDM theory suggest that the thermodynamic glass transition temperature is simply a convenient temperature for experimentalists and the more fundamental temperature is the Kauzmann temperature, where the second order phase transition occurs. However, the theory neither accounts for the two-step relaxation process in supercooled liquids nor the dynamic to thermally activated relaxation crossover that occurs at $T_c = T_x$. Both of these processes are precursors for the glass transition and occur at temperatures higher than T_K.

1.3.5 Frustration Limited Domains

Liquids exhibit short and medium-range order but do not have long-range order. The pair correlation function in metallic liquids (see Fig 1.2) damps to a value of 1.0 after 15Å, which is the value for a random distribution of atoms. This means that there is no correlation between atoms that are separated by greater than 15Å. In other words, there is no long-range order. However, there is structure in the pair correlation function for $q < 15$Å where the atoms are correlated. Short-range order describes the neighborhood of an atom in which a locally preferred structure exists. In crystalline materials, the locally preferred structure tessellates space to fill the entire volume. One might expect that as a liquid cools, its locally preferred structure should tessellate to fill all space and the glass should contain long-range order. However, this is not the case. In 1952, Frank proposed that liquids have locally preferred structures in the form of icosahedra that prevent long-range ordering due to their five-fold rotational symmetry[46]. Icosahedral ordering has been confirmed in metallic liquids using X-ray scattering[47]. Not all liquids contain icosahedral ordering but the prediction that locally preferred structures in the liquid are incompatible with long-range order holds significant weight[48].

Similar to the ADGM theory, the frustration limited domains (FLD) theory, also known as the avoided critical point theory, describes the growth of cooperative regions with a thermodynamic origin[49–52]. The origin of the cooperative regions is not from configurational entropy as in the ADGM theory. Instead, locally preferred structures exist in the liquid that are different from the crystal phase and the arrangement of the locally preferred structures minimizes energy[51]. Authors of the FLD theory propose a frustration mechanism that keeps atoms in the liquid from arranging into clusters of their locally preferred structure. The liquid experiences strain because the locally preferred structure is incompatible with long-range order. As the name suggests, geometric frustration breaks the liquid into domains where the size of the domain controls the relaxation time. Without frustration the liquid would reach a critical point at a temperature T^*, which is usually higher than the melting point. Frustration causes the critical point to be avoided[52]. At T^* the system changes from a high temperature liquid with little order to a low temperature liquid with a significant amount of local order. The avoided critical point is the reason for the transition from Arrhenius behavior to non-Arrhenius behavior in the supercooled liquid as temperature decreases. The FLD theory gives the viscosity in what is known as the KKZNT formula,

$$\eta = \eta_0 \exp\left[\frac{E_\infty + k_B T^* \left(\frac{T - T^*}{T^*}\right)^z \Theta(T^* - T)}{k_B T}\right], \qquad 1.9$$

where k_B is the Boltzmann constant, E_∞ is the high temperature activation energy, z is a constant typically taken to be $8/3$, and $\Theta(T^* - T)$ is the Heaviside function. The viscosity is Arrhenius at temperatures above $T^*$and super-Arrhenius below T^*. The FLD provides a natural explanation for the two-step relaxation process experimentally seen in liquids. Slow α-relaxation occurs because of the relaxations of the frustrated limited domain size. Fast β-relaxation is due to the relaxation of material not in the frustrated domains. Critics of the FLD theory suggest that it would be stronger if frustrated domains were experimentally observed[1].

1.4 Theories of Nucleation and Nucleation Measurements

This section is not a comprehensive review of all the theories of nucleation but an overview of the theories of nucleation used in later chapters of this dissertation. Both the classical nucleation theory and the diffuse interface theory will be described in detail. Additional theories such as the density functional approach will be mentioned.

Nucleation is the process by which a new phase is initiated. After the new phase is initiated, it grows until none of the initial phase remains if the transition is thermodynamically favored. In the liquid-crystal phase transformation, nucleation occurs in the supercooled liquid. Nucleation that occurs randomly in time and space (i.e. is stochastic) following a Poisson distribution is called homogenous nucleation. Heterogenous nucleation (which is stochastic in time) occurs when crystallization is initiated by an impurity, container wall, or a phase boundary. Homogenous nucleation occurs at lower temperatures (deeper supercoolings) than heterogeneous nucleation and is an intrinsic property of the liquid based on thermodynamic, kinetic, and structural properties. The discussions in the rest of this chapter are focused on homogenous nucleation. The goal of each nucleation theory is to determine the work required to create a cluster inside the parent phase that is large enough to be thermodynamically favored to grow.

1.4.1 Classical Nucleation Theory

The classical nucleation theory (CNT) is the first attempt to describe homogenous nucleation between phases. It was first derived to describe vapor-liquid phase transformations and later applied to liquid-crystal phase transformations. The CNT is based on the competition between a driving free energy term that encourages the new phase to form and a surface energy barrier term that opposes the new phase. It is easy to see in a simple one- or two-dimensional Ising model that when all lattice points (particles) have the same spin the system is in a ground state[53,54]. A spin that is flipped randomly in the lattice creates bonds of higher energy. This is analogous to the surface barrier term in the classical theory where the creation of a crystal cluster inside the liquid is thermodynamically unfavorable. However, if there is a sufficiently large fluctuation that brings together a cluster with n^* or more atoms or molecules of the new phase, or equivalently a cluster of radius r^* or larger, then the cluster prefers to grow. The nucleation rate, $I(T,t)$, is the temperature and time dependent rate at which critical clusters, clusters larger than r^* (or n^*), are formed.

The following derivation of the classical theory follows the work by Kelton and Greer[55]. Gibb's theory of thermodynamic fluctuations defines the probability that a density fluctuation creates a cluster of critical size or larger[56]. The minimum work of cluster formation is

$$W(n) = n\Delta\mu + \sigma A, \tag{1.10}$$

where n is the number of atoms or molecules in the cluster, $\Delta\mu$ is the difference in chemical potential between the parent and new phase for a single atom or monomer (i.e. the driving free energy), σ is the interfacial free energy (i.e. the barrier to nucleation energy term), and A is the surface area between the parent and new phase. For spherical clusters with an isotropic interfacial free energy, $A = (36\pi\bar{v}^2 n^2)^{1/3}$, where $\bar{v}$ is the volume of an atom or monomer. When deriving the CNT a few assumptions are made: (1) the clusters are spherical, (2) there is a sharp interface between the parent and new phase, and (3) bulk thermodynamic properties are good approximations for small cluster properties. Plotting the work of cluster formation as a function of the cluster size gives a maximum where the surface energy term dominates, then a decrease in work to zero where the surface and driving terms are equivalent. Figure 1.9 is a schematic of the work of cluster formation as a function of the cluster radius along with the competing surface and volume terms.

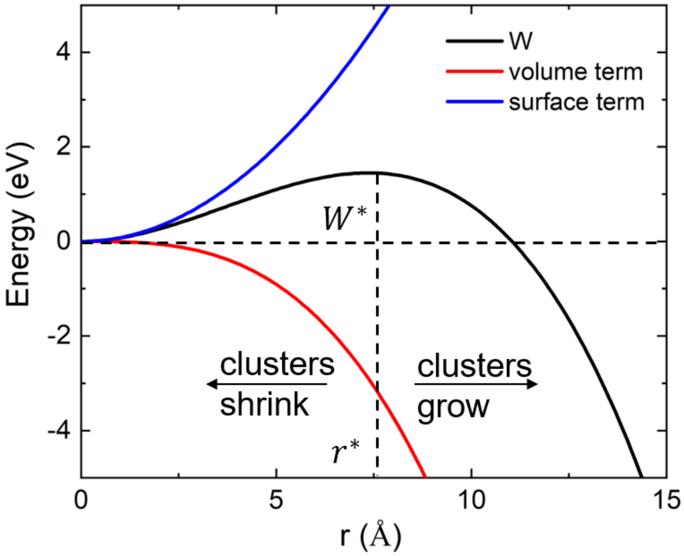

Figure 1.9 – A schematic of the work of cluster formation (black line) showing the competition between the driving free energy (red line) and the surface free energy (blue line). This figure is adapted from fig. 1 in Kelton, K. F. & Greer, A. L. The Classical Theory in *Nucleation in Condensed Matter: Applications in Materials and Biology* 19-54 (Elsevier, 2010) with permission.

Taking the derivative of the work of cluster formation and setting it to zero gives the critical cluster size

$$n^* = \frac{32\pi}{3\bar{v}}\left(\frac{\sigma}{|\Delta g|}\right)^3, \tag{1.11}$$

where $\Delta g = \Delta\mu/\bar{v}$. On average, clusters larger than n^* will grow and cluster smaller than n^* will shrink. Plugging n^* back into eq. 1.10 gives the critical work of cluster formation,

$$W^* = W(n^*) = \frac{16\pi}{3}\left(\frac{\sigma^3}{\Delta g^2}\right). \tag{1.12}$$

The work of cluster formation is often written in terms of the radius of a cluster,

$$W(r) = \frac{4\pi}{3} r^3 \Delta g + 4\pi r^2 \sigma, \tag{1.13}$$

where it is now obvious that there exists a driving volume term and a barrier surface term. In this notation the critical cluster size, r^*, is easily obtained, $r^* = 2\sigma / |\Delta g|$.

As previously stated, the classical theory assumes that the interface between the liquid or glass and the crystal phase is sharp. However, it has been shown in density functional calculations[57,58] and molecular dynamics simulations[59,60] that the interface is in fact diffuse and can be a significant fraction of the crystal size. The classical theory is relatively easy to use but it does not always explain experimental data. For example, in silicate glasses near the glass transition temperature the work of cluster formation must behave anomalously to account for the experimental steady state nucleation rate data[61–65]. A change in the slope of the interfacial free energy or the driving free energy with temperature is often used as the explanation of this anomalous behavior in the work. It is unclear, however, what a sign change in the slope of the interfacial free energy means. It is possible that this anomalous behavior is unphysical and is due to incorrectly measured steady-state nucleation rates, which have very long induction times. Finally, the CNT does not account for the structural similarities or differences of the amorphous phase and the crystal phase, which has been shown to influence the nucleation barrier.

1.4.2 Diffuse Interface Theory

The diffuse interface theory (DIT) provides a natural way to account for the interface width and gives a reasonable explanation for the temperature dependence of the interfacial free energy. Turnbull laid the groundwork for the development of the DIT[66]. It was then formally proposed independently by Gránásy[67,68] and Spaepen[69] to bypass the capillarity approximation used in the classical theory. The main difference between the CNT and the DIT comes from the development of the work of cluster formation. Both Gránásy and Spaepen realized that an order parameter exists in the new phase that decays over the course of the interface width to some smaller value in the amorphous parent phase. Figure 1.10 shows a structural order parameter, $M(r)$, that decays from the center of the crystal across the interface region of width, δ, to near 0 in the liquid phase. R_H and R_S are the boundaries given by the driving free energy profile that defines the interface region. Within the DIT, the interface width exists because of a free energy barrier, $g(r)$, between the amorphous and crystal phases. The work of cluster formation is then calculated as a radially symmetric volume integral over the free energy barrier across the interface,

$$W(n) = \int_{0}^{\infty} g(r) \cdot 4\pi r^2 \cdot dr, \tag{1.14}$$

where r is the distance from the cluster center. Without the help of density functional approaches, it is difficult to calculate the free energy barrier exactly.

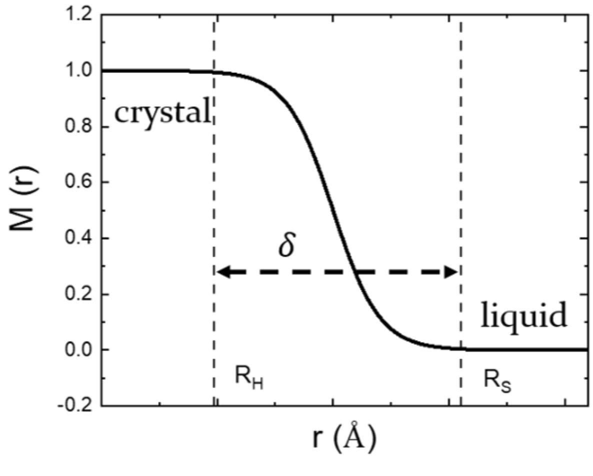

Figure 1.10 – A structural order parameter decaying over the crystal/liquid or crystal/glass interface.

Gránásy and Spaepen expressed the free energy as $g(r) = \Delta h(r) - T\Delta s(r)$, where Δh and Δs are the enthalpy and entropy differences between the liquid or glass and crystal. The terms are approximated by a series of step functions that define the interface width. The enthalpy is given by $\Delta h(r) = \Delta h_0[1 - \Theta(r - R_H)]$, where R_H is the step function location for the enthalpy. The entropy is given by $\Delta s(r) = \Delta s_0[1 - \Theta(r - R_S)]$, where R_S is the step function location for the entropy. Figure 1.11 is a schematic illustration of the enthalpy and entropy as a function of the distance from the crystal cluster center and the step functions used in the approximation.

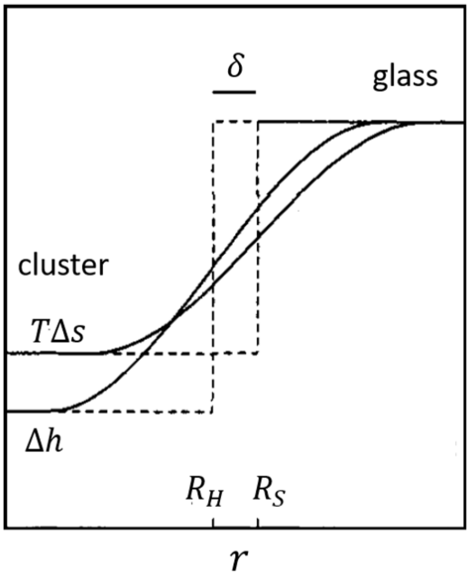

Figure 1.11 – The enthalpy and entropy curves as a function of the distance from the cluster center (solid lines) approximated by step functions (dashed lines) defining the interface width, δ. This schematic is reproduced from fig. 1b in Gránásy, L. Diffuse Interface Approach to Vapor Condensation. *Europhys. Lett.* **24**, 121–126 (1993) with permission.

Defining the enthalpy and entropy as step functions makes it simple to solve eq. 1.14 for the work of cluster formation,

$$W = \frac{4\pi}{3}(R_H^3\Delta h_0 - R_S^3 T\Delta s_0). \tag{1.15}$$

For sufficiently large clusters where the cluster is much larger than the interface thickness, it can be assumed that $R_S - R_H = \delta$. Using this relation, setting the derivative of the work with respect to R_S to zero, and solving for R_S gives the critical size,

$$R_S^* = \frac{\delta \Delta h_0 + \delta\sqrt{\Delta h_0 T \Delta s_0}}{\Delta h_0 - T\Delta s_0}. \tag{1.16}$$

The critical work of cluster formation is then given by

$$W^* = -\frac{\frac{4\pi}{3}\delta^3 \Delta h_0 T \Delta s_0}{\Delta h_0 + T\Delta s_0 - 2\sqrt{\Delta h_0 T \Delta s_0}}, \tag{1.17}$$

which is equivalent to eq. 4 by Gránásy[70]. The critical work of cluster formation is proportional to the cube of the interface width, giving the expression as the volume of the interface multiplied by the energy barrier per volume to transition from the amorphous phase to the crystal phase. To use this formulation of the DIT, one must know Δh_0 and Δs_0 separately. The Turnbull approximation is convenient because $\Delta g = \Delta h_f - T\Delta s_f$, where Δh_f is the heat of fusion and Δs_f is the entropy of fusion. The heat of fusion and the enthalpy of fusion are related by $\Delta h_f = T_m \Delta s_f$, where T_m is the melting temperature. Equating W^* from the classical theory and W^* from the diffuse interface theory and solving for the surface tension gives a reasonable justification for the temperature dependence of the interfacial free energy required in the CNT to match experimental data[71,72]. To first order, the interface width shows the significance of the amorphous and crystal phase structures in determining the nucleation rate.

1.4.3 Other Nucleation Theories

The goal of this subsection is to mention a few other theories of nucleation that go beyond the classical theory. Neither the diffuse interface theory nor the classical theory accounts for the structure of the amorphous and crystal phases directly. It is insightful to look at the more fundamental density functional theory (DFT), where the density or a bond orientational order parameter is used to describe the structure of the crystal and amorphous phases. The free energies are functions of the density (or an orientational order parameter) and are minimized to calculate the density profile over the region of the two phases. In the DFT treatment, fluctuations in the density lead to critical clusters that grow and transform the amorphous phase to the crystal phase. Results from density functional calculations agree with the diffuse interface theory in that the interface between the crystal and amorphous regions is not sharp. This leads to a different critical work of cluster formation from the one predicted by the classical theory. There are several DFT approaches for describing nucleation including the single-order-parameter approach, also known as the semi-empirical density functional approximation (SDFA), the perturbative density-functional approximation (PDFA), and weighted density functional approximation (WDA). For oxide glasses, Gránásy found that the DIT and the SDFA perform better than other nucleation theories[73]. The reader is referred to the text by Kelton and Greer[71] for an overview of these theories.

1.4.4 Kinetic Nucleation Model

The kinetic model for cluster formation was first developed by Volmer and Weber[74] who proposed that clusters evolve by the attachment or detachment of a single atom or monomer at a time following a set of bi-molecular reactions. The nucleation rate is defined as the number of clusters to pass by the critical size per time. The equilibrium distribution of clusters follows directly from the probability of a fluctuation to occur of a certain size. This distribution gives a non-physical cluster density for $n > n^*$, where the cluster distribution increases with increasing n. Volmer and Weber chose the equilibrium distribution for $n < n^*$ and avoided the unphysical part of the distribution by assuming that all clusters larger than the critical size grow quickly to large sizes so the cluster distribution for $n > n^*$ is zero. In this case, the Volmer Weber nucleation rate is given by

$$I^{VW} = k_{n^*}^{+} \, N_A \exp\left(-\frac{W^*}{k_B T}\right), \tag{1.18}$$

where $k_{n^*}^{+}$ is the forward reaction rate at the critical size and N_A is Avogadro's number. Becker and Döring[75] knew that after some time of nuclei development, a system must reach a steady-state where the nucleation rate is no longer time dependent. The steady-state distribution is continuously decreasing for all n and therefore deviates drastically from the equilibrium distribution for $n \geq n^*$. They found that the nucleation rate is given by a sum of contributions around the critical cluster size, known as the critical region. This summation of terms produces an additional contribution to the steady-state nucleation rate known as the Zeldovich factor,

$$Z = \left(\frac{|\Delta\mu|}{6k_B T n^*}\right)^{\frac{1}{2}}. \tag{1.19}$$

The steady state nucleation rate is given by $I^{st} = Z \, I^{VW}$. In all cases the steady-state nucleation rate can be written in the general form,

$$I^{st} = A^* \exp\left(-\frac{W^*}{k_B T}\right), \tag{1.20}$$

where A^* is a temperature-dependent prefactor that includes the diffusion coefficient.

1.4.5 Nucleation Rate Measurements

Nucleation rate measurements were not performed in this work. However, the data from the measurements of others was used to model nucleation and growth[76] (discussed in chapter 5). Here the process of measuring the nucleation rate in silicate glasses is described.

A two-step heating treatment is used to measure the steady-state nucleation rate of silicate glasses as long as the temperature region of significant nucleation does not overlap with the temperature region of significant nuclei growth. A schematic of a two-step heat treatment is shown in fig. 1.12 (left), where nuclei are first developed at the nucleation treatment temperature, T_N, and then are grown to visible size (for a microscope) at the crystal growth temperature, T_G. There is no significant nuclei production during the growth treatment. Figure 1.12 (right) shows that in some glasses the regions of nucleation and growth are well separated so that the two-step heating treatment is a reasonable method to determine the steady-state nucleation rate.

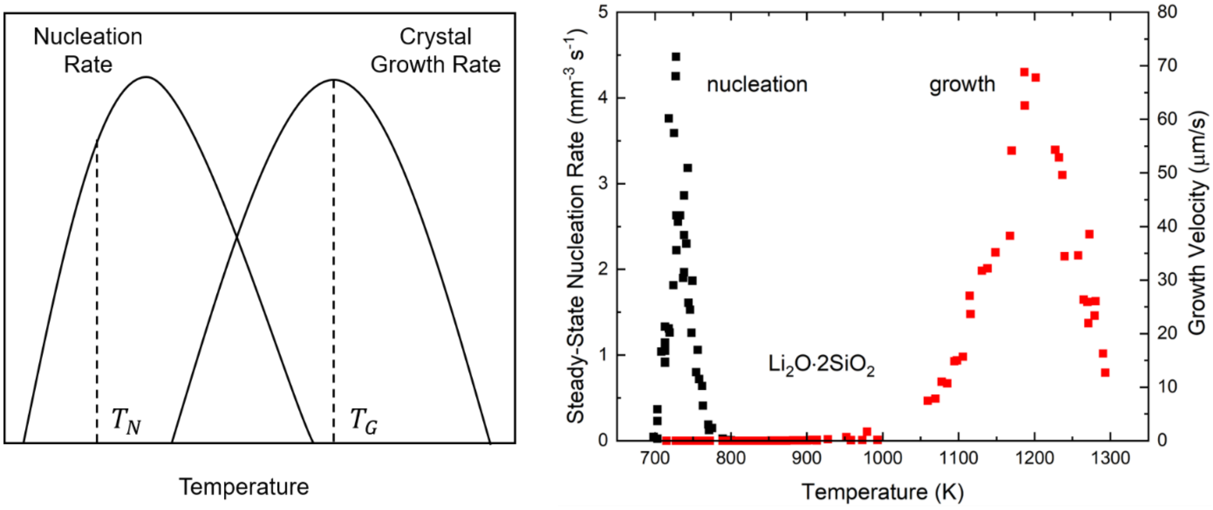

Figure 1.12 – A schematic of the two-step heat treatment that occurs at a nucleation temperature to develop nuclei and then at a growth temperature to grow the nuclei (left). The steady-state nucleation rate and the crystal growth velocity of lithium disilicate glass are shown on the right. The left-hand side of this figure is adapted from fig. 5 in Kelton, K. F. & Greer, A. L. Crystallization in Glasses in *Nucleation in Condensed Matter: Applications in Materials and Biology* 279–329 (Elsevier, 2010) with permission.

After the growth treatment, the sample is polished and etched using hydrofluoric acid to highlight the crystal/glass interface. The nuclei are counted to obtain the nuclei produced per volume per time, which is plotted against the nucleation treatment time. Initially the nucleation rate is time dependent. For later times, however, the number of nuclei produced becomes independent of time and the steady-state nucleation rate, I^{st}, is reached. The intercept of an extrapolation of the nuclei produced per time in the steady-state region back to the time-axis is the induction time, θ, which is related to the more fundamental transient time, τ. This is shown in fig. 1.13, where the number of nuclei produced per volume, N_v, is plotted as a function of the nucleation treatment time for a barium disilicate glass. The slope of the nuclei produced per time after the transient region gives the steady-state nucleation rate. Using the two-step nucleation and growth treatment method at various nucleation treatment temperatures gives I^{st} as a function of temperature. Figure 1.14 shows the steady-state nucleation rate for four silicate glasses.

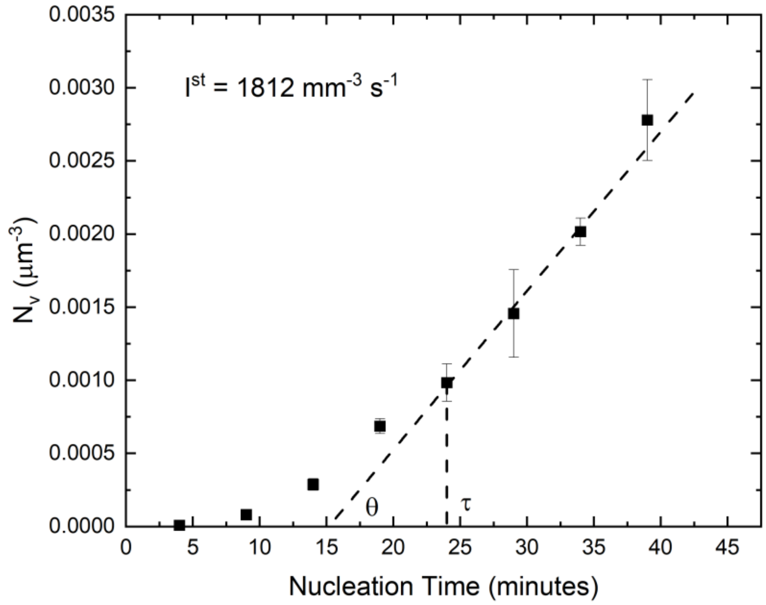

Figure 1.13 – The number of nuclei produced per volume as a function of the nucleation treatment time at the maximum nucleation rate temperature, 985 K, for a barium disilicate glass. The induction time and transient time are labeled on the x-axis. Data are from Xia et al. 2019[61].

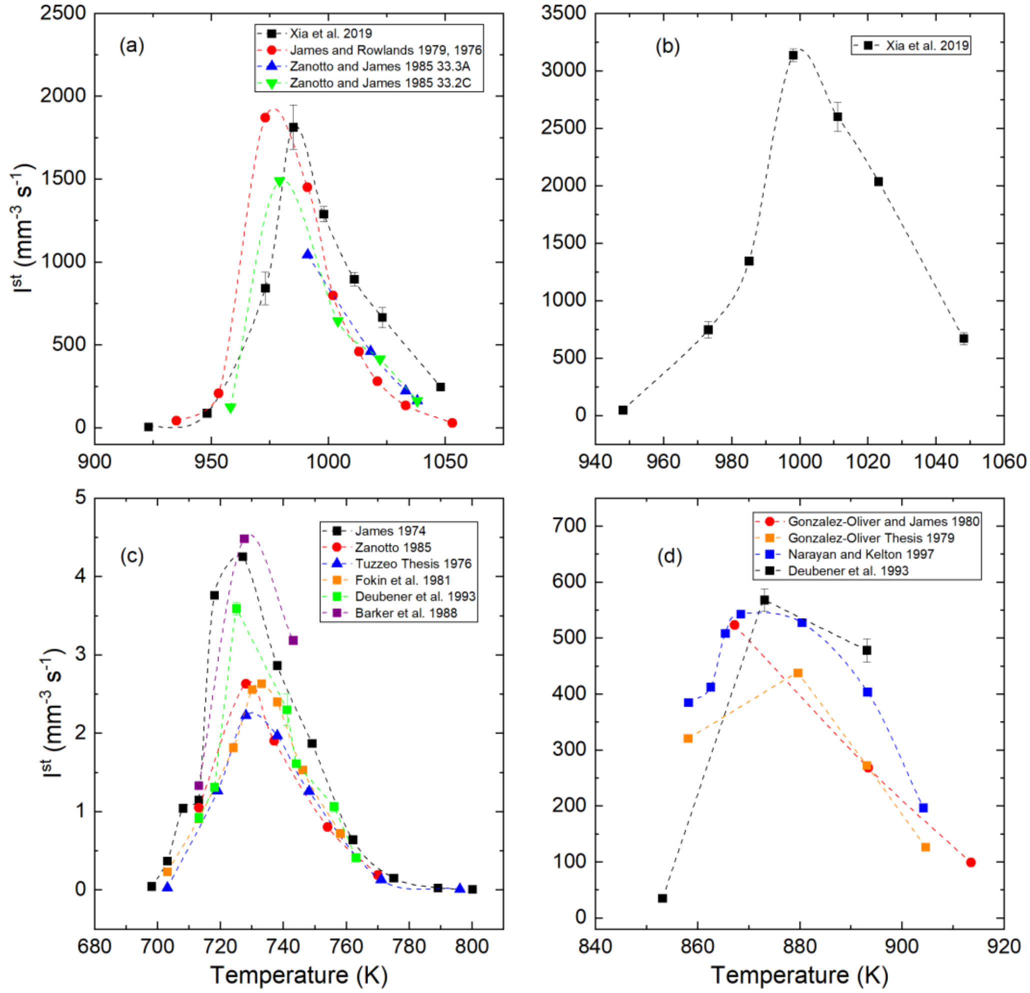

Figure 1.14 – The steady state nucleation rate as a function of temperature for (a) $BaO\cdot 2SiO_2$ glass[61,77,78], (b) $5BaO\cdot 8SiO_2$ glass[61], (c) $Li_2O\cdot 2SiO_2$ glass[65,78–82], and (d) $Na_2O\cdot 2CaO\cdot 3SiO_2$ glass[80,83–85].

1.4.6 The Low Temperature Anomaly

It is well known that the classical theory gives rise to anomalous results at low temperatures in many silicate glasses such as lithium disilicate, barium disilicate, and soda-lime silicate[61,62,86]. There is general agreement in the silicate glass community that the classical theory performs well at high temperatures, above the maximum nucleation rate temperature. In this region, the interfacial free energy with temperature is well described by a linearly increasing value with increasing temperature. The linear dependence of the interfacial free energy can be explained using the diffuse interface theory and a temperature-dependent interfacial width and solving for the equivalent interfacial free energy in the DIT. However, for lower temperatures, the work of cluster formation behaves anomalously, saturating or even starting to increase rather than decrease with decreasing temperature. In the classical theory, the work of cluster formation is a function of the interfacial free energy and the driving free energy. The anomalous behavior can therefore either be manifest in the surface free energy or in the driving free energy as a slope change or nonlinearity. Figure 1.15 shows the anomalous behavior of the critical work of cluster formation, interfacial free energy, driving free energy, and the interface width as a function of temperature in a barium disilicate glass. The deviations of the measured data from the solid lines (expected trends) clearly show the low temperature anomalous behavior.

Another possibility is that the classical theory breaks down at low temperatures because of one of the egregious assumptions made in its derivation, such as the assumption that bulk properties hold at the atomic scale, the clusters are spherical, or the nucleation kinetics are much more complicated than modeled in the classical theory. Others suggest that the classical theory works well and that the experimental measurements of the steady-state nucleation rate are incorrect. They claim that experiments measuring the number of nuclei formed as a function of time are not performed for a long enough time to reach the steady-state, and as such, the nucleation rate is larger than the experimentally measured values at the temperatures below the maximum nucleation rate. At the time of writing this dissertation, experiments where nuclei are developed in a barium silicate glass sample for greater than 100 days are in progress to test this latter view.

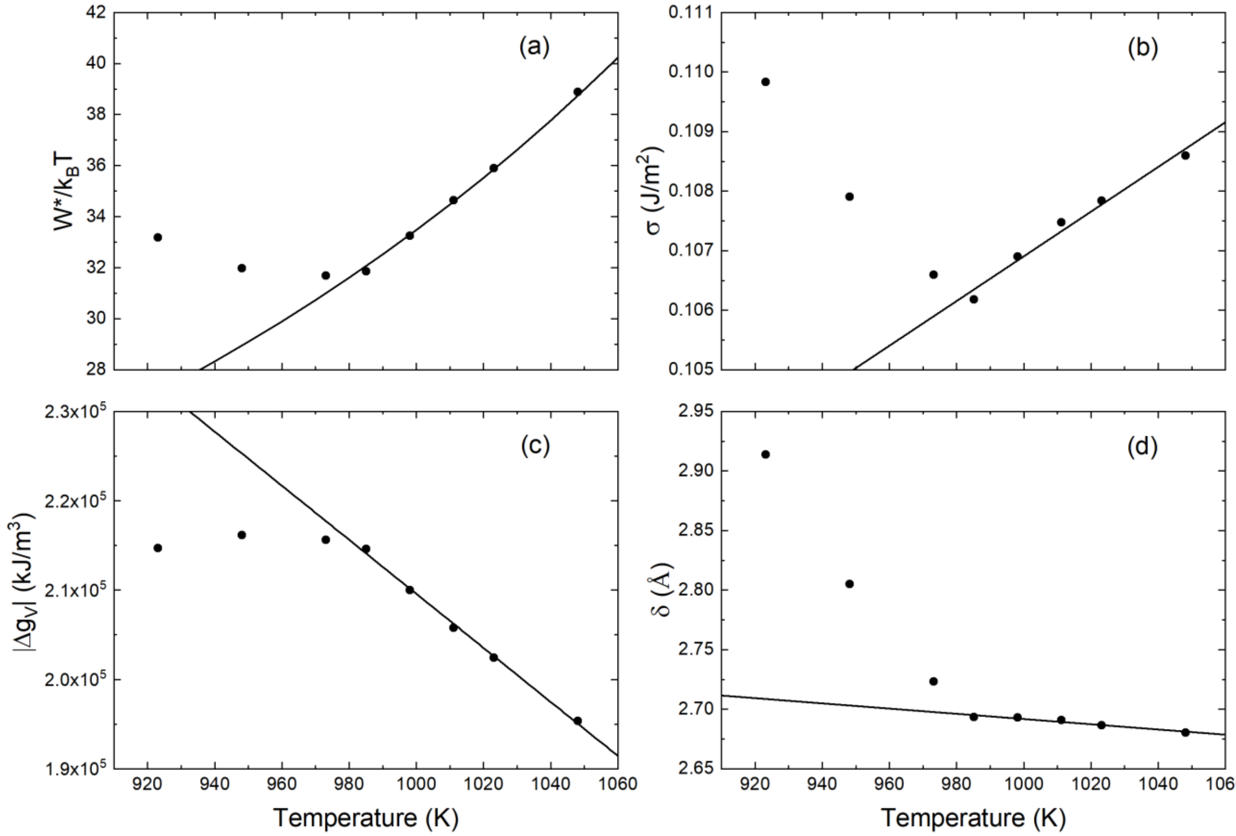

Figure 1.15 – The data points are the required values so that the measured steady-state nucleation rates match the classical (a-c) or the diffuse interface (a,d) theory steady-state nucleation rates. The solid lines are the expected trends assuming the CNT or DIT are valid and the steady-state nucleation rate data are incorrect in the plots of (a) the critical work of cluster formation, (b) the interfacial free energy assuming the Turnbull approximation for the driving free energy, (c) the driving free energy assuming the high temperature linear dependence of the interfacial free energy, and (d) the interface width. These data are for a barium disilicate glass with the growth velocity[87] used to determine the diffusion coefficient.

1.5 Containerless Processing

Bypassing heterogeneous nucleation so that homogeneous nucleation can be studied is a difficult task. Heterogeneous nucleation occurs when a supercooled liquid is in contact with a container wall, impurity, or other crystal. This occurs because the energy barrier for nucleation decreases at the contact sites, making nucleation easier. Many metals are particularly reactive to containers and have a high melting point compared to other materials making them difficult to study in the supercooled state.

It is possible to minimize these effects by using containerless processing. In containerless processing, samples are levitated so that there is no container wall that can initiate crystallization allowing for the deeply supercooled liquid to be studied. Containerless processing techniques include electrostatic levitation (ESL), electromagnetic levitation (EML), acoustic levitation, and aerodynamic levitation. In acoustic levitation, intense sound waves are used to levitate samples[88]. Both metal and non-metal samples can be levitated, unlike in EML where samples must be conducting. Samples levitating in sound waves are often unstable, so accurate measurements of the liquid can be difficult. In contrast, aerodynamic levitation uses a finely controlled stream of gas to levitate samples which typically has better stability than acoustic levitation[89]. However, the gas used for the levitation leads to large temperature gradients across the sample and gas impurities could lead to heterogeneous nucleation. A combination of acoustic and aerodynamic (aero-acoustic) levitation is used in some experiments to bypass the limitations of each method individually[90] but will not be discussed further in this dissertation.

In ESL, a sample is levitated between a series of electrodes that control the electric field around the sample. Temperature, density, viscosity, and crystal growth velocity can be measured accurately in ESL. A transportable ESL now exists so that the structure of metallic liquids can be studied using X-ray scattering at the Advanced Photon Source at Argonne National Lab[91]. An ESL is also permanently located at the Oak Ridge National Lab Spallation Neutron Source to measure the structure of liquids using neutron scattering. Both of these were designed and constructed in Kelton's group.

In EML metal samples are levitated between water cooled coils connected to a high power radio-frequency (rf) generator, producing rf electromagnetic fields at the location of the sample[92,93]. In many metals, the temperature due to levitation is enough to melt the sample, making it impossible to study the supercooled liquid without an additional cooling mechanism, such as processing the sample in an inert gas atmosphere so that additional heat is conducted away from the sample by the gas. Another method to study the supercooled liquid in EML is to use the microgravity environment on the International Space Station (ISS) to minimize the amount of power required to levitate the sample. Using electromagnetic levitation, it is possible to measure the same sample properties that are measured in ESL. In addition, it is possible to measure the specific heat using modulation calorimetry[94,95], and the electrical resistivity[96,97].

1.6 Summary

Chapter 1 covered the background for many of the topics in the remaining chapters of this dissertation including glasses and theories of the glass transition, nucleation theories, and containerless processing techniques. In addition, the qualitative differences between the liquid, supercooled liquid, glass, and crystal were discussed. The main takeaway is that relaxation timescales describing dynamics and the free energies controlling the thermodynamics help define the phases of matter and the transitions between them.

In chapter 2, the experimental and computational methods used for the experiments described in later chapters are discussed. Chapter 3 covers the resistivity measurements performed on the International Space Station on binary liquid alloys showing a saturation in the resistivity near the onset of cooperative structural rearrangement. In chapter 4, four methods of measuring the specific heat of liquids, glasses, and crystals are discussed. The methods include differential scanning calorimetry, modulated calorimetry, the τ_1 – method, and the power balance heat of fusion method. In chapter 5, differential thermal analysis nucleation and growth simulations are discussed for barium silicate glasses using the classical and diffuse interface theories of nucleation. Chapter 6 covers the X-ray scattering absorption and multiple scattering corrections developed for cylindrical sample geometries. Chapter 7 summarizes the findings of the work in the dissertation and describes remaining questions and future work.

1.7 References

1. Cavagna, A. Supercooled liquids for pedestrians. *Phys. Rep.* **476**, 51–124 (2009).

2. Blodgett, M. E. Thermophysical Properties and Structural Evolution of Supercooled Metallic Liquids. PhD Thesis. (2015).

3. Abraham, F. F. An isothermal-isobaric computer simulation of the supercooled-liquid/glass transition region: Is the short-range order in the amorphous solid fcc? *J. Chem. Phys.* **72**, 359–365 (1980).

4. Kauzmann, W. The Nature of the Glassy State and the Behavior of Liquids at Low Temperatures. *Chem. Rev.* **43**, 219–256 (1948).

5. DiMarzio, E. A. Equilibrium Theory of Glasses. *Ann. N. Y. Acad. Sci.* **371**, 1–20 (1981).

6. Angell, C. A., MacFarlane, D. R. & Oguni, M. The Kauzmann Paradox, Metastable Liquids, and Ideal Glasses: A Summary. *Ann. N. Y. Acad. Sci.* **484**, 241–247 (1986).

7. Speedy, R. J. Kauzmann’s paradox and the glass transition. *Biophys. Chem.* **105**, 411–420 (2003).

8. Yamamuro, O. *et al.* Calorimetric study of glassy and liquid toluene and ethylbenzene: Thermodynamic approach to spatial heterogeneity in glass-forming molecular Liquids. *J. Phys. Chem. B* **102**, 1605–1609 (1998).

9. Inoue, A., Zhang, T. & Masumoto, T. Zr-Al-Ni Amorphous Alloys with High Glass Transition Temperature and Significant Supercooled Liquid Region. *Materials Transactions, JIM* **31**, 177–183 (1990).

10. Peker, A. & Johnson, W. L. A highly processable metallic glass: Zr41.2Ti13.8Cu12.5Ni10.0Be22.5. *Appl. Phys. Lett.* **63**, 2342–2344 (1993).

11. Inoue, A. Stabilization of metallic supercooled liquid and bulk amorphous alloys. *Acta Mater.* **48**, 279–306 (2000).

12. Angell, C. A. Perspective on the glass transition. *J. Phys. Chem. Solids* **49**, 863–871 (1988).

13. Angell, C. A. Relaxation in liquids, polymers and plastic crystals - strong/fragile pattersn and problems. *J. Non. Cryst. Solids* **131–133**, 13–31 (1991).

14. Busch, R., Bakke, E. & Johnson, W. L. Viscosity of the supercooled liquid and relaxation at the glass transition of the Zr46.75Ti8.25Cu7.5Ni10Be27.5 bulk metallic glass forming alloy. *Acta Mater.* **46**, 4725–4732 (1998).

15. Lu, Z. P., Li, Y. & Ng, S. C. Reduced glass transition temperature and glass forming ability of bulk glass forming alloys. *J. Non. Cryst. Solids* **270**, 103–114 (2000).

16. Senkov, O. N. Correlation between fragility and glass-forming ability of metallic alloys. *Phys. Rev. B - Condens. Matter Mater. Phys.* **76**, 1–6 (2007).

17. Orava, J. & Greer, A. L. Fast and slow crystal growth kinetics in glass-forming melts. *J. Chem. Phys.* **140**, (2014).

18. Johnson, W. L., Na, J. H. & Demetriou, M. D. Quantifying the origin of metallic glass formation. *Nat. Commun.* **7**, 10313 (2016).

19. Lind, M. L., Duan, G. & Johnson, W. L. Isoconfigurational elastic constants and liquid fragility of a bulk metallic glass forming alloy. *Phys. Rev. Lett.* **97**, 1–4 (2006).

20. Johnson, W. L., Demetriou, M. D., Harmon, J. S., Lind, M. L. & Samwer, K. Rheology and ultrasonic properties of metallic glass forming liquids: A potential energy landscape perspective. *MRS Bull.* **32**, 644–650 (2007).

21. Richert, R. & Angell, C. A. Dynamics of glass-formig liquids. V. On the link between molecular dynamics and configurational entropy. *J. Chem. Phys.* **108**, 9016–9026 (1998).

22. Kaori, I., CT, M. & Angell, C. Thermodynamic determination of fragility in liquids and a fragile-to-strong liquid transition in water. *Nature* **398**, (1999).

23. Gangopadhyay, A. K. & Kelton, K. F. Measurements of the Temperature-Dependent Total Hemispherical Emissivity Using an Electrostatic Levitation Facility. *Int. J. Thermophys.* **38**, 1–8 (2017).

24. Dai, R., Gangopadhyay, A. K., Chang, R. J. & Kelton, K. F. A method to predict the glass transition temperature in metallic glasses from properties of the equilibrium liquid. *Acta Crystallogr. Sect. A* **172**, 1–5 (2019).

25. Dai, R., Ashcraft, R., Gangopadhyay, A. K. & Kelton, K. F. Predicting metallic glass formation from properties of the high temperature liquid. *J. Non. Cryst. Solids* **525**, 119673 (2019).

26. Mauro, N. A., Blodgett, M. E., Johnson, M. L., Vogt, A. J. & Kelton, K. F. A structural signature of liquid fragility. *Nat. Commun.* **5**, 4616 (2014).

27. Eyring, H. Viscosity, Plasticity, and Diffusion as Examples of Absolute Reaction Rates. *J. Chem. Phys.* **4**, 283–291 (1936).

28. Hirschfelder, J., Stevenson, D. & Eyring, H. A Theory of Liquid Structure. *J. Chem. Phys.* **5**, 896–912 (1937).

29. Fox, T. G. & Flory, P. J. Second-order transition temperatures and related properties of polystyrene. I. Influence of molecular weight. *J. Appl. Phys.* **21**, 581–591 (1950).

30. Doolittle, A. K. Studies in newtonian flow. II. the dependence of the viscosity of liquids

on free-space. *J. Appl. Phys.* **22**, 1471–1475 (1951).

31. Cohen, M. H. & Turnbull, D. Molecular transport in liquids and glasses. *J. Chem. Phys.* **31**, 1164–1169 (1959).

32. Turnbull, D. & Cohen, M. H. Free-volume model of the amorphous phase: Glass transition. *J. Chem. Phys.* **34**, 120–125 (1961).

33. Cohen, M. H. & Grest, G. S. Liquid-glass transition, a free-volume approach. *Phys. Rev. B* **20**, 1077–1098 (1979).

34. Goldstein, M. Viscous liquids and the glass transition: A potential energy barrier picture. *J. Chem. Phys.* **51**, 3728–3739 (1969).

35. Davies, R. O. & Jones, G. O. Thermodynamic and kinetic properties of glasses. *Adv. Phys.* **2**, 370–410 (1953).

36. Tool, A. Q. Relation between inelastic deformability and thermal expansion of glass in its annealing range. *J. Am. Ceram. Soc.* **29**, (1946).

37. Debenedetti, P. G. & Stillinger, F. H. Supercooled liquids and the glass transition. *Nature* **410**, 259–267 (2001).

38. Soklaski, R. A Molecular Dynamics Study of the Structure-Dynamics Relationships of Supercooled Liquids and Glasses. (Washington University in St. Louis, 2015). doi:10.1017/CBO9781107415324.004

39. Götze, W. & Sjögren, L. Relaxation processes in supercooled liquids. *Rep. Prog. Phys.* **55**, 241–376 (1992).

40. Leutheusser, E. Dynamical model of the liquid-glass transition. *Phys. Rev. A* **29**, 2765–2773 (1984).

41. U Bengtzelius, Götze, W. & Sjölander, A. Dynamics of supercooled liquids and the glass transition. *J. Phys. C Solid State Phys.* **17**, 5915–5934 (1984).

42. Sokolov, A. P. The glass transition: General scenario and crossover temperature. *J. Non. Cryst. Solids* **235**–**237**, 190–195 (1998).

43. Schrøder, T. B., Sastry, S., Dyre, J. C. & Glotzer, S. C. Crossover to potential energy landscape dominated dynamics in a model glass-forming liquid. *J. Chem. Phys.* **112**, 9834–9840 (2000).

44. Gibbs, J. H. & DiMarzio, E. A. Model of the glass transition and the glassy state. *J. Chem. Phys.* **28**, 373–383 (1958).

45. Gibbs, J. H. & Adam, G. On the Temperature Dependence of Cooperative Relaxation Properties in Glass-Forming Liquids. *J. Chem. Phys.* **43**, 139–146 (1965).

46. Frank, F. C. Supercooling of Liquids. *Proc. R. Soc. A Math. Phys. Eng. Sci.* **215**, 43–46

(1952).

47. Kelton, K. F. *et al.* First X-Ray Scattering Studies on Electrostatically Levitated Metallic Liquids: Demonstrated Influence of Local Icosahedral Order on the Nucleation Barrier. *Phys. Rev. Lett.* **90**, 195504 (2003).

48. Soklaski, R., Tran, V., Nussinov, Z., Kelton, K. F. & Yang, L. A locally preferred structure characterises all dynamical regimes of a supercooled liquid. *Philos. Mag.* **96**, 1212–1227 (2016).

49. Kivelson, D., Kivelson, S. A., Zhao, X., Nussinov, Z. & Tarjus, G. A thermodynamic theory of supercooled liquids. *Physica A* **219**, 27–38 (1995).

50. Chayes, L., Emery, V. J., Kivelson, S. A., Nussinov, Z. & Tarjus, G. Avoided critical behavior in a uniformly frustrated system. *Phys. A Stat. Mech. its Appl.* **225**, 129–153 (1996).

51. Tarjus, G., Kivelson, S. A., Nussinov, Z. & Viot, P. The frustration-based approach of supercooled liquids and the glass transition : a review and critical assessment. *J. Phys. Condens. Matter* **17**, (2005).

52. Sausset, F., Tarjus, G. & Viot, P. Tuning the fragility of a glass-forming liquid by curving space. *Phys. Rev. Lett.* **101**, 1–4 (2008).

53. Ising, E. Beitrag zur Theorie des Ferromagnetismus. *Zeitschrift für Phys.* **31**, 253–258 (1925).

54. Sethna, J. P. *Statistical Mechanics: Entropy, Order Parameters, and Complexity*. (Oxford University Press, 2006).

55. Kelton, K. F. & Greer, A. L. The Classical Theory. in *Nucleation in Condensed Matter: Applications in Materials and Biology* 19–54 (Elsevier, 2010).

56. Gibbs, J. W. *Scientific Papers, Vol. I, II*. (Longmans, Green, and CO., 1906).

57. Haymet, A. D. J. & Oxtoby, D. W. A molecular theory for the solid-liquid interface. *J. Chem. Phys.* **74**, 2559–2565 (1981).

58. Curtin, W. A. Density-functional theory of the solid-liquid interface. *Phys. Rev. Lett.* **59**, 1228–1231 (1987).

59. Broughton, J. Q. & Gilmer, G. H. Molecular dynamics of the crystal–fluid interface. V. Structure and dynamics of crystal–melt systems. *J. Chem. Phys.* **84**, 5749–5758 (1986).

60. Laird, B. B. & Haymet, A. D. J. The crystal-liquid interface of a body-centered-cubic-forming substance: Computer simulations of the r-6 potential. *J. Chem. Phys.* **91**, 3638–3646 (1989).

61. Xia, X. *et al.* Time-dependent nucleation rate measurements in BaO·2SiO2 and 5BaO·8SiO2 glasses. *J. Non. Cryst. Solids* **525**, (2019).

62. Fokin, V. M. *et al.* Crystal nucleation in glass-forming liquids: Variation of the size of the "structural units" with temperature. *J. Non. Cryst. Solids* **447**, 35–44 (2016).

63. Cassar, D. R., Serra, A. H., Peitl, O., Rodrigues, A. M. & Zanotto, E. D. The failure of the Classical Nucleation Theory at low temperatures resolved. *arXiv:1902.03193v1* (2019).

64. Sycheva, G. A. Determination of the size of the critical nucleus of crystals in lithium and sodium silicate glass. *Glas. Phys. Chem.* **41**, 302–306 (2015).

65. Fokin, V. M., Kalinina, A. M. & Filipovich, V. N. Nucleation in silicate glasses and effect of preliminary heat treatment on it. *J. Cryst. Growth* **52**, 115–121 (1981).

66. Turnbull, D. Thermodynamics and Kinetics of Formation of the Glass State and Initial Devitrification. in *Proceedings of the International Conference Delft* (ed. Prins, J. A.) 41–56 (North-Holland, 1964).

67. Gránásy, L. Diffuse interface theory of nucleation. *J. Non. Cryst. Solids* **162**, 301–303 (1993).

68. Gránásy, L. & Herlach, D. M. Diffuse interface approach to crystal nucleation in glasses. *J. Non. Cryst. Solids* **192** & **193**, 470–473 (1995).

69. Spaepen, F. Homogeneous nucleation and the temperature dependence of the crystal melt interfacial tension. in *Solid State Physics* (eds. Ehrenreich, H. & Turnbull, D.) 1–32 (Academic Press, 1994).

70. Gránásy, L. Diffuse Interface Approach to Vapor Condensation. *Europhys. Lett.* **24**, 121–126 (1993).

71. Kelton, K. F. & Greer, A. L. Beyond the Classical Theory. in *Nucleation in Condensed Matter: Applications in Materials and Biology* 85–123 (Elsevier, 2010).

72. Spaepen, F. *Solid State Physics, Volume 61*. (Academic Press, 2009).

73. Gránásy, L. & James, P. F. Nucleation in oxide glasses: comparison of theory and experiment. *Proc. R. Soc. London. Ser. A Math. Phys. Eng. Sci.* **454**, 1745–1766 (1998).

74. Volmer, A. & Weber, A. Keimbildung in übersättigten Gebilden. *Zeitschrift für Phys. Chemie* **119**, 277–301 (1926).

75. Becker, R. & Döring, W. Kinetic treatment of grain-formation in super-saturated vapours. *Ann. Phys. (N. Y).* **24**, 719–752 (1935).

76. Van Hoesen, D. C., Xia, X., McKenzie, M. E. & Kelton, K. F. Modeling nonisothermal crystallization in a BaO·2SiO 2 glass. *J. Am. Ceram. Soc.* (2020). doi:10.1111/jace.16979

77. James, P. F. & Rowlands, E. G. Kinetics of crystal nucleation and growth in barium disilicate glass. in *Phase Transformations* **2**, 27–29 (The Institution of Metallurgists, Northway House, 1979).

78. Zanotto, E. D. & James, P. F. Experimental tests of the classical nucleation theory for glasses. *J. Non. Cryst. Solids* **74**, 373–394 (1985).

79. James, P. F. Kinetics of crystal nucleation in lithium silicate glasses. *Phys. Chem. Glas.* **15**, 95–105 (1974).

80. Deubener, J., Brückner, R. & Sternitzke, M. Induction time analysis of nucleation and crystal growth in di- and metasilicate glasses. *J. Non. Cryst. Solids* **163**, 1–12 (1993).

81. Barker, M. F., Wang, T.-H. & James, P. F. Nucleation and growth kinetics of lithium disilicate and lithium metasilicate in lithia-silica glasses. *Phys. Chem. Glas.* **29**, 240–248 (1988).

82. Tuzzeo, J. J. Effects of pressure on kinetics of crystal nucleation in lithium disilicate glass. PhD Thesis. (Ohio State University, 1976).

83. Gonzalez-Oliver, C. J. R. & James, P. F. Crystal Nucleation and Growth in a Na2O.2CaO.3SiO2 Glass. *J. Non. Cryst. Solids* **38** & **39**, 699–704 (1980).

84. Gonzalez-Oliver, C. J. R. Crystal Nucleation and Growth in Soda-Lime-Silica Glasses. PhD Thesis. (University of Sheffield, 1979).

85. Narayan, K. L. & Kelton, K. F. First measurements of time-dependent nucleation as a function of composition in Na2O · 2CaO · 3SiO2 glasses. *J. Non. Cryst. Solids* **220**, 222–230 (1997).

86. Abyzov, A. S., Fokin, V. M., Rodrigues, A. M., Zanotto, E. D. & Schmelzer, J. W. P. The effect of elastic stresses on the thermodynamic barrier for crystal nucleation. *J. Non. Cryst. Solids* **432**, 325–333 (2016).

87. Rodrigues, A. M., Cassar, D. R., Fokin, V. M. & Zanotto, E. D. Crystal growth and viscous flow in barium disilicate glass. *J. Non. Cryst. Solids* **479**, 55–61 (2018).

88. Trinh, E. H. Compact acoustic levitation device for studies in fluid dynamics and material science in the laboratory and microgravity. *Rev. Sci. Instrum.* **56**, 2059–2065 (1985).

89. Hennet, L. *et al.* Structure and dynamics of levitated liquid materials. *Pure Appl. Chem.* **79**, 1643–1652 (2007).

90. Weber, J. K. R. *et al.* Aero-acoustic levitation: A method for containerless liquid-phase processing at high temperatures. *Rev. Sci. Instrum.* **65**, 456–465 (1994).

91. Mauro, N. A. & Kelton, K. F. A highly modular beamline electrostatic levitation facility, optimized for in situ high-energy x-ray scattering studies of equilibrium and supercooled liquids. *Rev. Sci. Instrum.* **82**, (2011).

92. Schenk, T., Holland-Moritz, D., Simonet, V., Bellissent, R. & Herlach, D. M. Icosahedral Short-Range Order in Deeply Undercooled Metallic Melts. *Phys. Rev. Lett.* **89**, 1–4 (2002).

93. Holland-Moritz, D., Schenk, T., Convert, P., Hansen, T. & Herlach, D. M. Electromagnetic levitation apparatus for diffraction investigations on the short-range order of undercooled metallic melts. *Meas. Sci. Technol.* **16**, 372–380 (2005).

94. Fecht, H. J. & Wunderlich, R. K. Development of containerless modulation calorimetry for specific heat measurements of undercooled melts. *Mater. Sci. Eng. A* **178**, 61–64 (1994).

95. Wunderlich, R. K. & Fecht, H. J. Modulated electromagnetic induction calorimetry of reactive metallic liquids. *Meas. Sci. Technol.* **16**, 402–416 (2005).

96. Lohöfer, G. High-resolution inductive measurement of electrical resistivity and density of electromagnetically levitated liquid metal droplets. *Rev. Sci. Instrum.* **89**, 4709 (2018).

97. Van Hoesen, D. C. *et al.* Resistivity Saturation in Metallic Liquids Above a Dynamical Crossover Temperature Observed in Measurements Aboard the International Space Station. *Phys. Rev. Lett.* **123**, 226601 (2019).

Chapter 2: Experimental Methods

Chapter 2 is divided into several sections relating to experimental and simulation techniques. Sample preparation, the beamline electrostatic levitator (BESL) at Washington University in St. Louis, the electromagnetic levitator (EML) on the International Space Station (ISS), and sample measurements are discussed in detail. The Fortran code used for simulating silicate glass nucleation and growth is also discussed.

2.1 Sample Preparation

The BESL supports spherical or nearly spherical samples between 35 and 70 mg. Samples with masses too far outside this range are difficult to levitate and process. To prepare BESL samples, 1.0g ingots are made from high purity (99.9 – 99.999%) bulk elemental material, typically from Alfa Aesar or Sigma-Aldrich, using an arc-melting technique. The mass of each component, m_i, is determined by

$$m_i = m_{ingot}\left(\frac{x_i z_i}{\sum_j x_j z_j}\right), \tag{2.1}$$

where m_{ingot} is the mass of the desired ingot, x_i is the atomic fraction of element i, z_i is the molar mass of element i, and the sum is over all elements in the composition. After measuring out the mass of each element in the desired ratio, they are placed in a machined groove on the water-cooled copper hearth of the arc-melter. The element with the highest melting point is placed on top (closest to the arc-melter tip) to ensure that the lower melting point elements do not significantly evaporate during heating. A $Ti_{50}Zr_{50}$ getter is placed in a separate groove on the copper hearth. The copper hearth is then sealed and evacuated to $2x10^{-5}$ torr three times, backfilling with high purity argon (grade 5.0, 99.999%) each time, to reduce the oxygen in the chamber. After the third backfill, the arc is struck using a Miller Synchrowave 250DX power source. The arc travels from the tungsten tip on the electrode to the copper hearth. The getter is melted first for 60 seconds to help absorb remaining oxygen in the chamber. Each 1.0g ingot batch of material is then melted for 15 seconds and flipped three times, melting each time, to ensure the sample is well mixed. The chamber is opened, and the 1.0g ingot is broken into pieces with a mass that is acceptable for the BESL. The arc-melting chamber is then evacuated and backfilled following the same process and the alloy pieces are re-melted into BESL sample spheres. The samples are measured for mass change after the melting process and observed for any dull appearance, which are indicative of oxygen contamination or non-uniform mixing.

As discussed in chapter 1, the cooling rate required to create a glass varies with composition. Good glass formers, like Vit106, can be cooled to a glass using the arc-melting technique. However, other samples such as $Cu_{50}Zr_{50}$ and $Zr_{64}Ni_{36}$ require a special high cooling rate, technique called melt spinning, to form a glass. Melt spinning can produce cooling rates between 10^5-10^6 K/s[1]. A 1.0g ingot is created using the arc-melting technique and then placed inside a boron nitride or quartz tube with a small hole in the bottom. The tube is placed in the melt spinning chamber between radio-frequency (rf) inductive coils. The chamber is then evacuated and flushed with high purity argon. During melt spinning, current runs through the rf coils, melting the sample by induction. A pressure is then applied to the sample container forcing the liquid to spray onto a copper wheel spinning with a rate of 3000-6000 rpm. This quickly cools the liquid and produces amorphous ribbons that are approximately $20\mu m$ thick. The structure of the ribbons is measured using X-ray scattering from a Cu K-alpha source and a Rigaku X-ray Diffractometer. A broad first peak in the scattering signal, with no sharp crystal peaks, indicates that the sample is amorphous.

2.2 Beamline Electrostatic Levitator

The beamline electrostatic levitator (BESL) is a highly specialized device that can be used to measure a host of liquid properties, including temperature, density, viscosity, and crystal growth velocity[2]. The BESL is transportable; when it is setup at the Advanced Photon Source (APS) at Argonne National Lab, it can be used to measure features of the structure of the supercooled liquid, such as the structure factor and the pair distribution function. Supercooled liquid structural information is inaccessible in typical scattering experiments where container walls cause heterogeneous nucleation in the liquid and prohibit the supercooled phase from being studied. Figure 2.1 shows the BESL and a diagram of the instrumentation used for levitation and measurements.

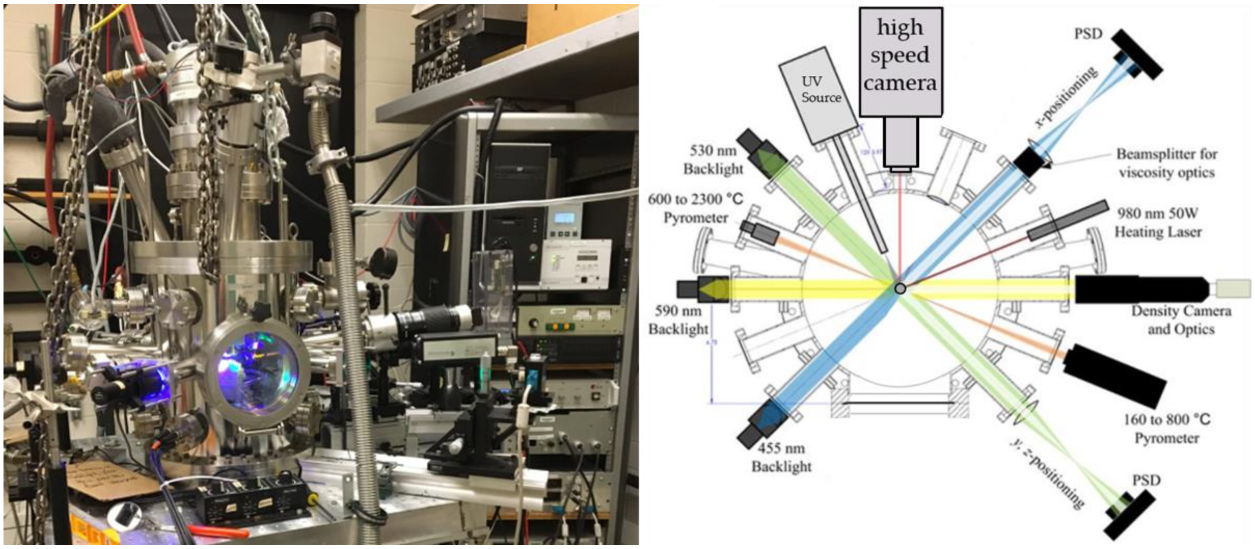

Figure 2.1 – Picture of the beamline electrostatic levitator at Washington University in St. louis, courtesy of Mark Sellers (left) and a diagram of the instrumentation layout of the BESL updated from Bendert[3] with permission (right).

For X-ray scattering measurements at the APS the high-speed camera is replaced with an entrance beryllium widow that allows the high intensity X-rays to scatter from the sample. The glass front window (fig. 2.1 – left) is replaced by a large beryllium window, which allows the scattered X-rays to impinge onto a detector located outside the vacuum chamber.

After 2-3 mm diameter samples are created using the arc-melting technique, they are placed in a sample carousel which is positioned at the top of the BESL chamber. The carousel is connected to a stepping-motor-controlled gear so that it can rotate. The BESL chamber is closed and evacuated to a high-vacuum ($\sim 10^{-8}$ Torr), using two turbo pumps (one for the main chamber, Osaka Vacuum compound molecular pump T642OMCWB and one for the ultraviolet source, Pfeiffer HiPace 80). Both are backed by an oil free roughing pump (SCROLLVAC SC 15D).

A top and bottom electrode controls the potential that allows the sample to overcome gravity while a set of four side electrodes keep the sample stable in the lateral directions. Two light emitting diodes (LEDs) located 90 degrees apart illuminate the sample. The sample shadow is detected on two position sensing detectors (PSDs) that are located in line with the two LEDs, but on the opposite side of the sample. The location of the sample shadow on the PSDs allows the control algorithm to identify the sample position. Earnshaw's theorem states that there is no stable energy minimum in a static electric field. Therefore, based on the outputs of the PSDs the computer code actively modifies the potentials on the electrodes at millihertz timescales to keep the sample stable within $10\mu m$. In detail, a 455nm blue LED illuminates the sample in the y-direction and a 530nm green LED illuminates the sample in the x-direction. The sample shadow from the blue LED is detected by an opposite PSD and used to determine the y position of the sample. The green LED shadow is used by the opposite PSD to determine the x- and z-position. Figure 2.2 is a schematic illustration of this process for the blue LED and corresponding PSD.

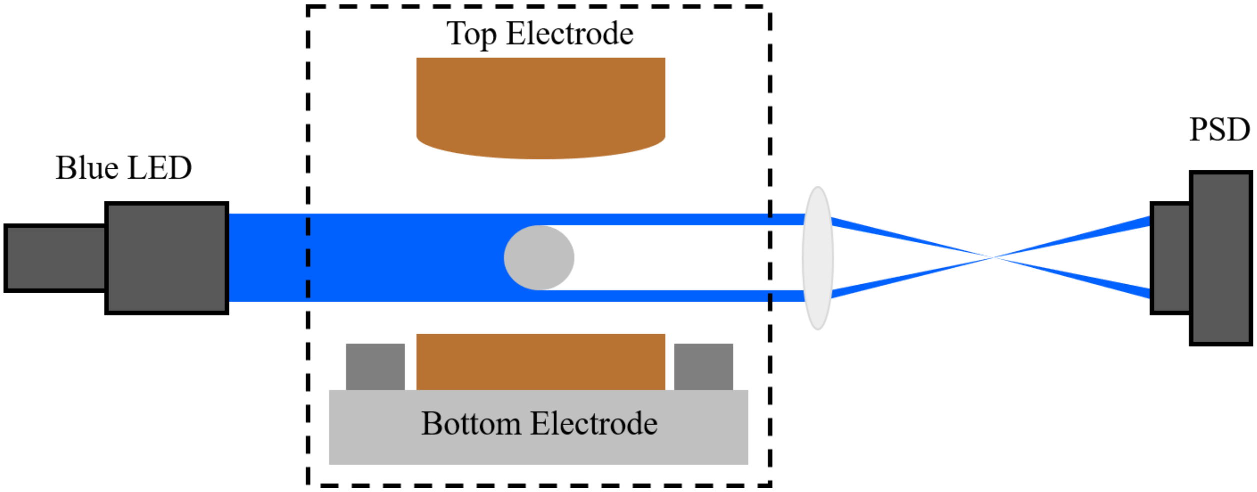

Figure 2.2 – Diagram showing the levitation control setup. The LED illuminates the sample casting a shadow that is detected by the PSD. The PSD sends the position signal to the TargetPC which controls the voltages of the electrodes. This figure is adapted from fig. 1.10 in James Bendert's dissertation[3] with permission.

The PSD signals are used in a MATLAB algorithm to control the three coordinates of the electric field produced from the top and bottom electrodes and the four side electrodes. The levitation algorithm runs on an external target computer (TargetPC). The top and bottom electrodes operate at high voltages (0 to 20 kV) to overcome gravity while the side electrodes operate at lower voltages (-3 to 3 kV) to keep the sample in the correct position.

The process of loading and launching a sample into the correct location is involved. A motor control LabVIEW program is first run to allow the user to turn the sample carousel and to raise a post that comes up from the bottom electrode. LabVIEW is also used to control the ESL measurement instrumentation and readouts including the laser, pyrometers, and the density camera. After the two programs are running, the post is raised to the top electrode and the carousel is rotated so that a sample drops onto the post. The post is then lowered to the correct sample launching position, which varies with sample composition and mass. The operating limits for the vertical electrodes are selected and the lateral and vertical gains (voltage multipliers that control the algorithm sensitivity) are optimized for launching. The MATLAB electrode control algorithm is then started, and the sample jumps up between the top and bottom electrodes. Lateral and vertical gains as well as the sample z-position are adjusted so that the sample is stable and in the correct position (i.e. the laser strikes the center of the sample and the pyrometers measure the sample temperature). See Appendix A of Mark Seller's dissertation[4] for a complete BESL operating procedure.

During the alignment of the BESL, the PSDs are adjusted (lateral, vertical, pitch, and yaw) so that the shadow from a precisely machined (1.98425 ± 0.000076 mm from Industrial Tectonics Inc.) spherical tungsten carbide sample is at the center of the detector while levitating. This is clear when the green and blue electrode readouts are near zero in the x- and y-directions. Additional fine lateral adjustments are made to the blue and green PSDs for each individual sample immediately following the sample launch.

Most samples require external charging to be stable during launching and levitation, particularly when heating. A high intensity vacuum ultraviolet (VUV) light source is used to charge the sample by the photoelectric effect, keeping it stable during processing as charged impurities leave the sample.

Once a sample is levitated and stable, a 980nm nLIGHT Pearl fiber-coupled diode laser is energized. The laser power is incrementally increased slowly raising the temperature of the sample. Sample temperatures are recorded using a Process Sensors Metis MI18 MB8 single color pyrometer for low temperatures (160-800 ^{o}C) and a Process Sensors MQ22 two-color pyrometer for high temperatures (600-2300 ^{o}C). The temperature measured by the two-color pyrometer is corrected using the sample melting plateau as a known reference temperature. The solidus and liquidus temperatures are known a priori from differential thermal analysis measurements where the melting temperature is indicated by a change in the heat flow. The corrected BESL sample temperature, T_c, is calculated from the observed temperature, T_{obs}, by

$$T_c = \frac{T_{obs}}{1 - \frac{T_{obs}}{C_\lambda} \ln\left(\frac{\epsilon_1}{\epsilon_2}\right)}, \tag{2.2}$$

where C_λ is a pyrometer-specific constant given by the two operating wavelengths of the two-color pyrometer (1.40 μm and 1.64 μm). C_λ is given by

$$C_\lambda = \frac{hc}{k_B}\left(\frac{\lambda_1 - \lambda_2}{\lambda_1 \lambda_2}\right), \tag{2.3}$$

where h is Planck's constant, c is the speed of light, and k_B is the Boltzmann constant. ϵ_1 and ϵ_2 are the emissivities measured at each wavelength by the pyrometer and are used to find the correct temperature of the sample. Additional details of sample temperature corrections can be found elsewhere[5]. A representative time-temperature profile of a cycle showing the melting plateau, supercooled liquid, and recalescence (nucleation and growth of the crystal or metastable phase) event in the BESL is shown in fig. 2.3. During cooling, the laser is turned off so that the sample is freely cooling. The sharp increase in temperature occurs during crystallization because the heat of fusion is released as the supercooled liquid changes to the lower energy crystal phase. The deep supercooling shown in fig. 2.3 is due to bypassing heterogeneous nucleation in the BESL, where the sample is not in contact with a container.

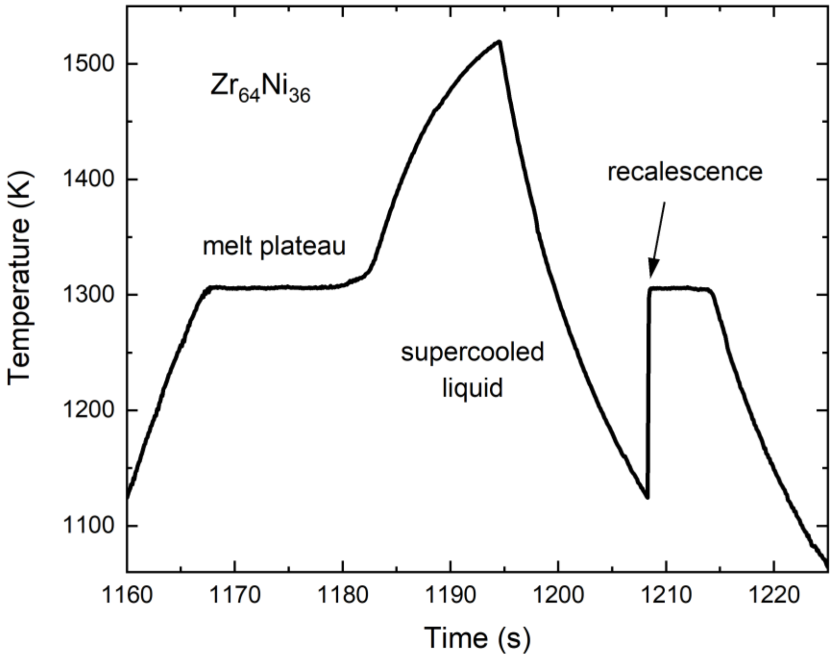

Figure 2.3 – The time-temperature profile of a $Zr_{64}Ni_{36}$ BESL sample showing the melting plateau, liquid phase, supercooled liquid phase, and the recalescence event.

2.2.1 Density Measurements

Density measurements are taken in the BESL during quiescent free cool cycles. A 590nm amber LED illuminates the sample and is detected by the density camera (PixeLINK B741G) that records the shadow of the sample. Before the sample is measured, a calibration tungsten carbide is levitated and recorded at 10 frames per second (fps) for several sets of 60 seconds. The calibration sample is used to calculate the distance per pixel in the video frames, since the diameter of this sample is known very accurately. After the calibration measurement, the sample of interest is loaded and heated to the liquid phase. Several free cooling cycles are performed to clean the sample and to ensure that the sample reaches the deeply supercooled state. During the density measurement a sample is heated to several hundred degrees above the melting temperature (less if significant evaporation is a concern) and free cooled while video is being recorded at 25 fps until the crystallization event. The distance per pixel, calculated using the tungsten carbide, is then used to calculate the diameter of the sample as a function of temperature. As an example, fig. 2.4 shows the density of a $Zr_{64}Ni_{36}$ BESL sample during three free cooling cycles. In the measurable temperature region, the liquid density changes linearly with temperature. Small distortions from spherical symmetry are observed in measurements, which contribute very little error due to the inherent symmetry about the vertical axis and sample rotation. Typically, volume changes are resolved to within 1 part in 10^4. The absolute precision is limited to about 1%, dictated by the precision of the tungsten carbide calibration spheres. Additional details on the density measurement technique and processing video data using LabVIEW are discussed elsewhere[6–8].

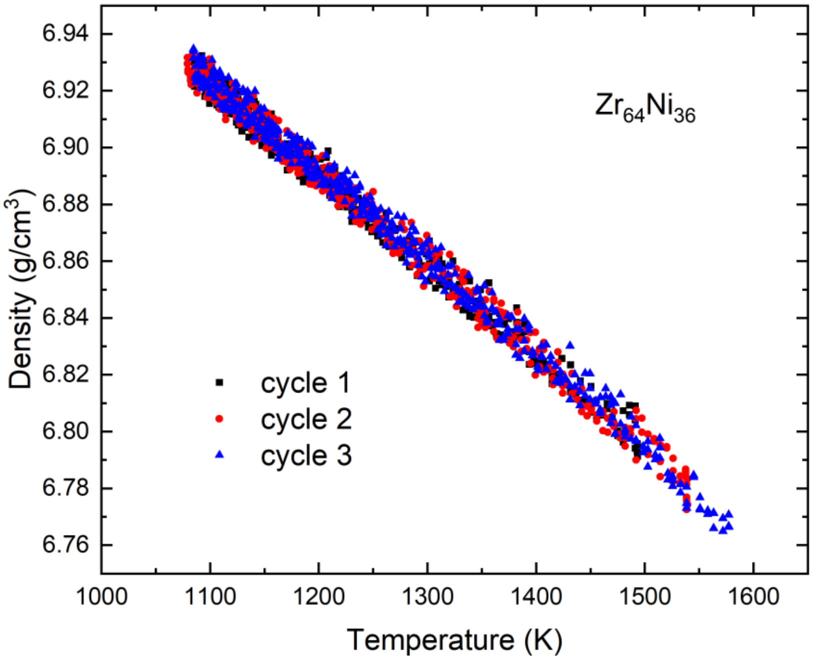

Figure 2.4 – Density measurements for a liquid $Zr_{64}Ni_{36}$ BESL sample during three free cooling cycles with video taken at 25 frames per second using a PixeLINK B741G camera.

2.2.2 Viscosity Measurements

The electrostatic levitator dynamically changes the levitation electric field at millisecond rates so that a liquid sample is stable in position to approximately $10\mu m$. The viscosity is measured using the oscillating drop technique[9], where an oscillating signal (sinusoid, square, or sawtooth wave) is superposed on the vertical potential. This modulation drives the liquid sample in its $l = 2$, $m = 0$ spherical harmonic. The superposed oscillation is stopped after one second and the spherical harmonic signal decays with a time constant, τ, that is related to the viscosity, η, by

$$\tau = \frac{\rho r^2}{(l-1)(2l+1)\eta}, \tag{2.4}$$

where ρ is the sample density, and r is the sample radius. The oscillation and decay are recorded using a PixeLINK B741G camera recording at 1500 fps. The images are processed to determine the sample edge in each frame and the sample image is integrated to determine the oscillation amplitude with time. Figure 2.5 shows the oscillation amplitude with time of a $Zr_{64}Ni_{36}$ liquid BESL sample. The decay of the oscillation amplitude with time is fit to a damped sine wave to extract the decay time constant. The oscillation intensity, $S(t)$, is given by

$$S(t) = A\, sin(2\pi f_0 t + \phi)\ \exp\left(-\frac{t}{\tau}\right). \tag{2.5}$$

Viscosity measurements are taken in the equilibrium liquid up to several hundred degrees above the melting temperature and in the supercooled liquid down to crystallization. Figure 2.6 shows the viscosity measurement data for the batch 1, batch 2, and batch 3 NASA samples aboard the International Space Station. Additional information about the viscosity measurements and analysis can be found elsewhere[8,10].

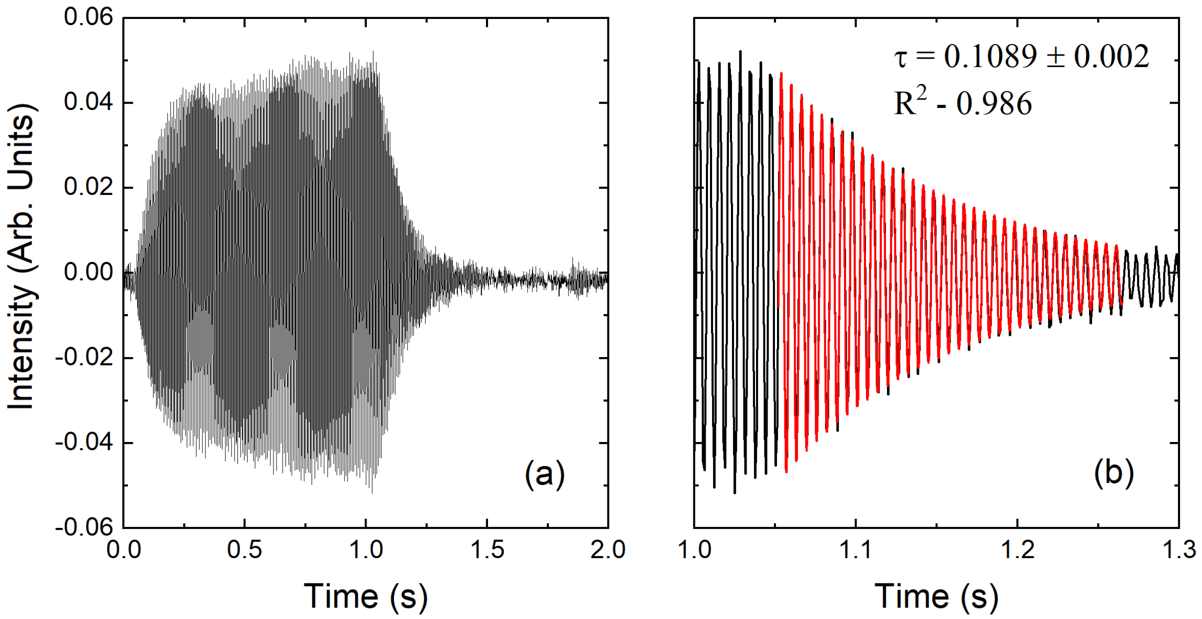

Figure 2.5 – Oscillating drop technique measurement on a $Zr_{64}Ni_{36}$ liquid BESL sample showing (a) the intensity of the sample oscillation as a function of time over the entire measurement and (b) the intensity of the sample as a function of time after the driving modulation finishes. A fit to the damped sine wave providing the decay time constant is shown in red.

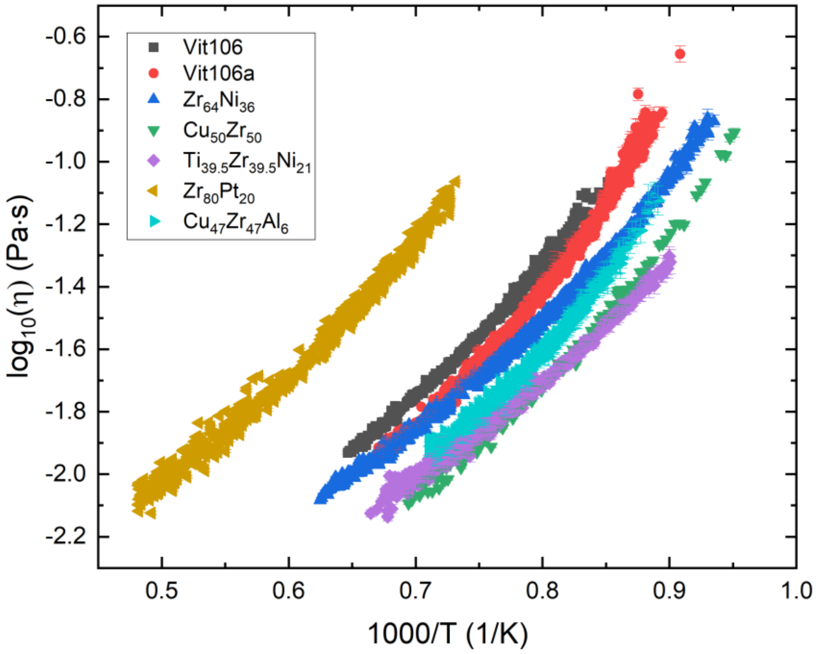

Figure 2.6 – Viscosity data for liquid droplets of liquid alloy samples measured in the BESL using the oscillating drop technique. The viscosity data shown here were measured by Chris Pueblo[8] and Matthew Blodgett[11].

2.2.3 Crystal Growth Velocity Measurements

The crystal growth velocity is an important parameter that gives information on the diffusion coefficient of a sample. The growth velocity with temperature changes by many orders of magnitude in the supercooled liquid. In the BESL, the crystal growth velocity is measured using a Nac Image Technology MEMRECAM HX-3 high-speed camera capable of recording up to 900,000 fps. The high-speed camera records in the visible spectrum and therefore requires a large temperature difference between the crystal and liquid to discern the crystal boundary during recalescence. To measure the growth velocity, a sample is processed and heated to the liquid phase. The laser is then turned off and the sample cools into the supercooled liquid. When a crystallization event occurs, the temperature of the sample increases quickly. If the temperature difference between the liquid and crystal is sufficiently large, then there is visible contrast between the two phases shown in the camera. For low melting point alloys, it is not possible to distinguish between the supercooled liquid and crystal phases. A high-speed infrared camera would be required to measure the crystal growth rates of such alloys. Typical metallic alloy crystal growth velocities can be measured with recording rates between 5000 and 30,000 fps. Some metal elemental liquids, such as zirconium, require a much higher frame rate (greater than 500,000 frames per second). As an example, fig. 2.7 shows a crystal growing on the surface of a $Zr_{64}Ni_{36}$ sample over the course of 8.6ms. The lightly colored region is the crystal and the shiny gray region is the supercooled liquid. The center of the crystal moves along the sample surface due to sample rotation. Measurements of crystal growth velocity are presented in chapter 7 of this dissertation in a discussion of future work.

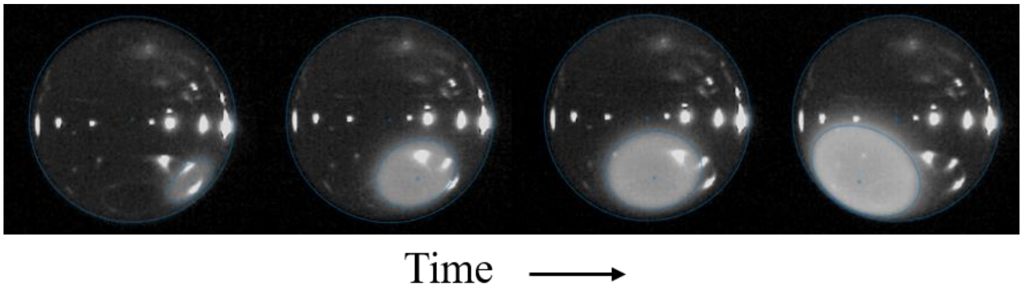

Figure 2.7 – A crystal growing on the surface of a $Zr_{64}Ni_{36}$ sample as a function of time. The white region is the crystal and the shiny gray region is the supercooled liquid.

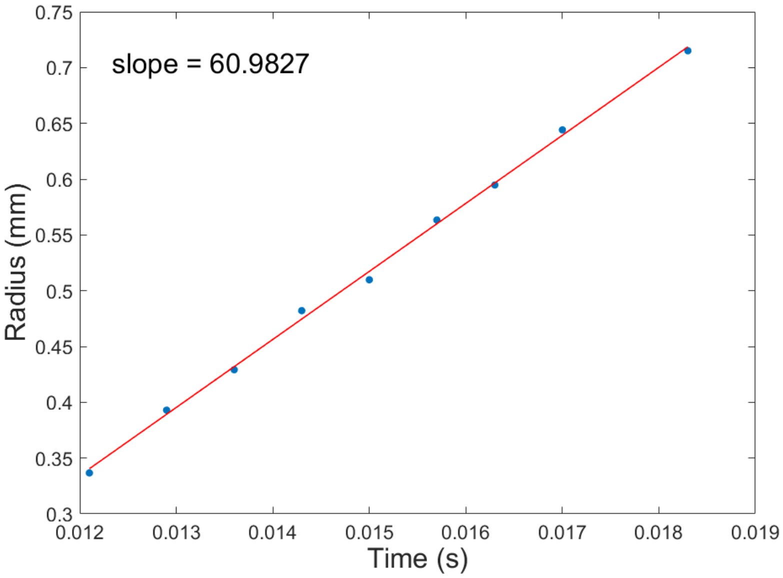

Figure 2.8 – The crystal growth radius as a function of time for a $Zr_{64}Ni_{36}$ sample measured at 225K below the liquidus temperature.

MATLAB code (ftt.m) is used to track the growth front size. The pixel size is determined by manually matching the sample diameter in the video to the known sample diameter at the given supercooling temperature. After the calibration, the crystal growth radius is tracked by progressing through the video frames and manually placing a circle around the crystal region on the sample surface. The growth velocity is then taken as a slope of the radius of the crystal with time as shown in fig. 2.8. There are several assumptions made here: (1) the nucleation event occurs on the surface of the sample because it is the coolest part of the sample, (2) the growth shape is approximately circular on the surface of the sample (i.e. spherical growth of the crystallite), and (3) the growth velocity is constant at the given supercooling temperature and is not a function of the size of the growing crystal.

2.2.4 X-Ray Scattering Measurements

Traditionally it has been nearly impossible to measure the structural properties of supercooled liquids due to heterogeneous nucleation and subsequent crystallization. However, with the BESL, X-ray scattering measurements of the supercooled liquid are possible. To make these measurements, the BESL is transported to the Argonne National Laboratory Advanced Photon Source (APS), where high-intensity X-rays are produced with a synchrotron. At the APS, linearly accelerated electrons are injected into an oval ring guided by high field magnets. After reaching 7 GeV, the electrons are guided into a storage ring where X-rays are produced and directed to the user facilities. The X-rays scatter off the sample, producing diffraction patterns. In the case of glasses, powders, or liquids, the diffraction patterns are radially symmetric. Data taken in this dissertation were measured at the APS beamline 6-ID-D.

The BESL is modified for X-ray scattering measurements by removing the high-speed camera (shown in fig. 2.1) and replacing the front and back windows with beryllium windows to decrease the scattering cross section and reduce the background noise. Scattering data were collected using a GE detector with 2048 by 2048 pixels. The BESL stage is vertically and laterally adjustable so that the sample floating location can be aligned with the incident X-ray beam. The typical BESL setup at the APS allows for a scattering angle, 2θ, range up to 20º. Figure 2.9 is a schematic illustration showing an incident beam hitting a sample, scattering, and detection at 2θ and ϕ on an area detector. The momentum transfer, $\boldsymbol{q}$, between the incident photon, $\boldsymbol{k_i}$, and the scattered photon, $\boldsymbol{k_f}$ is given by $\boldsymbol{q} = \boldsymbol{k_i} - \boldsymbol{k_f}$, where the magnitude of the momentum transfer is

$|\boldsymbol{q}| = 4\pi\sin{(\theta)}/\lambda$ with λ, the photon wavelength. In experiments with the BESL on beamline 6-ID-D, the maximum q is approximately 15Å^{-1}.

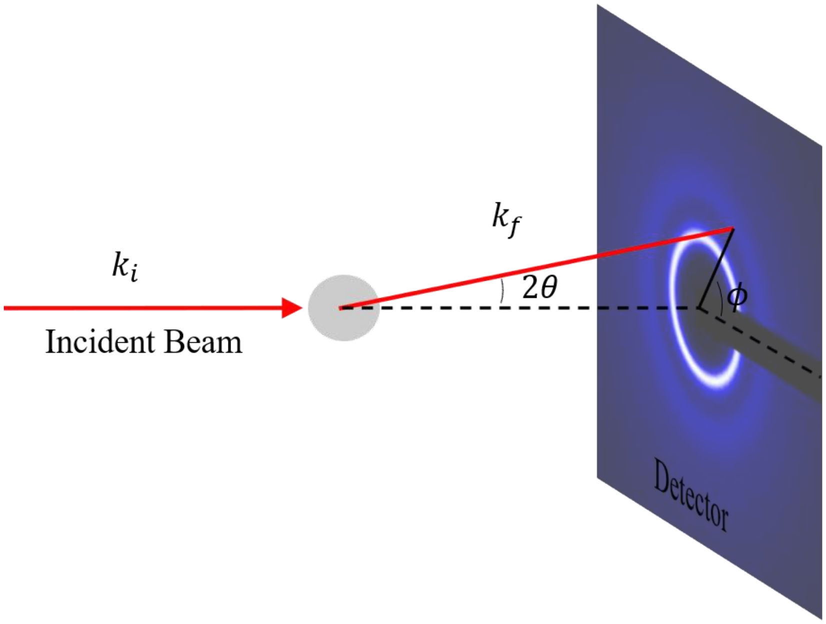

Figure 2.9 – A schematic of X-ray scattering in a spherical transmission geometry overlaid on data from liquid $Cu_{47}Zr_{47}Al_6$ at 900ºC. A beamstop and mount can be seen on the right-hand side of the detector image as the dark bar going into the center of the image. This figure is adapted from fig. 2.3.8 from Chris Pueblo's dissertation[8] with permission.

A NIST silicon standard is first levitated in the chamber and hit with the incident X-ray beam. Silicon has a well-studied diffraction pattern and known lattice distances and can therefore be used to calculate the distance from the sample to the detector. The working distance, tilt angle, and rotation angle are used as fitting parameters to match the measured diffraction pattern to the known silicon lattice distances. After the silicon is measured, samples are levitated and processed using the procedure described in section 2.2. Samples are heated above the melting temperature and allowed to freely cool or slowly cool (cooling where the laser power is slowly decreased) during the X-ray measurements. The structure as a function of temperature is measured from the high temperature equilibrium liquid until crystallization occurs in the deeply supercooled liquid. Additional measurements are made to account for the detected background intensity including the empty chamber, dark, and empty dark. In the empty chamber measurements, the beam travels through the chamber and hits a beam stop and the residual counts on the detector are recorded. In the dark measurements, the residual counts on the detector without any beam going through the sample chamber are recorded. The corrected intensity is given by

$$I_{corrected} = I_{raw} - I_{dark} - \left(I_{empty} - I_{empty-dark}\right). \tag{2.6}$$

This correction as well as other corrections are accounted for using a LabVIEW program built for the spherical sample geometry[3,12]. Details on the other corrections including oblique incidence, polarization, Compton scattering, fluorescence, absorption, and multiple scattering can be found elsewhere[13] and are discussed in chapter 6 of this dissertation for cylindrical geometries.

2.3 Electromagnetic Levitation on the ISS

Electromagnetic levitation (EML) is another containerless levitation method that allows the equilibrium and supercooled liquid phases to be studied. In EML, a metal sample is levitated by creating a magnetic field between a series of copper coils. Because of Lenz's law a counter magnetic field is set up in the sample to oppose the imposed external field by induced eddy currents near the surface of the sample. The counter magnetic fields cause the sample to levitate. A superposed radio frequency (rf) heater current produces a homogeneous magnetic field that controls the temperature of the sample. In gravitational fields, temperature control and levitation are connected because the power required to levitate the sample simultaneously heats the sample. For many samples, the power required to levitate the sample also causes the sample temperature to rise above the melting temperature. In this case, the supercooled liquid cannot be studied without an additional cooling mechanism such as convection from by an inert gas surrounding the sample. Cooling gases can contain small amounts of impurities which may contaminate the sample causing the sample to crystalize from heterogeneous nucleation sites. Contaminates are difficult to remove and if they persist, homogeneous nucleation and the deeply supercooled state are impossible to study. However, taking away most of the gravitational effects using an EML on the International Space Station (ISS) removes the need for a high levitation power. The EML on the ISS, therefore, decouples sample levitation and heating. With that said, a small amount power is still required to keep the sample stable in the microgravity environment causing the sample temperature to rise, but not as much as under terrestrial conditions.

For sample levitation there are two sets of coils, one located above and one below the sample, that have an equal current flowing in opposite directions. This produces a magnetic field that forces the sample to the center of the coils as shown in fig. 2.10 (left). Superimposed over the levitation current is current flowing in the same direction in the top and bottom coils producing a homogeneous linear magnetic field in the region of the sample as shown in fig. 2.10 (right). This magnetic field heats the sample due to the resistance of the sample and the introduced eddy currents, i.e. Ohmic heating[14]. The eddy currents in the sample interact with the magnetic fields to produce Lorentz forces perpendicular to both the current and the magnetic fields.

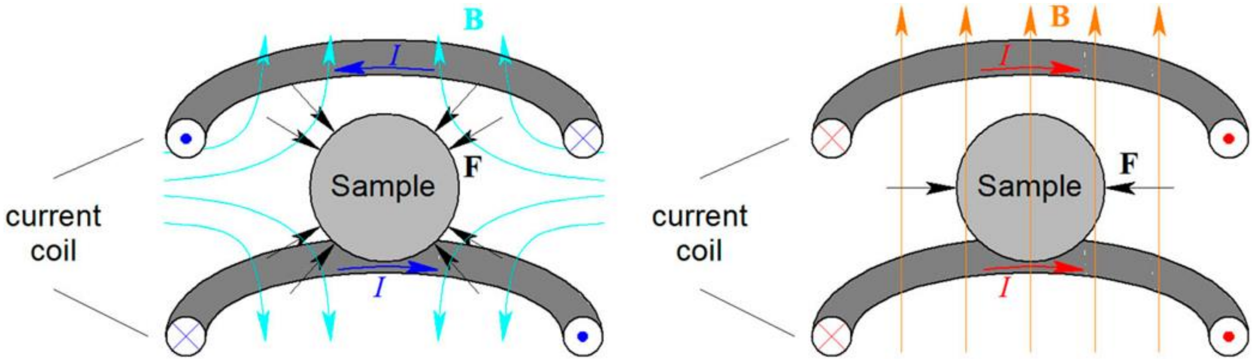

Figure 2.10 – A diagram of a sample sitting between two current carrying coils. The levitation (left) and heating (right) magnetic fields produced from the current carrying coils of the electromagnetic levitator on the ISS. The current in the coils above and below the sample for levitation is equal and in opposite directions. For sample heating, the current is equal and flowing in the same direction. This figure is reproduced from Georg Lohöfer; *Review of Scientific Instruments* **89,** 124709 (2018), with permission of AIP Publishing.

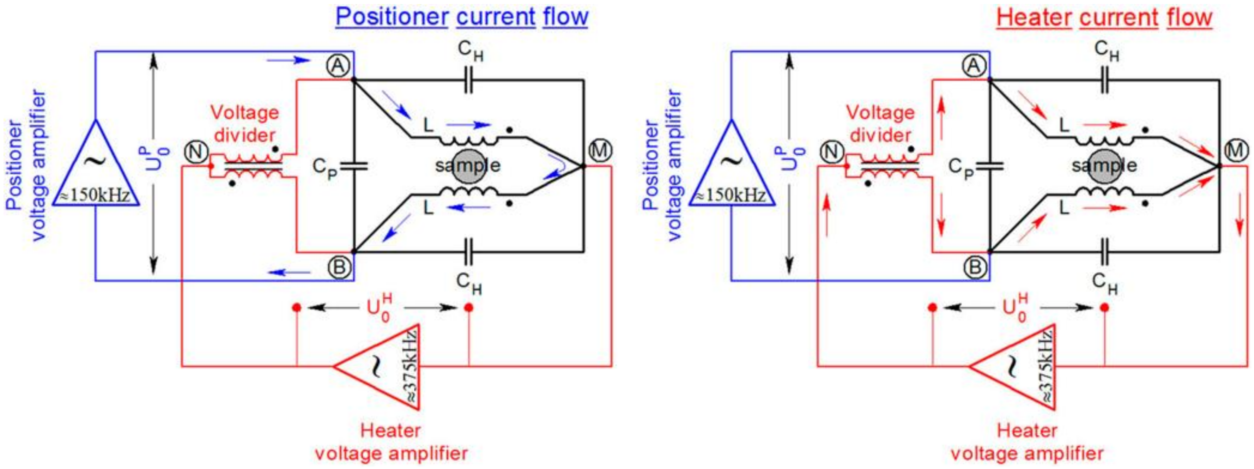

Figure 2.11 – A diagram of the electronics required to control the levitation (left) and heating (right) of a sample in the electromagnetic levitator on the International Space Station using the Supos technique. This figure is reproduced from Georg Lohöfer; *Review of Scientific Instruments* **89,** 124709 (2018), with permission of AIP Publishing.

The Supos technique[15] allows the simultaneous levitation and heating of samples in the EML. The Supos technique electrical circuit diagram is shown in fig. 2.11, with the positioning diagram on the left and the heating diagram on the right. The positioner alternating current flows at 150kHz and the heating alternating current flows at a different rate, 375kHz, so that the signals are distinct. The sample acts as an additional impedance in the EML circuit. This will be discussed in more detail in the section 2.3.2 when discussing electrical resistivity measurements.

The EML on the ISS allows samples ranging from 6.0 to 8.0 mm in diameter to be processed. These samples are held individually either in a metal cage or in a ceramic cup, which is placed between the EML coils for processing. There is some hesitation to use metal cage sample containers in future NASA batches because it has been shown that the cage may significantly interact with the magnetic fields from the EML. This is particularly relevant during electrical resistivity measurements. Once levitated, the sample temperature is controlled by adjusting the heater control voltage, which controls the strength of the heater magnetic field. The power absorbed by the sample through ohmic loss is proportional to the square of the magnetic field strength. A one-color pyrometer (1.45-1.80 μm) aimed at the sample pole measures the temperature at 100Hz between 300℃ and 2100℃. Emissivity temperature corrections are performed in a similar manner as the temperature corrections for the BESL, described in section 2.2.

Even though the heating and levitation are effectively decoupled, the power required to levitate in the ISS EML heats most samples to approximately 800 K, which is sufficiently far below the melting temperature for relevant measurements of the samples studied in this dissertation. The ISS EML is built to process samples in high vacuum (~10^{-7} torr) or in an inert gas atmosphere (~260 torr) if additional cooling is required. Measurements can be performed in either argon, for mid-range cooling rates, or in helium for rapid cooling. The thermal conductivity of helium is an order of magnitude larger than that of argon. Radiative cooling dominates when samples are in a vacuum environment and convective cooling dominates when samples are in an inert gas atmosphere.

2.3.1 Supercooling Measurements

Investigations of supercooled liquids on the ISS were, in part, intended to study the effect of diffusion on nucleation. In ESL on earth, the amount of fluid flow from the Marangoni effect and gravitational convection is greater than the fluid flow from diffusion, so that diffusion effects are masked. Marangoni flow occurs due to the liquid droplet surface tension driven convection from inhomogeneous sample heating. This is often caused by laser heating, where the laser strikes a single point on the sample. However, ground based ESL measurements of the amount of supercooling provide a baseline to compare against the quiescent conditions planned in the EML on the space station. Ground-based EML is not suitable to study diffusion effects because there is a large amount of stirring caused by the high power required to levitate the sample against gravity. The flow from levitation induced eddy currents is greater than the diffusion flow, making it difficult to study. The EML on the space station is ideal for studies of diffusion because the power required for levitation is significantly less than that on Earth and there is insignificant gravitational stirring. Additionally, the EML inductive heating is more uniform than laser heating in ESL. Initial calculations showed that radio frequency stirring on the space station should be an order of magnitude smaller than the diffusion fluid flow allowing for diffusion effects to be studied[16].

Nucleation measurements are performed in the EML on the ISS by letting the sample freely cool from the equilibrium liquid to crystallization with low positioner and heater voltages. Although, as mentioned, the EML is supposed to provide quiescent measurements, the actual required power to levitate and stabilize samples is larger than expected. The EML in space is therefore now used to probe the effect of stirring on nucleation because a change in the positioner/heater voltage changes the amount of stirring. Stirring effects may be manifest as a change in the distribution of maximum supercooling temperatures (the lowest temperature reached by the sample during cooling before crystallization occurs) as a function of the positioner and heater voltages, with larger stirring occurring with larger heater and positioner voltages. It is expected that the maximum supercooling temperature will increase with increasing stirring (i.e. there is less supercooling). Given sufficient data, the statistical method developed by Skripov[17] can be used to calculate the prefactor and work of cluster formation of the steady-state nucleation rate from a distribution of supercooling temperatures. In this method, the maximum supercooling temperature is recorded for each cycle each with the same time-temperature profile. Binning the amount of supercooling over many cycles gives a Poisson histogram distribution, since each supercooling cycle is independent of the previous cycle. Fitting a Poisson distribution to the histogram provides the work of cluster formation and the prefactor term in the steady-state nucleation rate equation (eq. 1.20). This method has recently been used on ground based ESL measurements of metallic liquids giving support to Frank's hypothesis that metallic liquids deeply supercool due to the formation of icosahedral short range order (ISRO)[18]. These data will be used to compare against space station data in future batches, where the amount of stirring is calculated as a function of heater and positioner voltages.

2.3.2 Electrical Resistivity Measurements

The electrical resistivity is sensitive to short and medium-range order in alloys because the scattering length of electrons is approximately the size of an atom or cluster of atoms. Because of this, the electrical resistivity can be used as a probe of changes in the liquid structure as a function of temperature. The electrical resistivity of a solid is straightforward to measure using a four-point method that eliminates the error associated with the resistance of the leads. Two outer probes provide a constant current while two inner probes measure the potential difference across a section of the solid. While this method is practical for solids and may work for some nonreactive equilibrium liquids, it is not possible to use on the majority of supercooled liquid alloys, since they will react with the measurement probes and sample containers at high temperatures. Additionally, the probes and the sample container provide heterogeneous nucleation sites so that the deeply supercooled state cannot be measured.

There are two EML techniques for measuring electrical resistivity. In the first method, a rotating direct current magnetic field induces eddy currents in the sample and generates a mechanical torque. The torque is proportional to the electrical conductivity. However, measuring the magnitude of the sample torque is nontrivial. In the second method, an alternating current is applied to the coils surrounding the sample creating a radio frequency magnetic field. Again, this drives eddy currents in the sample which act as current feedback in the coils. The electrical resistivity can be obtained from measurements of the current feedback as well as its phase compared to the applied current. The EML on the space station uses the second technique giving a reasonable containerless method to measure the electrical resistivity. The radio frequency current going through the heating coils causes eddy currents in the sample which provide a measurable feedback on the coils. The sample therefore acts as an additional impedance on the heating circuit. The circuit tasked with measuring the impedance of the sample is called the sample coupling electronics (SCE). Given that each designed circuit component is known, the only unknown is the sample impedance, which is a function of the electrical resistivity.

From fig. 2.11, it is clear that the sample impedance, Z_S, is split between two parallel loops in the circuit. The impedance from one of the identical coil inductors, Z_L, is in series with each half of the sample impedance. The heater capacitors, with inductance, Z_C, are in parallel with each of the top and bottom coils. Each impedance contribution is shown schematically in fig. 2.12, which bears striking resemblance to a four-point resistivity setup. The current, I, is supplied by the amplifier and the potential difference across the circuit, U, is measured. The magnetic fields produced by the induced eddy currents in the sample provide an additional current, so the total current and phase shift of the current, ϕ, is monitored. The total impedance of the circuit is given by

$$\frac{1}{Z_{total}} = \frac{2}{Z_C} + \frac{2}{Z_L + Z_S/2}, \tag{2.7}$$

where each of the circuit parameters is known except for the sample impedance. The total admittance of the circuit is the inverse of the total impedance. The components of the total admittance are measured during the experiment and are given by

$$Y_{total} = \frac{I}{U} = \frac{I_0}{U_0} \mathrm{e}^{-\mathrm{i}\phi}, \tag{2.8}$$

where I_0 and U_0 are the magnitude of the measured current and voltage and ϕ is the phase shift from the applied current and measured voltage. The functional dependence of the sample impedance is derived elsewhere[19] and is simplified to be only a function of the sample resistivity, ρ, the sample radius, R_S, and the measurement frequency, ω. The sample impedance is given as

$$Z_S(\omega, R_S, \rho) = c\ \omega\ R_S^3 \left[\frac{1}{q} - \frac{1}{q^2} + i\left(\frac{1}{q} - \frac{2}{3}\right)\right], \tag{2.9}$$

where c is a coupling constant and q gives the ratio of the sample radius over the skin depth, δ, with $\delta = \sqrt{2\rho/\mu_0\omega}$; μ_0 is the vacuum permeability. The ratio of the real and imaginary parts of the sample impedance gives the ratio of the sample resistivity to the square of the sample radius. The sample radius as a function of temperature is often known from density measurements, described in section 2.2.1. If not, both the sample radius and electrical resistivity can be determined if the coupling constant is determined by measuring the electrical resistivity of a known sample and backing out the coupling constant. A zirconium oxide sample is used on the space station to determine the coupling constant.

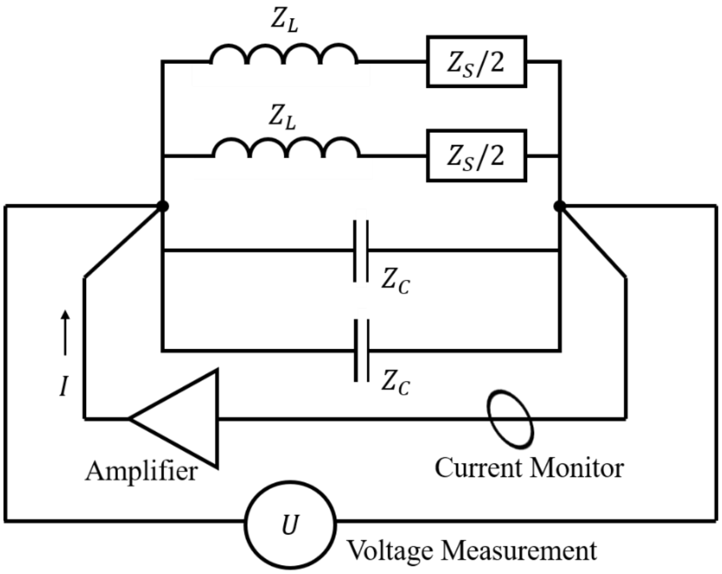

Figure 2.12 – A schematic of the contributing impedances to the EML circuit for electrical resistivity measurements. Also shown is the current supply, current monitor, and the voltage measurement. The figure is adapted and simplified from fig. 4 in Georg Lohöfer; *Review of Scientific Instruments* **89,** 124709 (2018) with permission of AIP Publishing.

Electrical resistivity measurements using the SCE with the EML on the space station must be done with samples that are levitated in a ceramic cup instead of a metal cage. It is believed that the metal cage interferes with the coil electronics and that extra error is produced as a result. The temperature dependence of the error is unknown. Additionally, during electrical resistivity measurements the positioner and heater voltages should remain constant after the initial heating to a temperature above the liquidus temperature. It takes approximately one second for the electronics in the heater and positioner to become quiescent after a change in value. This is noticeable in the data at high temperatures when the heater voltage is decreased so the sample will cool. The electrical resistivity data is unusable in this region. Changes in the positioner or heater during a measurement cause egregious scatter in the electrical resistivity data. Finally, the heater voltage must be set to a minimum of 0.1V during the measurements so that the signal to noise ratio is sufficiently high. A higher heater voltage can be used for more accurate results; however, the sample may not deeply supercool due to the added power. Figure 2.13 shows a time-temperature and time-current plot during an electrical resistivity measurement of $Zr_{64}Ni_{36}$. Both the heater and positioner are invariant during cooling.

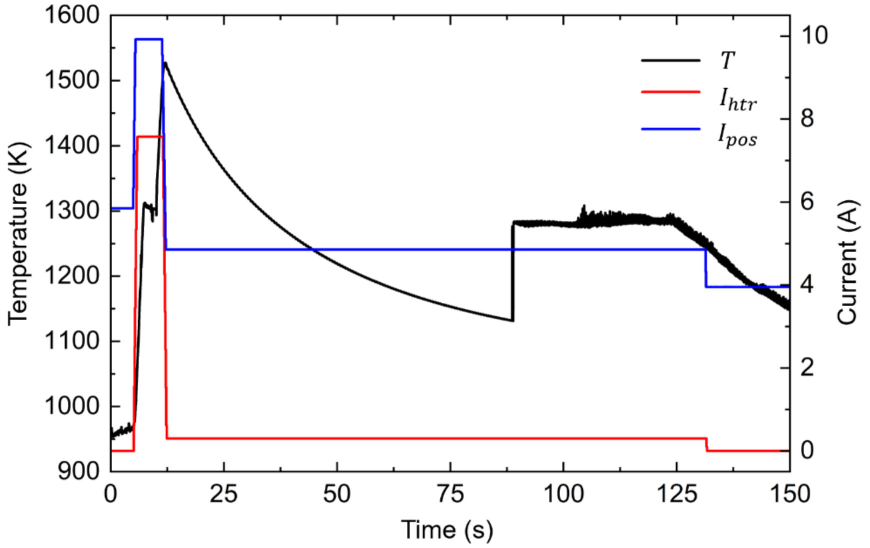

Figure 2.13 – A time-temperature curve during an electrical resistivity measurement of a $Zr_{64}Ni_{36}$ liquid droplet. The heater current, I_{htr}, and the positioner current, I_{pos}, are also shown.

After the electrical resistivity is measured, data are downloaded from the space station data website, hypertest, (https://vlab-ext.musc.dlr.de:8080/hypertest/projects/). Data are then analyzed following the instructions in the SCE manual (EML SCE Manual scientific measurement V2.1.pdf) using the OriginLab Notebook (EML-FM SCE data evaluation V2.1.opj) developed by Georg Lohöfer.

2.3.3 Specific Heat Measurements

A noncontact calorimetry technique first developed by Fecht and Johnson[20] has been updated so that it is possible to make specific heat measurements on board the International Space Station using the electromagnetic levitation facility. The technique was refined by Wunderlich and Fecht[21] and will be described in detail in chapter 4. Here, some basics are discussed to highlight how the measurements are made.

It is convenient to think about the sample as two distinct regions: a directly heated region with temperature T_H and a conductively heated region with temperature T_S. The directly heated region is close to the heater coils that supply power to the sample. Near the surface of the sample, the eddy currents produced by the heater and positioner magnetic fields heat the sample due to the sample's resistance, i.e. by ohmic loss. Figure 2.14 shows the directly heated and the conductively heated regions along with each of the power components, including the power provided to the sample by the positioner, P_{pos}, the heater power, P_{htr}, the radiative power going away from the sample, P_{rad}, the power conducted away from the sample by the gas conduction P_{con}^{gas}, and the conductive power providing heat to the internal region, P_{con}^{S}. A pyrometer measures the temperature of the sample at the sample pole, where the change in measured temperature comes from conductive transport of heat from the directly heated region. The power balance of the directly heated region is given by

$$c_H\left(\frac{dT_H}{dt}\right) = P_{pos} + P_{htr} - \left(P_{con}^{gas} + P_{con}^{S} + P_{rad}\right), \tag{2.10}$$

where c_H is the specific heat of the directly heated portion of the sample. Because the pyrometer aims at the sample in a location where the sample is not directly heated, there is a time delay between when the heater power is changed and when the temperature change is recorded by the pyrometer. The time delay gives information on the ratio of the specific heat over the thermal conductivity of the sample.

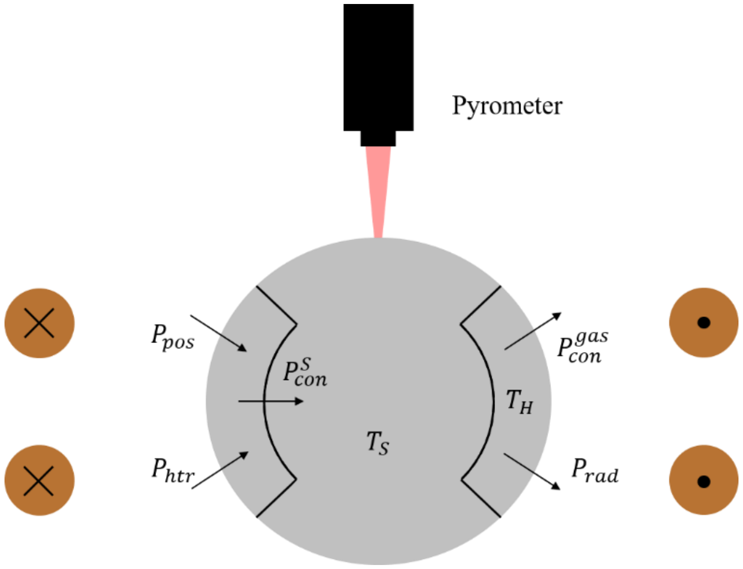

Figure 2.14 – A cross section schematic of a sample levitating between the inductive coils in the electromagnetic levitator on the space station. Each component of the sample power balance is shown as an arrow indicating the direction of heat transport. The solid lines indicate the region directly heated by the heater and positioner coils.

The power given to the sample by the positioner and the heater is proportional to the square of the current through the heater and positioner multiplied by a coupling coefficient, $P_{htr} = G_{htr}I_{htr}^2$ and $P_{pos} = G_{pos}I_{pos}^2$. Radiative power follows the Stefan-Boltzmann law as

$$P_{rad} = A\epsilon\sigma(T_H^4 - T_{env}^4), \tag{2.11}$$

where A is the sample area, ϵ is the sample emissivity, $\sigma = 5.67 \cdot 10^{-8}\ Wm^{-2}K^{-4}$ is the Stefan-Boltzmann constant, and T_{env} is the environment temperature surrounding the sample (~300K). In the EML on the space station samples are nearly spherical, so $A = 4\pi R_S^2$. The emissivity is the ratio of the energy emitted by the sample over the energy emitted by a perfect blackbody, giving a value between 0 and 1. A few assumptions must be made to solve the power balance equation: (1) c_p, ϵ, A, and the thermal conductivity of the sample, κ^S, are considered constant over small temperature intervals and (2) the power supplied to the sample by the positioner is negligible compared to the power supplied by the heater.

It is necessary to design the heater current in such a way that the power balance equations are easy to solve. In the method referred to as the "amplitude modulation method", the heater current is given by a modulation of amplitude I_ω with frequency ω around an average value, I_0,

$$I_{htr}(t) = I_0 + I_\omega \sin(\omega t)\,. \tag{2.12}$$

The power from the heater gives three terms because the square of the heater current is used. The $\sin^2(\omega t)$ term is on average non-zero, so the sample heats up due to the additional power from the oscillations. In the second method, known as the "power modulation method", the heater current is given by

$$I_{htr}(t) = [I_0^2 + I_\omega^2 \sin(\omega t)]^{\frac{1}{2}}. \tag{2.13}$$

In this case, the heater power is composed of two terms and the sample temperature remains constant on average. Measurements on the space station use the power modulation method so that the change in power due to the modulation is given by

$$\Delta P = G_{htr} I_\omega^2 \sin(\omega t)\,. \tag{2.14}$$

The amplitude of the temperature change is derived elsewhere[20,22] and is given by

$$\Delta T = \frac{\Delta P}{c_p \omega} f(\omega, \tau_1, \tau_2), \tag{2.15}$$

where τ_1 and τ_2 are the external and internal heat transport time constants and $f(\omega, \tau_1, \tau_2)$ is a correction factor accounting for the internal and external heat loss. Experiments are designed so that $f(\omega, \tau_1, \tau_2) \approx 1$, known as the adiabatic regime. The amplitude of the temperature change is offset from the original heater current input by a phase shift, ϕ, associated with the internal time constant. In the modulation calorimetry experiments, the current profile is supplied, and the temperature response is measured by the pyrometer. From eq. 2.15, the specific heat is determined by measuring the amplitude of the temperature response. At the time of writing this dissertation, the majority of the measurements completed on the space station use the power modulation method. Figure 2.15 shows the time-temperature and time-current profiles of a Vit106 sample during four different temperature modulation calorimetry measurements, each at two different frequencies.

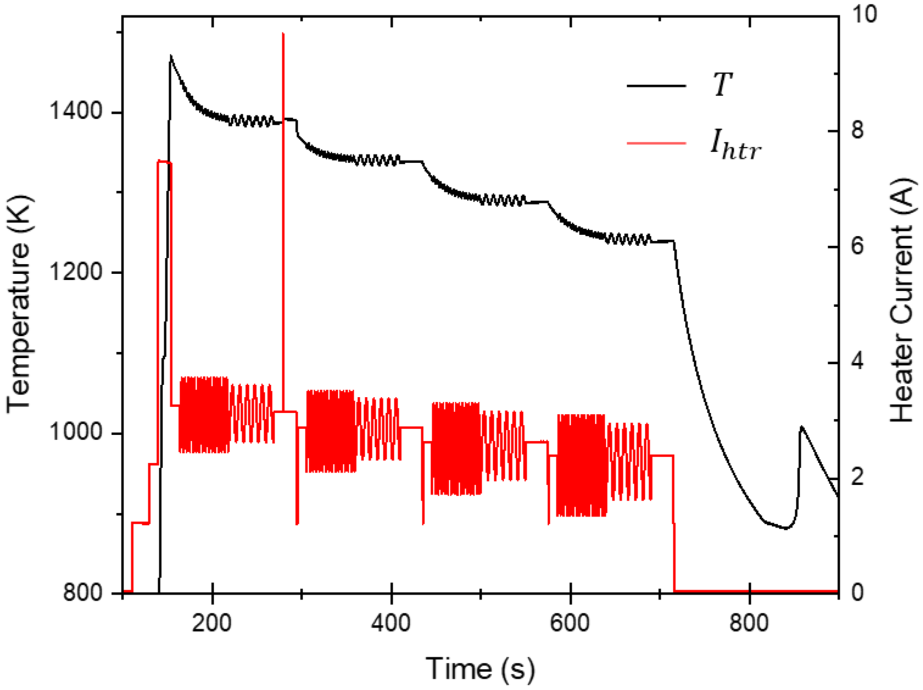

Figure 2.15 – A modulation calorimetry cycle for a Vit106 sample at four different temperatures in the liquid. A current pulse is seen after the first set of modulations causing the sample to oscillate in its $l = 2$, $m = 0$ spherical harmonic. The decay of the surface oscillations is related to the viscosity of the sample.

2.3.4 Crystal Growth Velocity Measurements

Measuring the crystal growth velocity in space using the EML is done in the same way as measuring the growth velocity in the BESL as discussed in section 2.2.3. A radial high-speed camera (CMOS Phantom V7.3) records the recalescence event and the spherical crystal growth front is manually tracked with time. The camera records up to 30k frames per second with varying resolution, depending on the rate. The spectrum of the camera on the space station extends into the infrared making it possible to see the growth fronts of samples with low liquidus temperatures. Figure 2.16 shows crystal growth of a sample in the EML on the ISS. The slope of the radius of the crystal front with time gives the crystal growth velocity.

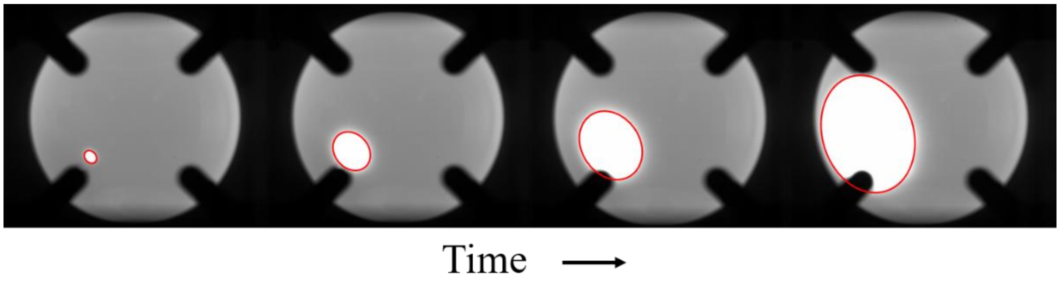

Figure 2.16 – Tracking the crystal growth with time of a sample in the EML on the space station using the radial high-speed camera. The four shadows overlapping the corners of the sample are the sample container. The red lines outline the growth front edge and are used to measure the crystal radius.

2.3.5 Viscosity Measurements

Measurements of viscosity and surface tension in the EML on board the ISS use the oscillating drop technique[9]. A magnetic field pulse created from a pulse of current through the heater coil is used to oscillate the sample at its $l = 2$, $m = 0$ spherical harmonic. During the measurement, the radial camera records the sample, capturing the surface modulations. Post processing of the video allows the amplitude of the oscillation to be tracked with time and fit to a decaying sinusoid. The decay time constant is related to the viscosity as described in section 2.2.2.

Figure 2.15 shows the heater current pulse around 200s during a modulation calorimetry cycle of Vit106 on board the ISS. Viscosity measurements in the microgravity environment are compared with measurements taken in the BESL. Some evidence suggests that the gravitational force on earth is strong enough to deform the sample and obscure the viscosity measurements[23]. However, likely due to non-quiescent ideal conditions in the EML on the space station, the BESL viscosity measurements appear to be more accurate and are less scattered. Viscosity data presented in the remainder of this dissertation were measured using the ground based BESL.

2.4 Modeling Silicate Glasses

Modeling non-isothermal nucleation and growth of glasses requires numerical methods, where time is divided into small intervals over which the temperature is assumed to remain constant. The method of modeling performed in this dissertation involves solving the kinetic nucleation equations discussed in section 1.4.4. Fortran code is used to solve the equations given thermodynamic inputs at each temperature, including the driving free energy, the surface free energy, the diffusion coefficient, and the interfacial width if the diffuse interface theory is used. Other parameters including the distribution of particles and the type of nucleation and growth (surface, volume, or both) are also specified. The user inputs an initial temperature, a final temperature, and a heating/cooling rate or isothermal hold time for the code to follow. At every desired time or temperature interval, the code saves the volume fraction transformed and the distribution of clusters and nuclei. Clusters larger than a user specified value ($10n^*$ for barium disilicate) are referred to as nuclei, which no longer grow by single monomer attachment and detachment in the code. Instead, nuclei grow according to the bulk growth velocity, which follows from the asymptotic limit of the forward and backward rate equations for large clusters[24]. When the experimentally measured growth velocity is used as the diffusion coefficient for the simulation, the bulk growth velocity in the code matches the measured growth velocity. The nuclei and cluster distributions can then be used as initial distributions for the next step of the simulation. In this dissertation, the numerical simulations follow the time-temperature profile of differential thermal analysis (DTA) experiments to prove the validity of the numerical technique, to probe theories of nucleation, and to explore the robustness of the DTA technique.

2.4.1 Fortran Code Structure and Objective

The code described below was originally developed by Ken Kelton. The Fortran code is separated into several subroutines that are called from the main program. As the program begins, the input and output files are initialized, arrays are created for holding the nuclei and cluster distributions, and subroutines are called depending on the user input for the type of calculation. Many experiments begin with a high temperature liquid, which is quenched to room temperature. If this is the case, the quenching subroutine is called, and a steady-state initial distribution is developed before performing the iterative calculation with the desired quench rate. The cluster and nuclei distributions are saved to output files and the Fortran code ends. The simulation can follow any series of isothermal or non-isothermal time-temperature steps, saving the distributions after each. During any non-isothermal steps, the thermodynamic parameters are re-calculated at each temperature.

The calculation timestep starts at a small value so that the forward and backward reaction equations are solved accurately. However, using the small timestep throughout the simulation is costly and not necessary. As such, after a user-defined number of calculational steps, the timestep is doubled if a projected calculation using the doubled timestep does not differ from a projected calculation using the current timestep. The calculation may encounter unphysical distributions (i.e. negative cluster densities) if the timestep is too large. If this occurs, the timestep is halved and the step is repeated until an acceptable timestep is found.

In the main calculational loop at a given timestep, the rate of change of each cluster density is calculated following the kinetic solution of the classical theory. Then the number of clusters of each size is updated using the rate of change. If any clusters become larger than the cutoff size specified by the user, then the clusters are promoted to nuclei, which can only grow. Any promoted nuclei grow according to the bulk growth velocity, which is calculated from the asymptotic limit of the forward and backward rate reaction for large clusters and taking the diffusion coefficient from the induction time, bulk growth velocity, or the Stokes-Einstein relation[24]. The volume fraction transformed is then calculated using the volume of the clusters and nuclei. The Johnson-Mehl-Avrami-Kolmogorov (JMAK) method[25–29] is used to account for overlapping nuclei. Then the time and temperature are incremented according to the heating/cooling rate, and the procedure begins again with the updated cluster and nuclei distributions. The thermodynamic properties are recalculated if the temperature has changed. The volume fraction transformed, the number of clusters at the critical size, the nucleation rate defined at the cluster/nuclei cutoff size, and the DTA signal are saved in the output files at user specified times or temperatures. The simulation ends when the time-temperature profile is completed, or the sample has completely crystallized.

As previously stated, many simulations begin with a quench from the high temperature liquid where dynamics are quick enough to set up a steady-state distribution in a short time. After the quench, any number of steps can occur. For example, in a DTA simulation, the sample quickly heats up to the desired nucleation treatment temperature where the growth rate is small and the nucleation rate is appreciable. The sample is isothermally held at the nucleation treatment temperature for a desired time. Then the sample is heated with a constant rate until the volume is completely transformed into the crystal phase. DTA simulations of barium silicate glasses following this procedure are described in chapter 5.

An important aspect of the code is the ability to track the cluster and nuclei distributions with time. Most importantly, this is used to track the volume fraction transformed from the glass to the crystal. However, another application involves designing a time-temperature profile to develop a specific nuclei distribution for a specific application in an industrial or research setting. It is reasonable to imagine the nuclei distribution affecting the optical, thermophysical, or dynamical properties of a glass.

2.4.2 Fortran Code Python Wrapper

The Fortran code itself is designed to perform a single step of a time-temperature profile, given the initial and final temperature as well as the heating/cooling rate. After one step, the user can use the outputs and manually modify the inputs to perform the next step in the profile. This may take a long time especially when a large number of profiles are to be explored. In the DTA experiments described in chapter 5, there are greater than 20 nucleation treatment temperatures tested while the remaining heating profile is the same. Because of this, a wrapper designed in Python was built. The wrapper assembles each input file for multiple simulations automatically, based on input from the user. The user can specify many steps to be performed in succession as well as parallel steps involving different nucleation treatment temperatures.

Running the Python wrapper builds directories hierarchically, where some data is shared between simulations. For example, if the user is exploring the DTA signal as a function of the nucleation treatment temperature, then the quench is only performed once and shared between each nucleation treatment cycle. Each time a new step is reached, the code calls the Fortran simulation routines with the appropriate input files and flags for the specific step. This code can be run either on a desktop or on a cluster with very few changes in the wrapper depending on the operating system.

2.5 Summary

Chapter 2 covers the experimental methods required for the remaining work completed in this dissertation. Methods for creating electrostatic levitator samples were first discussed. Raw material is arc-melted together to form ingots, which are then broken and arc-melted again into 35-70 mg spherical ESL samples. Melt spinning was also discussed for making glasses where traditional quenching techniques do not cool quickly enough to bypass crystallization. Then the beamline electrostatic levitator at Washington University in St. Louis was discussed in detail. Samples are levitated between a series of electrodes producing a dynamically changing electric field based on the measured position of the sample. Using the BESL it is possible to measure thermophysical and dynamical properties of liquid droplets including the density, viscosity, maximum supercooling, and the crystal growth velocity. The density is measured by recording the sample in a quiescent state over a range of temperature and using edge detection to determine the sample diameter. The oscillating drop technique, where a sinusoidal electric field is superposed on the vertical potential in the ESL to oscillate the sample in its $l = 2, m = 0$ spherical harmonic, is used to measure the viscosity. A high-speed camera, capable of measuring up to 900,000 fps records samples as they crystallize to capture the growth front with time. Finally, X-ray measurements using the BESL at the Argonne National Lab APS were discussed.

The electromagnetic levitator on the International Space Station was also discussed in detail. The EML was built and sent to space to study diffusion effects and nucleation in a quiescent state. The EML can measure the maximum supercooling temperature, electrical resistivity, specific heat, growth velocity, and viscosity of metal samples as a function of temperature. The electrical resistivity is measured using the sample coupling electronics by determining the additional circuit impedance caused by feedback from the eddy currents induced in the sample from the heater magnetic field. Specific heat is measured using the modulation calorimetry technique where the power is modulated, and the temperature response is recorded. Growth velocity and viscosity are measured in the EML using similar techniques to the BESL.

The methods for modeling the crystallization of silicate glasses were discussed. Numerical Fortran simulations track the cluster and nuclei distributions as a function of time and temperature by solving the kinetic nucleation equations until the sample is completely crystallized or the desired time-temperature profile is completed. This process has been made easier by the development of a Python wrapper allowing for more than one time-temperature profile step to be completed automatically in succession.

2.6 References

1. El-Eskandarany, M. S. *Mechanical Alloying: Nanotechnology, Materials Science and Powder Metallurgy*. (Elsevier Science, 2015).
2. Mauro, N. A. & Kelton, K. F. A highly modular beamline electrostatic levitation facility, optimized for in situ high-energy x-ray scattering studies of equilibrium and supercooled liquids. *Rev. Sci. Instrum.* **82**, (2011).
3. Bendert, J. C. Thermophysical and Structural Measurements of Liquid Metallic Alloys Using Electrostatic Levitation. PhD Thesis. (Washington University in St. Louis, 2013).
4. Sellers, M. E. Studies of Maximum Supercooling and Stirring in Levitated Liquid Metallic Alloys. PhD Thesis. (Washington University, 2020).
5. Bendert, J. C., Pueblo, C. E., Veligati, S., Mauro, N. A. & Kelton, K. F. Temperature calibration for optical pyrometry in containerless systems using differential scanning calorimetry: Application to Cu100−xZrx(x = 45–50). *Int. J. Thermophys.* **35**, 1687–1696 (2014).
6. Rhim, W. K. *et al.* An electrostatic levitator for high-temperature containerless materials processing in 1-g. *Rev. Sci. Instrum.* **64**, 2961–2970 (1993).
7. Bradshaw, R. C., Schmidt, D. P., Rogers, J. R., Kelton, K. F. & Hyers, R. W. Machine vision for high-precision volume measurement applied to levitated containerless material

processing. *Rev. Sci. Instrum.* **76**, 1–8 (2005).

8. Pueblo, C. E. Ground and Flight Based Studies of Nucleation and Thermophysical Properties in Metallic Glass Forming Systems. PhD Thesis. (Washington Univeristy in St. Louis, 2016).

9. Rhim, W. K., Ohsaka, K., Paradis, P. F. & Erik Spjut, R. Noncontact technique for measuring surface tension and viscosity of molten materials using high temperature electrostatic levitation. *Rev. Sci. Instrum.* **70**, 2796–2801 (1999).

10. Bendert, J. C. & Kelton, K. F. Containerless measurements of density and viscosity for a Cu48Zr52liquid. *Int. J. Thermophys.* **35**, 1677–1686 (2014).

11. Blodgett, M. E., Egami, T., Nussinov, Z. & Kelton, K. F. Proposal for universality in the viscosity of metallic liquids. *Sci. Rep.* **5**, 1–8 (2015).

12. Bendert, J. C., Blodgett, M. E. & Kelton, K. F. Calculation of absorption and secondary scattering of X-rays by spherical amorphous materials in an asymmetric transmission geometry. *Acta Crystallogr. Sect. A* **69**, 131–139 (2013).

13. Egami, T. & Billinge, S. J. L. *Underneath the Bragg Peaks: Structural Analysis of Complex Materials*. *Pergamon Materials Series* **16**, (Pergamon, 2012).

14. Lohöfer, G. High-resolution inductive measurement of electrical resistivity and density of electromagnetically levitated liquid metal droplets. *Rev. Sci. Instrum.* **89**, 4709 (2018).

15. Lohöfer, G. Device for positioning and melting electrically conductive materials without a receptacle. U. S. Patent 4993043. (1991).

16. Kelton, K. F., Gangopadhyay, A. K., Hyers, R. W. & Holland-Moritz, D. *Studies of nucleation and growth, specific heat and viscosity of undercooled melts of quasicrystals and polytetrahedral-phase-forming alloys. Science Requirement Document*. (2002).

17. Skripov, V. P. Crystal Growth and Materials. in *Current Topics in Materials Science* (eds. Kaldis, E. & Scheel, H. J.) 328 (North-Holland, 1977).

18. Sellers, M. E., Van Hoesen, D. C., Gangopadhyay, A. K. & Kelton, K. F. Maximum supercooling studies in Ti39.5Zr39.5Ni21, Ti40Zr30Ni30, and Zr80Pt20 liquids — Connecting liquid structure and the nucleation barrier. *J. Chem. Phys.* **150**, (2019).

19. Lohöfer, G. Magnetization and impedance of an inductively coupled metal sphere. *Int. J. Eng. Sci.* **32**, 107–117 (1994).

20. Fecht, H. J. & Johnson, W. L. A conceptual approach for noncontact calorimetry in space. *Rev. Sci. Instrum.* **62**, 1299–1303 (1991).

21. Wunderlich, R. K. & Fecht, H. J. Modulated electromagnetic induction calorimetry of reactive metallic liquids. *Meas. Sci. Technol.* **16**, 402–416 (2005).

22. Wunderlich, R. K. & Fecht, H.-J. Thermophysical Property Measurements by

Electromagnetic Levitation Methods under Reduced Gravity Conditions. *J. Jpn. Soc. Microgravity Appl.* **20**, 192–205 (2003).

23. Bratz, A. & Egry, I. Surface oscillations of electromagnetically levitated viscous metal droplets. *J. Fluid Mech.* **295**, 341–359 (1995).

24. Kelton, K. F. & Greer, A. L. Transient Nucleation Effects in Glass Formation. *J. Non. Cryst. Solids* **79**, 295–309 (1986).

25. Johnson, W. A. & Mehl, R. F. Reaction Kinetics in Processes of Nucleation and Growth. *Am. Inst. Min. Metall. Eng.* **135**, 416–442 (1939).

26. Avrami, M. Kinetics of Phase Change. I General Theory. *J. Chem. Phys.* **7**, (1939).

27. Avrami, M. Kinetics of Phase Change. II Transformation-Time Relations for Random Distribution of Nuclei. *J. Chem* **8**, (1940).

28. Avrami, M. Granulation, Phase Change, and Microstructure Kinetics of Phase Change. III. *J. Chem. Phys.* **9**, (1941).

29. Kolmogorov, N. A. A statistical theory for the recrystallization of metals. *Izu. Akad. Nauk SSSR* **3**, 355–359 (1937).

Chapter 3: Resistivity Saturation in Metallic Liquids Above a Dynamical Crossover Temperature Observed in Measurements Aboard the International Space Station

The work in this chapter is published in Van Hoesen, D. C. *et al.*, "Resistivity Saturation in Metallic Liquids Above a Dynamical Crossover Temperature Observed in Measurements Aboard the International Space Station," *Phys. Rev. Lett.* **123**, 226601 (2019)[1]. Figures and text are reproduced with permission from the American Physical Society.

Although a resistivity saturation (minimum conductivity) is often observed in disordered metallic solids, such phenomena in the corresponding liquids are not known. Here we report a saturation of the electrical resistivity in $Zr_{64}Ni_{36}$ and $Cu_{50}Zr_{50}$ liquids above a dynamical crossover temperature for the viscosity (T_A). The measurements were made for the levitated liquids under the microgravity conditions of the International Space Station. Based on recent molecular dynamics simulations, the saturation is likely due to the ineffectiveness of electron-phonon scattering above T_A when the phonon lifetime becomes too short compared to the electron relaxation time. This is different from the conventional resistivity saturation mechanisms in solids.

3.1 Introduction

The dynamical properties (viscosity (η), diffusivity (D), and structural relaxation time (τ)) of all liquids undergo enormous changes with temperature. If the metastable state of a liquid below its melting (or liquidus) temperature, T_l, can be retained by preventing crystallization, it ultimately freezes into a glass at some characteristic, cooling-rate-dependent, temperature, T_g. The magnitude of the temperature interval $T_l - T_g$ (a few hundreds to a thousand degrees Kelvin) is small compared to the twelve to fourteen orders of magnitude change in the highly non-linear dynamical properties over the same temperature interval. It may be expected that a significant change in structure occurs in the same temperature range as the large change in dynamics. However, a relationship between structure and dynamics has been difficult to experimentally measure. Electron scattering, which is the source of the electrical resistivity, is sensitive to the local structure in liquid binary alloys, which is difficult to probe in conventional (X-ray and neutron scattering) structural measurements.

Electron transport in metals is influenced by disorder, electron-electron correlation, and various elastic and inelastic scattering processes. While the effect of disorder is usually temperature independent (except for temperature induced defect formation), the characteristic energy scales with respect to temperature determine the relative importance of the various temperature-dependent scattering processes. The electrical resistivity usually increases with disorder and temperature. Therefore, with a sufficient amount of disorder and high thermal energy (temperature) it may saturate at high temperatures, reaching a minimum conductivity, when the mean free path becomes comparable to the interatomic spacings ($l \sim d$), as was suggested by Ioffee and Regel[2] and Mott[3]. Most solids melt before this condition can be reached. However, many examples of resistivity saturation exist in disordered solids and glasses at low temperatures[4], A-15[5], and Chevrel-phase[6] superconductors in the normal state, and heavy-fermion compounds[7]. There are also some indications for an approach to saturation in a few refractory high melting temperature elemental solids[8]. In contrast, many crystalline *metallic* systems, the so-called "bad metals" (*e.g.* high-T_C oxides[8,9] and quantum-critical systems[10]), show no evidence for resistivity saturation even after attaining much higher values (in some cases up to a factor of ten) than the

Ioffee-Regel-Mott (IRM) limit. The mechanisms responsible for this behavior in these exotic materials are currently under debate[10,11] and are outside the scope of this work.

3.2 Viscosity and the Crossover Temperature

Here, we demonstrate the saturation of the resistivity at high temperature in two marginal glass-forming metallic liquids, $Zr_{64}Ni_{36}$ and $Cu_{50}Zr_{50}$. Interestingly, the saturation occurs just above the dynamical crossover temperature T_A, which is determined as the temperature at which the viscosity changes from an Arrhenius $\left(\eta \propto \exp\left(-\frac{E}{k_B T}\right)\right)$ behavior to a low temperature non-Arrhenius behavior, where the activation energy, E, increases with decreasing temperature, T. (k_B is the Boltzmann constant). The crossover temperature has become a subject of intense discussion in recent years[12–21]. Molecular dynamics simulations[12–15] have been particularly useful in elucidating the role of T_A. It has been related to the temperature-dependent lifetimes of the coordination numbers of local clusters, which begin to exceed the time required to communicate coordination changes to the neighboring atoms below this temperature. This communicated information sets the stage for correlated motion of atoms below T_A, which becomes increasingly more cooperative until glass formation. This suggests a natural link between liquid structure and dynamics. Since the resistivity is determined by structural disorder leading to elastic and inelastic scattering, the observation of a resistivity saturation above T_A in the present case is taken as a clear demonstration of such a link between structure and liquid dynamics. Unlike the case in crystals and glasses, the saturation does not correspond to the largest electrical resistivity; the resistivities of the corresponding glasses are much larger. The behavior in the liquids, then, differs remarkably from that observed in conventional crystalline metallic crystals and glasses.

A direct link between structural changes at T_A with the liquid dynamics has not been convincingly established from experiments thus far. Some evidence has been reported in the static structure factor, $S(q)$[22]. However, while correlated, the value of T_A that is determined from the viscosity is larger than from the structural data. The overlap of the many different partial structure factors that contribute to the total $S(q)$ and the simultaneous presence of many different types of order in a liquid[23] likely obscure the onset of cooperativity in the $S(q)$ data. Moreover, as the lifetime of the coordination numbers/atomic bonds become too short above T_A[14,15], the static structure factor may become insensitive to such changes. Electron scattering is very sensitive to static and rapidly changing chemical- and structural-order/disorder. Therefore, electrical transport (resistivity) measurements are routinely used to study order-disorder transformations in solids[24]. Naturally then, electrical resistivity is well-suited to study rapid structural changes over small length scales, such as in the onset of cooperativity.

3.3 Experimental Methods

3.3.1 Viscosity

With the above objectives, the electrical resistivity was measured in the equilibrium and supercooled (i.e. below the liquidus temperature, T_l) liquids of two marginal glass-forming alloys, $Cu_{50}Zr_{50}$ and $Zr_{64}Ni_{36}$, in the microgravity environment of the International Space Station (ISS) using the electromagnetic levitation (EML) facility. The viscosities of equilibrium and supercooled liquid droplets ($\sim 2.5\ mm$ diameter) were measured under terrestrial conditions using our electrostatic levitation (ESL) facility[25] and the oscillating drop technique[26]. They are in agreement with measurements aboard the ISS under microgravity[27] and in parabolic flight experiments[28]. However, because of higher resolution, data from the ground-based studies[17] were used for the determination of T_A. As shown in fig. 3.1, T_A is identified from the onset of deviation of the high temperature viscosity from a plot of $\log(\eta)$ with inverse temperature. A statistical method[22] was used to give the most objective values of T_A as 1283 K ± 19 K for $Zr_{64}Ni_{36}$ and 1196 K ± 21 K for $Cu_{50}Zr_{50}$, with a two-sigma error.

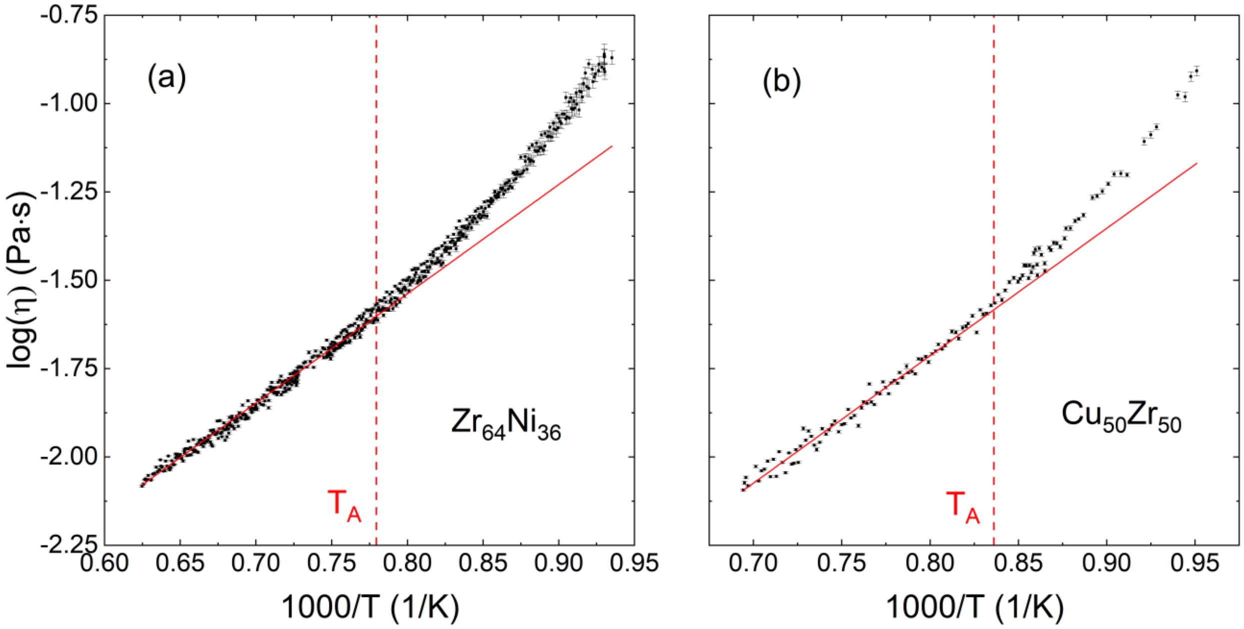

Figure 3.1 – The liquid shear viscosity for (a) $Zr_{64}Ni_{36}$ and (b) $Cu_{50}Zr_{50}$ liquids including the crossover temperatures (T_A), measured by the oscillating drop technique on electrostatically levitated samples.

3.3.2 Electrical Resistivity

The alloy ingots were prepared from high purity elements (Zr (Smart Elements, Vienna, 99.97 at.%), Ni (Alfa Aesar 99.999 at.%), Cu (Alfa Aesar 99.999 at.%)) that were mixed in the appropriate amounts and arc-melted under an argon atmosphere (5N purity), which was further purified by melting a $Ti_{50}Zr_{50}$ getter. Spherical samples of 7 mm diameter were prepared by casting the alloys in water-cooled copper molds. The samples were stored in an argon filled glove box and transported to the ISS in dedicated sample holders under a helium atmosphere.

Since an unconventional technique was used for the electrical resistivity measurements, a brief description of the facility and the experimental procedures are provided below; details may be found elsewhere[29]. Conventional four-probe techniques for the measurement of high melting-temperature liquids face major challenges due to contamination from the container and chemical reactions with probes and sample atmosphere, which are absent in the EML (containerless) processing under high vacuum. EML also enables studies of supercooled metastable liquids below T_l. However, EML studies under terrestrial conditions require large radio-frequency (RF) generated magnetic fields to levitate metallic samples. This produces large eddy currents that heat and melt the samples, preventing studies of supercooled liquids. While it is possible to bypass this problem by processing in a helium atmosphere, even the highest purity commercially available gases often contaminate the sample. Further, the strong magnetic forces produce turbulent flow in the liquid, which can disturb the measurements. These issues are alleviated using EML processing in a microgravity environment.

The MSL-EML facility aboard the ISS consists of water-cooled Cu-coils that generate two RF magnetic fields: (i) a quadrupole field that provides sample positioning and (ii) a superposed homogeneous dipole field to provide independent inductive sample heating (fig. 3.2). The homogeneous RF field allows non-invasive, inductive measurements of the electrical resistivities[29] of the levitated solids and equilibrium and supercooled liquids. The decoupled heating and levitation allows the ISS/EML facility to be used to measure other thermophysical properties of metallic liquids, such as the specific heat[30]. The measurements are made on $6.5 - 8\ mm$ diameter spherical samples.

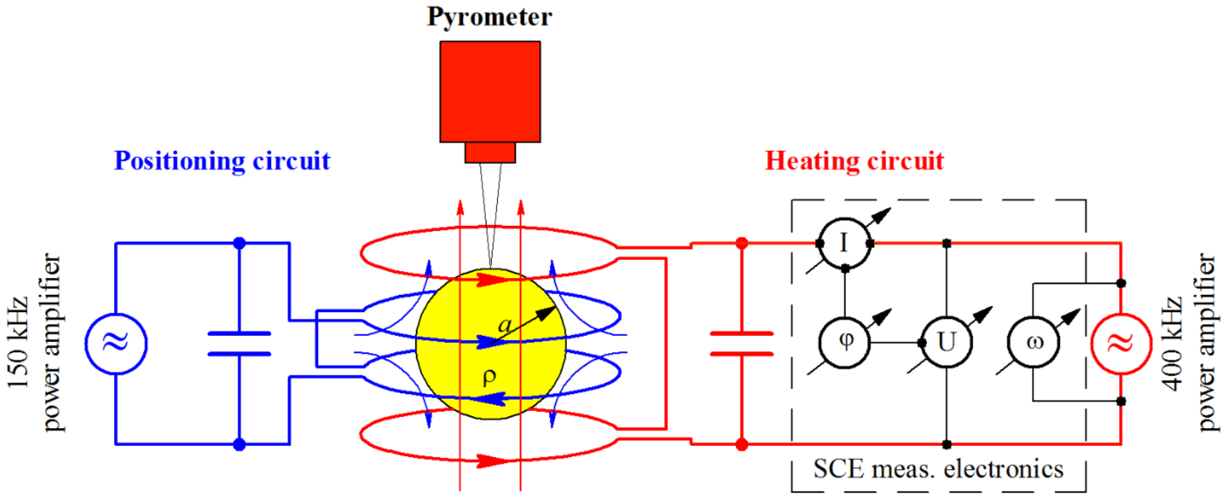

Figure 3.2 – A sample (yellow) at the center of the positioning and heating coils. A RF current in the opposite direction (left circuit) through the upper and lower coil generates a magnetic quadrupole field for the positioning of the sample. A RF current in the same direction through the coil generates a magnetic dipole field for heating the sample (right circuit). Also shown are the sample coupling electronics (SCE) for measuring the electrical admittance and a pyrometer for sample temperature measurement.

As shown in fig. 3.2, the sample is inductively coupled by the RF magnetic heating field to the resonant heating circuit, which is powered by a 400 kHz RF power amplifier. The total complex admittance of the electrical heating circuit is

$$Y_{tot} = 2i\omega C + \frac{2}{R_L + i\omega L + Z_S(a,\rho)/2}, \tag{3.1}$$

where i denotes the imaginary unit, C is the condenser capacitance, L is the coil inductance, and R_L is the coil resistance. $Z_S(a,\rho)$ is the complex impedance of the sample, which depends on the sample radius, a, and the electrical resistivity, ρ. To obtain the total admittance of the circuit, defined by

$$Y_{tot} = \frac{I_0}{U_o} e^{-i\varphi}, \tag{3.2}$$

the sample coupling electronics (SCE) in the EML facility measures the amplitude of the RF current through the circuit, I_o, the voltage drop over the circuit, U_o, and the phase shift between the voltage and current, φ, at a frequency, ω. Without a sample ($Z_S = 0$), measurements of these quantities enable the determination of the circuit parameters C, L, and R_L from eq. 3.1. A subsequent measurement of Y_{tot} with a sample in the levitator yields the sample impedance, $Z_S(a, \rho)$. For a spherical sample (as is the case for the liquid under microgravity) in a homogeneous RF magnetic field, the theoretical relation between $Z_S(a, \rho)$, the sample radius, a, and the resistivity, ρ, have been calculated by Lohöfer[31].

Although the samples levitated on its own under microgravity, a small voltage ($2.5V$) to the positioner coil was applied to prevent them from wandering. They were processed both under high vacuum ($10^{-8} Torr$) or $300\ mbar$ He/Ar atmospheres. A high voltage (~$10V$) was applied to the heater coil to melt and heat the samples 300 to 400 K above the liquidus temperature. Overheating was necessary to achieve maximum supercooling (about $1.20\ T_l$ for both samples). Nearly spherical ingots prepared on ground turned spherical after the first melting cycle under microgravity. The heater voltage was kept at a minimum of $0.1V$ during cooling to acquire impedance data from the SCE circuit. Data were collected during repeated melt-cool cycles.

3.3.3 Liquid Density

Two-dimensional video images of the levitated spherical droplets were analyzed to obtain the specific volume/density as a function of temperature, as described elsewhere[32,33]. Such data are required to determine the temperature dependence of the sample radius, which is an input parameter in the resistivity measurements. Small distortions from spherical symmetry were observed in terrestrial measurements, which contributed very little error due to inherent symmetry about the vertical axis and sample rotation due to radiation pressure. Typically, volume changes could be resolved within 1 part in 10^4. The absolute precision was limited to about 1%, dictated by the precision of the tungsten carbide calibration spheres (McMaster-Carr Inc., USA). Figure

3.3 shows the specific volume as a function of temperature for the $Cu_{50}Zr_{50}$ and $Zr_{64}Ni_{36}$ liquids. 10-point adjacent averaging was used to reduce noise in the data.

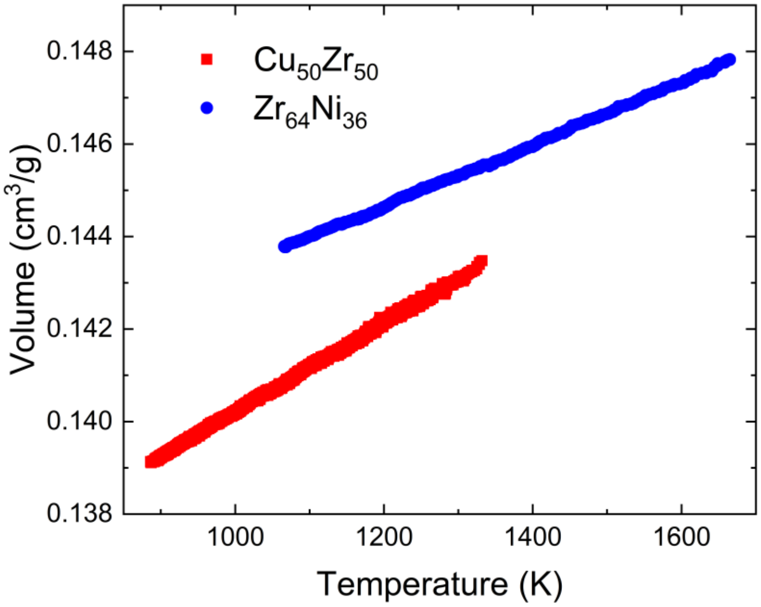

Figure 3.3 – The specific volumes of $Cu_{50}Zr_{50}$ and $Zr_{64}Ni_{36}$ liquids as a function of temperature as measured by the ESL technique.

3.4 Results and Discussion

In a typical measurement cycle, the sample is levitated and then melted by increasing the current through the heater coils. The heater and positioner currents are then reduced and kept constant during cooling throughout the resistivity measurement. Figure 3.4 shows the resistivity data for both liquids during two representative thermal cycles. In some cases, small cycle-to-cycle variations (<1%) in the absolute magnitude of resistivity were observed. This could be due to small changes in the sample position relative to the coil and/or small changes in temperature of the measurement electronics. Considering this and the precision in radius measurements (1% in absolute magnitude and 0.01% in relative changes), the error in the absolute resistivity would be close to 2% and relative changes to about 0.7%. However, the temperature dependence of the resistivity remained the same in all measurement cycles. For both alloys, the temperature coefficients of the resistivity ($dln\rho/dT$) are negative, which are usually observed in high resistivity metallic glasses[4,34]. The most interesting observation is the near saturation of resistivity above the crossover temperature, T_A, determined from the viscosity measurements. We are not aware of any previous report demonstrating the saturation of the resistivity in a metallic liquid. While the resistivity of $Zr_{64}Ni_{36}$ saturates precisely at T_A, the $Cu_{50}Zr_{50}$ resistivity goes through a minimum around T_A before saturating at a higher temperature. The reason for this slightly different behavior for the $Cu_{50}Zr_{50}$ liquid is currently unclear.

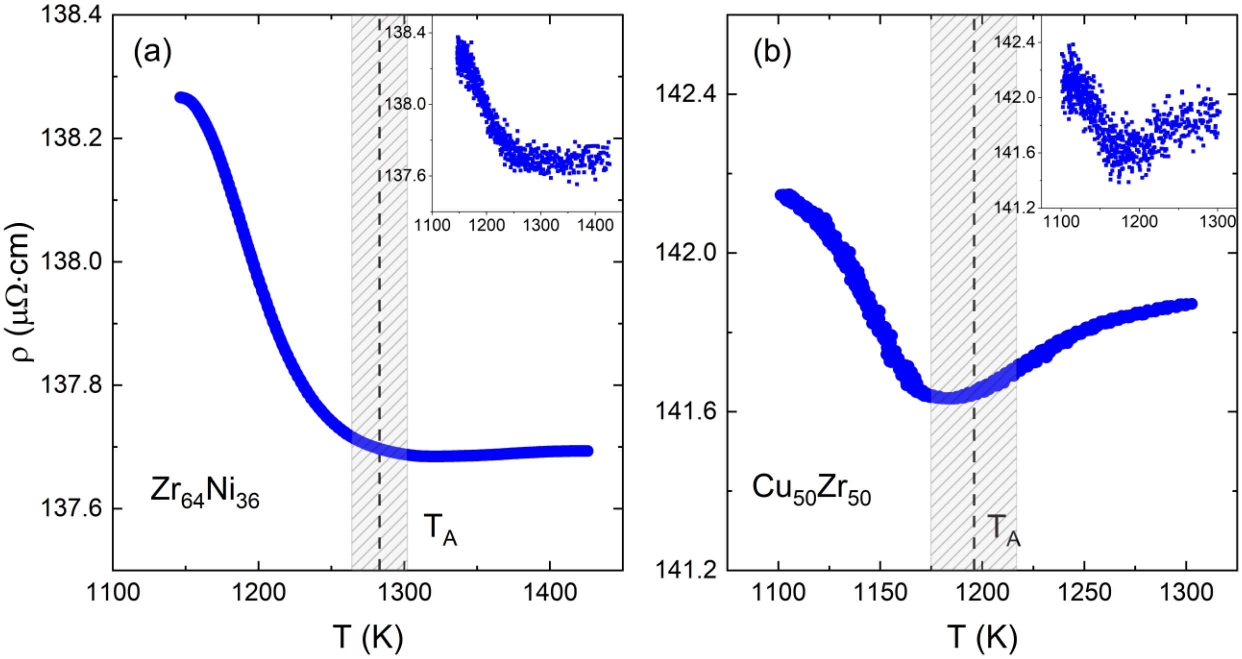

Figure 3.4 – The electrical resistivity, smoothed by 200-point averaging, as a function of temperature in liquid (a) $Zr_{64}Ni_{36}$ and (b) $Cu_{50}Zr_{50}$, showing near saturation at or above T_A. The shaded regions represent the uncertainties in T_A. The original data are shown in the insets.

The sign of $dln\rho/dT$ depends very much on the magnitude of the resistivity of the alloy, as was observed by Mooij[34] quite a while ago. A sign change from positive to negative coefficient was observed around 150 $\mu\Omega - cm$, although this was later found to be not universal[35]. This may be explained in many different ways[4,36]. The pseudopotential based Ziman theory[37–39] or its extension, the t-matrix based Ziman theory for the elemental[40] and alloy[41] liquids, are some of these. Both approaches express the resistivity in terms of the structure factor, $S(q)$ (partial $S(q)s$ for the alloys) and the pseudopotential, $|V(q)|$[37,38], or the scattering matrix (t-matrix)[40,41]. In both cases, the temperature dependence of resistivity arises from the change in the $S(q)$ with temperature, since the pseudopotentials or the t-matrix are temperature independent in these theories. When the Fermi wave vector, $2k_F$, lies on the higher q-side of the first peak of $S(q)$, $dln\rho/dT$ becomes negative because of the decrease of $S(q_{2k_F})$ with increasing temperature. Using the liquid partial structure factors from the molecular dynamics (MD) simulations of $Zr_{64}Ni_{36}$ and $Cu_{50}Zr_{50}$ and reasonable values for k_F, negative temperature coefficients of resistivities for both alloys could be reproduced as shown in fig. 3.7. A quantitative agreement with experiments is not expected, since such calculations are very sensitive to the choice of E_F and k_F[42]. However, most importantly, while the negative $dln\rho/dT$ can be qualitatively explained by the Faber-Ziman type theories the saturation of resistivity above T_A cannot be because the $S(q)$ and its partials continue to decrease at nearly the same rates above and below T_A[43,44].

Given that the $Zr_{64}Ni_{36}$ and $Cu_{50}Zr_{50}$ liquids contain valence electrons coming from both $s-$ and $d-electron$ shells, Mott's[45] idea of scattering of s-electrons into the partially empty d-bands due to *fluctuations* of atomic separations in disordered and liquid alloys may also be relevant. The probability of an $s-d$ transitions in this model does not explicitly depend on the structure factor, but on the available empty states near the Fermi level, $N(E_F)$. Since the density of states is weakly temperature dependent, if $N(E_F)$ lies on the higher energy side of a maximum, the probability of $s-d$ transitions may show a small decrease, and therefore a small negative $dln\rho/dT$, as observed for the two liquids. However, a saturation at high temperatures is not expected.

Electron transport theories are typically based on the Boltzmann equation, which treats electrons in-between collisions as classical particles. However, when the mean free path approaches the IRM limit, interference of the incident and scattered electron waves become important and the Boltzmann transport theory must be modified. This is called the "weak or incipient electron localization" regime, which occurs when there is sufficient quantum interference of the incident and scattered waves[46–48]. The idea is similar to those developed by Anderson for electron localization in disordered solids[49]. However, instead of conduction by hopping with increasing temperature in Anderson localization, the increase in conductivity for weak localization is due to the dephasing (loss of coherence) of the scattered waves from inelastic scattering by phonons, which weakens localization. The conductivity, σ, then rises linearly with temperature far below the Debye temperature, θ_D, and as $\sqrt{T}$ above it[47,48].

To check this, the resistivities of the corresponding glasses were measured by a commercial PPMS (Physical Property Measurement System, Quantum Design, CA) at low temperatures. $2\,mm$ wide and $20\mu m$ thick amorphous ribbons, produced by the conventional melt-quench technique, were used for this purpose. Figure 3.5 shows the conductivity of both glasses and liquids of $Zr_{64}Ni_{36}$ and $Cu_{50}Zr_{50}$. In the glass at temperatures above approximately 100 K, $\sigma \propto \sqrt{T}$, which is consistent with weak localization theories. A change to $\sigma \propto T$ at the lowest temperatures ($T \ll \theta_D$) is also expected in the same theoretical framework, which was observed by Howson and Grieg[48] in the $Cu_{50}Zr_{50}$ glass. Because of the limited amount of data for the liquid at temperatures below T_A, it is difficult to state clearly whether the liquid follows the same functional relationship with temperature as the glass at high temperatures. However, it is clear from fig. 3.4 that the temperature dependence is non-linear.

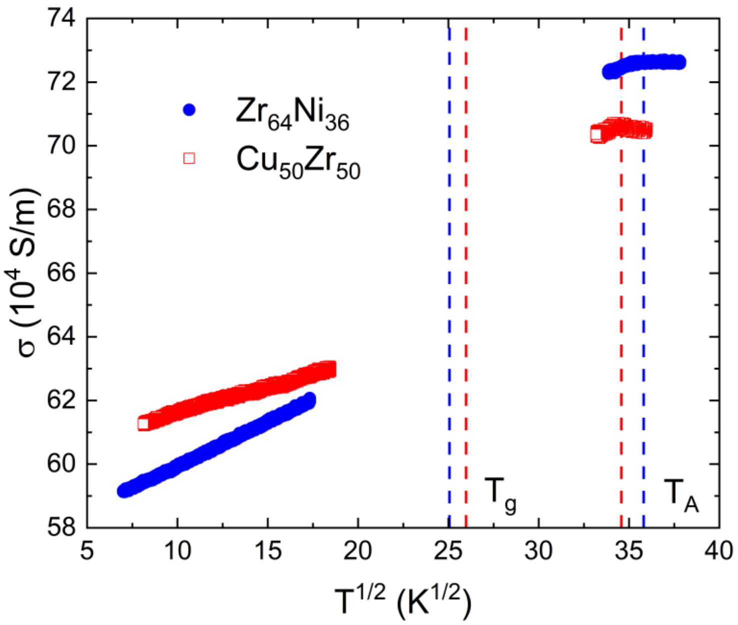

Figure 3.5 – The electrical conductivities of glassy and liquid $Zr_{64}Ni_{36}$ and $Cu_{50}Zr_{50}$. The glass transition (T_g) and crossover (T_A) temperatures are also shown.

The local order in a glass below T_g does not change with temperature (except for very slow structural relaxation) and the increase in conductivity is entirely due to decreasing elastic/inelastic scattering. In contrast, above T_g in the supercooled liquid and above T_l in the equilibrium liquid, the spatial and temporal SRO changes continuously. This is expected to change the active high-frequency phonons responsible for the inelastic scattering of electrons. Such changes in phonon scattering are not considered in the weak localization theories.

Since no theory for "weak localization" for systems with changing short/medium range order is available, it is not yet possible to quantitatively understand the mechanism responsible for the saturation of the resistivity in the liquid. However, we put forward a qualitative explanation. Saturation above T_A for both liquids is a strong indication that it is related to the liquid structure. It is well-known that the spatial and temporal changes of the liquid structure (structural relaxations) are strongly temperature dependent. The time scales for structural relaxation change from about

$100s$ near T_g to $10^{-12} - 10^{-14}$s in the equilibrium liquid[13–15,50]. Since the typical scattering time for electrons is in the nano- to femto-seconds range, the liquid structure appears as static to the electrons in most of the supercooled states. It is, therefore, reasonable to assume that the resistivity/conductivity changes in this temperature range are mostly due to electron-phonon scattering. Although liquids cannot sustain long wavelength phonons, short wavelength (high frequency) phonons are excited in short-lived solid-like regions, as suggested by Frenkel[51], and has been observed in inelastic scattering experiments[52]. With increasing temperature, the length- and time-scales of the dynamically evolving solid-like regions (atomic clusters) in a liquid decrease[13–15,44,50]. Above some temperature, the mean electron scattering time and the structural relaxation time may become comparable. The effectiveness of electron-phonon scattering will also depend on the relative time scales of the phonon frequencies and the electron scattering times. Therefore, above some characteristic temperature, the scattering of electrons by structural disorder and phonon scattering will become ineffective, resulting in a saturation of the electrical resistivity/conductivity. It is reasonable that this temperature appears to be T_A, since above this temperature the lifetime of a local cluster is too short to communicate this information to neighboring atoms and the phonons become effectively localized[12]. Since the dynamical crossover is observed in all liquids[12,19,53], except for the very strong ones, resistivity saturation may be a universal property of liquids. That the saturation coincides with T_A, is perhaps the most direct evidence that the structure of the liquid at the atomic level strongly couples to the dynamics at a longer, hydrodynamic, level[50].

Using the nearly free electron theory, it is possible estimate the electron mean free path in the liquids. Assuming effective valences (2.43 for $Cu_{50}Zr_{50}$ and 2.77 for $Zr_{64}Ni_{36}$, see section 3.5), Fermi wave vectors ($k_f = 1.40\ \text{Å}^{-1}$ and $1.52\ \text{Å}^{-1}$ for $Cu_{50}Zr_{50}$ and $Zr_{64}Ni_{36}$, respectively, see section 3.5), and molar volumes ($10.99x10^{-6}\ m^3$ and $11.54x10^{-6}\ m^3$ for $Cu_{50}Zr_{50}$ and $Zr_{64}Ni_{36}$, respectively, see fig. 3.3), these are 3.04 Å for $Cu_{50}Zr_{50}$ and 3.14 Å for $Zr_{64}Ni_{36}$. They are close to the positions of the first maximum in the experimentally determined pair correlation functions (2.81 Å for $Cu_{50}Zr_{50}$ and 3.12 Å for $Zr_{64}Ni_{36}$)[54], which supports the idea that the mean-free-path is close to the interatomic spacing in the liquids.

3.5 Extended Faber-Ziman Theory

The Ziman theory of liquid metals[37–39] was initially formulated for simple s-band materials (Na, K, Rb, etc.) in terms of the x-ray scattering factor, $S(q)$, and a pseudopotential. Later it was extended to transition metal[40] and alloy[41] liquids replacing the pseudopotential by a single-site scattering matrix, $t(q)$, as:

$$\rho = \frac{3\pi m_e^2 \Omega_o}{4e^2 Z \hbar^3 k_F^6} \int_0^{2k_F} dq\, q^3\, S(q) |t(q)|^2 \,, \tag{3.3}$$

where Ω_o, Z, k_f are the molar volume, effective valence, and Fermi wave vector, respectively. The other parameters are the electron charge, e, mass, m, and Planck's constant, $\hbar$. For binary alloys the transition matrix and structure factor terms are replaced by

$$\begin{gathered} \langle T_{alloy} \rangle^2 = c_1 |t_1|^2 \big(1 - c_1 + c_1 s_{11}(q)\big) + \\ c_2 |t_2|^2 \big(1 - c_2 + c_2 s_{22}(q)\big) + c_1 c_2 (t_1^* t_2 + t_1 t_2^*)(s_{12}(q) - 1) \,, \end{gathered} \tag{3.4}$$

where $s_{ij}(q)$ are the partial structure factors, c_1 and c_2 are the chemical concentrations, and t_1 and t_2 are the transition matrices of each component in the alloy. The expression for resistivity is then,

$$\rho = \frac{3\pi m_e^2 \Omega_o}{4e^2 Z \hbar^3 k_F^6} \int_0^{2k_F} dq\, q^3\, \langle T_{alloy} \rangle^2 . \tag{3.5}$$

For the alloy liquids, the partial structure factors were generated from molecular dynamics simulations, shown in fig. 3.6. Phase shifts were determined using the method described by Baria and Jani[55], using the static dielectric function and Taylor's exchange and correlation effects[56]. The Fermi wave vector and the effective valence are not known at the present time for the alloys; to match the experimental data approximate values were used ($k_f = 1.40$ Å^{-1} and $Z = 2.43$ for $Cu_{50}Zr_{50}$ and $k_f = 1.52$ Å^{-1} and $Z = 2.77$ for $Zr_{64}Ni_{36}$). The effective valence required to match the magnitude of the experimental data is clearly too high. It is well-known that within the framework of this theory the electrical resistivity is extremely sensitive to the choice of k_f. Figure 3.7 shows the estimated electrical resistivity for both $Cu_{50}Zr_{50}$ and $Zr_{64}Ni_{36}$. Although the magnitudes change dramatically for a small change in k_f, the temperature dependence remains negative in both cases and is consistent with our experimental results. However, it cannot explain the saturation of resistivity near or slightly above T_A as emphasized above.

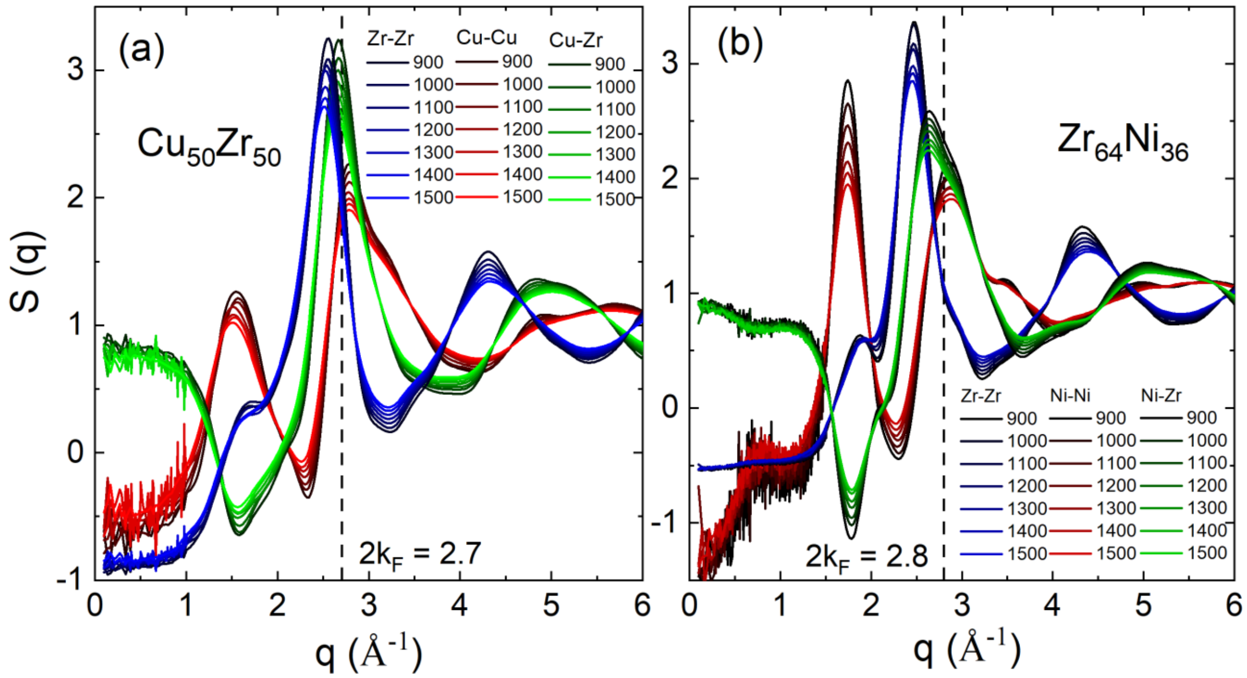

Figure 3.6 – The partial structure factors for various temperatures (in Kelvin) for (a) $Cu_{50}Zr_{50}$ and (b) $Zr_{64}Ni_{36}$ determined by molecular dynamics simulations of 50,000 atoms with a 0.005 picosecond timestep relaxed for 1,000,000 steps at each temperature.

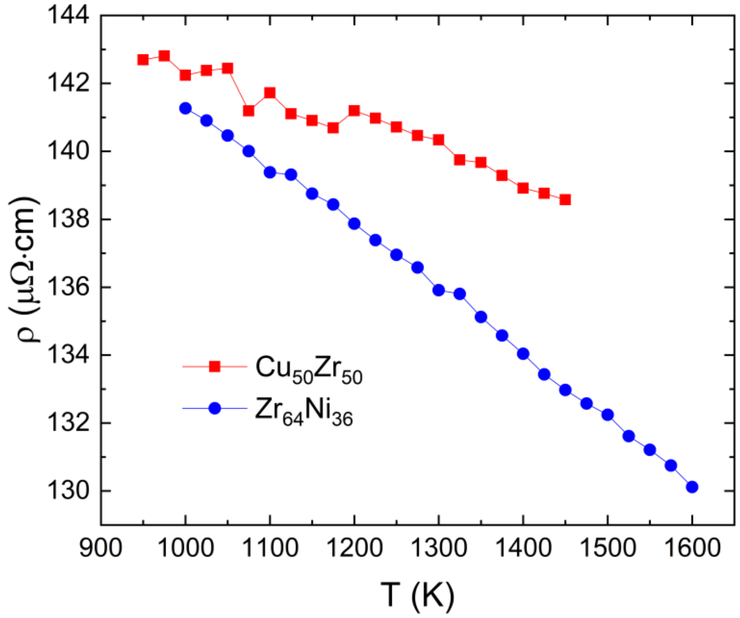

Figure 3.7 – The electrical resistivity as a function of temperature calculated from the extended Faber-Ziman theory using approximations for the Fermi wave vector and effective valency.

3.6 Conclusions

The electrical resistivity of binary liquid alloys is measured using the electromagnetic levitator on the International Space Station. The sample is an additional impedance in the circuit of the EML. Measuring the properties of the circuit gives this impedance, which is a function of the electrical resistivity. The temperature dependence of the electrical resistivity saturates at temperatures higher than the onset of cooperative rearrangement temperature, T_A, where the liquid shear viscosity goes from Arrhenius at high temperatures to super Arrhenius at temperatures below T_A. The saturation likely occurs because of phonon localization where at temperature above T_A, atoms can no longer communicate structural information beyond their nearest neighbors. The electrical resistivity is sensitive to the local structure of the liquid because the scattering length of electrons is of the order of atomic spacing. This work demonstrates that electrical transport, in-lieu of dynamical properties, can be used as a powerful tool to determine T_A and the local order in liquids. Finally, it should be emphasized that such contamination-free precision measurements were only possible by a unique combination of the containerless processing technique, a novel measurement technique, and the microgravity environment of the International Space Station.

3.7 Acknowledgements

This work was partially supported by NASA under Grants NNX10AU19G and NNX16AB52G as well as the German Aerospace Center (DLR), Space Administration under contract no. 50WM1541. The authors acknowledge the access to the ISS/EML, which is a joint undertaking of the European Space Agency (ESA) and the DLR Space Administration. The reported work was conducted in the framework of the ESA research projects: Electrical Resistivity (AO-2000-038), MULTIPHAS (AO-2004-114) and QUASI (AO-2009-0959). The experiments were operated from the "Microgravity User Support Center" (MUSC) at the Deutsches Zentrum für Luft- und Raumfahrt (DLR) in Cologne, Germany. The authors express their gratitude to the members of the MUSC for their cooperation and assistance throughout the inception, planning, and execution of the experiments in the ISS/EML facility onboard the International Space Station. Any opinions, findings, and conclusions or recommendations expressed in this material are those of the author(s) and do not necessarily reflect the views of NASA.

3.8 References

1. Van Hoesen, D. C. *et al.* Resistivity Saturation in Metallic Liquids Above a Dynamical Crossover Temperature Observed in Measurements Aboard the International Space Station. *Phys. Rev. Lett.* **123**, 226601 (2019).

2. Ioffe, A. F. & Regel, A. R. Non-crystalline, amorphous and liquid electronic semiconductors. *Prog. Semicond.* **4**, 237–291 (1960).

3. Mott, N. F. *Metal-Insulator Transitions*. (Taylor & Francis, 1974).

4. Howson, M. A. & Gallagher, B. L. The Electron Transport Properties of Metallic Glasses. *Phys. Lett.* **170**, 265–324 (1988).

5. Fisk, Z. & Webb, G. W. Saturation of the High-Temperature Normal-State Electrical Resistivity of Superconductors. *Phys. Rev. Lett.* **36**, 1084–1086 (1976).

6. Sunandana, C. S. On the electrical resistivity of chevrel phases. *J. Phys. C Solid State Phys.* **12**, L165–L168 (1979).

7. de Visser, A., Franse, J. J. M. & Menovsky, A. Resistivity of single-crystalline UPt3 and its pressure dependence; Interpretation by a spin-fluctuation model. *J. Magn. Magn. Mater.* **43**, 43–47 (1984).

8. Gunnarsson, O., Calandra, M. & Han, J. E. Colloquium: Saturation of electrical resistivity. *Rev. Mod. Phys.* **75**, 1085–1099 (2003).

9. Cooper, R. A. *et al.* Anomalous criticality in the electrical resistivity of La 2-xSrxCuO4. *Science (80-.).* **323**, 603–607 (2009).

10. Sachdev, S. *Quantum Phase Transitions*. (Cambridge University Press, 1999).

11. Hartnoll, S. A. Theory of universal incoherent metallic transport. *Nat. Phys.* **11**, 54–61 (2015).

12. Jaiswal, A., Egami, T., Kelton, K. F., Schweizer, K. S. & Zhang, Y. Correlation between fragility and the Arrhenius crossover phenomenon in metallic, molecular, and network liquids. *Phys. Rev. Lett.* **117**, (2016).

13. Fan, Y., Iwashita, T. & Egami, T. Crossover from Localized to Cascade Relaxations in Metallic Glasses. *Phys. Rev. Lett.* **115**, 1–5 (2015).

14. Iwashita, T., Nicholson, D. M. & Egami, T. Elementary excitations and crossover phenomenon in liquids. *Phys. Rev. Lett.* **110**, 1–5 (2013).

15. Soklaski, R., Nussinov, Z., Markow, Z., Kelton, K. F. & Yang, L. Connectivity of icosahedral network and a dramatically growing static length scale in Cu-Zr binary metallic glasses. *Phys. Rev. B - Condens. Matter Mater. Phys.* **87**, 1–8 (2013).

16. Hu, Y. C., Li, F. X., Li, M. Z., Bai, H. Y. & Wang, W. H. Structural signatures evidenced in dynamic crossover phenomena in metallic glass-forming liquids. *J. Appl. Phys.* **119**, (2016).

17. Blodgett, M. E., Egami, T., Nussinov, Z. & Kelton, K. F. Proposal for universality in the viscosity of metallic liquids. *Sci. Rep.* **5**, 1–8 (2015).

18. Schmidtke, B., Petzold, N., Kahlau, R. & Rössler, E. A. Reorientational dynamics in molecular liquids as revealed by dynamic light scattering: From boiling point to glass transition temperature. *J. Chem. Phys.* **139**, (2013).

19. Mallamace, F. *et al.* Transport properties of glass-forming liquids suggest that dynamic crossover temperature is as important as the glass transition temperature. *Proc. Natl. Acad. Sci.* **107**, 22457–22462 (2010).

20. Garrahan, J. P. & Chandler, D. Coarse-grained microscopic model of glass formers. *Proc. Natl. Acad. Sci.* **100**, 9710–9714 (2003).

21. Sastry, S., Debenedetti, P. G. & Stillinger, F. H. Signatures of distinct dynamical regimes in the energy landscape of a glass-forming liquid. *Nature* **393**, 554–557 (1998).

22. Dai, R., Ashcraft, R. & Kelton, K. F. A possible structural signature of the onset of cooperativity in metallic liquids. *J. Chem. Phys.* **148**, 204502 (2018).

23. Gangopadhyay, A. K. & Kelton, K. F. A re-evaluation of thermal expansion measurements of metallic liquids and glasses from x-ray scattering experiments. *J. Chem. Phys.* **148**, 204509 (2018).

24. Shacklette, L. W. & Williams, W. S. Influence of Order-Disorder Transformations on the Electrical Resistivity of Vanadium Carbide. *Phys. Rev. B* **7**, 5041–5053 (1973).

25. Mauro, N. A. & Kelton, K. F. A highly modular beamline electrostatic levitation facility, optimized for in situ high-energy x-ray scattering studies of equilibrium and supercooled liquids. *Rev. Sci. Instrum.* **82**, (2011).

26. Rhim, W. K., Ohsaka, K., Paradis, P. F. & Erik Spjut, R. Noncontact technique for measuring surface tension and viscosity of molten materials using high temperature electrostatic levitation. *Rev. Sci. Instrum.* **70**, 2796–2801 (1999).

27. Mohr, M. *et al.* Surface Tension and Viscosity of Cu50Zr50 Measured by the Oscillating

Drop Technique on Board the International Space Station. *Microgravity Sci. Technol.* (2019).

28. Heintzmann, P., Yang, F., Schneider, S., Lohöfer, G. & Meyer, A. Viscosity measurements of metallic melts using the oscillating drop technique. *Appl. Phys. Lett.* **108**, (2016).

29. Lohöfer, G. High-resolution inductive measurement of electrical resistivity and density of electromagnetically levitated liquid metal droplets. *Rev. Sci. Instrum.* **89**, 4709 (2018).

30. Wunderlich, R. K., Fecht, H.-J. & Willnecker, R. Power modulation technique for noncontact high-temperature calorimetry. *Appl. Phys. Lett.* **62**, 3111–3113 (1993).

31. Lohöfer, G. Magnetization and impedance of an inductively coupled metal sphere. *Int. J. Eng. Sci.* **32**, 107–117 (1994).

32. Rhim, W. K. *et al.* An electrostatic levitator for high-temperature containerless materials processing in 1-g. *Rev. Sci. Instrum.* **64**, 2961–2970 (1993).

33. Bradshaw, R. C., Schmidt, D. P., Rogers, J. R., Kelton, K. F. & Hyers, R. W. Machine vision for high-precision volume measurement applied to levitated containerless material processing. *Rev. Sci. Instrum.* **76**, 1–8 (2005).

34. Mooij, J. H. Electrical Conduction in Concentrated Disordered Transition Metal Alloys. *Phys. Status Solidi A* **17**, 521–530 (1973).

35. Tsuei, C. C. Nonuniversality of the Mooij correlation-the temperature coefficient of electrical resistivity of disordered metals. *Phys. Rev. Lett.* **57**, 1943–1946 (1986).

36. Lee, P. A. & Ramakrishnan, T. V. Disordered electronic systems. *Rev. Mod. Phys.* **57**, 287–337 (1985).

37. Ziman, J. M. A theory of the electrical properties of liquid metals. I: The monovalent metals. *Philos. Mag.* **6**, 1013–1034 (1961).

38. Faber, T. E. & Ziman, J. M. A theory of the electrical properties of liquid metals III. the resistivity of binary alloys. *Philos. Mag.* **11**, 153–173 (1965).

39. Faber, T. E. *Introduction to the Theory of Liquid Metals*. (Cambridge University Press, 1972).

40. Evans, R., Greenwood, D. A. & Lloyd, P. Calculations of the transport properties of liquid transition metals. *Phys. Lett.* **35**, 57–58 (1971).

41. Dreirach, O., Evans, R., Guntherodt, H. J. & Kunzi, H. U. A simple muffin tin model for the electrical resistivity of liquid noble and transition metals and their alloys. *J. Phys. F Met. Phys.* **2**, 709–725 (1972).

42. Esposito, E., Ehrenreich, H. & Gelatt, C. D. Electrical transport in transition-metal liquids and metallic glasses. *Phys. Rev. B* **18**, 3913–3920 (1978).

43. Gangopadhyay, A. K. *et al.* Thermal expansion measurements by x-ray scattering and breakdown of Ehrenfest's relation in alloy liquids. *Appl. Phys. Lett.* **104**, 1–5 (2014).

44. Gangopadhyay, A. K. *et al.* Correlation of the fragility of metallic liquids with the high temperature structure, volume, and cohesive energy. *J. Chem. Phys.* **146**, (2017).

45. Mott, N. F. The electrical resistivity of liquid transition metals. *Philos. Mag.* **26**, 1249–1261 (1972).

46. Imry, Y. Possible Role of Incipient Anderson Localization in the Resistivities of Highly Disordered Metals. *Phys. Rev. Lett.* **44**, 469–471 (1980).

47. Howson, M. A. Incipient localisation and electron-electron correlation effects in metallic glass alloys. *J. Phys. F Met. Phys.* **14**, L25–L31 (1984).

48. Howson, M. A. & Greig, D. Localisation and interaction effects in the temperature and magnetic field dependence of the resistivity of metallic glasses. *J. Phys. F Met. Phys.* **16**, 989–1004 (1986).

49. Anderson, P. W. Absence of diffusion in certain random lattices. *Phys. Rev.* **109**, 1492–1505 (1958).

50. Ashcraft, R. *et al.* Experimental measurements of the temperature-dependent Van Hove function in a Zr80Pt20 liquid. *arXiv:1810.02351v2* (2018).

51. Frenkel, J. *Kinetic Theory of Liquids*. (Oxford University Press, 1947).

52. Burkel, E. Reports on Progress in Physics Related content. *Rep. Prog. Phys.* **63**, 171–232 (2000).

53. Gangopadhyay, A. K. & Kelton, K. F. Recent progress in understanding high temperature dynamical properties and fragility in metallic liquids, and their connection with atomic structure. *J. Mater. Res.* **32**, 2638–2657 (2017).

54. Gangopadhyay, A. K. *et al.* Anomalous thermal contraction of the first coordination shell in metallic alloy liquids. *J. Chem. Phys.* **140**, (2014).

55. Baria, J. K. & Jani, A. R. Comprehensive study of lattice mechanical properties of some FCC transition metals. *Phys. B* **328**, 317–335 (2003).

56. Taylor, R. A simple, useful analytical form of the static electron gas dielectric function. *J. Phys. F Met. Phys.* **8**, 1699–1702 (1978).

Chapter 4: Specific Heat Measurements of Metallic Alloys

4.1 Introduction

The specific heat is an important fundamental material property. Of interest to our studies of crystal nucleation and growth on the International Space Station, the specific heat plays a central role in determining the driving free energy. The specific heat is determined by the number of degrees of freedom in the material, which are related to the structure. As stated in chapter 3, the search continues for determining the relationship between liquid structure and dynamics. The onset of cooperativity in the liquid, T_A, is the temperature at which a locally preferred structural organization begins to become prominent in the liquid. T_A is also the temperature at which the viscosity goes from a high temperature Arrhenius behavior to a low temperature super-Arrhenius behavior, linking structure and dynamics. A signature of T_A in the specific heat would be further evidence of this connection. For temperatures above T_A the Maxwell relaxation time (the viscosity over the infinite frequency shear modulus) is equal to the local cluster time (the time to change the local coordination number by one). Below T_A, the Maxwell relaxation time becomes much larger than the local cluster time and the viscosity becomes super-Arrhenius. One direct connection between the structure and dynamics of liquids was discussed in chapter 3 from the electrical resistivity measurements.

Measuring the specific heat of near room temperature solids is straightforward and can be done using conventional differential scanning calorimetry (DSC) techniques. However, complications arise for high temperature solids and liquids. In particular, the specific heat of supercooled liquid alloys is very difficult to measure. At high temperatures, metals often react with containers influencing the measurement of the heat released. Additionally, in the supercooled liquid container walls provide heterogeneous nucleation sites that lower the energy required for nucleation, prohibiting access to the deeply supercooled liquid. As such, specific heat measurements in the supercooled liquid must be performed in a containerless environment. To do this metallic liquid droplets are levitated in either an electromagnetic levitator (EML) or in an electrostatic levitator (ESL). Details of four different specific heat measurement techniques are described in this chapter. Each measurement requires solving a power balance equation.

4.2 Differential Scanning Calorimetry

In DSC, the objective is to measure the power required to keep a sample and a reference material at the same temperature during some time-temperature profile, typically with a constant heating rate[1]. It is possible to see why measuring the power output of the sample with time and temperature gives the specific heat from thermodynamic arguments. The enthalpy is defined as

$$H = U + pV, \tag{4.1}$$

where $U = TS - PV + \mu N$ is the internal energy and pV is the pressure multiplied by the volume. The differential internal energy is given by

$$dU = TdS - pdV + \mu dN, \tag{4.2}$$

where T is the temperature, S is the entropy, μ is the chemical potential or the driving free energy per atom or monomer, and N is the number of atoms or monomers. The other components of the differential internal energy are equal to zero from the Gibbs-Duhem relation. The differential of the enthalpy at constant pressure is then

$$dH = dU + pdV = TdS + \mu dN. \tag{4.3}$$

In specific heat measurements, the operations are number conserving so that $dH = TdS = dQ$, where dQ is the heat exchange. Measuring the heat flow in DSC simultaneously measures the enthalpy change. The isobaric (constant pressure) specific heat is given by $c_p = dH/dT$. The power balance equation in the DSC is then

$$heat\ flow = c_p \frac{dT}{dt} = \frac{dH}{dt} = \frac{dQ}{dt} = P, \tag{4.4}$$

where P is the measured power. However, the DSC measures the power difference between the reference pan and the sample pan instead of the sample power. Setting up a power balance equation for both the sample and reference and accounting for the mass of the sample and reference gives two similar equations

$$c_p^{S,R} \frac{dT}{dt} = \frac{P^{S,R}}{m^{S,R}}, \tag{4.5}$$

where c_p is now the specific heat per mass, the superscript, S, refers to the sample and the superscript, R, refers to the reference. The reference is a sample of known specific heat. The calorimeter measures the difference in the power $\Delta P = P^S - P^R$ under the conditions that the heating rate, dT/dt, is the same for the sample and reference. Solving the two power balance equations gives

$$m^S c_p^S = \frac{\Delta P}{\beta} + m^R c_p^R, \tag{4.6}$$

where β is the heating rate. In DSC, the power associated with the sample and the reference pan accounts for the sample and the sample holder. As such, an empty DSC scan must be subtracted from the sample scan to calculate the correct specific heat. For illustration, the specific heat of a

$Zr_{64}Ni_{36}$ glass and crystal sample measured with a PerkinElmer DSC 8500 is shown as a function of temperature in fig. 4.1. The large decrease in the specific heat is due to crystallization and does not reflect the actual glass c_p.

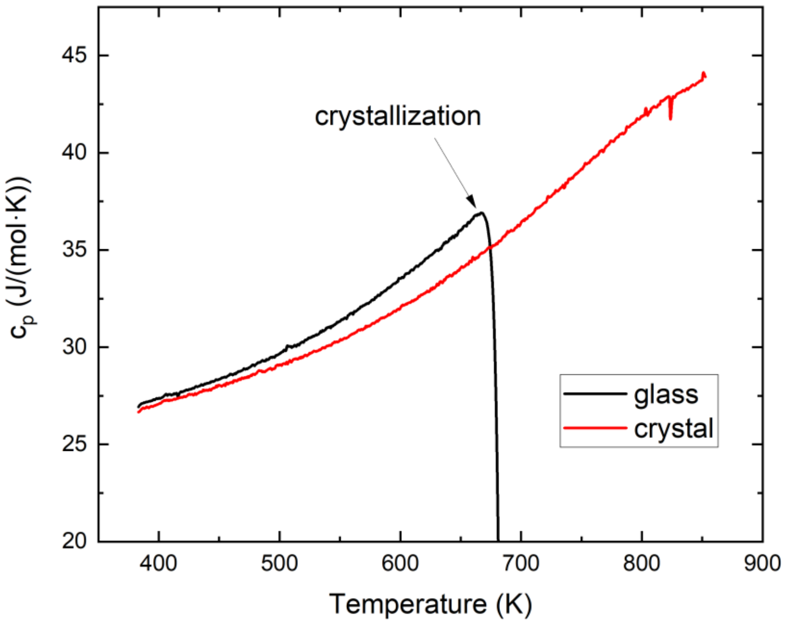

Figure 4.1 – The specific heat of a $Zr_{64}Ni_{36}$ glass and crystal measured using differential scanning calorimetry. The glass specific heat drops drastically as the sample crystallizes, releasing its heat of fusion. These measurements were performed by Anup Gangopadhyay.

4.3 Modulation Calorimetry using the EML on the ISS

An overview of the EML apparatus and experimental technique for modulation calorimetry is discussed in chapter 2. Additional detail is provided here for the application and theory. An explanation of the reservations held about the results from the EML aboard the International Space Station (ISS) is also given.

AC Modulation calorimetry was first developed and used by Corbino[2] in 1910. It was then developed as a technique for measuring specific heat in electromagnetic levitation facilities by Fecht and Johnson[3] and later refined by Wunderlich[4–10]. The goal of modulation calorimetry is to solve the coupled power balance equations of a levitated liquid in an EML. Assuming that the levitated sample is in a vacuum so that there is no gas conduction, the power balance equations of the directly and indirectly heated regions are given by

$$g_H c_p \frac{dT_H(t)}{dt} = P(t) - kc[T_H(t) - T_S(t)] - s_H \sigma \epsilon A T_H^4(t) \tag{4.7}$$

$$(1 - g_H) c_p \frac{dT_S(t)}{dt} = kc[T_H(t) - T_S(t)] - (1 - s_H) \sigma \epsilon A T_S^4(t), \tag{4.8}$$

where subscript H represents quantities in the region of the sample directly heated by the EML heating coils through induction, subscript S represents quantities in the region of the sample that are heated through conduction, g is the volume fraction, s is the surface area fraction, and kc is the conductive heat transfer coefficient. The equator of the sample is directly heated by the EML, but the temperature of the sample is measured at the pole in the EML aboard the space station, so $T_S(t)$ is the desired quantity to determine. Setting the time derivatives in eq. 4.7 and eq. 4.8 to zero gives the steady state temperatures for each region, T_0, which are equal after a transient time. During the applied power modulation, the temperature is given by $T_{H,S}(t) = T_0 + \Delta T_{H,S}(t)$. Because the experiment is designed so that the temperature oscillation amplitude is small, the radiative T^4 term can be linearized, $T_{H,S}^4(t) \approx T_0^4 + 4T_{H,S}^3(t)\Delta T_{H,S}(t)$. The rate of change of the temperature is equal to the rate of change of the difference in temperature due to the modulations and is now given by

$$\Delta\dot{T}_H(t) = \left(\frac{1}{g_h c_p}\right) P(t) - kch[\Delta T_H(t) - \Delta T_S(t)] - krh\, \Delta T_H(t) \tag{4.9}$$

$$\Delta\dot{T}_S(t) = kcs[\Delta T_H(t) - \Delta T_S(t)] - krs\, \Delta T_S(t), \tag{4.10}$$

where $kch = kc/g_H c_p$, $kcs = kc/(1-g_H)c_p$, $krh = s_H k_r / g_H c_p$, and $krs = (1-s_H)k_r/(1-g_H)c_p$. The coupled equations are solved using matrix manipulation to find the eigenvalues that diagonalize the equation $\Delta\dot{\hat{T}} = M\Delta\hat{T} + \hat{P}$ where the "hat" symbol represents a matrix. The components of the matrix are given by

$$\Delta\hat{T} = \begin{pmatrix} \Delta T_H(t) \\ \Delta T_S(t) \end{pmatrix}, \tag{4.11}$$

$$M = \begin{pmatrix} -kch - krh & kch \\ kcs & -kcs - krs \end{pmatrix}, \tag{4.12}$$

$$P = \frac{1}{g_H}\begin{pmatrix} \mathrm{P(t)} \\ 0 \end{pmatrix}. \tag{4.13}$$

The eigenvectors of matrix M are λ_1 and λ_2 and the goal is to find the matrix S such that $S^{-1}MS$ is diagonal. Applying S^{-1} on the left-hand side of the matrix equation gives

$$\Delta\dot{\tilde{T}} = S^{-1}\,\Delta\dot{\hat{T}} = S^{-1}M\hat{T} + S^{-1}\hat{P} \tag{4.14}$$

and letting $\hat{T} = S\begin{pmatrix} T_1(t) \\ T_2(t) \end{pmatrix}$ gives the equation

$$\frac{\mathrm{d}}{\mathrm{dt}}\begin{pmatrix} T_1(t) \\ T_2(t) \end{pmatrix} = S^{-1}MS\begin{pmatrix} T_1(t) \\ T_2(t) \end{pmatrix} + \begin{pmatrix} \widetilde{P_1}(t) \\ \widetilde{P_2}(t) \end{pmatrix} = \begin{pmatrix} \lambda_1 & 0 \\ 0 & \lambda_2 \end{pmatrix}\begin{pmatrix} T_1(t) \\ T_2(t) \end{pmatrix} + \begin{pmatrix} \widetilde{P_1}(t) \\ \widetilde{P_2}(t) \end{pmatrix}. \tag{4.15}$$

Equation 4.15 has a known solution,

$$\begin{pmatrix} T_1(t) \\ T_2(t) \end{pmatrix} = \begin{pmatrix} \exp\,(\lambda_1 t)\displaystyle\int_0^t \exp(-\lambda_1 t')\ \widetilde{P_1}(t')\,dt' \\ \exp\,(\lambda_2 t)\displaystyle\int_0^t \exp(-\lambda_2 t')\ \widetilde{P_2}(t')\,dt' \end{pmatrix}. \tag{4.16}$$

Applying the matrix S to the power and temperature gives back the temperature matrix,

$$\Delta\hat{T} = \frac{kcs}{(\lambda_1 - \lambda_2) g_H c_p} S \begin{pmatrix} \exp(\lambda_1 t) \int_0^t \exp(-\lambda_1 t')\, P(t')\, dt' \\ \exp(\lambda_2 t) \int_0^t \exp(-\lambda_2 t')\, P(t')\, dt' \end{pmatrix}, \tag{4.17}$$

where the input power $P(t)$ is selected so that the integral is solvable. The diagonalizing matrix is given by

$$S = \begin{pmatrix} \frac{(\lambda_1 + kcs + krs)}{kcs} & \frac{(\lambda_2 + kcs + krs)}{kcs} \\ 1 & 1 \end{pmatrix}. \tag{4.18}$$

Applying the power modulation method where $P(t) = P_0 + G_{htr} I_\omega^2 \sin(\omega t)$ gives the temperature response as a transient term and a stationary modulation term. For the conductively heated pole, where the pyrometer measures the sample temperature, the transient term decays. The stationary term given from the conductively heated pole is

$$\Delta T_S = \frac{G_{htr} I_\omega^2}{c_p \omega} f(\omega, \lambda_1, \lambda_2), \tag{4.19}$$

where ω is the frequency of the current through the heating coils and $f(\omega, \lambda_1, \lambda_2)$ is a correction term that accounts for the actual temperature measured at the pole. The Biot number, Bi, gives the ratio of radiative heat loss to the internal heat transfer, $Bi = kr/kc$. In the adiabatic region, the region where the Biot number is small ($Bi \ll 0.01$), the correction term is close to one. In the low frequency limit (small ω), the correction term is given by

$$f(\omega, \lambda_1, \lambda_2) = \left[1 + \frac{\lambda_1^2}{\omega^2}\right]^{-\frac{1}{2}}, \tag{4.20}$$

otherwise, the correction term is given by

$$f(\omega, \lambda_1, \lambda_2) = \left[1 + \frac{\lambda_1^2}{\omega^2} + \frac{\omega^2}{\lambda_2^2}\right]^{-\frac{1}{2}}. \tag{4.21}$$

Even when the Biot number is nonnegligible, the difference in the amplitude of the temperature response measured at the pole and the actual temperature response near the equator varies very little. For $Bi = 0.03$, Wunderlich found that the difference in the amplitude of the temperature response between the two regions was only 2%, implying that the correction function is a small number[10]. λ_1 is related to the external heat transport time constant by $\lambda_1 \approx -kr/c_p = -1/\tau_1$ and $\lambda_2 \approx -1/\tau_2$, where τ_2 is the internal time constant associated with heat transport from the directly heated equatorial region to the polar conductively heat region. In the adiabatic regime, $\tau_2 \approx 1/(\omega^2\tau_1)$. Finally, the coupling coefficient between the EML heater coils and the sample, G_{htr}, must be determined. It was derived for the power absorption of a sphere in a magnetic field by Fromm and Jehn[11] and is given as

$$G_{htr} = \frac{3\pi}{4}\, R(T)\, \rho(T)\, F(R/\delta)\, L_H, \tag{4.22}$$

where R is the radius of the sample, ρ is the electrical resistivity of the sample, L_H is a geometric constant that is specific to the EML/sample configuration, and $F(R/\delta)$ gives the scale for inductive coupling to the sample as a function of the sample radius and the skin depth, δ. The scale for the inductive coupling was derived by Fromm and Jehn[11] and is given by

$$F(x) = \frac{x[\sinh(2x) + \sin(2x)] - \cosh(2x) + \cos(2x)}{\cosh(2x) - \cos(2x)}. \tag{4.23}$$

In the initial experiments the coupling coefficient could not be determined because the electrical resistivity was not known. For those experiments the coupling coefficient was assumed to be a constant, determined by taking modulation calorimetry measurements in the low temperature crystalline phase, where it is possible to measure the specific heat using ground-based DSC. The heater coupling coefficient was the fitting parameter used to match the specific heat from modulation calorimetry to the specific heat from DSC. However, power modulations in the crystalline phase often have significant scatter making it difficult to determine the modulation amplitude of the temperature. Specific heat measurements using this technique show erroneous temperature dependencies and are incorrect.

By measuring the electrical resistivity using the EML on the ISS, the coupling coefficient can be determined exactly. The geometric constant, L_H, is determined from the geometry of the coils in the EML and is given by

$$L_H = \left[\sum_n \frac{b_n^2}{[b_n^2 + (z - z_n)^2]^{\frac{3}{2}}}\right]^2 , \tag{4.24}$$

where the sum is over each current carrying coil, n, in the EML, b_n is the radius of copper coil n, and $z - z_n$ is the vertical distance the coil is from the center of the sample floating in the coils. There are six coils in the EML on the space station with loop radii of 10.5, 14.5, 18.5, 10.5, 14.5, and 18.5 mm with $z - z_n$ offsets of 5.5, 5.5, 5.5, -5.5, -5.5, and -5.5 mm respectively. This gives $L_H = 115842\, m^{-2}$. Figure 4.2 shows the specific heat determined from modulation calorimetry for several batch 1 and batch 2 NASA ISS samples, measured in a vacuum. There are very few data points below the melting temperatures because of poor supercooling. Additionally, the data are either scattered or have an incorrect temperature dependence.

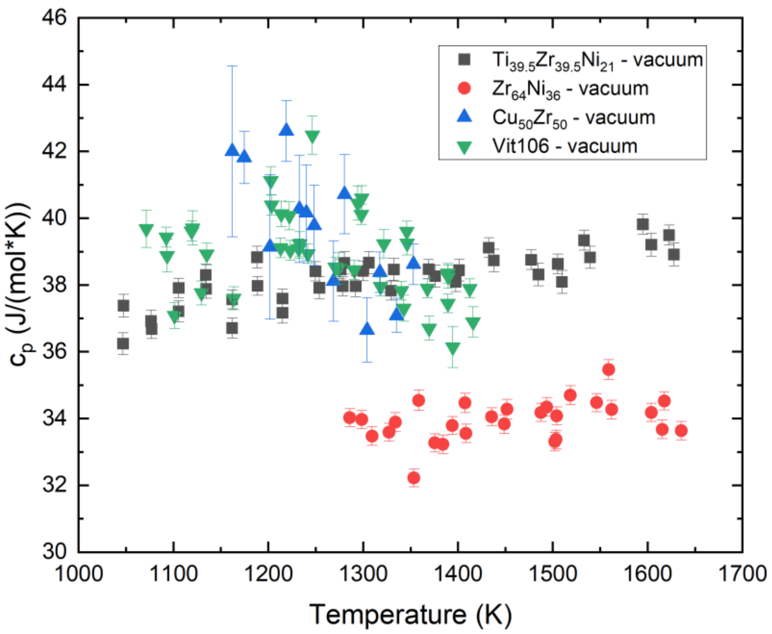

Figure 4.2 – Measurements of specific heat as a function of temperature for NASA samples aboard the International Space Station. Measurements were made with the modulation calorimetry technique using the EML. This data has not been corrected for any change in the radius due to a squeezing effect from the heater voltage.

It may be necessary to account for a change in the sample radius as a function of the heater current due to the sample being squeezed by the imposed field. The first order correction would be to take the contracted x-direction radius instead of the sample radius determined from a perfect sphere. A better correction would be to use spherical harmonics in place of the radially symmetric integral used by Smyth[12] and Fromm and Jehn[11] to derive the power absorbed by the ellipsoidal sample. For $Ti_{39.5}Zr_{39.5}Ni_{21}$, the first order approximation does not account for the positive temperature dependence even though the ratio of the y-radius over the x-radius is approximately 1.2 and changes with the heater voltage. Additionally, for many samples there is a discrepancy between the specific heat measured in vacuum and the specific heat measured in an inert gas atmosphere. The specific heat values from measurements performed in vacuum are lower than from measurements made in a gas atmosphere. Personal correspondence with Markus Mohr and Rainer Wunderlich at Ulm University suggests that these issues can be overcome. The heater current likely contracts the sample when in vacuum differently than when the sample is in an inert gas atmosphere because the heater magnetic field must be stronger to keep the sample at a given temperature when gas conduction is appreciable.

4.4 Specific Heat from the External Time Constant

The external heat time constant, τ_1, is associated with sample cooling. In an electromagnetic or electrostatic levitator, the sample cools by radiation or gas conduction only. For a small change in the power provided to a sample (by a laser in ESL or by induction in EML), the temperature change can be approximated with an exponential function. The power balance equation is given by

$$c_p \frac{dT}{dt} = P_0 - A\epsilon\sigma(T^4 - T_{env}^4) - h(T - T_{env}), \tag{4.25}$$

where P_0 is the power provided to the sample by an external source (i.e. laser or induction), A is the sample surface area, ϵ is the emissivity of the sample, σ is the Stefan-Boltzmann constant, T_{env} is the temperature of the surrounding environment, and h is the heat transfer coefficient from the sample to the gas. The second term on the right-hand side is the radiative heat loss and the third term is the loss of heat by conduction through the gas environment. If the sample is processed in a vacuum, then the third term is zero. For small temperature changes, the power balance equation can be linearized without introducing a significant amount of error. The Taylor expansion of a function $f(T)$ around T_0 is

$$f(T) = f(T_0) + \frac{df}{dT}|_{T_0}(T - T_0) + \frac{d^2 f}{dT^2}|_{T_0}(T - T_0)^2 + \ldots \tag{4.26}$$

Taking the first two terms on the right-hand side of eq. 4.26 gives the linearization of $f(T)$. In the steady state, when the temperature is constant at T_0, $dT/dt = 0$ and the power supplied to the sample is equal to the power removed from the sample by radiation and convection,

$$P_0 = A\epsilon\sigma(T_0^4 - T_{env}^4) + h(T_0 - T_{env}). \tag{4.27}$$

Assuming that the specific heat, emissivity, surface area, and heat transfer coefficient of the sample are temperature independent over small temperature changes, the first term in the linearization of eq. 4.25 with $f(T) = dT/dt$ is

$$c_p f(T_0) = P_0 - A\epsilon\sigma(T_0^4 - T_{env}^4) - h(T_0 - T_{env}) = 0. \tag{4.28}$$

The linearized power balance is then

$$c_p \frac{dT}{dt} = \frac{d}{dT}\left(P_0 - A\epsilon\sigma(T^4 - T_{env}^4) - h(T - T_{env})\right)|_{T_0}(T - T_0). \tag{4.29}$$

Simplifying eq. 4.29 and separating the variables in time and temperature gives

$$\frac{dT}{T - T_0} = \frac{1}{c_p}(-4A\epsilon\sigma T_0^3 - h)\,dt. \tag{4.30}$$

This has the exponential solution

$$\Delta T = B \exp\left(-\frac{t}{\tau_1}\right), \tag{4.31}$$

where ΔT is the small change in temperature due to a small change in power, B is a prefactor integration constant, and τ_1 is the external heat transfer coefficient given as

$$\tau_1 = \frac{c_p}{4A\epsilon\sigma T_0^3 + h}. \tag{4.32}$$

Because this derivation assumes a conductive gas, the τ_1 from eq. 4.32 will be referred to as τ_1^{gas} and τ_1^{vac} will refer to the same equation, but with $h = 0$. The inverse of τ_1^{gas} is

$$\frac{1}{\tau_1^{gas}} = \frac{4A\epsilon\sigma T_0^3}{c_p} + \frac{h}{c_p}. \tag{4.33}$$

Here, the first term on the right-hand side is equal to $1/\tau_1^{vac}$. Measuring the external time constant in vacuum and in an inert gas atmosphere gives the specific heat

$$c_p = \frac{h}{\left(\frac{1}{\tau_1^{gas}} - \frac{1}{\tau_1^{vac}}\right)}. \tag{4.34}$$

The external heat time constant in vacuum and in gas can be measured in either an EML or an ESL. The heat transfer rate is unknown, but the temperature dependence should follow that of the thermal conductivity of the gas at the sample/gas interface. Figure 4.3 is a time-temperature curve of a $Zr_{80}Pt_{20}$ sample for τ_1^{vac} measurements made in the Washington University BESL. Each small change in temperature is fit to an exponential giving τ_1^{vac} as a function of temperature. As shown by the dotted black line, τ_1^{vac} is measured in both the equilibrium liquid and the supercooled liquid until the recalescence event. It is clear from fig. 4.3 that the time constant is larger for lower temperatures, which is due to the lower radiative power. The time constant measured in a gas atmosphere is less temperature dependent because conduction is the dominant power term and it is less temperature dependent than the radiative power. Figure 4.4 shows τ_1^{vac} as a function of temperature for the batch 1, batch 2, and batch 3 NASA ISS samples measured in the BESL. The τ_1^{vac} data are nearly equivalent across each composition, suggesting that $c_p/(A\epsilon)$ does not change significantly with composition. Figure 4.4 combines data from samples of different mass, whereas, in fig. 4.5 the compositions and masses are separated. Within the scatter of the data in fig. 4.5, the mass change has no effect on τ_1.

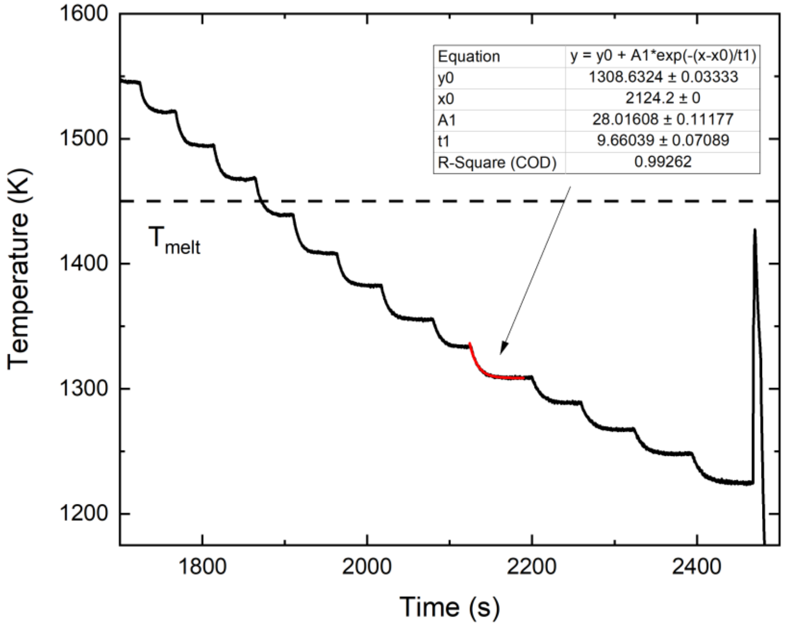

Figure 4.3 – Measurements of τ_1^{vac} as a function of temperature in the BESL for a $Zr_{80}Pt_{20}$ sample. Each small change in temperature is fit to an exponential to give the time constant. Recalescence occurs around 2475 seconds and is seen as the sharp rise in temperature.

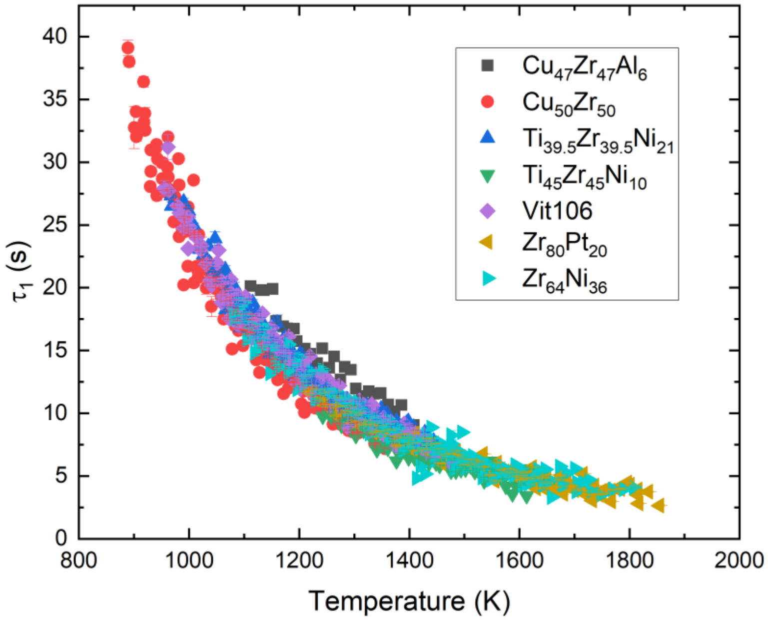

Figure 4.4 – τ_1^{vac} as a function of temperature measured in the BESL for NASA ISS batch 1, 2, and 3 samples. Samples with different mass, but the same composition have been combined in this figure.

The external temperature time constant is also measured in a spherical solid pure zirconium sample (see fig. 4.5). The specific heat of zirconium in the α and β phases is known, so the τ_1 – method of measuring specific heat can be tested using the τ_1^{vac} and τ_1^{gas} of pure zirconium. Zirconium can also be used to gauge the effect of the heat transfer coefficient as a function of temperature by matching the literature values for the specific heat and the τ_1 – method measured specific heat.

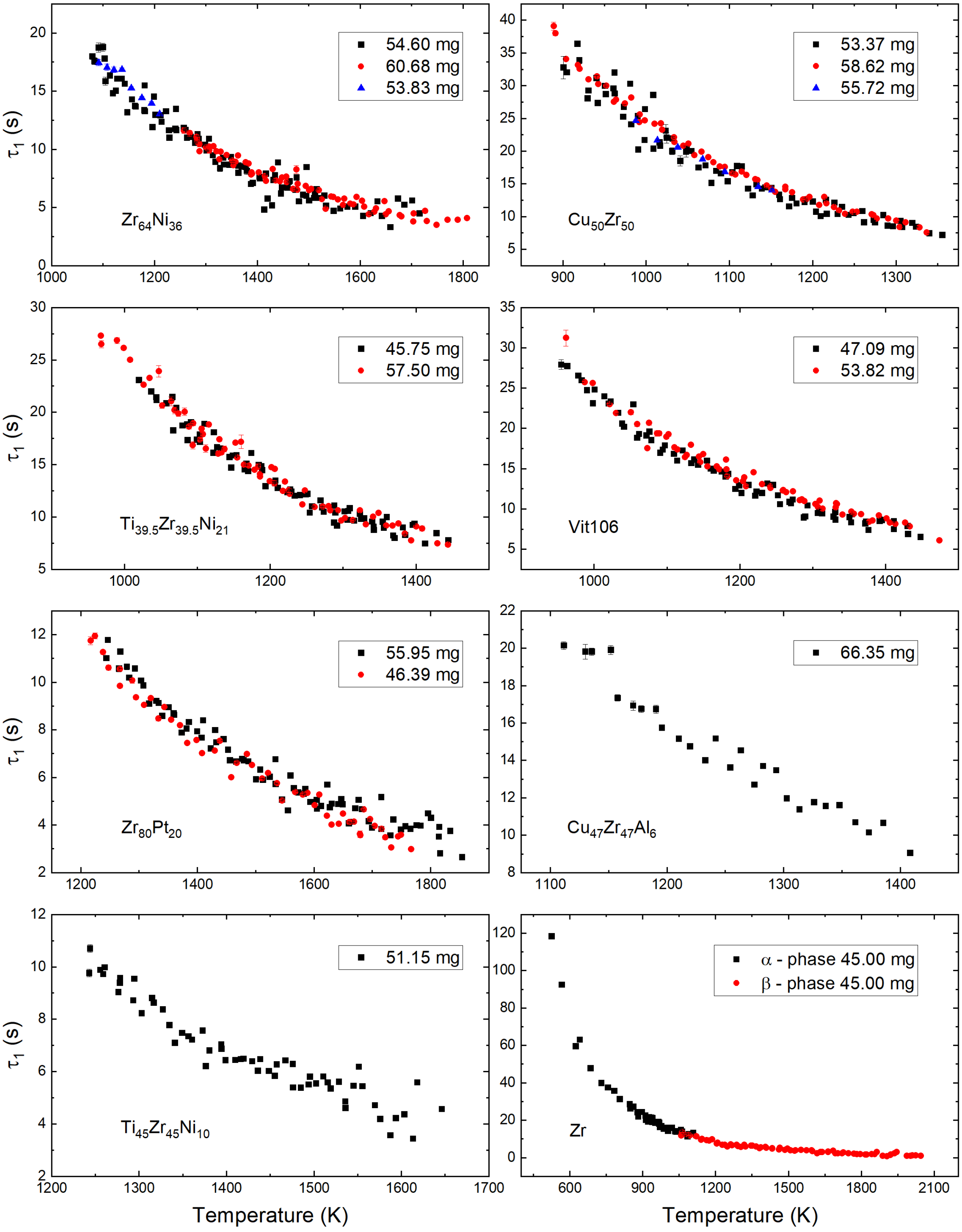

Figure 4.5 – τ_1^{vac} as a function of temperature measured in the BESL for NASA ISS batch 1, 2, and 3 samples. Data are separated by mass and composition.

In ESL, there are a few sticking points associated with the τ_1 – method. To begin with, as previously stated, the heat transfer coefficient may be difficult to extract. In addition to this, it is difficult to use a gas atmosphere in most electrostatic levitators due to the dielectric breakdown of the gas caused by the potential difference between the top and bottom electrodes. The voltage required for dielectric breakdown is the same order of magnitude as the voltage required to levitate samples. It is a function of the gas pressure and the separation distance of the electrodes. Measuring samples in ESL in an inert gas atmosphere may be possible if the chamber is pressurized because the breakdown voltage drastically increases above atmospheric pressure. However, metallic liquids are highly reactive and may form surface oxide contamination due to the gas atmosphere.

Even with the ground-based ESL concerns, it still may be possible to measure τ_1 in vacuum and in an inert gas using the EML on the space station. At the time of writing this dissertation, however, no τ_1 specific measurements have been made using the ISS EML. With that said, many free-cooling cycles have been performed for the batch 1 and batch 2 samples. Even though the derivation above is for step changes in the power resulting in exponential changes in the temperature, the same external time constant is found if the power balance equation is linearized using a free-cool, during which small time intervals are taken. In this case, the $f(T_0)$ term in eq. 4.28 is nonzero, but the solution to the separable differential equation still gives an exponential function with the time constant given in eq. 4.32. In these free-cool measurements of τ_1, the time-temperature curve is separated into many small time intervals over which an exponential function is fit, as shown in fig. 4.6. A much larger temperature region is required for a good fit to the time-temperature data when the free-cool is used instead of a step-cool, leading to additional error.

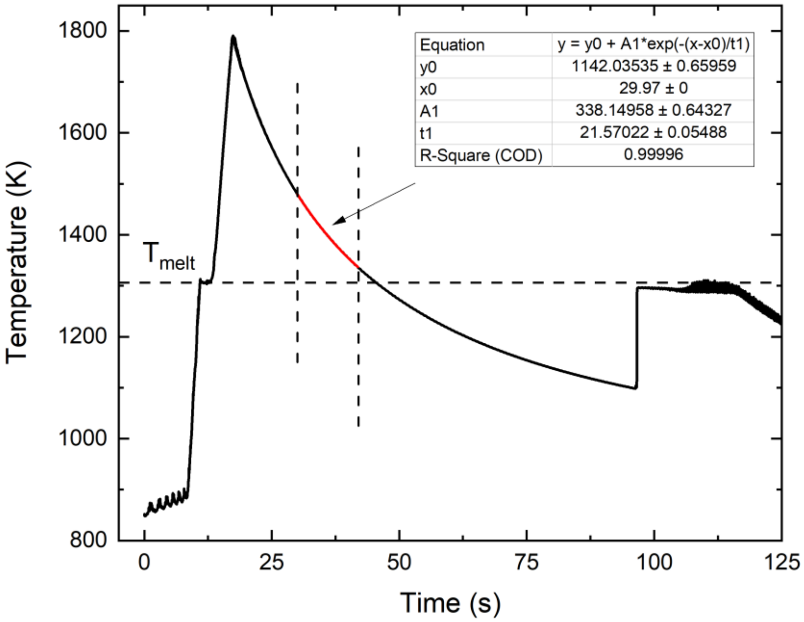

Figure 4.6 – Determining τ_1 from a free cooling cycle of a $Zr_{64}Ni_{36}$ sample in the EML on the ISS in an argon atmosphere by dividing the time into small increments and fitting an exponential in the region.

Figure 4.7 shows τ_1 as a function of temperature measured using the free-cool method described above for batch 1 and batch 2 samples in vacuum, helium, and argon. The helium and argon atmospheres are at a pressure of approximately 350 mbar. Samples cool faster in helium than in argon because the thermal conductivity of helium is an order of magnitude larger than the thermal conductivity of argon. As such, the external time constant for helium is lower than argon. There are no argon or helium data for the $Cu_{50}Zr_{50}$ sample.

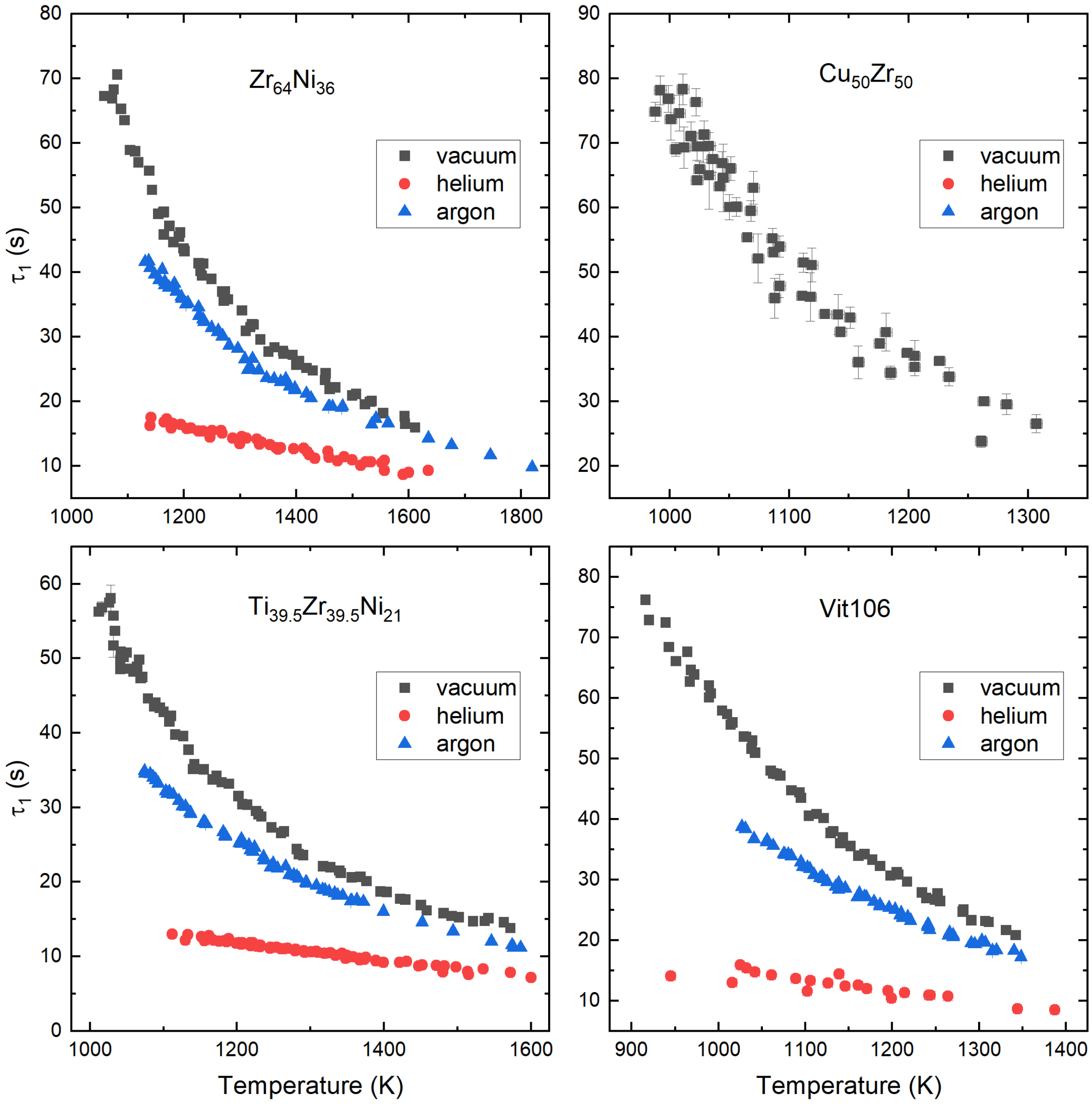

Figure 4.7 – τ_1 as a function of temperature for the batch 1 and batch 2 ISS EML samples in vacuum, helium, and argon atmospheres measured using the free-cool method. There are no argon or helium data for the $Cu_{50}Zr_{50}$ sample.

An assumption made using the τ_1 – method is that the change in temperature, $T - T_0$, is small, so that terms beyond the linear term in the Taylor approximation are small. Simplifying the power balance equation to

$$f(T) = T^4 + P_0, \tag{4.35}$$

where P_0 is the required power to keep the sample at temperature, T_0, and writing out the first four terms of the Taylor expansion gives

$$f(T) = 0 + \frac{d}{dT}(T^4)|_{T_0}(T - T_0) + \frac{d^2}{dT^2}(T^4)|_{T_0}(T - T_0)^2 + \frac{d^3}{dT^3}(T^4)|_{T_0}(T - T_0)^3 + .. \quad (4.36)$$

Reducing eq. 4.36 gives the full Taylor expansion in terms of the temperature,

$$f(T) = 4T_0^3(T - T_0) + 12T_0^2(T - T_0)^2 + 24T_0(T - T_0)^3 + 24(T - T_0)^4. \quad (4.37)$$

Table 4.1 shows the magnitude of each term, giving the error associated with making the linearization assumption for varying values of T_0 and $\Delta T = T - T_0$ normalized by the first nonzero term (the linearization term). Normalizing by the first term removes the need to account for the constants in the power balance equation. Higher temperatures and fitting to smaller changes in temperatures give smaller errors when determining τ_1.

Table 4.1 – The magnitude of each term giving the error associated with making the linearization approximation when solving for the external heat transport time constant, τ_1. Several values of T_0 and $\Delta T = T - T_0$ are given to show the range of possibilities. The magnitudes are normalized by the first nonzero term.

T_0	ΔT	$4T_0^3\Delta T$	$12T_0^2\Delta T^2$	$24T_0\Delta T^3$	$24\Delta T^4$
500	10	1.0	0.06	0.0024	4.8E-5
1000	10	1.0	0.03	0.0006	6E-6
1500	10	1.0	0.02	0.00027	1.8E-6
500	20	1.0	0.12	0.0096	0.00038
1000	20	1.0	0.06	0.0024	4.8E-5
1500	20	1.0	0.04	0.0011	1.4E-5
500	30	1.0	0.18	0.022	0.0013
1000	30	1.0	0.09	0.0054	0.00016
1500	30	1.0	0.06	0.0024	4.8E-5

In vacuum, c_p/ϵ is given by eq. 4.32 with $h = 0$. The specific heat over the emissivity can also be measured in free-cool experiments and is given by the power balance equation

$$c_p \frac{dT}{dt} = -A\sigma\epsilon(T^4 - T_{env}^4), \tag{4.38}$$

where dT/dt is the cooling rate as a function of temperature during the free cool. The derivative dT/dt is determined by dividing the free cool into small time increments (3-8 data points) and taking the slope of a line fit to each increment. Without a significant amount of smoothing, experimental measures of c_p/ϵ have a significant amount of scatter. This suggests that the temperature dependence of the specific heat largely depends on the temperature dependence of the emissivity and is highly sensitive to the scatter in the experimentally measured τ_1 or dT/dt.

4.5 Emissivity Measurements in ESL

The heat of fusion power balance method was developed by Dr. Anup Gangopadhyay to measure the total hemispherical emissivity as a function of temperature using an electrostatic levitator[13]. Here the method is explained in detail and applied to the NASA ISS batch 1, batch 2, and batch 3 samples.

Even though the current provided to the laser on heating a sample in ESL is known, the exact power absorbed by the sample is unknown due to reflections from the sample surface. For this reason, the emissivity cannot be extracted from a balance of the laser power and the radiative power. The power balance giving the emissivity as a function of the laser power, P_{laser}, during an isothermal hold is

$$c_p \frac{dT}{dt} = 0 = P_{laser} - A\sigma\epsilon(T^4 - T_{env}^4). \tag{4.39}$$

Differential scanning calorimetry or differential thermal analysis (DTA) can be used to measure the heat of fusion, ΔH_f, of many metallic alloys. Using the heat of fusion and a power balance equation during sample melting provides a method to determine the laser power absorbed by the sample. Assuming that the absorbed laser power does not change as a function of the sample temperature, the laser power in eq. 4.39 can be replaced by the radiate power at the melting temperature plus the power absorbed by the laser during the melting process,

$$P_{laser} = A_l \sigma \epsilon_l (T_l^4 - T_{env}^4) + \frac{\Delta H_f}{\Delta t_{melt}} = A_F \sigma \epsilon_F (T_F^4 - T_{env}^4), \tag{4.40}$$

where the subscript F represents the value at the final sample temperature after melting. The subscript l represents the value at the liquidus temperature, and Δt_{melt} is the time required to melt the sample. Figure 4.8 shows a cycle in which the melting time is measured at a constant laser power and the final sample temperature is determined in a $Zr_{64}Ni_{36}$ sample. After the sample melts, the laser is not changed until the final temperature is determined.

The melting plateau method can only be used for temperatures above the liquidus temperature, otherwise, there is no melt plateau to calibrate the laser power. Extrapolating the laser power as a function of temperature below the liquidus temperature may not be accurate. The emissivity at the liquidus temperature, ϵ_l, is not known but can be estimated by setting the emissivity in the longest melting time plateau cycle (i.e. the cycle with the final temperature closest to the melting plateau) equal to the final temperature emissivity. Once ϵ_l is determined, the emissivity at the final temperature, ϵ_F, is given by solving eq. 4.40,

$$\epsilon_F = \frac{\left(A_l \sigma \epsilon_l (T_l^4 - T_{env}^4) + \frac{\Delta H_f}{\Delta t_{melt}} \right)}{A_F \sigma (T_F^4 - T_{env}^4)}. \tag{4.41}$$

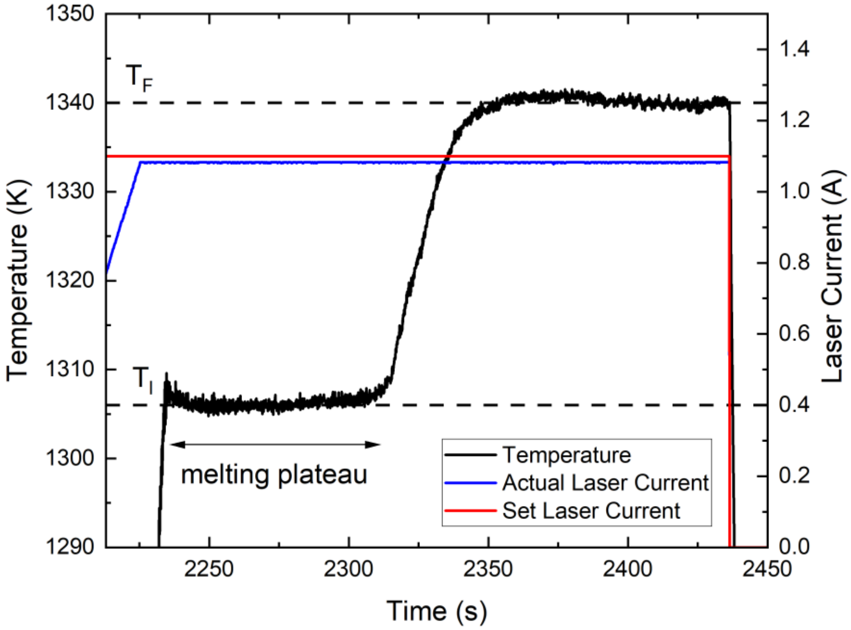

Figure 4.8 – An example time-temperature cycle of a heat of fusion power balance measurement with a $Zr_{64}Ni_{36}$ sample where the melt plateau time is determined. The user set laser current and the actual laser current are also shown. The response time of the laser is not instantaneous, so the set and actual laser currents are different at the beginning of the experiment.

Figure 4.9a shows the laser power of a $Zr_{64}Ni_{36}$ sample determined by the melting plateau method and an attempt to extrapolate the laser power to temperatures below the liquidus temperature using an exponential of the logarithm of the power. The emissivity and subsequent specific heat are extremely sensitive to the fit function used for extrapolating to low temperatures. Figure 4.9b shows the melting plateau time as a function of temperature. The melting time goes to infinity as the sample temperature approaches the melting temperature. Table 4.2 gives the liquidus temperature, heat of fusion measured by DTA, and the heat of fusion using Richard's Rule[14] for the NASA ISS batch 1, 2, and 3 samples.

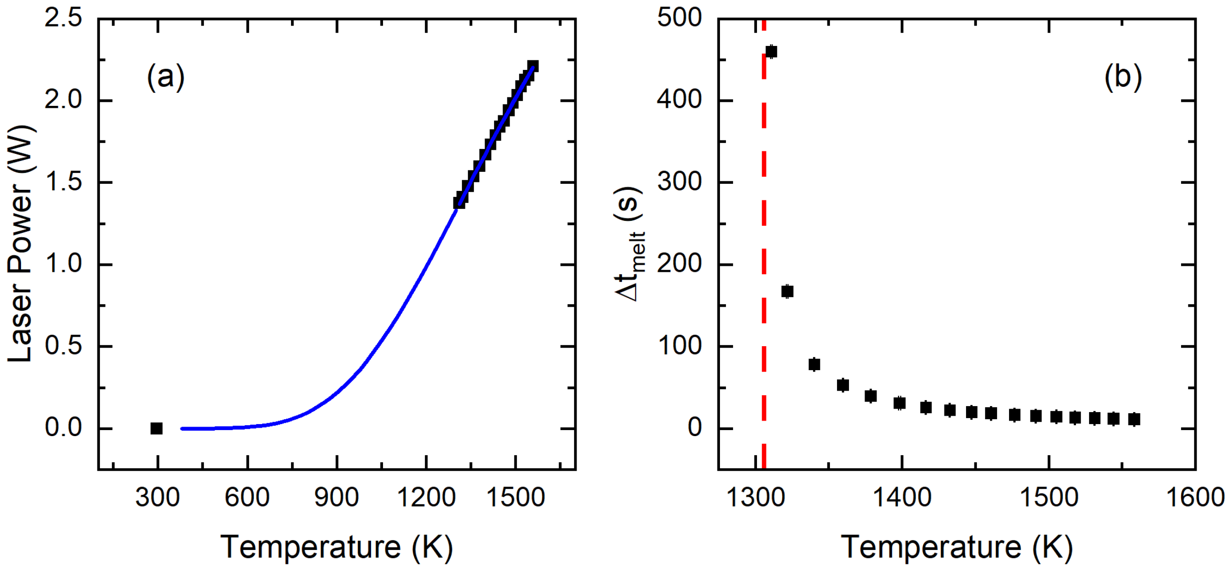

Figure 4.9 – The laser power (a) and melting time (b) determined for a 53.83mg $Zr_{64}Ni_{36}$ sample measured in the BESL. The laser power is extrapolated to temperatures below the melting temperature using an exponential of the logarithm of the power. The vertical red dashed line in the melting time is the liquidus temperature at which the melting time goes to infinity.

Table 4.2 – The liquidus temperature and the heat of fusion for the NASA ISS batch 1, 2, and 3 samples. Richard's Rule is used when the DTA measured value heat of fusion is not known.

sample	T_l (K)	ΔH_f DTA (kJ/mol)	ΔH_f error (kJ/mol)	Richard's Rule (kJ/mol)
Vit106	1115	10.2	-	9.7
$Zr_{64}Ni_{36}$	1306	14.4	0.4	11.36
$Cu_{50}Zr_{50}$	1208	-	-	10.51
$Ti_{39.5}Zr_{39.5}Ni_{21}$	1093	10.6	0.3	9.51
$Zr_{80}Pt_{20}$	1450	-	-	12.62
$Cu_{47}Zr_{47}Al_6$	1172	10.9	0.2	10.20
$Ti_{45}Zr_{45}Ni_{10}$	1543	-	-	13.42

Figure 4.10 shows the emissivity as a function of temperature above the liquidus temperature for each sample. $Ti_{45}Zr_{45}Ni_{10}$ is not shown because the solidus liquidus gap is large and the melt plateau time is difficult to determine. The $Cu_{50}Zr_{50}$ ΔH_f (9.219 kJ/mol) used in fig. 4.10a is from the literature[15], not from DTA measurements. Once the emissivity is known, the

specific heat can be determined using eq. 4.32 with $h = 0$, using the measured τ_1 data. Figure 4.11 shows the specific heat as a function of temperature above the liquidus temperature for each sample.

With the exception of Vit106, the specific heat increases with decreasing temperature in the liquid above the melting temperature. It is unclear why the Vit106 sample shows a decrease specific heat with decreasing temperature. The specific heat data measured using the melting plateau laser calibration method are of the correct order. However, the heat of fusion must be known accurately for the specific heat to be known accurately. The error in the measurements is dominated by the error in the heat of fusion.

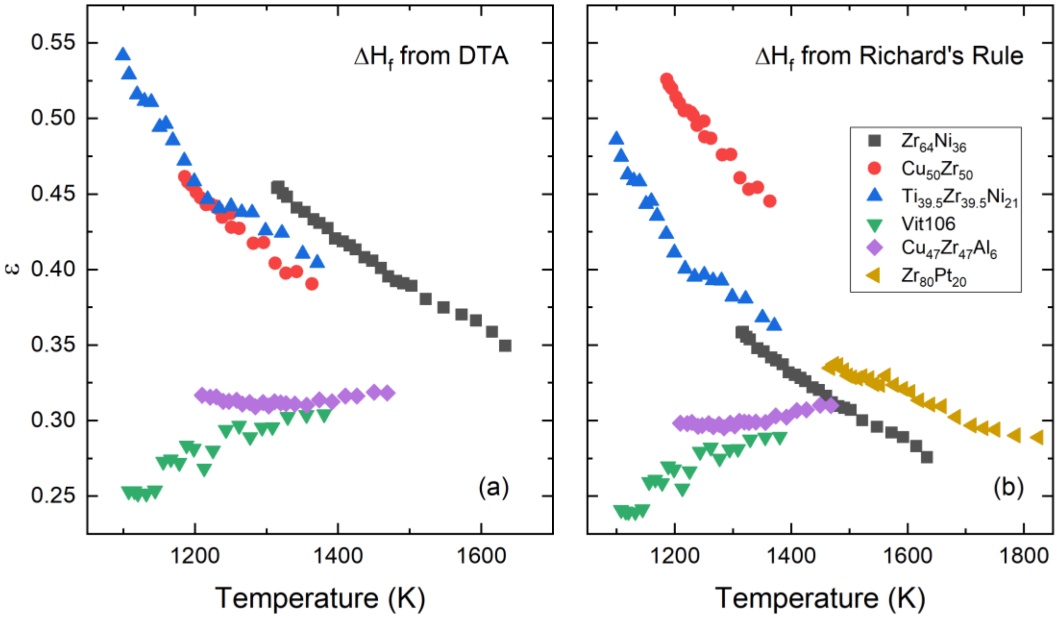

Figure 4.10 – The emissivity as a function of temperature measured in the BESL using the melt plateau and the heat of fusion from (a) DTA measurements or literature values (for Cu$_{50}$Zr$_{50}$) and (b) Richard's rule as the calibration for the laser power. Data shown here are above the liquidus temperature so that no laser power extrapolation is necessary. Richard's rule is likely an overestimate for the Cu$_{50}$Zr$_{50}$ alloy.

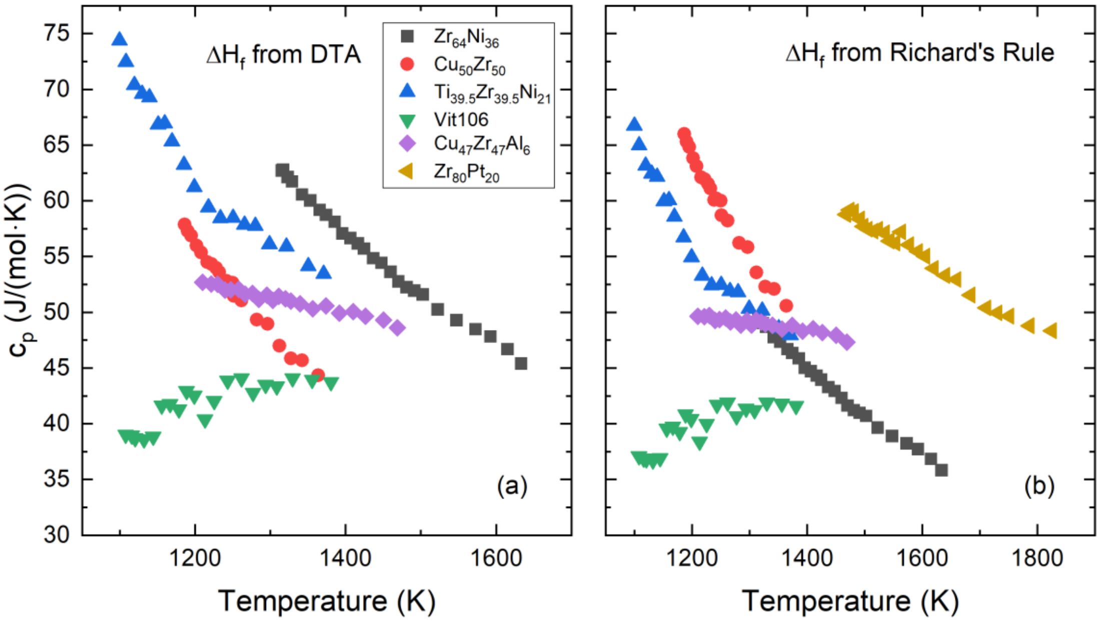

Figure 4.11– The specific heat as a function of temperature measured in the BESL using the melt plateau and the heat of fusion from (a) DTA measurements or literature values (for $Cu_{50}Zr_{50}$) and (b) Richard's rule as the calibration for the laser power and the experimentally determined τ_1. Data shown here are above the liquidus temperature.

It should be noted that the absorbed laser power may be a function of temperature because the sample reflectivity may change with temperature. As such, it may be a poor assumption that the absorbed laser power calculated at the melting plateau is approximately equal to the absorbed laser power at elevated temperatures. In addition, the BESL laser requires a small time (~1s) to reach the steady-state power. The power at the beginning of the melt plateau may be lower than the value at the end of the plateau. This disproportionately effects measurements when the laser power is high and the melting time is low. This effect is shown in fig. 4.8, where the set laser current deviates from the actual laser current at the beginning of the measurement cycle. In fig. 4.8, the actual laser current reaches the steady-state value before the melting plateau begins. This will not always be the case. The error can be avoided by cooling the sample to near room temperature before setting the laser current to the desired value. The emissivity ESL method may also be inaccurate with samples that have a large gap between the solidus and liquidus temperatures. When this is the case, the melting plateau time is difficult to obtain. To avoid this difficulty, calculating the melting time explicitly is avoided, and instead, an integration over the melt region is performed so that the total power, which is a function of the sample temperature at each time during the melt, is accurately calculated.

4.6 Conclusions

Four methods of measuring the specific heat have been discussed. The differential scanning calorimetry method is used to measure the specific heat of glasses or crystalline material from room temperature to near 1000K. In the modulation calorimetry specific heat method, data from DSC is necessary for calibration. However, the DSC method cannot measure the specific heat of many alloys at high temperature or in the liquid phase because they are reactive. The specific heat of most supercooled liquids cannot be measured either due to the sample container causing heterogeneous nucleation. Modulation calorimetry is used aboard the International Space Station to measure the specific heat of levitated samples in both the equilibrium and supercooled liquid. However, some reservations remain about the accuracy of the data measured on the space station. From radiative cooling measurements, where the power provided to a levitating sample in either EML or ESL is decreased by a small amount, the external heat transport time constant can be determined in both vacuum and in a gas environment. If the heat transport coefficient from the sample to the gas is known, then the specific heat can be determined by taking the difference between the time constants in vacuum and in gas. Otherwise, the emissivity is required to determine the specific heat from measurements of the time constant. An ESL technique using the melting plateau time to calibrate the laser power provided to a levitated sample is used to determine the sample emissivity above the liquidus temperature. The specific heat is determined from a combination of the τ_1 – method and the heat of fusion melting plateau method. The specific heat is found to have a negative temperature coefficient in the equilibrium liquid for most compositions.

4.7 References

1. Brown, M. E. *Introduction to Thermal Analysis: Techniques and Applications*. (Kluwer Academic, 2004).

2. Corbino, O. M. Oscillazioni termiche delle lampade a filamento sottile percorse da correnti alternate, e conseguente effetto raddrizzatore per la presenza di armonichi pari. *Nuovo Cim.* **19**, 75–84 (1910).

3. Fecht, H. J. & Johnson, W. L. A conceptual approach for noncontact calorimetry in space. *Rev. Sci. Instrum.* **62**, 1299–1303 (1991).

4. Wunderlich, R. K., Fecht, H.-J. & Willnecker, R. Power modulation technique for noncontact high-temperature calorimetry. *Appl. Phys. Lett.* **62**, 3111–3113 (1993).

5. Wunderlich, R. K. & Fecht, H. J. Specific heat measurements by non-contact calorimetry. *J. Non. Cryst. Solids* **156–158**, 421–424 (1993).

6. Wunderlich, R. K. & Fecht, H. J. Measurements of thermophysical properties by contactless modulation calorimetry. *Int. J. Thermophys.* **17**, 1203–1216 (1996).

7. Wunderlich, R. K., Ettl, C. & Fecht, H. J. Specific Heat and Thermal Transport Measurements of Reactive Metallic Alloys by Noncontact Calorimetry in Reduced Gravity 1. *Int. J. Thermophys.* **22**, 579–591 (2001).

8. Wunderlich, R. K. Non-contact thermophysical property measurement of liquid Zr-alloys - An investigation under microgravity conditions. *Adv. Eng. Mater.* **3**, 924–932 (2001).

9. Wunderlich, R. K. & Fecht, H.-J. Thermophysical Property Measurements by Electromagnetic Levitation Methods under Reduced Gravity Conditions. *J. Jpn. Soc. Microgravity Appl.* **20**, 192–205 (2003).

10. Wunderlich, R. K. & Fecht, H. J. Modulated electromagnetic induction calorimetry of reactive metallic liquids. *Meas. Sci. Technol.* **16**, 402–416 (2005).

11. Fromm, E. & Jehn, H. Electromagnetic forces and power absorption in levitation melting. *Br. J. Appl. Phys.* **16**, 653–663 (1965).

12. Smythe, W. R. Eddy Currents. in *Static and Dynamic Electricity* 368–414 (McGraw-Hill, 1968).

13. Gangopadhyay, A. K. & Kelton, K. F. Measurements of the Temperature-Dependent Total Hemispherical Emissivity Using an Electrostatic Levitation Facility. *Int. J. Thermophys.* **38**, 1–8 (2017).

14. Kubaschewski, O. & Alcock, C. B. *Metallurgical Thermochemistry*. (Pergamon Press, 1979).

15. Wang, Q. *et al.* Diffusion-controlled crystal growth in deeply undercooled melt on approaching the glass transition. *Phys. Rev. B - Condens. Matter Mater. Phys.* **83**, 1–5 (2011).

Chapter 5: Modeling Non-Isothermal Crystallization in $BaO{\cdot}2SiO_2$ and $5BaO{\cdot}8SiO_2$ glasses

Much of the work in this chapter is published in Van Hoesen, D. C. *et al.*, "*Modeling nonisothermal crystallization in a $BaO{\cdot}2SiO_2$ glass*," *JACS.* (2020)[1]. Figures and text are reproduced with permission from the American Ceramic Society. A manuscript discussing studies of the $5BaO{\cdot}8SiO_2$ glass is under preparation at the time of this dissertation.

The accuracy of a differential thermal analysis (DTA) technique for predicting the temperature range of significant nucleation is examined in $BaO{\cdot}2SiO_2$ and $5BaO{\cdot}8SiO_2$ glasses by iterative numerical calculations. The numerical model takes account of time-dependent nucleation, finite particle size, size-dependent crystal growth rates, and surface crystallization. The calculations were made using the classical and, for the first time, the diffuse interface theories of nucleation. The results of the calculations are in agreement with experimental measurements, demonstrating the validity of the DTA technique. They show that this is independent of the DTA scan rate used and that surface crystallization has a negligible effect for the glass particle sizes studied. A breakdown of the Stokes-Einstein relation between viscosity and the diffusion coefficient is demonstrated for low temperatures, near the maximum nucleation rate. However, it is shown that accurate values for the diffusion coefficient can be obtained from the induction time for nucleation and the growth velocity in this temperature range.

5.1 Introduction

A quantitative knowledge of the time dependent nucleation rate as a function of temperature, $I(t,T)$, is critically important for developing new glasses and for preparing glass ceramics with a desired microstructure. If the temperature ranges for nucleation and growth are sufficiently separated, $I(t,T)$ can be accurately measured using a two-step heat treatment method. Nuclei are first developed by heating for different amounts of time in a temperature range where the nucleation rate is significant (nucleation treatment). These nuclei are subsequently grown to observable crystals with a heat treatment at a higher temperature, where the growth rate is significant (growth treatment). The steady-state nucleation rate and the transient time for nucleation can be determined from the number of crystals produced as a function of the isothermal heating time at the nucleation temperature[2].

Nucleation measurements made using this two-step method are very time consuming, requiring many weeks or even months to obtain a complete set of data. Further, for such measurements to even be feasible a prior knowledge of the temperature range where significant nucleation occurs is required. As suggested previously from studies of crystallization in lithium disilicate glasses[3–5], thermal analysis methods such as differential thermal analysis (DTA) and differential scanning calorimetry (DSC) can be used to determine this. This was also recently experimentally confirmed in two barium-silicate glasses[6]. Ray et al.[7] and Ranasinghe et al.[8] argued that the DTA/DSC method can be used to quantitatively measure the nucleation rate. However, this technique was critically reviewed and refined by Fokin et al.[9] who found that it could only give accurate quantitative nucleation rate data if a significant amount of preliminary data were known. The DTA/DSC method has been examined numerically for the lithium silicate glasses assuming the classical theory of nucleation (CNT) and demonstrated to be valid[10,11]. However, no numerical investigation has been made for other silicate glasses. Here the accuracy of the DTA/DSC technique to find the temperature region of significant nucleation is examined by numerical modeling in two barium silicate ($BaO{\cdot}2SiO_2$ and $5BaO{\cdot}8SiO_2$) glasses. It should be emphasized that it is not the purpose of the investigation to determine whether the DTA technique can be used to obtain quantitative information on the nucleation rate data.

Two models are used to describe the time-dependent nucleation behavior, the CNT and a more recently developed model, the diffuse interface theory (DIT)[12–14]. The CNT based calculations describe the DTA only if at low temperatures the work of critical cluster formation is radically different from the form that is expected[15,16]. A similar anomalous behavior was also noted by Xia et al.[17] in experimental measurements of the steady-state nucleation rate and transient times using a two-step heating method. The steady-state rate was much smaller than predicted by the CNT for temperatures below that of the peak nucleation rate. For those measurements, the possibility was left open that the heating times at the nucleation temperature were too short to reach the steady-state. The DTA calculation was used to try to resolve this possibility. The anomalous work of cluster formation was examined in terms of a nonlinear change in the driving free energy as a function of temperature, a nonlinear change in the interfacial width as a function of temperature, or a breakdown of the CNT. A possible nonlinear change in the interfacial free energy as a function of temperature is also considered in the modeling of the $5BaO{\cdot}8SiO_2$ glass. Two methods were used to calculate the driving free energy used in the CNT, (i) the Turnbull approximation and (ii) the values obtained by forcing the CNT to fit to the anomalous low temperature nucleation data. For the DIT fits, the interfacial width was either taken to be linear, giving similar steady-state nucleation rates as the CNT when the Turnbull approximation is used, or to have a temperature dependence described by a piecewise linear fit obtained when the calculated rates were forced to agree with the measured nucleation data, giving similar steady-state nucleation rates as the CNT when the anomalous driving free energy is used. Unfortunately, the DTA method was not sufficiently sensitive to obtain a clear answer to the question of the anomalous low temperature nucleation data. However, the DIT calculations showed that the experimental data indicate an increase in the interfacial width between the nucleating cluster and the parent glass phase with decreasing temperature, which is not considered within the CNT.

5.2 Numerical Model

As mentioned, the classical and diffuse interface theories of nucleation are used to model the DTA data. A brief description of the model is given here; a more detailed description can be found elsewhere[3,10,18–22].

The CNT and the DIT differ in the way in which the work required to form a crystal cluster, $W(n)$, is calculated. Assuming spherical clusters, within the CNT gives

$$W(n) = n\Delta\mu + (36\pi\bar{v}^2 n^2)^{1/3}\sigma, \tag{5.1}$$

where $\Delta\mu$ is the difference in the Gibbs free energies of the glass and crystal phases per formula unit (hereon referred to as a *monomer*), σ is the interfacial free energy, $\bar{v}$ is the volume of a monomer, and n is the number of monomers in the cluster. In deriving this expression, it is assumed that there is a sharp interface between the nucleating cluster and the original phase. Density functional calculations show that this is an inaccurate picture[23]. The actual interface is diffuse, constituting a large fraction of the cluster diameter when nucleation occurs far from equilibrium, as is the case for glass crystallization. A phenomenological model to take the diffuse interface into account was proposed independently by Gránásy[12,13] and Spaepen[14]. Within the

DIT, the work of cluster formation is expressed in terms of the Gibbs free energy as a function of distance from the cluster center,

$$W = \int_0^\infty 4\pi r^2 g(r)\, dr\,, \tag{5.2}$$

where $g(r) = \Delta h - T\Delta s$, with Δh, the enthalpy difference between the glass and crystal, and Δs, the entropy difference between the glass and crystal. Within the DIT $g(r)$, Δh, and Δs are expressed by a series of step functions that define the interface width.

The difference between the CNT and the DIT is then in the thermodynamic model; the kinetics are assumed to follow those of the CNT. In this model, the clusters evolve one monomer at a time, following the bi-molecular reactions as shown in fig. 5.1. From this, the rate of change of the cluster population of size n at time t, $N_{n,t}$, is given by

$$\frac{dN_{n,t}}{dt} = N_{n-1,t}k_{n-1}^{+} + N_{n+1,t}k_{n+1}^{-} - N_{n,t}k_n^{-} - N_{n,t}k_n^{+}, \tag{5.3}$$

where k_n^+ and k_n^- are the forward and backward reaction rates at cluster size n,

$$\begin{aligned} k_n^{+} &= \frac{6D}{\lambda^2} O_n \exp\left(-\frac{W_{n+1} - W_n}{2k_BT}\right) \\ k_n^{-} &= \frac{6D}{\lambda^2} O_{n-1} \exp\left(+\frac{W_{n+1} - W_n}{2k_BT}\right). \end{aligned} \tag{5.4}$$

Here, D is the diffusion coefficient in the glass/liquid, λ is the atomic jump distance, and O_n is the number of attachment sites (equal to $4n^{2/3}$ for a spherical cluster containing n monomers).

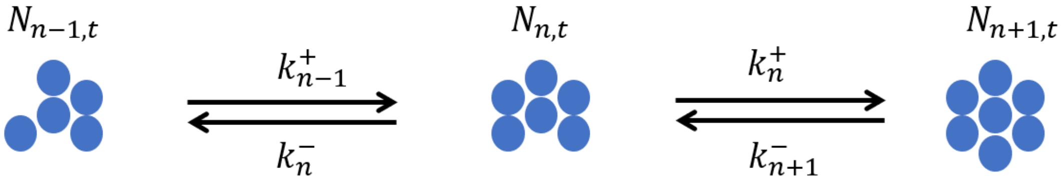

Figure 5.1 – The bi-molecular reaction controlling the cluster size n at time t, where $N_{n,t}$ is the cluster population density, k_n^{+} is the forward reaction rate, and k_n^{-} is the backward reaction rate.

The time-dependent cluster population can be obtained using a finite difference method, in which the time is divided up into small increments, δt

$$N_{n,t+dt} = N_{n,t} + \delta t\left(\frac{dN_{n,t}}{dt}\right). \tag{5.5}$$

With the results of the iteration the time-dependent nucleation rate, $I_{n,t}$, is readily computed at any cluster size n, since it is the flux of clusters growing or shrinking past that size

$$I_{n,t} = N_{n,t}k_n^{+} - N_{n+1,t}k_{n+1}^{-}. \tag{5.6}$$

To model the non-isothermal crystallization of the glass in DTA, it is necessary to calculate the growth rate as a function of cluster size. The growth of very small clusters, near the critical size for nucleation, is stochastic[24]. However, when the clusters are sufficiently large, they transition to growth kinetics, which are well described by an expression due to Kelton and Greer[19],

$$\frac{dr}{dt} = \frac{16D}{\lambda^2}\left(\frac{3\bar{v}}{4\pi}\right)^{1/3}\sinh\left[\frac{\bar{v}}{2k_BT}\left(\Delta G_v - \frac{2\sigma}{r}\right)\right], \tag{5.7}$$

where ΔG_v is the free energy decrease per unit volume on crystallization and k_B is the Boltzmann constant. Often D is computed from the measured viscosity using the Stokes-Einstein equation. However, it has been shown that the Stokes-Einstein equation breaks down above the glass transition temperature[25]. The breakdown for BaO·2SiO$_2$ occurs near 1140K[26] ($1.18T_g$) which is approximately equal to the DTA crystallization peak maximum temperature (see fig. 5.7 and fig. 5.4 respectively). Here we show additional evidence of this breakdown in the DTA results. The diffusion coefficient can also be obtained from experimental measurements of the induction time[17] or experimental measurements of the growth velocity for macroscopic crystals[26]. Following the work of Kashchiev[27], the diffusion coefficient computed from the induction time, Θ, is

$$D = \frac{k_B T \lambda^2 n^{*1/3}}{6\Theta|\Delta\mu|}, \tag{5.8}$$

where n^* is the critical cluster size, beyond which clusters tend to grow, and $\Delta\mu$ is the driving free energy for a single monomer. Equation 5.7 can be used to obtain the diffusion coefficient from growth velocity data.

For each time step, δt, the extended volume transformed (assuming no overlap of the transformed regions) is calculated as

$$x_e(t) = \frac{1}{v}\sum_{i=l} \frac{4\pi}{3} N_i r_{i,t}^3, \tag{5.9}$$

where v is the total volume, N_i is the population of the cluster or nuclei at size i, $r_{i,t}$ is the radius of the cluster or nuclei at size i at the time of the calculation, t, and l is the lower limit on the cluster size distribution. The lower limit is set to two monomers in the simulations. The actual volume fraction transformed as a function of time, $x(t)$, must take into account the overlap between crystals. Assuming that the crystals form by homogeneous nucleation (so that they appear randomly in space and time) and that the sample size may be taken to be infinite, the Johnson-Mehl-Avrami-Kolmogorov (JMAK) method[28–32] allows $x(t)$ to be computed from $x_e(t)$,

$$x(t) = 1 - \exp(-x_e(t)). \tag{5.10}$$

Since powder samples are typically used for the DTA experiments, they cannot be assumed to be infinite in size. Instead, corrections for the finite particle size effects follow the method discussed by Levine[22]. It was found in studies of lithium disilicate glass that for powders with particle sizes greater than 300μm internal crystallization controls the location of the peak temperature and surface crystallization matters very little[5]. The DTA experiments on barium disilicate glasses, used powders with an average particle size of 526μm with a 400μm lower limit[6]. For the numerical calculations an even distribution of particle sizes with the same range and an upper limit of 652μm was assumed. Additionally, the internal nucleation rate at the maximum nucleation rate temperature for barium disilicate[17,33,34] is greater than 300 times larger than that of lithium disilicate[33,35–37], suggesting that for larger particles and faster internal nucleation rates, surface crystallization should not have a strong influence. To check this, surface crystallization was also included in the numerical calculation in the following way. First, it was assumed that surface nucleation was very fast, quickly leading to a surface crystallization shell around the particle during the quench. The shell was allowed to grow inward, toward the particle center, with the measured surface growth velocity[26] (which is approximately 1.27 times the internal growth velocity). While it is unknown if the surface nucleation is sufficiently fast to create a complete surface layer during the quench, this assumption gives the maximum possible effect due to surface nucleation and growth. The DTA experiments on $5BaO{\cdot}8SiO_2$ glasses, used powders with an average particle size of 489μm with a 400μm lower limit[6]. For the numerical calculations an even distribution of particle sizes with the same range and an upper limit of 578μm was assumed.

The measured DTA signal reflects the amount of heat (enthalpy) released during crystallization. Assuming that this is proportional to the volume transformed, the DTA signal can be calculated as

$$\text{DTA signal} \propto \frac{x(t_i+\delta t)-x(t_i)}{\delta t}. \tag{5.11}$$

The temperature profile used in the DTA experiments is adopted for the numerical calculations, an example of which is shown in fig. 5.2.

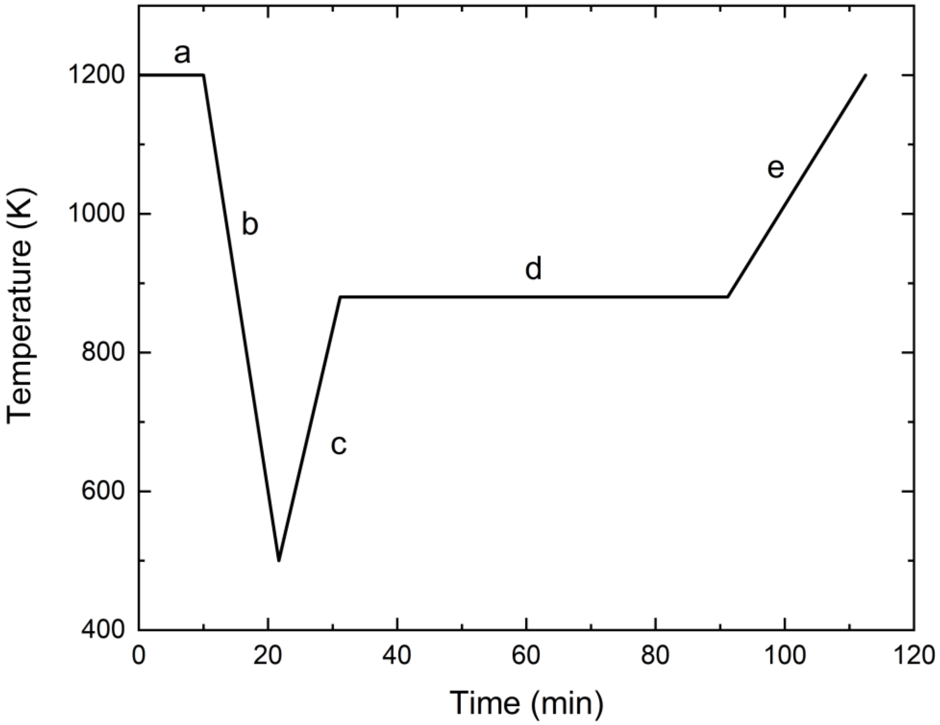

Figure 5.2 – An example of the profile used in the experimental measurements and the simulations. The steps are: (a) establish an equilibrium distribution at a high temperature; (b) quench the system at 60 K/min to a low temperature; (c) heat at 40 K/min to the nucleation temperature; (d) isothermally heat for 60 minutes; (e) scan at 15 K/min through the crystallization peak.

5.3 Results and Discussion

The driving free energy and the interfacial free energy are key parameters in the CNT. Two methods were used to extract them from the experimental measurements of the steady-state nucleation rates. In the first method the driving free energy was calculated as

$$\Delta G = \frac{\Delta H_f (T - T_l)}{T_l}, \tag{5.12}$$

where ΔH_f is the heat of fusion, T is the temperature, and T_l is the liquidus temperature (often called the Turnbull approximation). A more accurate calculation of the driving free energy could be made if the specific heats of the crystal and glass were known. However, while this would change the value quantitatively, qualitatively the driving free energy would remain the same. The interfacial free energy was obtained by matching the fit of the high temperature steady-state nucleation rate data to the rate predicted by CNT. While these give good fits at high temperature, anomalies appear at low temperatures. The source of the anomalies is of current debate. Experimental and theoretical considerations show that the interfacial free energy increases linearly with increasing temperature[2]. Assuming this, the second method obtains the interfacial free energy at low temperatures from an extrapolation of the high temperature values. The driving free energy is then computed by forcing agreement between the steady-state nucleation rate predicted by CNT and the measured value. In the first method, the Turnbull approximation is used, and the interfacial free energy is assumed to be linear. For this to be true, the measured steady-state nucleation rate data[17,33,34] would have to be incorrect, which could be the case if steady-state were not achieved during the two-step heating treatment. The second method assumes that the steady-state is achieved and that either the CNT breaks down or the driving free energy behaves anomalously at temperatures below the maximum nucleation rate temperature. Values obtained from both methods were used to calculate the DTA curves using the CNT. Additional modeling studies of the $5BaO \cdot 8SiO_2$ glass were performed assuming the Turnbull approximation for the driving free energy and an anomalous behavior of the interfacial free energy, matching the measured steady-state nucleation rates to the calculated rates.

The DTA scans were also calculated using the diffuse interface theory, presuming that the anomalous behavior of the nucleation rate at low temperature is real and reflects a failure of the CNT. In the first DIT method, the width of the interface was adjusted in a piecewise linear fit to force the experimental data to match the values predicted by the DIT. Assuming that the measured steady-state nucleation rate data at low temperatures are lower than the real steady-state values, the interface width that was obtained at high temperatures by forcing a match between the experimental steady-state data with those calculated from the DIT was extrapolated to low temperatures in a linear fit for the second DIT method.

Table 5.1 – The temperature-independent parameters used in the simulations.

Parameter	Symbol	Units	$BaO{\cdot}2SiO_2$	$5BaO{\cdot}8SiO_2$
Liquidus temperature	T_l	K	1693	1719.6
Heat of fusion	ΔH_f	kJ mol^{-1}	37.5	212.3
Monomer volume	$\overline{v}$	m^3	1.216×10^{28}	5.275×10^{28}
Jump distance	λ	Å	$\overline{v}^{1/3} = 4.954$	$\overline{v}^{1/3} = 8.08$

Table 5.1 lists the temperature-independent parameters used in the simulations, which were obtained from the literature[2]. These include the liquidus temperature, the heat of fusion, the monomer volume, and the atomic jump distance.

In simulations of the $BaO{\cdot}2SiO_2$ glass, the diffusion coefficient is found from the measured growth velocity, induction time, or Stokes-Einstein equation. In simulations of the $5BaO{\cdot}8SiO_2$ glass, however, only the growth velocity and induction time are used. The diffusion coefficient calculated from the growth velocity and induction time has the form

$$\log_{10}(D) = \log_{10}(D_0) + Aexp\left(-\frac{T}{\tau}\right), \tag{5.13}$$

where D_0, A, and τ are fitting parameters. The validity of the Stokes-Einstein equation was assumed to calculate the diffusion coefficient from the viscosity. The avoided critical point model (KKZNT)[38–40] was used to fit the viscosity data,

$$\log_{10}(\eta) = \log_{10}(\eta_0) + \frac{1}{T}\left[E_\infty + T^*B\left(\frac{T^* - T}{T^*}\right)^{8/3}\theta(T^* - T)\right], \tag{5.14}$$

where η_0, E_∞, B, and T^* are fitting parameters. The diffusion coefficient is then

$$D = \frac{k_B T}{6\pi\eta r}, \tag{5.15}$$

where r is the monomer radius. Other parameters in Table 5.2 (for $BaO{\cdot}2SiO_2$) and Table 5.3 (for $5BaO{\cdot}8SiO_2$) use either the diffusion coefficient obtained from the growth velocity, the induction time, or the viscosity to match the steady-state nucleation rate data. The interfacial free energy is taken to be linear with temperature, $\sigma = \sigma_0 + \sigma_1 T$. Both the Gibb's driving free energy, ΔG, and the interfacial width, δ, are fit with piecewise linear functions of the form

$$\Delta G, \delta = \begin{cases} a + k_1 T & \text{for } T < T_i \\ a + k_1 T_i + k_2(T - T_i) & \text{for } T \geq T_i\,, \end{cases} \tag{5.16}$$

where a, k_1, k_2, and T_i are fitting parameters. The driving free energy at high temperatures follows the Turnbull approximation, as previously mentioned. The interfacial free energy for the $5BaO{\cdot}8SiO_2$ also follows from eq. 5.16 when the anomalous behavior is assumed.

5.3.1 Modeling $BaO{\cdot}2SiO_2$

Table 5.2 lists the parameters required to match the experimental steady-state nucleation rate data to the calculated steady-state nucleation rate data for each diffusion coefficient used in the $BaO{\cdot}2SiO_2$ simulations.

Table 5.2 – The Diffusion coefficient dependent parameters used in the $BaO\cdot 2SiO_2$ simulations, determined by matching the calculated steady-state nucleation rate to the experimentally measured rate.

Parameter	Symbol	Units	Growth velocity	Induction time	Stokes-Einstein
Diffusion coefficient	$\log_{10}(D_0)$	$m^2\ s^{-1}$	-13.005	-11.130	–
	A	unitless	-750.501	-256.705	–
	τ	K	219.141	307.427	–
Viscosity (KKZNT)	$\log_{10}(\eta_0)$	Pa s	–	–	-5.427
	E_∞	K	–	–	10423
	B	unitless	–	–	67.98
	T^*	K	–	–	1456.6
Interfacial free energy	σ_0	$J\ m^{-2}$	0.06995	0.07383	0.04281
	σ_1	$J\ m^{-2}\ K^{-1}$	3.707×10^{-5}	3.266×10^{-5}	6.187×10^{-5}
Gibb's driving free energy	a	$kJ\ m^{-3}$	-198740	-159790	-197130
	k_1	$kJ\ m^{-3}\ K^{-1}$	-17.656	-57.33	-19.542
	k_2	$kJ\ m^{-3}\ K^{-1}$	303.01	302.825	303.279
	T_i	K	978.80	979.102	978.053
Interface width	a	Å	5.7459	6.205	4.9116
	k_1	$Å\ K^{-1}$	-0.0031	-0.00358	-0.00232
	k_2	$Å\ K^{-1}$	-3.487×10^{-4}	-4.525×10^{-4}	2.948×10^{-4}
	T_i	K	978.8	978.99	978.1

The calculated nucleation rates as a function of temperature for the two methods assumed for the CNT and the DIT, using the diffusion coefficient calculated from the growth velocity, are compared with recent experimental measurements by Xia[17] in fig. 5.3. The calculations using the Turnbull approximation in the CNT and the linear interface width in the DIT match the experimental data at high temperatures but deviate at low temperatures. The quality of the fit in the calculations using the piecewise linear driving free energy in the CNT and the piecewise linear interface width in the DIT, as well as the high temperature portions of the other two calculations, reflects the quality of the fit parameters.

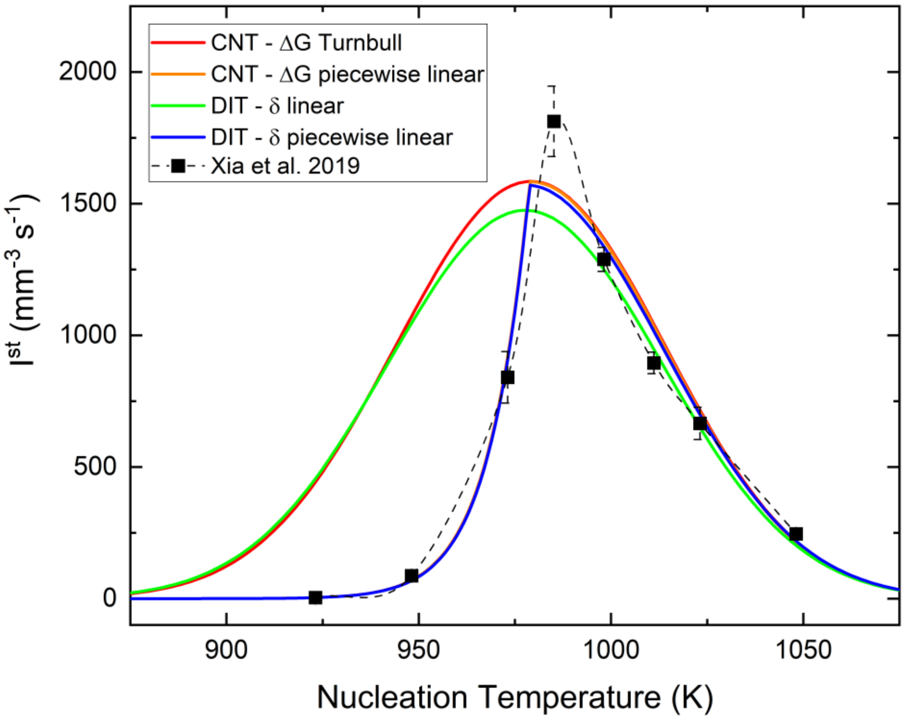

Figure 5.3 – The calculated steady-state nucleation rates for the methods discussed using the diffusion coefficient obtained from growth velocity compared with the experimental data for the $BaO{\cdot}2SiO_2$ glass.

Shown in fig. 5.4 are several selected experimental DTA curves for $BaO{\cdot}2SiO_2$ glasses for different nucleation temperatures (a)[6], and the numerical results obtained using the CNT along with the Turnbull approximation for the driving free energy and the three methods for determining the diffusion coefficients (b-d). There are several sources of error that must be considered to account for the differences in the experimental DTA curves and the numerically calculated ones. The diffusion coefficient controls both the nucleation and growth of the clusters. As observed in fig. 5.4, the choice of diffusion coefficient makes a large difference in the DTA curves. Additionally, The $BaO{\cdot}2SiO_2$ glass is known to form irregularly shaped crystals at some temperatures[17,34]. If the crystals are irregularly shaped, then the assumption of spherical growth in the simulation will give an overestimate for the extended volume transformed. Accounting for the irregularly shaped crystals increases the peak temperature and decrease the peak width because the growth rate is larger at higher temperatures. A rough estimate for the real volume fraction transformed due to the irregularly shaped crystals was made from the $BaO{\cdot}2SiO_2$ image in the manuscript by Xia[17]. When the growth velocity is used to calculate the diffusion coefficient, the peaks in the DTA scan shift by 5K higher in temperature, becoming more similar to the experimental data. This shift would account for half the vertical offset in the numerical and the experimental data in fig. 5.5a. Also, since the simulation uses the fits to the experimental data to determine the driving free energy, the interfacial free energy, and the interface width, the predicted steady-state nucleation rates may be incorrect at low temperatures.

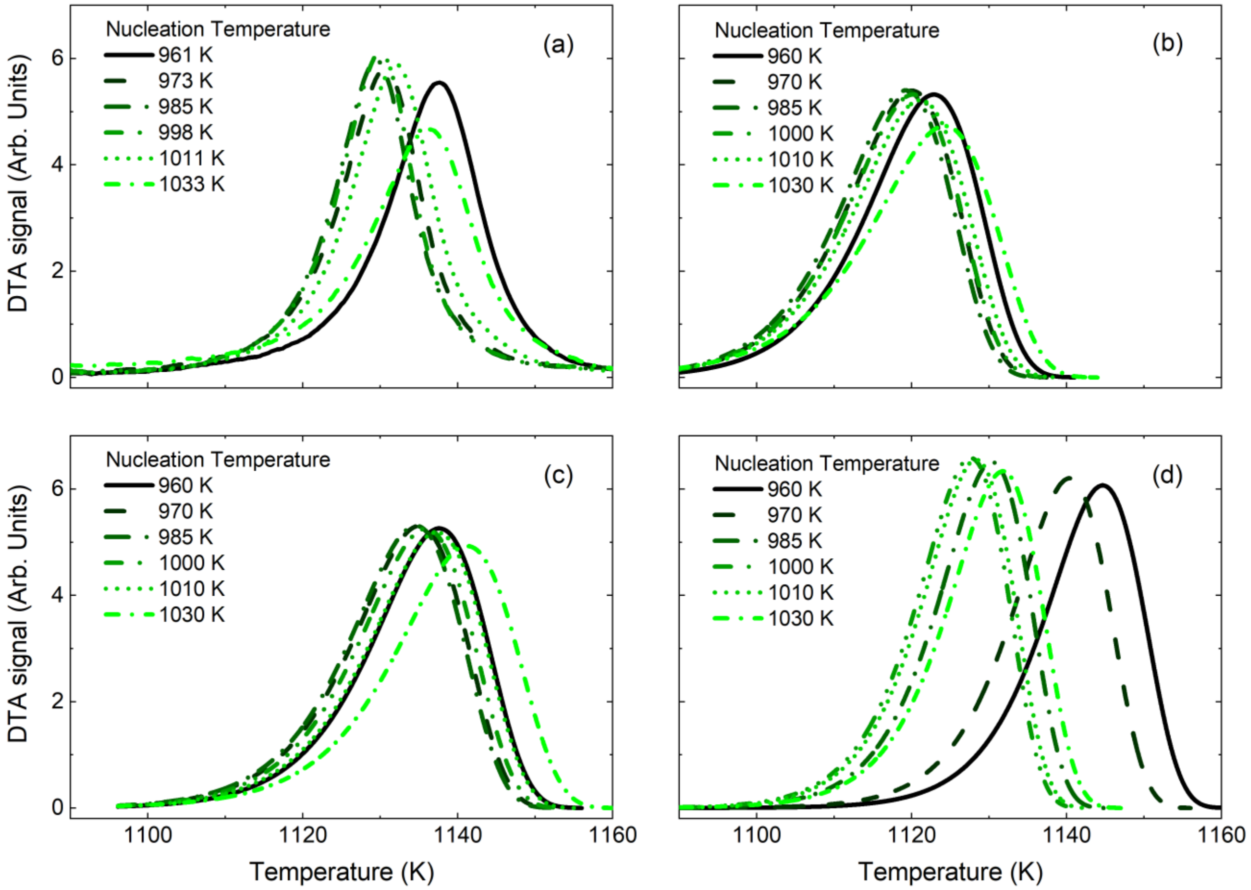

Figure 5.4 – The calculated DTA signals during a 15 K/min scan after one hour of isothermal heating at various temperatures (listed in the legend) neglecting surface crystallization: (a) experimental data; (b) numerical calculation for the CNT, calculating the driving free energy from the Turnbull approximation, and calculating the diffusion coefficient from the growth velocity; (c) numerical calculation for the CNT, calculating the driving free energy from the Turnbull approximation, and calculating the diffusion coefficient from the induction time; (d) numerical calculation for the CNT, calculating the driving free energy from the Turnbull approximation, and calculating the diffusion coefficient from the viscosity using the Stokes-Einstein relation.

As discussed in the introduction, several studies have shown that differential thermal analysis (DTA) and differential scanning calorimetry (DSC) measurements can be used to determine the temperature range for significant nucleation[5–8,41]. Most recently the DTA technique was used to estimate this for $BaO \cdot 2SiO_2$ and $5BaO \cdot 8SiO_2$ glasses[6]; it was determined that the inverse peak temperature from the DTA scans for different nucleation temperatures gave the best estimates. A comparison between those experimental DTA data for $BaO \cdot 2SiO_2$ and the numerical calculations made as a function of the nucleation temperature using the three methods previously described is given in fig. 5.5.

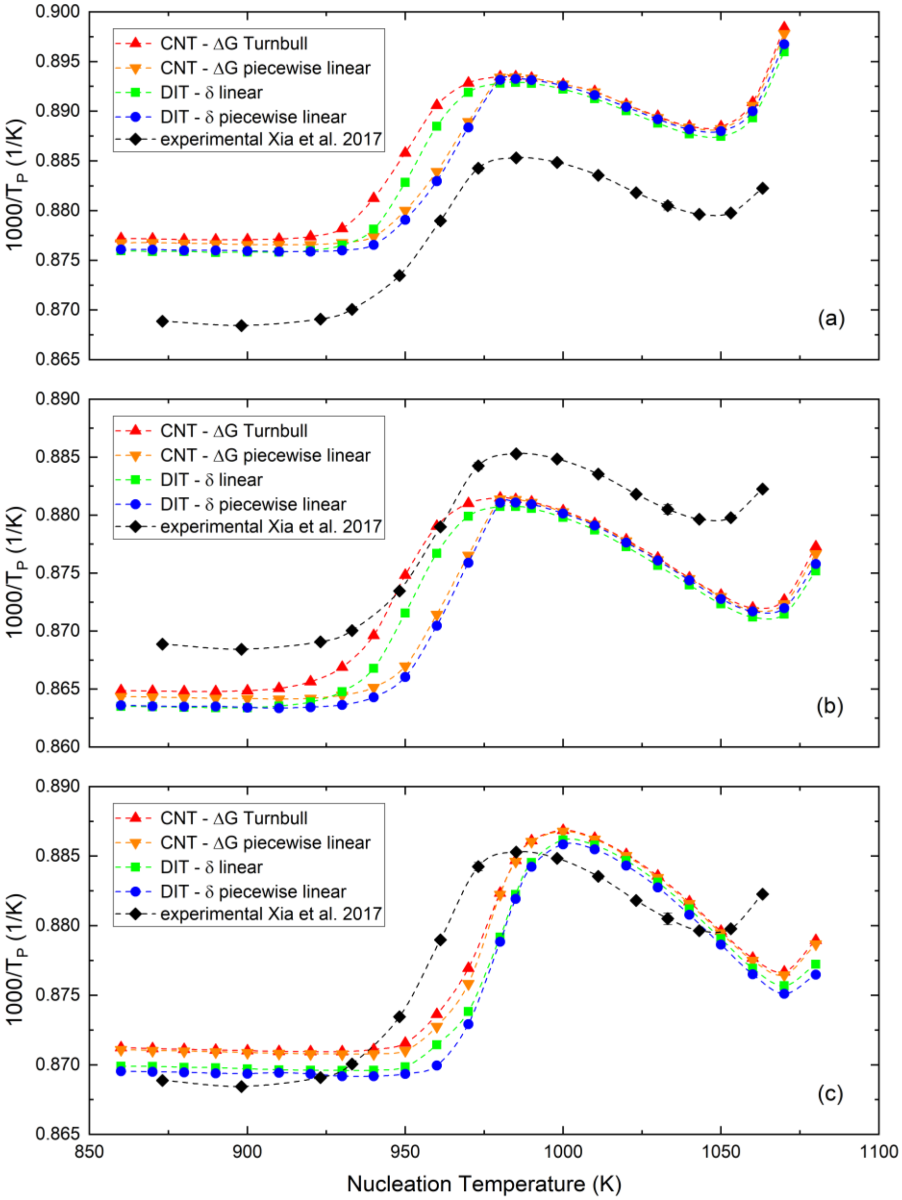

Figure 5.5 – The inverse peak temperature for the experimental and numerical DTA data for the BaO·2SiO$_2$ glass with (a) the diffusion coefficient calculated from the growth velocity; (b) the diffusion coefficient calculated from the induction time; (c) the diffusion coefficient calculated from the viscosity assuming the Stokes-Einstein relation. The errors in the experimental data are the size of the symbols[6]. The propagated errors in the numerical DTA data from the diffusion coefficient produce differences in the data smaller than the size of the symbols.

The inverse peak temperature as a function of the nucleation temperature in the DTA data that were numerically calculated using both the CNT and DIT agree well with the experimental data when the diffusion coefficient is calculated from the growth velocity and from the induction time. Most importantly, the maximum in the inverse peak temperature agrees with the maximum nucleation rate measurement and the experimental inverse peak temperature maximum. In contrast, the calculated DTA values based on the viscosity and assuming the Stokes-Einstein relation are in striking disagreement with the experimental data. This provides additional strong evidence for the breakdown of the Stokes-Einstein equation for temperatures near the crystallization temperature. It is less clear, however, which nucleation theory compares best to the experimental data. To investigate this question the calculated inverse peak temperature for the maximum nucleation rate was matched to the experimentally measured value. The diffusion coefficient used for the numerical calculations was obtained from the measured growth velocity. As observed in fig. 5.6, the agreement between the calculated and measured data is very good for temperatures above the peak nucleation temperature, indicating that theories examined are all in good agreement at high temperatures. However, for temperatures less than the maximum nucleation rate temperature, they disagree and there is no clear indication of a better model.

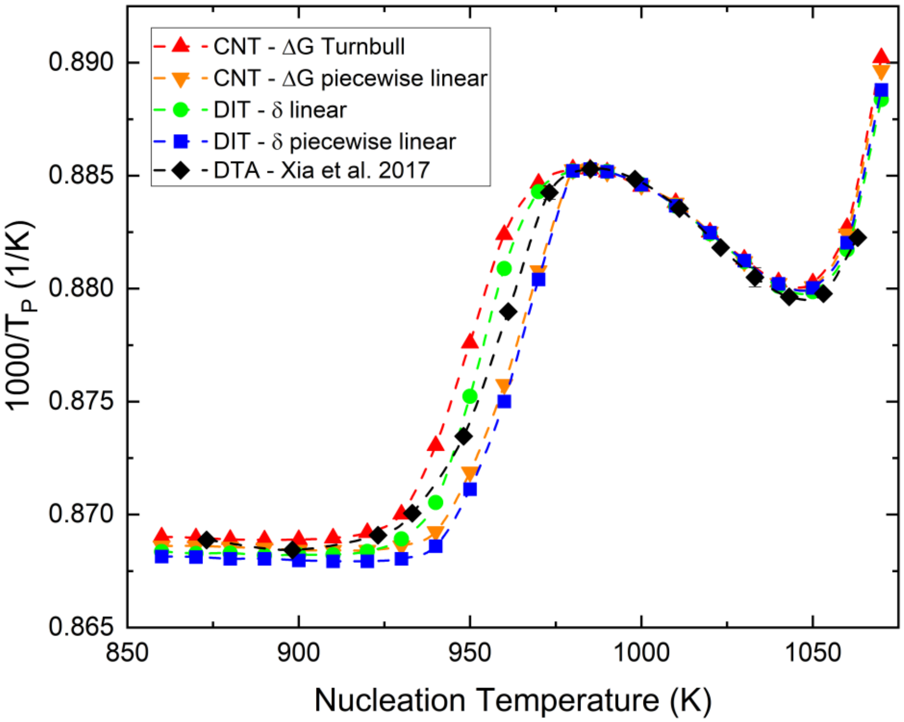

Figure 5.6 – The inverse peak temperature for the experimental and calculated DTA data for the $BaO{\cdot}2SiO_2$ glass. The numerical calculation has been shifted to match the experimental data at a single data point, 985 K.

A failure of the CNT to fit time-dependent nucleation data at temperatures lower than that of the peak nucleation rate was reported by Xia et al.[17]. This is similar to behavior reported earlier in other silicate glasses where a changing size of the structural units, spatial heterogeneity and dynamical heterogeneity have been proposed to explain these results[16,42–44], but the question still remains unclear. A recent publication suggests that the failure may be an experimental artifact arising from insufficient time in the experiments for steady-state to be reached[45]. Unfortunately, the DTA calculations discussed here do not appear to be sensitive enough to support or oppose the validity of the experimental time-dependent nucleation results.

The numerical calculations show that for the particle size used, surface crystallization plays no role in determining the peak temperature during the DTA scan. Figure 5.7 shows the calculated DTA signals for three different temperatures with and without surface crystallization. Changes in the peak temperatures are negligible and changes in the magnitude of the peaks are extremely small. Even though the surface layer is numerically determined to be between 3% and 10% of the particle diameter for 526μm particles, surface crystallization plays no role in determining the peak temperature during the simulated DTA scan. The thickness of the crystallization layers in the DTA simulations is near 20μm for low nucleation treatment temperatures, drops to 8μm for nucleation treatment temperatures near the maximum internal nucleation rate temperature, and then rises to 27μm for the highest nucleation treatment temperature. As previously stated, these surface layer thicknesses are calculated assuming the maximum possible surface crystallization effect.

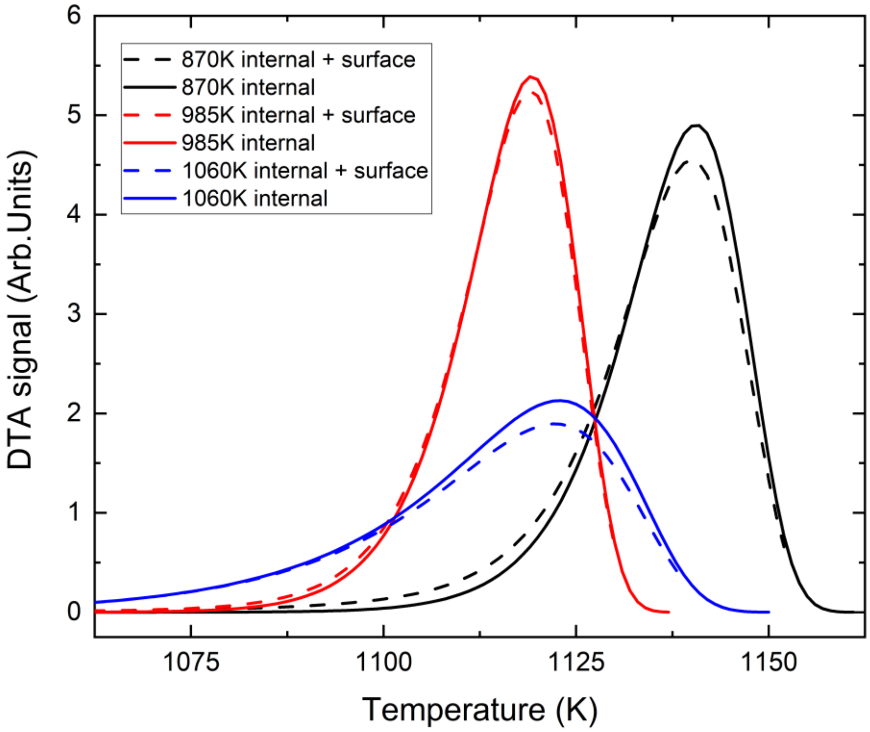

Figure 5.7 – The calculated DTA signals during a 15 K/min scan after one hour of isothermal heating at various temperatures (listed in the legend) for simulations when internal and surface nucleation and growth are taken into account (dashed lines) and when only internal nucleation and growth are present (solid lines).

For a heating rate of 15 K/min, our studies have shown that the DTA method is a reasonable way to determine the range of significant nucleation. However, it could be that other heating rates might not be as effective. This was tested using the numerical model by heating at half the experimental heating rate (7.5 K/min) and two times that rate (30 K/min). The diffusion coefficient obtained from the growth velocity was assumed. Figure 5.8 shows the calculated inverse peak temperature as a function of the nucleation treatment temperature for the three different DTA scan heating rates. Although the peak temperature shifts to a higher value with a faster heating rate and to a lower temperature for a lower heating rate, the region of significant nucleation remains the same. This indicates that the method is insensitive to the heating rate (within these limits) for the measurements, a point that to our knowledge has not been explored previously.

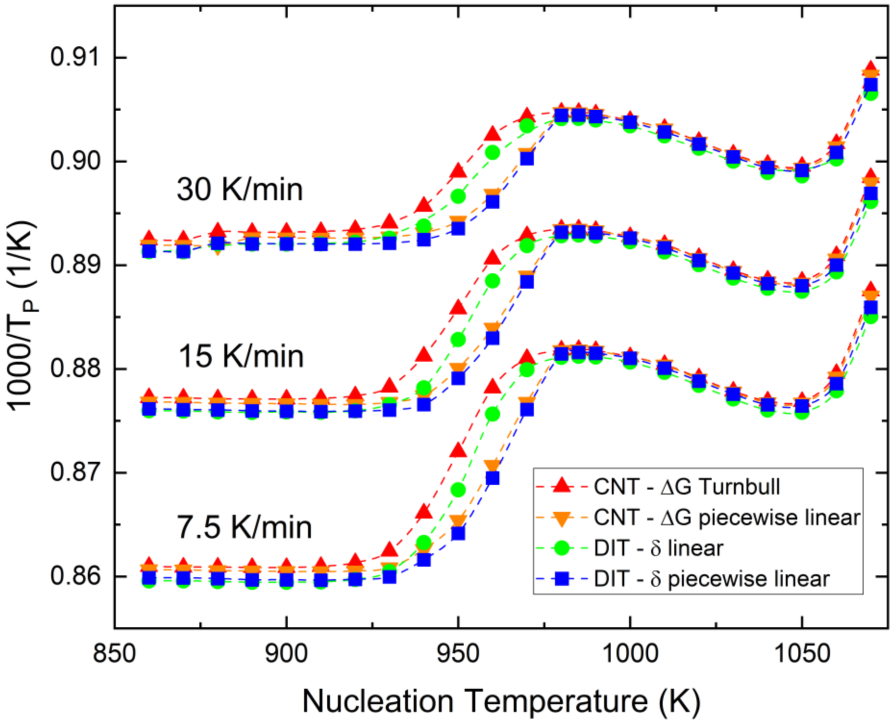

Figure 5.8 – The inverse peak temperature of the calculated DTA data for the $BaO \cdot 2SiO_2$ glass using three different DTA scan rates. The predicted temperature range for significant nucleation is the same.

Evidence for the breakdown of the Stokes-Einstein equation is shown in fig. 5.9. The diffusion coefficient is shown as a function of temperature from experimental measurements of the viscosity[26,33,46] using the Stokes-Einstein relation, from experimental measurements of the growth velocity[26] along with eq. 5.7 for large nuclei, and experimental measurements of the induction time[17] using eq. 5.8. The diffusion coefficients obtained from the growth velocity and the induction time are in reasonable agreement, albeit on a log scale over the temperature range where experimental data are available. However, the diffusion coefficient from the viscosity and the Stokes-Einstein relation is dramatically different. Assuming that the growth velocity and induction time measures of the diffusion coefficient are correct, these data show that the Stokes-Einstein relation breaks down near 1140K ($1.18T_g$) as suggested by Rodrigues et al.[26] The crystallization peaks in the DTA simulations occur between 1120K and 1150K, so the majority of the crystallization occurs in the region where the Stokes-Einstein equation is not valid. This is the cause of the error seen in fig. 5.5c, where the peak of the inverse peak temperature of the experimental data does not match that from the simulated data using the Stokes-Einstein relation.

The reasonable agreement found between the diffusion coefficient obtained from the growth velocity and the induction time at low temperatures in barium disilicate is in disagreement with the $Li_2O{\cdot}2SiO_2$ data reported by Nascimento et al.[25] and the binary $Li_2O{\cdot}2SiO_2$ – $BaO{\cdot}2SiO_2$ data reported by Fokin et al.[47], where the diffusion coefficient from the Stokes-Einstein relation is shown to better match with the diffusion coefficient obtained from the induction time. However, as in the manuscripts by Nascimento and Fokin, the diffusion coefficient obtained from the measured growth velocity is above the one obtained from the Stokes-Einstein relation at low temperatures and matches better at high temperatures. Additionally, the reasonable agreement between the diffusion coefficient from the growth velocity and induction time disagrees with the activation energy data found for $2Na_2O{\cdot}CaO{\cdot}3SiO_2$ by Kalinina et al.[48]. However, in the paper for the soda-lime-silica glass, the temperature range for determining the activation energy is less than 100K and the temperature range is not the same between the growth velocity, induction time, and viscosity. Given that it is widely understood that the Stokes-Einstein relation fails at lower temperatures, the agreement between the viscosity and the induction time in these other glasses is puzzling. However, the agreement between the diffusion coefficient obtained from the growth velocity and the induction time in barium disilicate, where it is not necessary to invoke the Stokes-Einstein relation, is certainly more understandable.

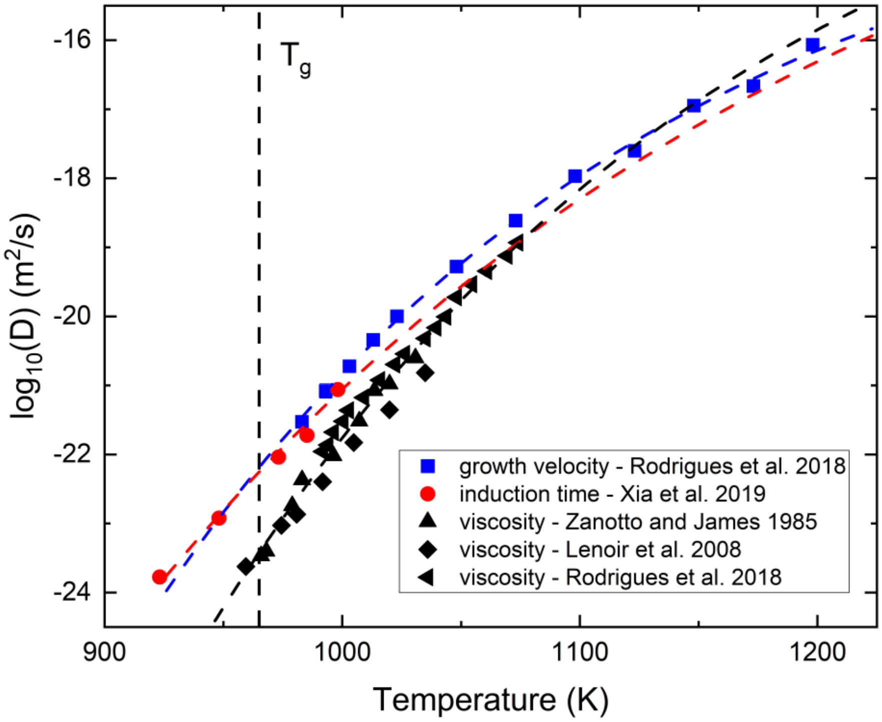

Figure 5.9 – The calculated diffusion coefficient as a function of temperature from experimental measurements of the viscosity, the induction time, and the growth velocity. The fits used in the DTA simulations are shown as dashed lines, taking the parameters from Table 5.2. The errors for the diffusion coefficient calculated from the growth velocity and induction time are smaller than the size of the symbols. The error in the viscosity was not reported.

5.3.2 Modeling $5BaO\cdot 8SiO_2$

The small crystals of $5BaO\cdot 8SiO_2$ glasses are more spherical than those of $BaO\cdot 2SiO_2$ glasses (see fig. 5.10). The calculation of the volume transformed in the model assumes that the nuclei are spherical. The crystallization peak temperatures in the simulated $5BaO\cdot 8SiO_2$ glass system should then better match the experimentally measured DTA crystallization peaks than for barium disilicate.

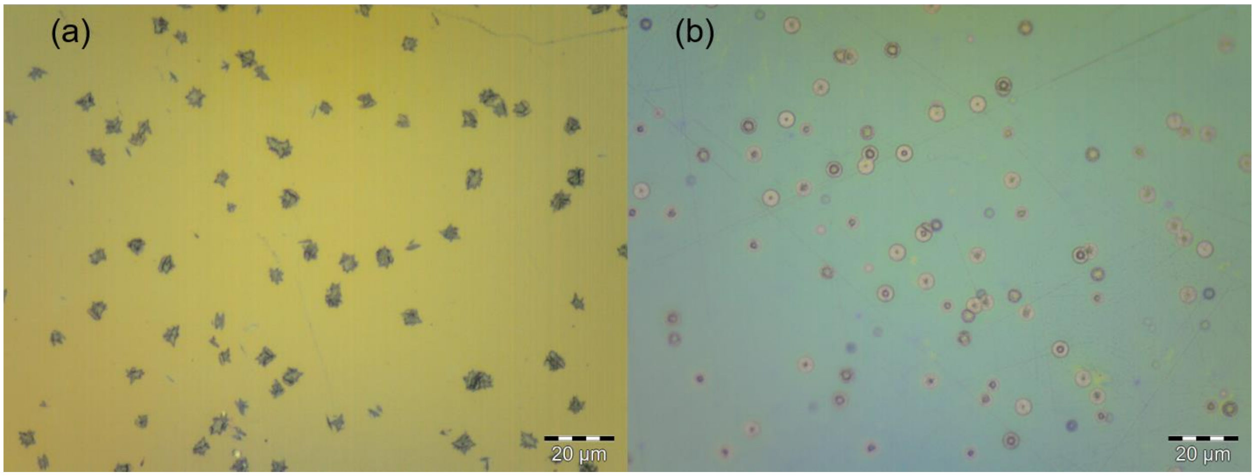

Figure 5.10 – Optical microscope images of (a) $BaO{\cdot}2SiO_2$ glass and small crystals showing the non-spherical nuclei formation and of (b) $5BaO{\cdot}8SiO_2$ glass and the crystals showing the spherical nuclei formation. The $BaO{\cdot}2SiO_2$ sample was nucleated at $998K$ for 9 minutes; the nuclei were then grown to observable size at $1113K$. The $5BaO{\cdot}8SiO_2$ sample was nucleated at $998K$ for 12 minutes and the nuclei were grown to observable size at $1119K$.

Table 5.3 lists the parameters required to match the experimental steady-state nucleation rate data to the calculated steady-state nucleation rate data for each diffusion coefficient used in the $5BaO{\cdot}8SiO_2$ simulations. With a given diffusion coefficient, there are five sets of simulation parameters, including three assuming the classical nucleation theory: (1) Δg from the Turnbull approximation with a linear σ, (2) Δg from the Turnbull approximation with an anomalous (piecewise linear) σ, and (3) an anomalous (piecewise linear) Δg with a linear σ. There are two assuming the diffuse interface theory: (1) Δg from the Turnbull approximation with a linear δ and (2) Δg from the Turnbull approximation with an anomalous (piecewise linear) δ.

Table 5.3 – The diffusion coefficient dependent parameters used in the 5BaO·8SiO$_2$ simulations, determined by matching the calculated steady-state nucleation rate to the experimentally measured rate.

Parameter	Symbol	Units	Growth velocity	Induction time
Diffusion coefficient	$\log_{10}(D_0)$	$m^2\ s^{-1}$	-13.044	-10.507
	A	unitless	-512.606	-193.52
	τ	K	255.5164	353.3738
Interfacial free energy	a	$J\ m^{-2}$	016272	0.20193
	k_1	$J\ m^{-2}\ K^{-1}$	-4.56×10^{-5}	-8.013×10^{-5}
	k_2	$J\ m^{-2}\ K^{-1}$	8.806×10^{-5}	5.713×10^{-5}
	T_i	K	993.8	994.117
Gibb’s driving free energy	a	$kJ\ m^{-3}$	-175173	-177548
	k_1	$kJ\ m^{-3}\ K^{-1}$	-107.671	-105.051
	k_2	$kJ\ m^{-3}\ K^{-1}$	388.4124	389.8955
	T_i	K	993.453	993.9792
Interface width	a	Å	4.35133	5.1868
	k_1	Å K^{-1}	-0.00207	-0.00281
	k_2	Å K^{-1}	-6.149×10^{-4}	-2.387×10^{-4}
	T_i	K	993.517	993.799

The calculated steady-state nucleation rate as a function of temperature for the three methods assumed for the CNT and the two methods for the DIT, using the diffusion coefficient calculated from the growth velocity, are compared with recent experimental measurements by Xia[17] in fig. 5.11 for the 5BaO·8SiO$_2$ glass. The calculations using the Turnbull approximation in the CNT and the linear interface width in the DIT match the experimental data at high temperatures but deviate at low temperatures. These parameters were chosen to show the crystallization process, assuming that the low temperature measured steady-state nucleation rate data are incorrect because the real steady-state had not been reached in the experiments.

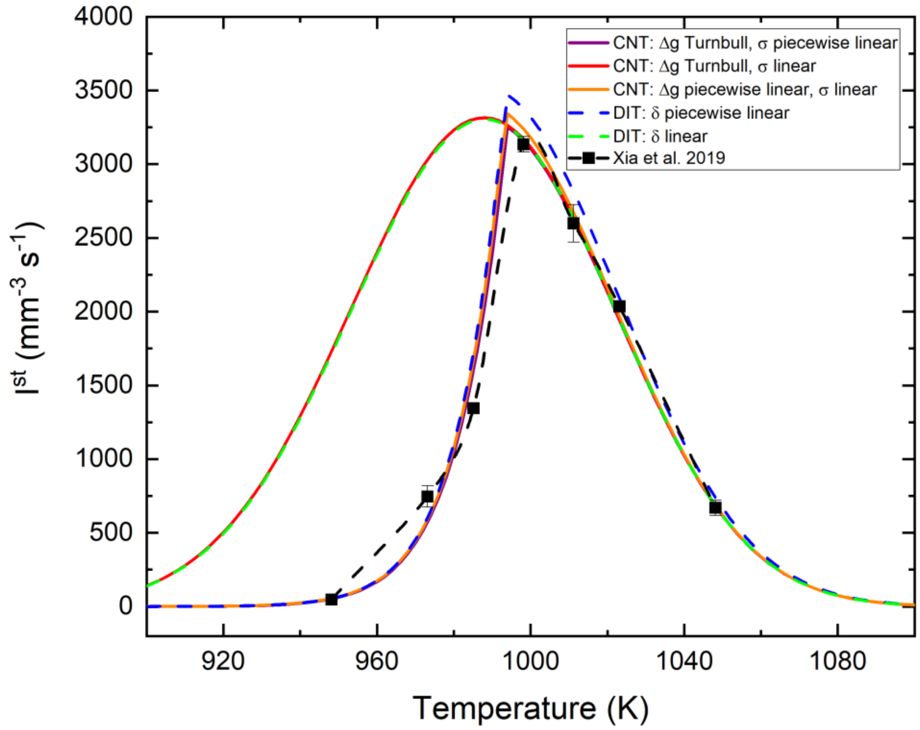

Figure 5.11 – The calculated steady-state nucleation rates for the methods discussed using the diffusion coefficient obtained from growth velocity compared with the experimental data for the $5BaO{\cdot}8SiO_2$ glass.

The inverse peak temperature as a function of the nucleation treatment temperature for the $5BaO{\cdot}8SiO_2$ glass is shown in fig. 5.12 for both (a) the diffusion coefficient from the growth velocity and (b) the diffusion coefficient from the induction time. When the growth velocity is used to calculate the diffusion coefficient (fig. 5.12a), the location of the maximum nucleation rate in the inverse peak temperature plot is $25K$ higher than the measured maximum. Otherwise, the general trend of the inverse peak temperature plot is similar to the measured results. This suggests that the growth velocity is not describing the nucleation step correctly, while the macroscopic growth rate controlling the crystallization process is accurate. When the diffusion coefficient is calculated from the induction time (fig. 5.12b), the location of the maximum in the nucleation rate appears to be the same as that of the measured maximum. However, the modeled inverse peak temperature is drastically different than the measured inverse peak temperature. This suggests that the extrapolation of the induction time diffusion coefficient to high temperatures, where growth is dominant, is inaccurate. Figure 5.13 shows the diffusion coefficient as a function of temperature for both the growth velocity and the induction time. The diffusion coefficient from the Stokes-Einstein equation and viscosity data near T_g (provided by Corning Inc.) using the MYEGA[49,50] viscosity fit is also shown. The growth velocity curve is drastically different than the induction time curve, likely because a single monomer of the $5BaO{\cdot}8SiO_2$ glass is five times larger than the $BaO{\cdot}2SiO_2$ glass and the attachment of this large monomer does not represent the actual nucleation process. The volume term comes in the hyperbolic sine portion of eq. 5.6 and plays a large role on the diffusion coefficient from the growth velocity.

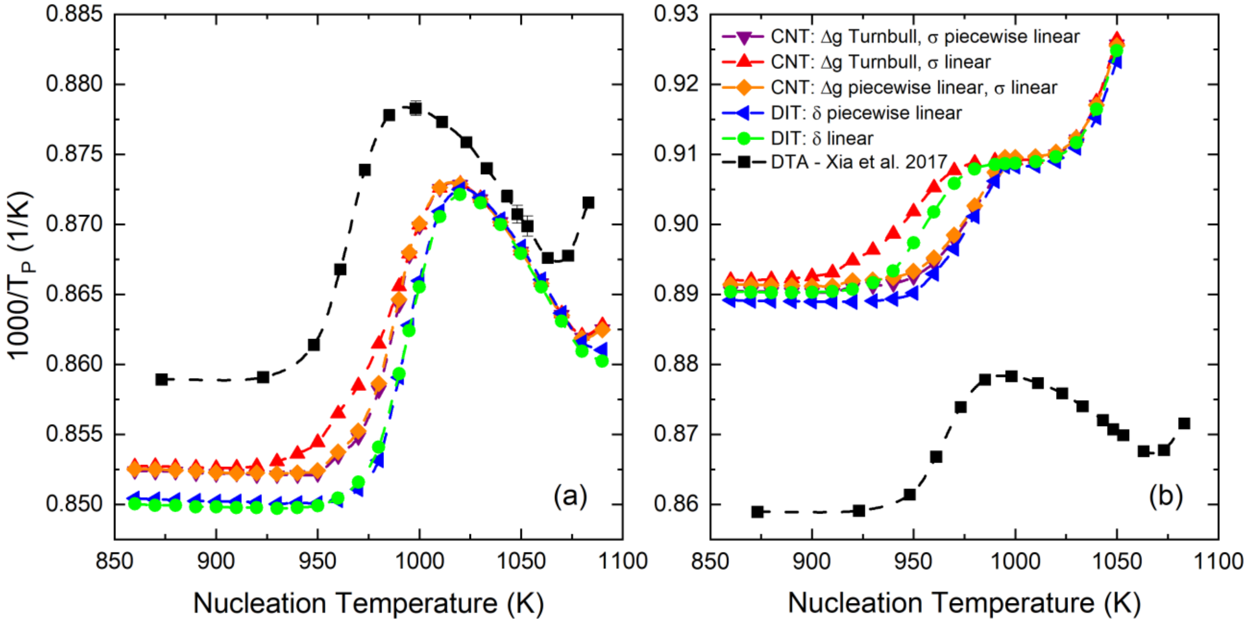

Figure 5.12 – The inverse peak temperature for the experimental and numerical DTA data for the $5BaO{\cdot}8SiO_2$ glass with (a) the diffusion coefficient calculated from the growth velocity and (b) the diffusion coefficient calculated from the induction time. The errors in the experimental data are the size of the symbols[6]. The propagated errors in the numerical DTA data from the diffusion coefficient produce differences in the data smaller than the size of the symbols.

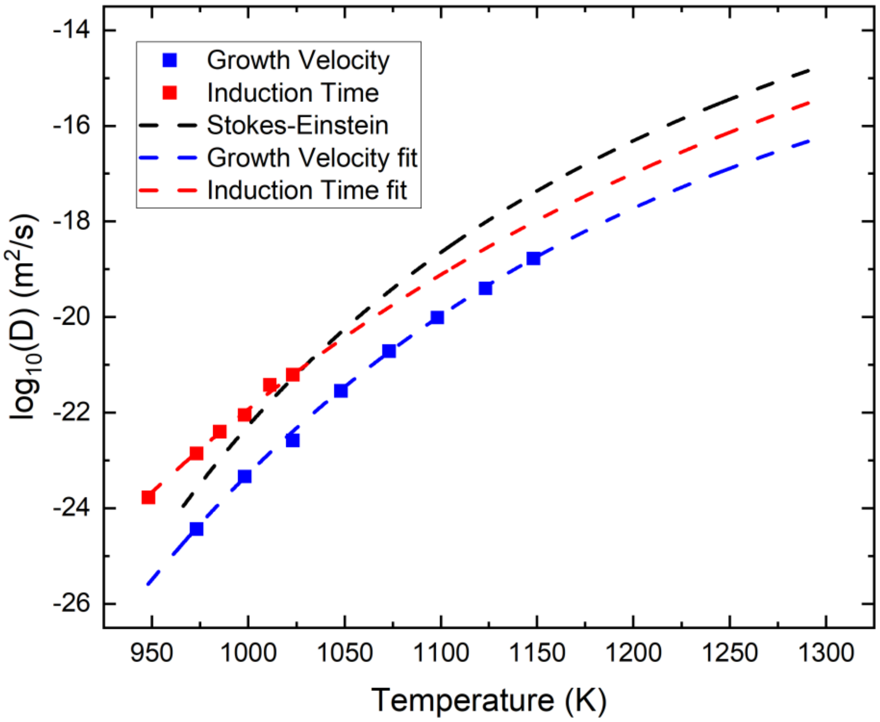

Figure 5.13 – The diffusion coefficient calculated from the growth velocity, induction time, and Stokes-Einstein equation. The fit curves are those shown in Table 5.3.

A better model of the DTA crystallization process for the $5BaO{\cdot}8SiO_2$ glass may be to use the induction time to control the nucleation process and the measured growth velocity to control the crystallization process. This combination method accounts for both the nucleation and growth processes distinctly. Figure 5.14 shows the inverse peak temperature as a function of the nucleation treatment temperature when the nucleation event is controlled by the diffusion coefficient from the induction time ($n < 30n^*$) and the crystallization process is controlled by the experimentally measured growth velocity ($n > 30n^*$). Both the magnitude and the temperature dependence of the data in fig. 5.14 match the measured inverse peak temperature data. This suggests that the nucleation process in the $5BaO{\cdot}8SiO_2$ glass may be more complicated than single monomer attachment/detachment.

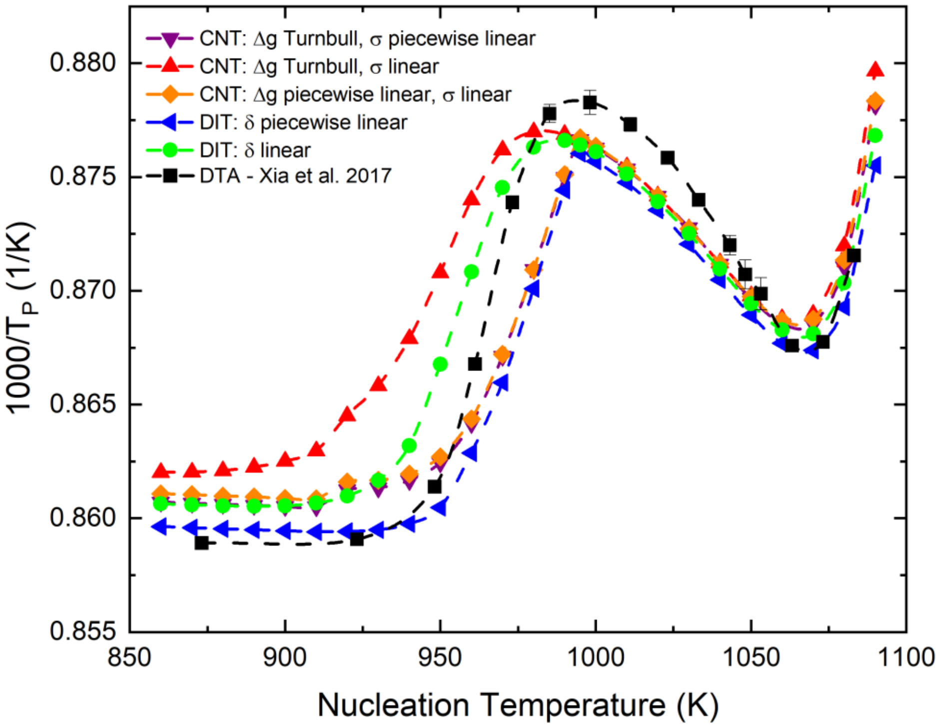

Figure 5.14 – The inverse peak temperature for the experimental and numerical DTA data for the $5BaO{\cdot}8SiO_2$ glass with the diffusion coefficient calculated from the induction time for small nuclei and the crystallization process controlled by the experimentally measured growth velocity. The errors in the experimental data are the size of the symbols[6]. The propagated errors in the numerical DTA data from the diffusion coefficient produce differences in the data smaller than the size of the symbols.

Figure 5.15 shows the measured (a) and simulated (b-f) DTA crystallization curves as a function of temperature for each of the five sets of parameters. In fig 5.15(b-f) the diffusion coefficient for small nuclei is controlled by the induction time and growth is controlled by the measured rates. It is difficult to tell from fig. 5.14 whether the low temperature anomaly is real or if it is a manifestation of experiments not reaching the steady state. In the low temperature regime, the measured inverse peak temperature curve sits between the curves that assume the low temperature steady-state data are correct and the curves that assume that the low temperature steady-state data are incorrect. However, fig. 5.15b and fig. 5.15e look more similar to the measured results (fig. 5.15a), which suggests that the low temperature anomaly may not be real.

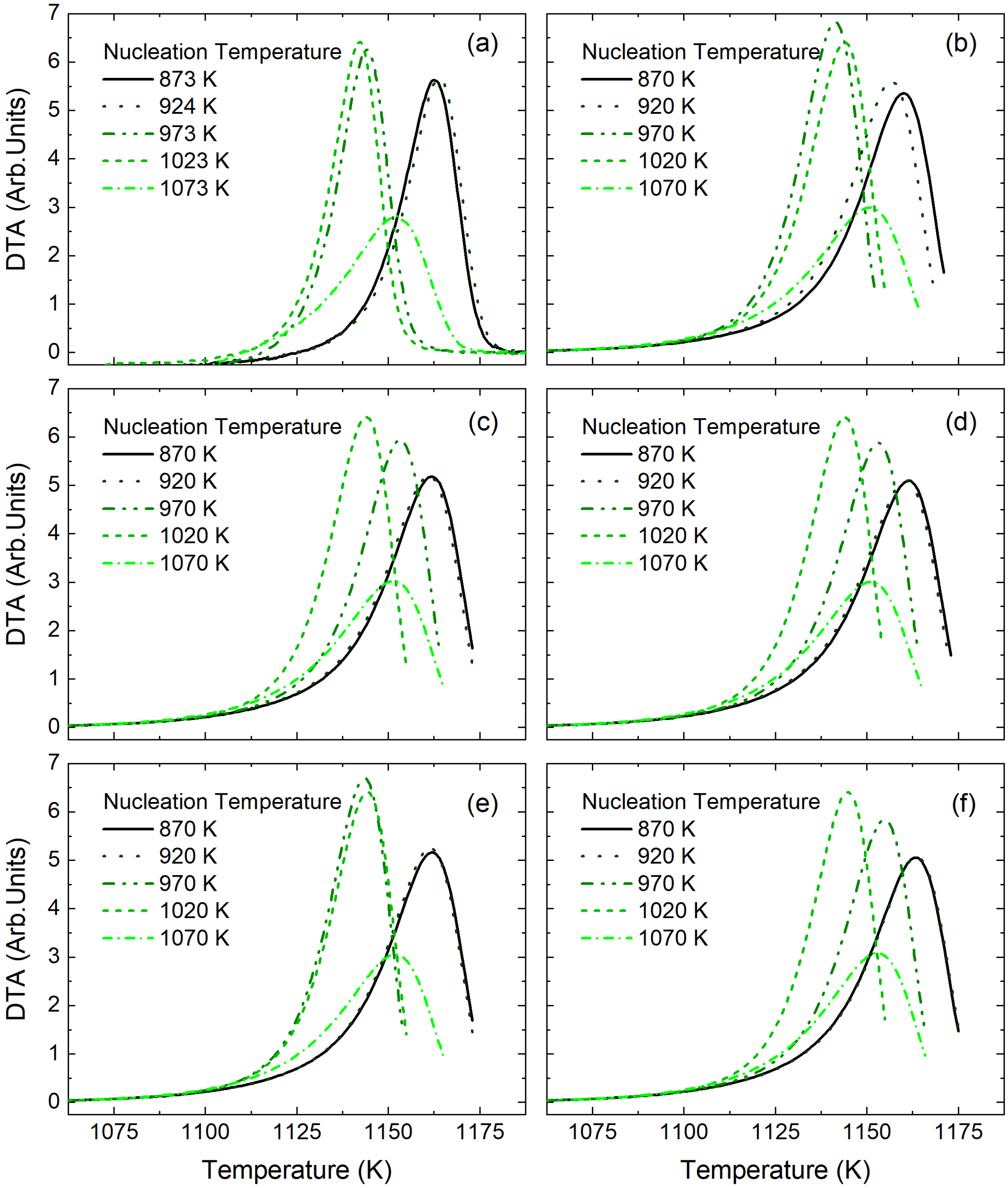

Figure 5.15 – The calculated DTA signals during a 15 K/min scan after one hour of isothermal heating at various temperatures (listed in the legend), assuming that the induction time controls diffusion for small nuclei and the measured growth velocity controls crystallization: (a) experimental data; (b) numerical calculation for the CNT, calculating the driving free energy from the Turnbull approximation, and using a linear interfacial free energy; (c) numerical calculation for the CNT, calculating the driving free energy from the Turnbull approximation, and using an anomalous interfacial free energy; (d) numerical calculation for the CNT, assuming an anomalous driving free energy, and a linear interfacial free energy; (e) numerical calculation for the DIT, assuming the interface width is linear; and (f) numerical calculation for the DIT, assuming the interface width is anomalous.

The region of significant nucleation in the $5BaO{\cdot}8SiO_2$ glass system is accurately predicted using the simulated DTA technique, just as for the barium disilicate glass. However, the nuclei grow spherically in the $5BaO{\cdot}8SiO_2$ composition. The magnitude of the inverse peak temperature curve (fig. 5.14) matches the experimental data, providing evidence that the offset shown in fig. 5.5a for the $BaO{\cdot}2SiO_2$ glass is due to non-spherical growth.

5.3.3 Cluster and Nuclei Development

The ability to numerically simulate heating schedules for nucleation in a glass provides an important tool for engineers and industrial scientists seeking to develop glasses or glass ceramics with specific properties. Using the simulation presented here, it becomes possible to determine the heating schedule required to develop specific cluster and nuclei distributions. The nuclei distributions at the end of each step in the DTA simulation for the $BaO{\cdot}2SiO_2$ glass for one isothermal hold temperature below, at, and above the maximum nucleation rate temperature are shown in fig. 5.16. This illustrates creation of as-quenched nuclei, then the development of nuclei during the isothermal hold, and finally the growth of the nuclei during the DTA scan.

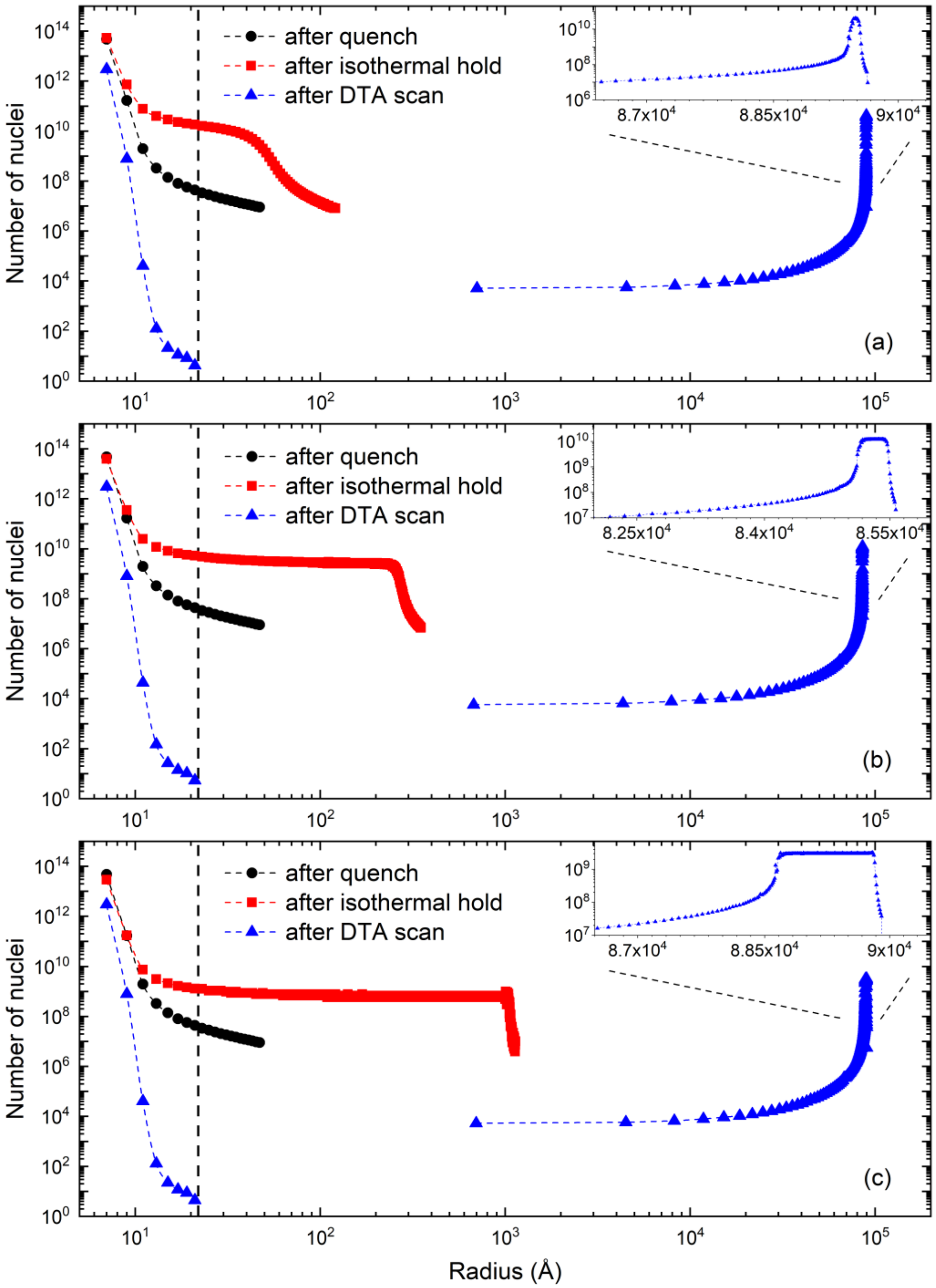

Figure 5.16 – The nuclei distribution at the end of each step in a DTA simulation using the CNT, the Turnbull approximation for the driving free energy, and the diffusion coefficient from the growth velocity. The isothermal hold temperatures were (a) 970 K, (b) 985 K, and (c) 1000 K. Each data point represents the number of nuclei per mol in a bin of width 2 Å. Because the density of data points increases with increasing radius on the log plot, insets are shown of the nuclei distribution after the DTA scan for large radii. The vertical black dashed line is the cutoff between clusters grown by the bi-molecular reaction and nuclei grown by eq. 5.7 at $10r^*$ (10 times the critical size).

5.4 Conclusions

A numerical model that takes into account time-dependent nucleation during nonisothermal heating treatments was used to quantitatively model differential thermal analysis (DTA) data in a $BaO{\cdot}2SiO_2$ glass and a $5BaO{\cdot}8SiO_2$ glass. Two nucleation models were assumed for the calculations, the classical theory of nucleation (CNT) and the diffuse interface theory (DIT). Earlier experimental studies in this glass showed that the inverse peak temperatures of a DTA scan made after a series of isothermal nucleation treatments at different temperatures gave an accurate measure of the range of significant nucleation. The calculated DTA scans assuming the CNT and the DIT confirm this. For both the CNT and the DIT, good agreement with the experimental data is obtained if the diffusion coefficient is calculated from the growth velocity or the induction time in the $BaO{\cdot}2SiO_2$ system. However, if the viscosity and the Stokes-Einstein relation are used to calculate the diffusion coefficient, the numerical results deviate markedly from the experimental data, demonstrating a breakdown of this relation. In the $5BaO{\cdot}8SiO_2$ glass, however, a combination of the induction time and growth velocity are required to match the experimental data. This suggests that assuming that the large $5BaO{\cdot}8SiO_2$ monomer attaches/detaches to form the critical nuclei may not be an accurate picture. However, because the $5BaO{\cdot}8SiO_2$ nuclei are spherical, the magnitude of the inverse peak temperature plot matches the experimental results better than in the $BaO{\cdot}2SiO_2$ system where nuclei are not spherical.

For the sizes of particles studied in this work, the numerical simulations show that surface crystallization does not play a role in determining the peak crystallization temperature during a DTA scan. The numerical model was used to investigate, for the first time (to our knowledge), the sensitivity of the DTA technique to the scan rate. While the actual crystallization peak temperature changes as a function of the scan rate, the temperature range for significant nucleation remains the same, demonstrating more broadly the validity of the DTA method.

5.5 Acknowledgements

This research was partially funded by the National Science Foundation under grant DMR 17-20296 and Corning Inc.

5.6 References

1. Van Hoesen, D. C., Xia, X., McKenzie, M. E. & Kelton, K. F. Modeling nonisothermal crystallization in a BaO·2SiO 2 glass. *J. Am. Ceram. Soc.* (2020). doi:10.1111/jace.16979

2. Kelton, K. F. & Greer, A. L. Crystallization in Glasses. in *Nucleation in Condensed Matter: Applications in Materials and Biology* 279–329 (Elsevier, 2010).

3. Kelton, K. F. Estimation of the Nucleation Rate by Differential Scanning Calorimetry. *J. Am. Ceram. Soc.* **75**, 2449–2452 (1992).

4. Ray, C. S. & Day, D. E. Nucleation and Crystallization in Glasses as Determined by DTA. *J. Am. Ceram. Soc.* **30**, 207–223 (1993).

5. Ray, C. S. & Day, D. E. Determining the Nucleation Rate Curve for Lithium Disilicate Glass by Differential Thermal Analysis. *J. Am. Ceram. Soc.* **73**, 439–442 (1990).

6. Xia, X., Dutta, I., Mauro, J. C., Aitken, B. G. & Kelton, K. F. Temperature dependence of crystal nucleation in BaO.2SiO2 and 5BaO.8SiO2 glasses using differential thermal analysis. *J. Non. Cryst. Solids* **459**, 45–50 (2017).

7. Ray, C. S., Fang, X. & Day, D. E. New method for determining the nucleation and crystal-growth rates in glasses. *J. Am. Ceram. Soc.* **83**, 865–872 (2000).

8. Ranasinghe, K. S., Ray, C. S. & Day, D. E. A generalized method for determining the crystal nucleation and growth rates in glasses. *J. Mater. Sci.* **37**, 547–555 (2002).

9. Fokin, V. M., Cabral, A. A., Reis, R. M. C. V., Nascimento, M. L. F. & Zanotto, E. D. Critical assessment of DTA-DSC methods for the study of nucleation kinetics in glasses. *J. Non. Cryst. Solids* **356**, 358–367 (2010).

10. Kelton, K. F., Narayan, K. L., Levine, L. E., Cull, T. S. & Ray, C. S. Computer modeling of non-isothermal crystallization. *J. Non. Cryst. Solids* **204**, 13–31 (1996).

11. Ray, C. S. *et al.* Non-isothermal calorimetric studies of the crystallization of lithium disilicate glass. *J. Non* **204**, 1–12 (1996).

12. Gránásy, L. Diffuse interface theory of nucleation. *J. Non. Cryst. Solids* **162**, 301–303

(1993).

13. Gránásy, L. Diffuse Interface Approach to Vapor Condensation. *Europhys. Lett.* **24**, 121–126 (1993).

14. Spaepen, F. Homogeneous nucleation and the temperature dependence of the crystal melt interfacial tension. in *Solid State Physics* (eds. Ehrenreich, H. & Turnbull, D.) 1–32 (Academic Press, 1994).

15. Abyzov, A. S., Fokin, V. M., Rodrigues, A. M., Zanotto, E. D. & Schmelzer, J. W. P. The effect of elastic stresses on the thermodynamic barrier for crystal nucleation. *J. Non. Cryst. Solids* **432**, 325–333 (2016).

16. Fokin, V. M. *et al.* Crystal nucleation in glass-forming liquids: Variation of the size of the "structural units" with temperature. *J. Non. Cryst. Solids* **447**, 35–44 (2016).

17. Xia, X. *et al.* Time-dependent nucleation rate measurements in BaO·2SiO2 and 5BaO·8SiO2 glasses. *J. Non. Cryst. Solids* **525**, (2019).

18. Kelton, K. F., Greer, A. L. & Thompson, C. V. Transient nucleation in condensed systems. *J. Chem. Phys.* **79**, (1983).

19. Kelton, K. F. & Greer, A. L. Transient Nucleation Effects in Glass Formation. *J. Non. Cryst. Solids* **79**, 295–309 (1986).

20. Kelton, K. F. Crystal Nucleation in Liquids and Glasses. *Solid State Phys.* **45**, 75–177 (1991).

21. Kelton, K. F. Numerical model for isothermal and non-isothermal crystallization of liquids and glasses. *J. Non. Cryst. Solids* **163**, 283–296 (1993).

22. Levine, L. E., Narayan, K. L. & Kelton, K. F. Finite size corrections for the Johnson-Mehl-Avrami-Kolmogorov equation. *J. Mater. Res.* **12**, 124–132 (1997).

23. Bagdassarian, C. K. & Oxtoby, D. W. Crystal nucleation and growth from the undercooled liquid: A nonclassical piecewise parabolic free-energy model. *J. Chem. Phys.* **100**, (1994).

24. Kelton, K. F. & Greer, A. L. The Classical Theory. in *Nucleation in Condensed Matter: Applications in Materials and Biology* 19–54 (Elsevier, 2010).

25. Nascimento, M. L. F., Fokin, V. M., Zanotto, E. D. & Abyzov, A. S. Dynamic processes in a silicate liquid from above melting to below the glass transition. *J. Chem. Phys.* **135**, (2011).

26. Rodrigues, A. M., Cassar, D. R., Fokin, V. M. & Zanotto, E. D. Crystal growth and viscous flow in barium disilicate glass. *J. Non. Cryst. Solids* **479**, 55–61 (2018).

27. Kashchiev, D. Solution of the Non-Steady State Poblem in Nucleaiton Kinetics. *Surf. Sci.* **14**, 209–220 (1969).

28. Johnson, W. A. & Mehl, R. F. Reaction Kinetics in Processes of Nucleation and Growth. *Am. Inst. Min. Metall. Eng.* **135**, 416–442 (1939).

29. Avrami, M. Kinetics of Phase Change. I General Theory. *J. Chem. Phys.* **7**, (1939).

30. Avrami, M. Kinetics of Phase Change. II Transformation-Time Relations for Random Distribution of Nuclei. *J. Chem* **8**, (1940).

31. Avrami, M. Granulation, Phase Change, and Microstructure Kinetics of Phase Change. III. *J. Chem. Phys.* **9**, (1941).

32. Kolmogorov, N. A. A statistical theory for the recrystallization of metals. *Izu. Akad. Nauk SSSR* **3**, 355–359 (1937).

33. Zanotto, E. D. & James, P. F. Experimental tests of the classical nucleation theory for glasses. *J. Non. Cryst. Solids* **74**, 373–394 (1985).

34. James, P. F. & Rowlands, E. G. Kinetics of crystal nucleation and growth in barium disilicate glass. in *Phase Transformations* **2**, 27–29 (The Institution of Metallurgists, Northway House, 1979).

35. Fokin, V. M., Kalinina, A. M. & Filipovich, V. N. Nucleation in silicate glasses and effect of preliminary heat treatment on it. *J. Cryst. Growth* **52**, 115–121 (1981).

36. Deubener, J., Brückner, R. & Sternitzke, M. Induction time analysis of nucleation and crystal growth in di- and metasilicate glasses. *J. Non. Cryst. Solids* **163**, 1–12 (1993).

37. Barker, M. F., Wang, T.-H. & James, P. F. Nucleation and growth kinetics of lithium disilicate and lithium metasilicate in lithia-silica glasses. *Phys. Chem. Glas.* **29**, 240–248 (1988).

38. Kivelson, D., Kivelson, S. A., Zhao, X., Nussinov, Z. & Tarjus, G. A thermodynamic theory of supercooled liquids. *Physica A* **219**, 27–38 (1995).

39. Tarjus, G., Kivelson, S. A., Nussinov, Z. & Viot, P. The frustration-based approach of supercooled liquids and the glass transition : a review and critical assessment. *J. Phys. Condens. Matter* **17**, (2005).

40. Nussinov, Z. Avoided phase transitions and glassy dynamics in geometrically frustrated systems and non-Abelian theories. *Phys. Rev. B* **69**, (2004).

41. Xiaojie, J. X., Chandra, S. R. & Delbert, E. D. Nucleation and Crystallization of Na2O. 2CaO. 3Si02 Glass by Differential Thermal Analysis. *J. Am. Ceram. Soc.* **14**, 909–914 (1991).

42. Abyzov, A. S., Fokin, V. M., Yuritsyn, N. S., Rodrigues, A. M. & Schmelzer, J. W. P. The effect of heterogeneous structure of glass-forming liquids on crystal nucleation. *J. Non. Cryst. Solids* **462**, 32–40 (2017).

43. Gupta, P. K., Cassar, D. R. & Zanotto, E. D. Role of dynamic heterogeneities in crystal

nucleation kinetics in an oxide supercooled liquid. *J. Chem. Phys.* **145**, (2016).

44. Schmelzer, J. W. P. & Abyzov, A. S. Crystallization of glass-forming liquids: Thermodynamic driving force. *J. Non. Cryst. Solids* **449**, 41–49 (2016).

45. Cassar, D. R., Serra, A. H., Peitl, O., Rodrigues, A. M. & Zanotto, E. D. The failure of the Classical Nucleation Theory at low temperatures resolved. *arXiv:1902.03193v1* (2019).

46. Lenoir, M., Grandjean, A., Linard, Y., Cochain, B. & Neuville, D. R. The influence of Si, B substitution and of the nature of network-modifying cations on the properties and structure of borosilicate glasses and melts. *Chem. Geol.* **256**, 316–325 (2008).

47. Fokin, V. M. *et al.* Effect of non-stoichiometry on the crystal nucleation and growth in oxide glasses. *Acta Mater.* **180**, 317–328 (2019).

48. Kalinina, A. M., Filipovich, V. N. & Fokin, V. M. Stationary and non-stationary crystal nucleation rate in a glass of 2Na2O.CaO.3SiO2 stiochiometric composition. *J. Non. Cryst. Solids* **38** & **39**, 723–728 (1980).

49. Mauro, J. C., Yue, Y., Ellison, A. J., Gupta, P. K. & Allan, D. C. Viscosity of glass-forming liquids. *Proc. Natl. Acad. Sci.* **106**, 19780–19784 (2009).

50. Zheng, Q., Mauro, J. C., Ellison, A. J., Potuzak, M. & Yue, Y. Universality of the high-temperature viscosity limit of silicate liquids. *Phys. Rev. B* **83**, (2011).

Chapter 6: Absorption and Secondary Scattering of X-rays with an Off-Axis Small Beam for a Cylindrical Sample Geometry

The work in this chapter is published in Van Hoesen, D. C. *et al.*, "*Absorption and secondary scattering of X-rays with an off-axis small beam for a cylindrical sample geometry*," Acta Crystallographica Section A. **75**, 362-369, (2019)[1]. Figures and text are reproduced with permission from the IUCr Journals.

Expressions for X-ray absorption and secondary scattering are developed for cylindrical sample geometries. The incident beam size is assumed to be smaller than the sample and in general directed off-axis onto the cylindrical sample. It is shown that an offset beam has a non-negligible effect on both the absorption and multiple scattering terms, resulting in an asymmetric correction that must be applied to the measured scattering intensities. The integral forms of the corrections are first presented. A small beam limit is then developed for easier computation.

6.1 Introduction

Understanding the structure of glasses and liquids, and how that structure changes with temperature and time, is important for understanding processes such as structural relaxation, topological ordering, and chemical ordering. The local amorphous structure has also been demonstrated to couple to the crystal nucleation barrier[2,3]. If the local structures of the liquid or glass and the primary nucleating phase are similar, nucleation will be promoted; if the structures are different it will be inhibited. It has been demonstrated recently that topological ordering in the liquid and glass also couples with the shear viscosity[4–7]. The subtle changes are small, however, making it essential that X-ray or neutron scattering data be analysed carefully, taking proper account of sample geometry.

The importance of the effects of absorption and multiple scattering are well known and the general steps to correct scattering experiments have been discussed[8,9]. However, the software packages used to process x-ray scattering experiments are not capable of accounting for every geometry and beam parameter. Correction methods for planar geometries have been developed for both transmission and reflection scenarios[10–12] as well as spherical geometries[13–15]. However, samples are often contained in capillaries, requiring correction methods for cylindrical sample geometries. Absorption corrections for this geometry have been developed for several cases, including those when the beam fully encompasses the sample[16], the beam has limited width[17], for isotropic scattering[18], and for an inclined beam through an infinite cylinder[19]; the Paalman and Pings[16] study is most frequently cited. The study by Blech and Averbach is most frequently cited for multiple scattering corrections for cylindrical sample geometries[20]. However, this paper neither considers the realistic case of a finite beam size, or cases where the beam is not centered on the sample. It should also be noted that Monte Carlo integration can be used to account for a wide range of absorption and multiple scattering scenarios, but this method is computationally costly[21].

Here more generalized expressions for absorption and secondary scattering for a cylindrical sample geometry are given for the two cases when the sample is larger than the beam and the beam is transmitted through the sample off-center from the cylindrical axis. This development follows earlier work for the case of spherical amorphous samples with an off-axis beam [15].

6.2 Theory

While the introductory theory for absorption and multiple scattering of a generalized geometry and material is described elsewhere[15], a few concepts are reviewed for reference. The infinitesimal scattered intensity, dI, at a distance r from scattering volume dV is given by

$$dI(r, 2\theta, \phi) = I_0 \left(\frac{\sigma_e n}{r^2}\right) P(\kappa_0, 2\theta, \phi)\, J(2\theta) dV, \tag{6.1}$$

where σ_e is the differential Thomson scattering cross section for electrons, n is the number density of the scattering sample, $P(\kappa_0, 2\theta, \phi)$ accounts for polarization effects, and $J(2\theta)$ is the first order approximation to the scattering intensity. The intensities of both the incident and scattered beams are attenuated on passing through the sample according to Beer's law, $I(r) = I_0 \exp{(-\mu r)}$, which must be considered in the integration of eq. 6.1. The experimentally measured intensities are, therefore multiplied by an absorption correction factor V/V', where V is the volume of intersection between the beam and the sample and V' $(= \iiint \exp(-\mu r)\, dV)$ is the effective volume of intersection between the beam and the sample. Elastic scattering is assumed, i.e. there is no change in μ for the scattered beam.

Secondary scattering is also considered in the form of a multiplicative factor, $(1 + I_2/I_1)^{-1}$, where I_1 is the intensity of the beam after a single scattering event and I_2 is the intensity of the beam after the second scattering event. While there are actually multiple scattering events, the probability of these becomes significantly less, so only secondary scattering need be considered as a correction. Multiplying the sum of scattering events, $I_1 + I_2$, by the factor above recovers the primary scattering intensity, I_1. Integrating eq. 6.1 for the first scattering event, considering the attenuated scattering volume, gives

$$I_1 = \frac{I_0 \sigma_e n}{r^2} P(\kappa_0, 2\theta, \phi) \; J(2\theta) \; V'. \tag{6.2}$$

6.2.1 Absorption Correction

Assume a rectangular beam of height a and width b intersecting a cylindrical sample (fig. 6.1), with the center of the beam offset from the center of the cylinder by a distance l in the y-direction and a distance l_h in the z-direction.

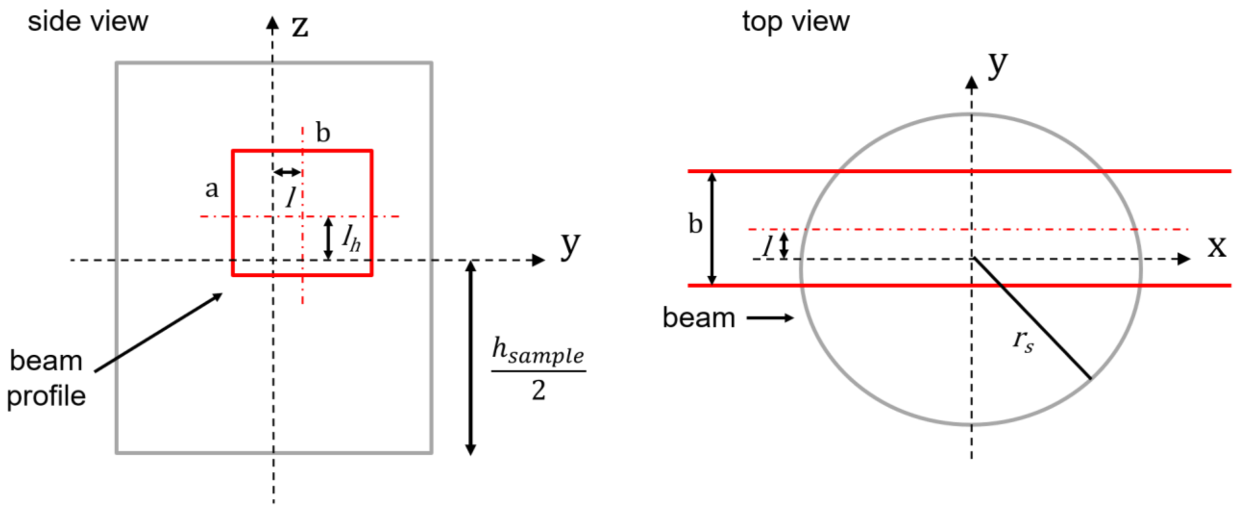

Figure 6.1 – Diagram of the sample geometry and the beam profile.

Consider first, a cylinder of infinite height. When the beam profile does not encounter the top and bottom of the cylinder the intersection volume is

$$V = \int_{l_h - \frac{a}{2}}^{l_h + \frac{a}{2}} dz \int_{-\left(\frac{b}{2} - l\right)}^{\frac{b}{2} + l} dy \int_{-\sqrt{r_s^2 - y^2}}^{\sqrt{r_s^2 - y^2}} dx \, . \tag{6.3}$$

The effective intersection volume, considering attenuation of the beam, is

$$V' = \int_{l_h-\frac{a}{2}}^{l_h+\frac{a}{2}} dz \int_{-\left(\frac{b}{2}-l\right)}^{\frac{b}{2}+l} dy \int_{-\sqrt{r_s^2-y^2}}^{\sqrt{r_s^2-y^2}} dx \exp\left[-\mu\left(\sqrt{r_s^2-y^2}+x+R(2\theta,\phi,x,y,z)\right)\right]. \tag{6.4}$$

The beam first travels a distance $\sqrt{r_s^2-y^2}+x$ in the x-direction before a scattering event at the point (x_0, y_0, z_0). The beam then travels an additional $R(2\theta, \phi, x_0, y_0, z_0)$ distance to the edge of the cylinder, causing the detection of an event on the detector at 2θ and ϕ. Similar to the method of Sulyanov *et al.*, 2012, the value for R is calculated by constraining spherical coordinates to the edge of the cylinder. Edge points on the cylinder are given by

$$\begin{aligned} x_e &= x_0 + R\cos(2\theta) \\ y_e &= y_0 + R\sin(2\theta)\ \cos(\phi) \\ z_e &= z_0 + R\sin(2\theta)\ sin(\phi). \end{aligned} \tag{6.5}$$

R is found by constraining the equations by $r_s^2 = x_e^2 + y_e^2$,

$$R = \frac{-(x_0\, cos(2\theta) + y_0\, p) + \sqrt{(x_0\, cos(2\theta) + y_0\, p)^2 - (x_0^2 + y_0^2 - r_s^2)(\cos(2\theta)^2 + p^2)}}{\cos(2\theta)^2 + p^2}, \tag{6.6}$$

where $p = \sin(2\theta)\cos(\phi)$. For a cylinder of finite height, there are cases when the scattered beam exits the top or bottom of the cylinder, as shown in fig. 6.2. For this case, the value of R from eq. 6.6 will be for point (x', y', z') outside the sample instead of (x_e, y_e, z_e) (see fig. 6.2). For correctly accounting for sample absorption, R is constrained between the values $h_{sample}/2 = z_0 + R\sin(2\theta)\sin(\phi)$ and $-h_{sample}/2 = z_0 + R\sin(2\theta)\sin(\phi)$. Also, from eq. 6.6, R becomes infinite if $\cos(2\theta)^2 + p^2 = 0$, since the beam is scattered in the $\pm$ z-direction. For this case, R becomes equal to the distance from z_0 to the top or bottom of the cylinder.

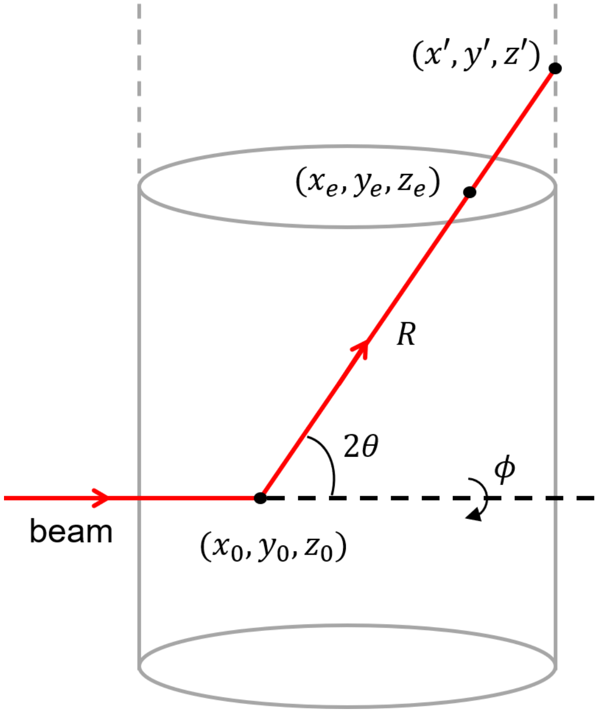

Figure 6.2 – Scattering event at point (x_0, y_0, z_0) inside the cylindrical sample leading to the beam, cylinder wall intersection at point (x', y', z') above the cylinder. The distance the beam travels inside the sample is the distance from point (x_0, y_0, z_0) to point (x_e, y_e, z_e).

Taking account of these points the scattered beam path, $R\big(2\theta, \phi, x_0, y_0, z_0, h_{sample}\big)$, for a finite cylinder is

$$R = \begin{cases} \dfrac{-(x_0\, cos(2\theta) + y_0\, p) + \sqrt{\big((x_0\, cos(2\theta) + y_0\, p)^2 - (x_0^2 + y_0^2 - r_s^2)(\cos(2\theta)^2 + p^2)\big)}}{\cos(2\theta)^2 + p^2} \\ \qquad \text{for} \quad -h_{sample}/2 < z_{\mathrm{e}} < h_{sample}/2 \\ \dfrac{\frac{h_{sample}}{2} - z_0}{\sin(2\theta)\sin(\phi)} \quad \text{for} \quad z_{\mathrm{e}} > \dfrac{h_{sample}}{2} \\ -\dfrac{\frac{h_{sample}}{2} + z_0}{\sin(2\theta)\sin(\phi)} \quad \text{for} \quad z_{\mathrm{e}} < -\dfrac{\mathrm{h_{sample}}}{2}. \end{cases} \tag{6.7}$$

For faster computation, the attenuated volume integration (eq. 6.3 and eq. 6.4) can be simplified in the small beam limit. Two of the three integrals in eq. 6.4 are reduced, giving the effective scattering volume as

$$V' = ab \int_{-\sqrt{r_s^2 - l^2}}^{\sqrt{r_s^2 - l^2}} dx \ \exp\left[-\mu\left(\sqrt{r_s^2 - l^2} + x + R(2\theta, \phi, x, l, l_h)\right)\right]. \tag{6.8}$$

As $2\theta \to 0$, for $-h_{sample}/2 < z_e < h_{sample}/2$, and $a, b \to 0$ the asymptotic calculation reduces significantly and can be expressed in terms of unitless sample fractions, $l_s = l/r_s$, $x_s = x/r_s$, $R_s = R/r_s$, and μr_s. The effective scattering volume is then

$$V' = abr_s \exp\left[-\mu r_s\sqrt{1 - l_s^2}\right] \int_{-\sqrt{1-l_s^2}}^{\sqrt{1-l_s^2}} dx_s \ \exp[-\mu r_s(x_s + R_s(2\theta, \phi, x_s))], \tag{6.9}$$

where

$$R_s = \frac{-(x_s\, cos(2\theta) + l_s\, p) + \sqrt{\left((x_s\, cos(2\theta) + l_s\, p)^2 - (x_s^2 + l_s^2 - 1)(\cos(2\theta)^2 + p^2)\right)}}{\cos(2\theta)^2 + p^2}. \tag{6.10}$$

For $V = 2abr_s$, the asymptotic expansion of the off-axis absorption correction (V/V') is

$$\frac{V}{V'} \approx \frac{\exp\left(2\mu r_s\sqrt{1 - l_s^2}\,\right)}{\sqrt{1 - l_s^2}} \times \sum_{i=0}^{\infty} A_i(\mu r_s, l_s, \phi)(2\theta)^i\,, \tag{6.11}$$

with the first five coefficients listed in Table 6.1. Equation 6.8 is easily solved when $z_e < -h_{sample}/2$ and $h_{sample}/2 < z_e$, because R takes on the much simpler form as shown above. It is important to note that in the small beam limit, at $\phi = 0$ and $\phi = \pi$ the cylindrical absorption correction is equivalent to the spherical absorption correction derived earlier[15].

Table 6.1 – Coefficients for the expansion of the cylindrical absorption correction

i	A_i
0	1
1	$-\mu r_s l_s \cos(\phi)$
2	$\begin{aligned} &\frac{-\mu r_s}{6(l_s^2-1)}\Big[-2\mu r_s l_s^4 \cos(\phi)^2 + 2\mu r_s l_s^2 \cos(\phi)^2 + 6\sqrt{1-l_s^2}\, l_s^2 \cos(\phi)^2 \\ &\quad - 3\sqrt{1-l_s^2}\, l_s^2 - 4\sqrt{1-l_s^2} \cos(\phi)^2 + 3\sqrt{1-l_s^2}\, \Big] \end{aligned}$
3	$\begin{aligned} &\frac{\mu r_s l_s \cos(\phi)}{6(l_s^2-1)}\Big[4\mu r_s l_s^2 \cos(\phi)^2 \sqrt{1-l_s^2} + 6 l_s^2 \cos(\phi)^2 - 2\mu r_s \sqrt{1-l_s^2}\, l_s^2 - 5 l_s^2 \\ &\quad + 2\mu r_s \sqrt{1-l_s^2} - 2\mu r_s \sqrt{1-l_s^2} \cos(\phi)^2 + 5 - 6\cos(\phi)^2 \Big] \end{aligned}$
4	$\begin{aligned} &\frac{-\mu r_s}{360(l_s^2-1)}\Big[8(\mu r_s)^3 l_s^6 \cos(\phi)^4 + 30\mu r_s l_s^4 - 320\mu r_s l_s^4 \cos(\phi)^2 \\ &\quad - 8(\mu r_s)^3 l_s^4 \cos(\phi)^4 + 360\mu r_s l_s^4 \cos(\phi)^4 - 75\sqrt{1-l_s^2}\, l_s^2 \\ &\quad + 32(\mu r_s)^2 l_s^2 \cos(\phi)^4 \sqrt{1-l_s^2} - 60\mu r_s l_s^2 - 360\sqrt{1-l_s^2} \cos(\phi)^4 l_s^2 \\ &\quad + 420\sqrt{1-l_s^2}\, l_s^2 \cos(\phi)^2 - 336\mu r_s l_s^2 \cos(\phi)^4 + 380\mu r_s l_s^2 \cos(\phi)^2 \\ &\quad + 75\sqrt{1-l_s^2} + 216\sqrt{1-l_s^2} \cos(\phi)^4 - 60\mu r_s \cos(\phi)^2 + 30\mu r_s \\ &\quad + 16\mu r_s \cos(\phi)^4 - 280\sqrt{1-l_s^2} \cos(\phi)^2\Big] \end{aligned}$
5	$\begin{aligned} &\frac{-\mu r_s l_s \cos(\phi)}{360(l_s^2-1)}\Big[-16(\mu r_s)^3 l_s^4 \cos(\phi)^2 \sqrt{1-l_s^2} + 32(\mu r_s)^3 l_s^4 \cos(\phi)^4 \sqrt{1-l_s^2} \\ &\quad + 480\mu r_s l_s^2 \cos(\phi)^4 \sqrt{1-l_s^2} - 88(\mu r_s)^2 l_s^2 \cos(\phi)^4 \\ &\quad - 24(\mu r_s)^3 l_s^2 \cos(\phi)^4 \sqrt{1-l_s^2} + 32(\mu r_s)^2 l_s^2 \cos(\phi)^2 \\ &\quad + 16(\mu r_s)^3 l_s^2 \cos(\phi)^2 \sqrt{1-l_s^2} + 360\cos(\phi)^4 l_s^2 + 183 l_s^2 \\ &\quad + 150\mu r_s \sqrt{1-l_s^2}\, l_s^2 - 540 l_s^2 \cos(\phi)^2 - 600\mu r_s l_s^2 \cos(\phi)^2 \sqrt{1-l_s^2} \\ &\quad - 183 + 540\cos(\phi)^2 + 348\mu r_s \sqrt{1-l_s^2} \cos(\phi)^2 \\ &\quad + 48(\mu r_s)^2 \cos(\phi)^4 - 150\mu r_s \sqrt{1-l_s^2} - 192\mu r_s \cos(\phi)^4 \sqrt{1-l_s^2} \\ &\quad - 360\cos(\phi)^4 - 32(\mu r_s)^2 \cos(\phi)^2\Big] \end{aligned}$

6.2.2 Secondary Scattering Correction

The path steps for the beam in the sample when multiple scattering is considered are listed below and illustrated in fig. 6.3.

1. beam enters the sample traveling in the x-direction
2. beam scatters at point (x_0, y_0, z_0) with scattering angles $2\theta_1$ and ϕ_1
3. beam travels distance r_1 to point (x_1, y_1, z_1)
4. beam scatters at point (x_1, y_1, z_1) with scattering angles $2\theta_2$ and ϕ_2
5. beam travels distance $R(2\theta, \phi, x_1, y_1, z_1)$ to the sample edge at point (x_e, y_e, z_e)

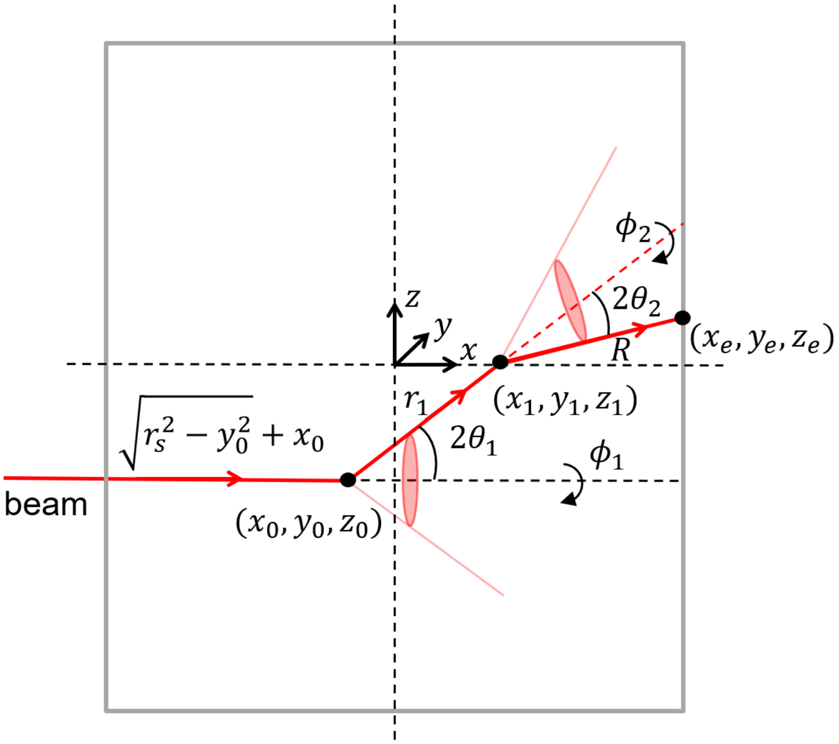

Figure 6.3 – Multiple scattering steps showing two scattering events.

When the detector is far from the sample, the three sets of scattering angles are related by a $2\theta_1$ rotation about the z-axis and a ϕ_1 rotation about the x-axis. These are found given a point on the detector $(2\theta, \phi)$ and the first scattering angles $2\theta_1$ and ϕ_1[15].

Equation 6.1 only considers the first scattering event. The infinitesimal scattering intensity of the second event is

$$dI_2 = \frac{I_0 n^2 \sigma_e^2}{r_1^2 r_2^2}\ P(\kappa_0, 2\theta_1, \phi_1)\, J(2\theta_1)\, P(\kappa_1, 2\theta_2, \phi_2)\ J(2\theta_2) \exp(-\mu(r_1 + r_2))\ dV_1\, dV_2. \quad (6.12)$$

This must be integrated over two volumes. The first is the volume intersection of the beam with the sample. The second is the volume of the cone produced by the first scattering event, defined by sweeping out the angles $2\theta_1$ and ϕ_1. It is important to note that the polarization changes after the first scattering event giving $P(\kappa_1, 2\theta_2, \phi_2)$ (see Bendert *et al.*, 2013). The first volume is given in eq. 6.4. The second volume is

$$V_2 = \int_0^{\pi} \sin(2\theta_1)\, d2\theta_1 \int_0^{2\pi} d\phi_1 \int_0^{R(2\theta_1,\, \phi_1, x, y, z)} r_1^2\, dr_1\,. \quad (6.13)$$

Integrating eq. 6.12,

$$\begin{aligned} I_2 = \frac{I_0 n^2 \sigma_e^2}{r^2} \int_{l_h - \frac{a}{2}}^{l_h + \frac{a}{2}} dz \int_{-\left(\frac{b}{2} + l\right)}^{\frac{b}{2} - l} dy \int_{-\sqrt{r_s^2 - y^2}}^{\sqrt{r_s^2 - y^2}} dx \int_0^{\pi} \sin(2\theta_1)\, d2\theta_1 \int_0^{2\pi} d\phi_1 \int_0^{R(2\theta_1,\, \phi_1, x, y, z)} dr_1 \\ \times P(\kappa_0, 2\theta_1, \phi_1)\ J(2\theta_1)\ P(\kappa_1, 2\theta_2, \phi_2)\ J(2\theta_2) \quad (6.14) \\ \times \exp\left[-\mu\left(x + \sqrt{r_s^2 - y^2} + r_1 + R(2\theta, \phi, x_1, y_1, z_1)\right)\right], \end{aligned}$$

where r_1 defines the distance from the first scattering point to the second scattering point and the bound on r_1 is defined by the distance from the first scattering point to the edge of the sample. The positions $x_1, y_1,$ and z_1 are given by

$$\begin{aligned} x_1 &= x_0 + r_1 \cos(2\theta_1) \\ y_1 &= y_0 + r_1 \sin(2\theta_1) \cos(\phi_1) \quad (6.15) \\ z_1 &= z_0 + r_1 \sin(2\theta_1)\, sin(\phi_1). \end{aligned}$$

The self-scattering intensity is used for $J(2\theta)$ here. Additional approximations and discussions of the accuracy for $J(2\theta)$ are summarized elsewhere[10,12,15,22]. While the secondary scattering correction is complete with I_2/I_1, it is computationally expensive to solve the integrals required to find I_2. If we again take the small beam limit, eq. 6.14 becomes

$$\begin{aligned} I_2 = \frac{I_0 n^2 \sigma_e^2 ab}{r^2} \int_{-\sqrt{r_s^2-l^2}}^{\sqrt{r_s^2-l^2}} dx \int_0^{\pi} \sin(2\theta_1)\, d2\theta_1 \int_0^{2\pi} d\phi_1 \int_0^{R(2\theta_1,\,\phi_1,x,l,h_{beam})} dr_1 \\ \times P(\kappa_0, 2\theta_1, \phi_1)\ J(2\theta_1)\ P(\kappa_1, 2\theta_2, \phi_2)\ J(2\theta_2) \\ \times \exp\left[-\mu\left(x + \sqrt{r_s^2 - l^2} + r_1 + R(2\theta, \phi, x_1, y_1, z_1)\right)\right], \end{aligned} \tag{6.16}$$

and a simpler approximation results,

$$\begin{aligned} \frac{I_2}{I_1} = \frac{n\sigma_e V}{2r_s\, P(\kappa_0, 2\theta, \phi)\, J(2\theta, \phi)\, V'} \int_{-\sqrt{r_s^2-l^2}}^{\sqrt{r_s^2-l^2}} dx \int_0^{\pi} \sin(2\theta_1)\, d2\theta_1 \int_0^{2\pi} d\phi_1 \int_0^{R(2\theta_1,\,\phi_1,x,l,h_{beam})} dr_1 \\ \times P(\kappa_0, 2\theta_1, \phi_1)\ J(2\theta_1)\ P(\kappa_1, 2\theta_2, \phi_2)\ J(2\theta_2) \\ \times \exp\left[-\mu\left(x + \sqrt{r_s^2 - l^2} + r_1 + R(2\theta, \phi, x_1, y_1, z_1)\right)\right]. \end{aligned} \tag{6.17}$$

6.3 Results and Discussion

Three elements, Au, Zr, and Si, which have dramatically different attenuation coefficients, are selected to illustrate the results of absorption and multiple scattering of a small beam for a cylindrical sample geometry. A non-polarized beam ($\kappa_0 = 0$) is assumed for the calculations. Figure 4 shows the dependence of the sample height on secondary scattering (I_2/I_1) from an Au sample as a function of the ratio of cylinder height to radius (h_s/r_s). It is assumed for these calculations that the incident beam has no offset ($l_s = 0$) and that $\phi = 0$. As observed, the effect of the sample height only becomes significant when the radius of the sample becomes larger than the height. The following discussions will focus on the case when the height of the cylinder is significantly larger than the radius as is the case for most X-ray experiments.

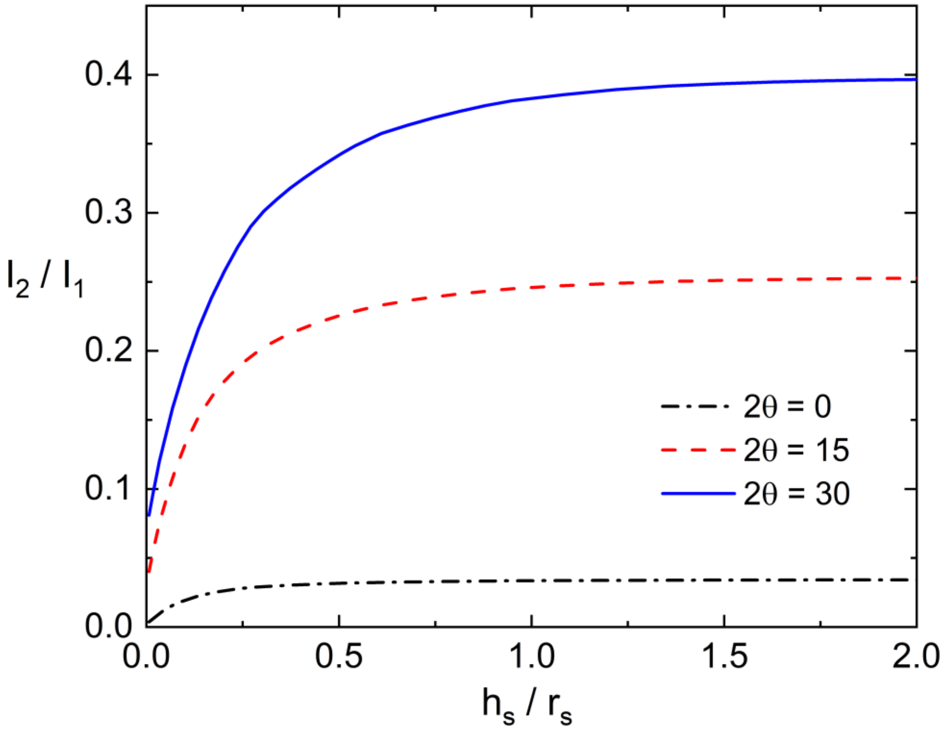

Figure 6.4 – Dependence of the cylinder height on secondary scattering intensity for Au at multiple 2θ angles with $2\mu r_s = 10$, $l_s = 0$, $\lambda = 0.1$Å, and $\phi = 0$.

The attenuation coefficient is strongly dependent on the energy of the incident photons. The changes in the multiple scattering correction in the cylindrical Zr sample for several values of the wavelength of the incident beam are shown in fig. 6.5. They are compared with the result for a spherical sample, using the corrections developed by Bendert *et al*., 2013. Low energy photons have a small multiple scattering correction and cannot probe large q-ranges. For $\lambda = 2.0$ Å the maximum q is 2π Å^{-1} as shown below.

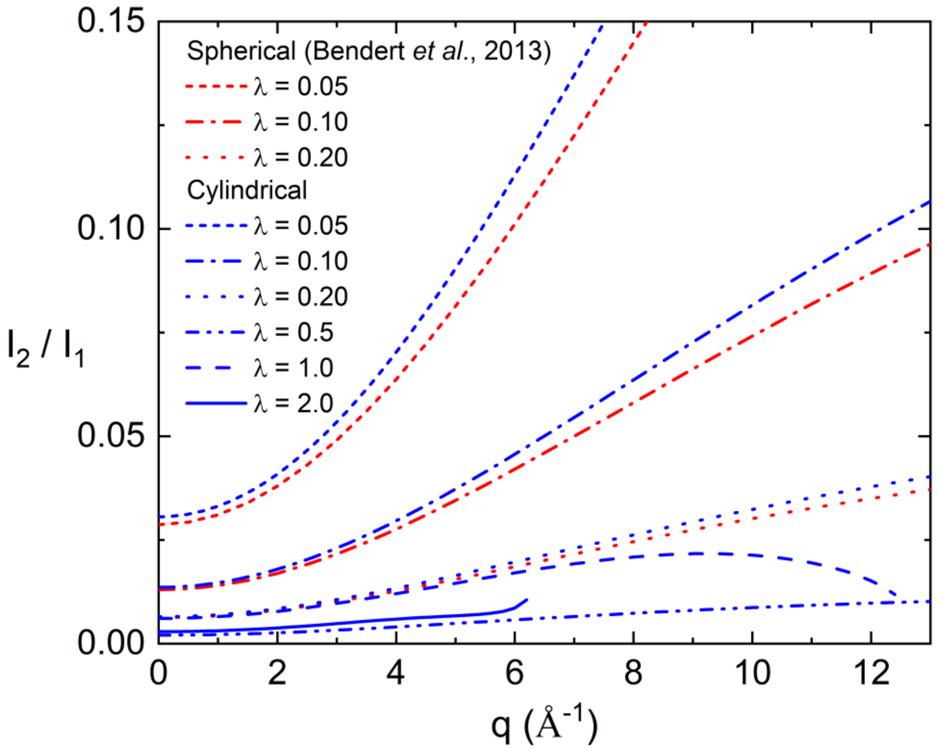

Figure 6.5 – Comparison of secondary scattering correction as a function of q and beam wavelength for cylindrical and spherical geometries for a Zr sample with $2\mu r_s = 1$, $l_s = 0$, and $\phi = 0$.

The absorption corrections for cylindrical and spherical samples of Au, Zr, and Si, at $\phi = 0$ detector location, are shown in fig. 6.6. The absorption correction is normalized by $\exp(-2\mu r_s)$. It is not surprising that in the small beam limit the absorption correction for spherical and cylindrical samples at $\phi = 0$ are equivalent (fig. 6.6), since there the curvature of cylinder matches the curvature of the sphere. This is shown by setting ϕ to zero in eq. 6.11 and in eq. 6.19 in Bendert *et al.*, 2013. There are differences in the secondary scattering corrections, however, because the beam can travel in the z-direction after the first scattering event. The small differences in multiple scattering corrections are shown in fig. 6.5 and can also be seen in Bendert *et al.*, 2013 (fig. 6b).

In the cylindrical geometry at the $\phi = \pi/2$ detector position, the distance that the beam travels through the sample for $2\theta > 0$ or $2\theta < 0$, $d_{2\theta}$, is greater than the distance traveled when the incident beam is normal to the surface of the sample, d_0 (fig. 6.7). There is then a greater attenuation, with V/V' increasing with increasing magnitude of 2θ. The opposite is true for the spherical geometry ($d_0 < d_{2\theta}$), with V/V' decreasing as 2θ deviates from 0. These trends are shown in fig. 6.8 and fig. 6.12.

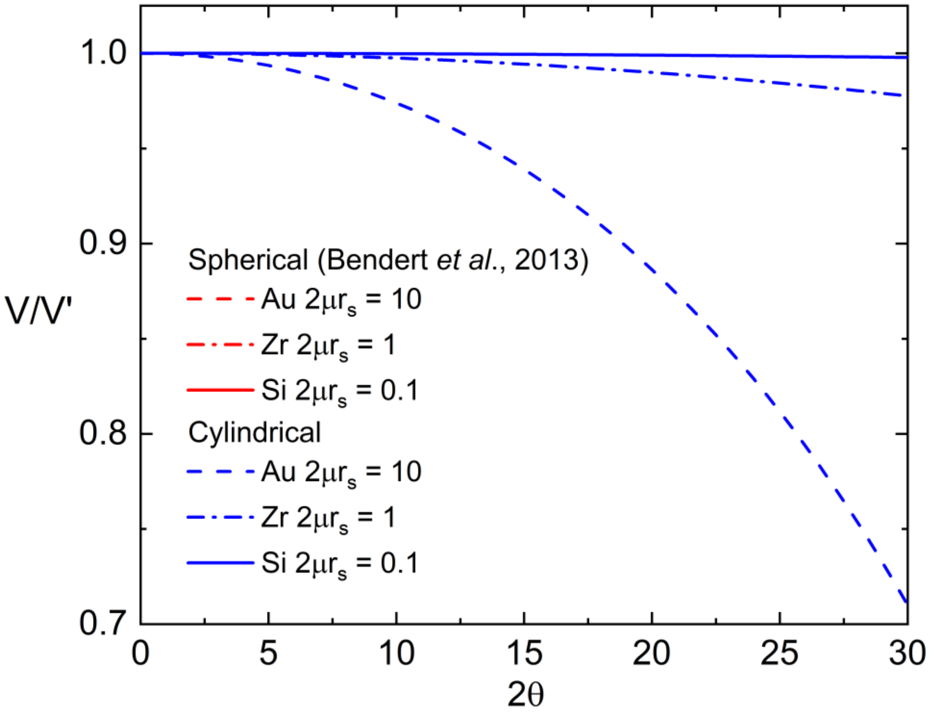

Figure 6.6 – Comparison of spherical and cylindrical absorption corrections for three different test cases with $l_s = 0$ and $\phi = 0$.

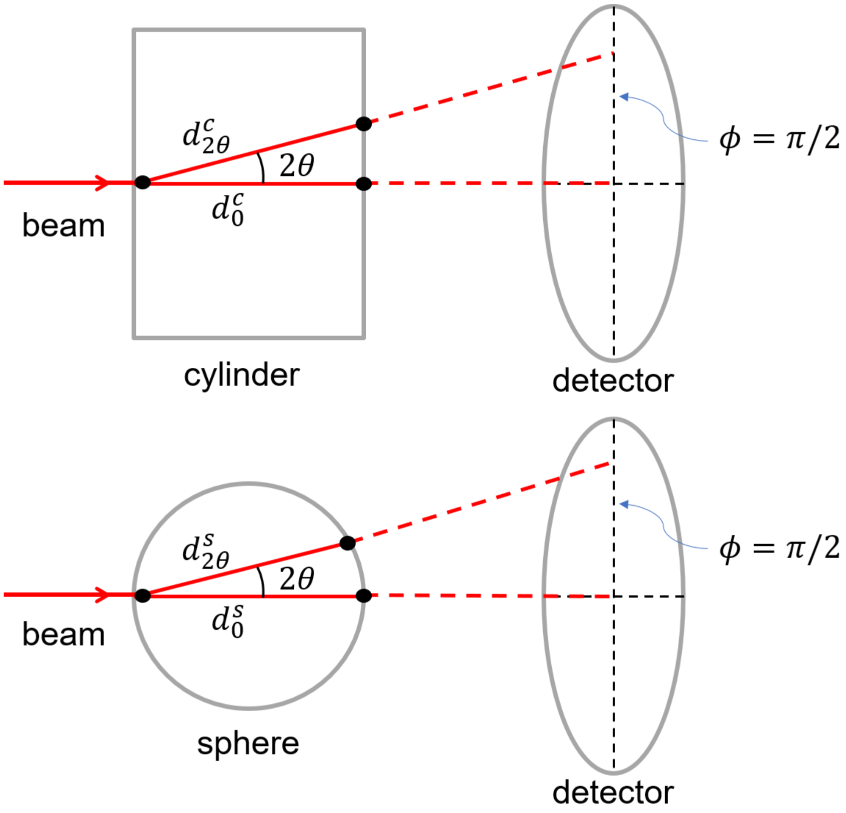

Figure 6.7 – The difference between the absorption correction for cylindrical and spherical geometries at $\phi = \pi/2$. In the cylindrical geometry $d_0^c < d_{2\theta}^c$; however, in the spherical geometry $d_0^s > d_{2\theta}^s$.

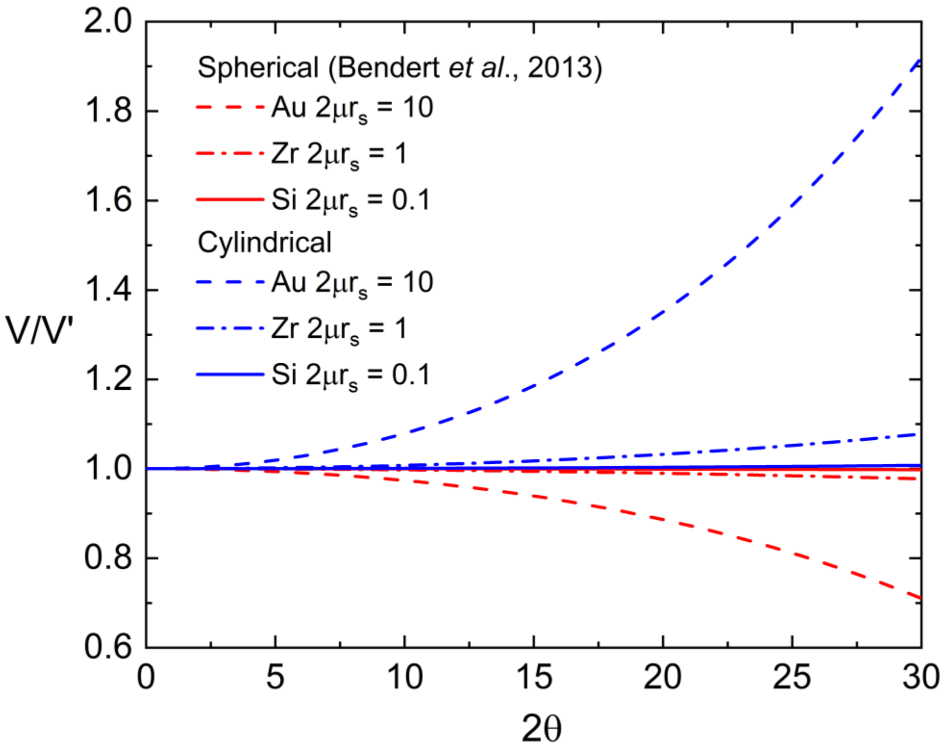

Figure 6.8 – Comparison of spherical and cylindrical absorption corrections for three different test cases with $l_s = 0$ and $\phi = \pi/2$.

The incident beam may not be aligned with the center of the cylinder; if this is the case, it is important to account for the offset, l. The offset can be characterized by a comparison to the radius of the sample, r_s. Let $l_s = l/r_s$ be the metric for the beam offset. Figures 6.9 and 6.10 show the two-dimensional detector asymmetric absorption and the asymmetric secondary scattering corrections as a function of 2θ and ϕ for a test sample of Au for four different offsets. Figure 6.11 shows line profiles of fig. 6.9 and fig. 6.10 at $\phi = 0$. The $l_s = 0$ case is the same as the case when $2\mu r_s = 10$ in fig. 6.6. Absorption corrections can be dramatically asymmetric if the beam center is far from the cylinder center. Additionally, asymmetry from the off-axis scattering beam creates an asymmetry in the secondary scattering correction. As expected, the zero offset, $l_s = 0$, case is symmetric about $2\theta = 0$ and the curves become more asymmetric as the beam offset increases. Again, it is shown that for absorption the spherical and cylindrical cases are equivalent for $\phi = 0$.

Figure 6.12 shows asymmetric absorption and the asymmetric secondary scattering correction line profiles of fig. 6.9 and fig. 6.10 for the Au test sample when $\phi = \pi/2$. For this case, there is a difference in the absorption corrections for spherical and cylindrical geometries because of the surface curvature differences between spheres and cylinders, as mentioned above.

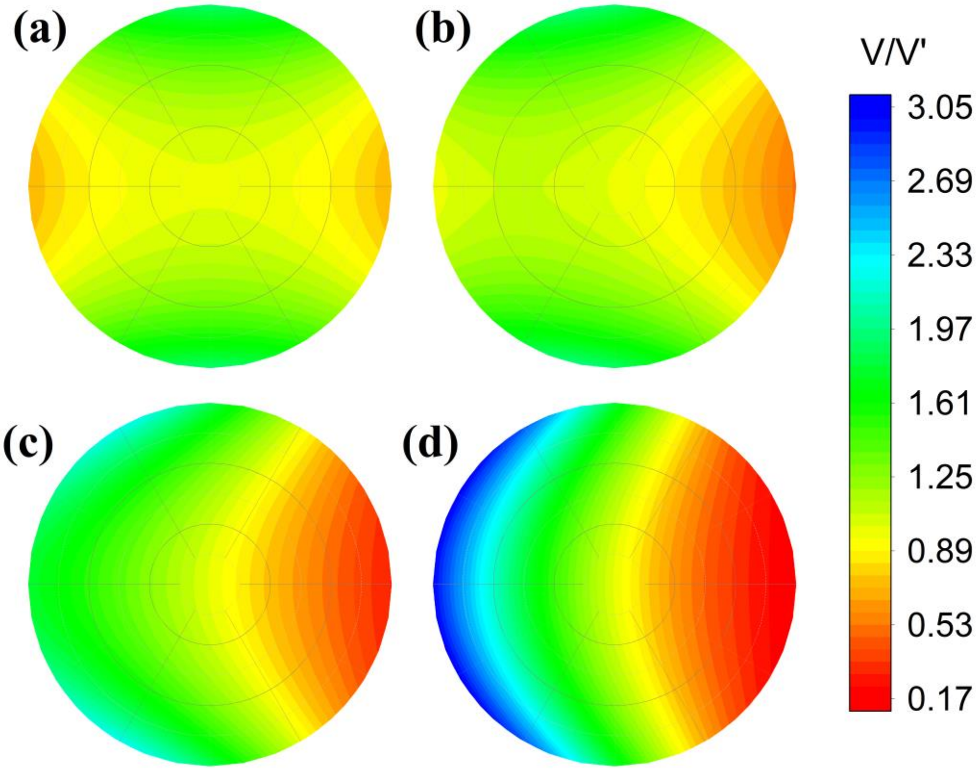

Figure 6.9 – Asymmetric detector image for the absorption correction with offset distance (a) $l_s = 0$, (b) $l_s = 0.1$, (c) $l_s = 0.3$, and (d) $l_s = 0.5$ for a test sample with $2\mu r_s = 10$.

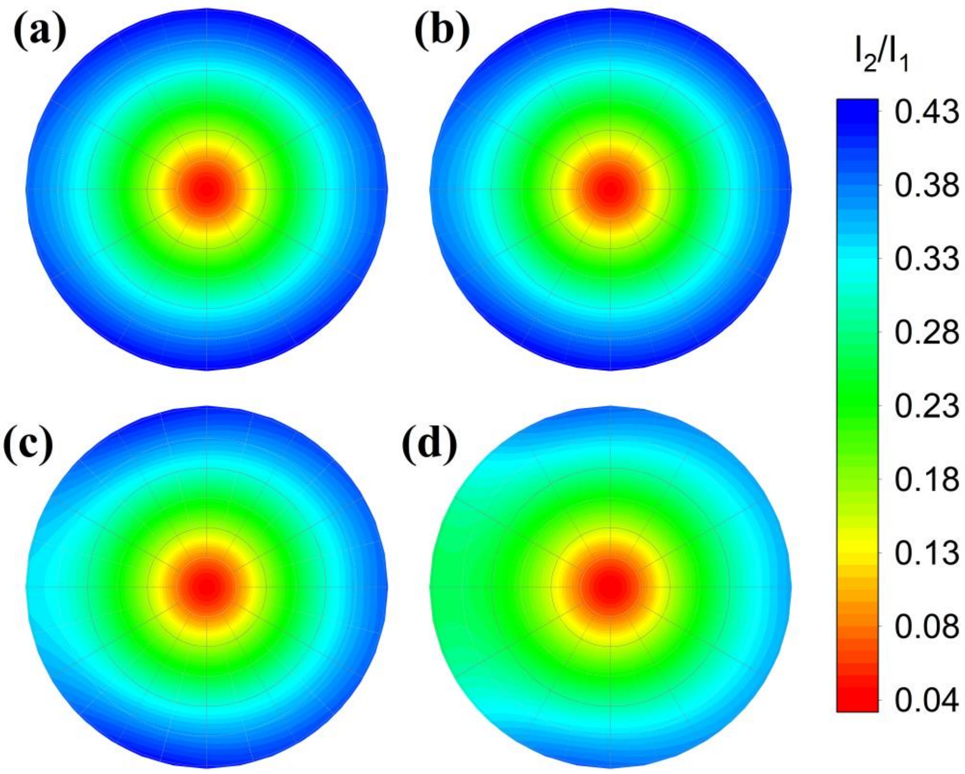

Figure 6.10 – Asymmetric detector image for the multiple scattering correction with offset distance (a) $l_s = 0$, (b) $l_s = 0.1$, (c) $l_s = 0.3$, and (d) $l_s = 0.5$ for an Au test sample with $2\mu r_s = 10$ and $\lambda = 0.1$Å.

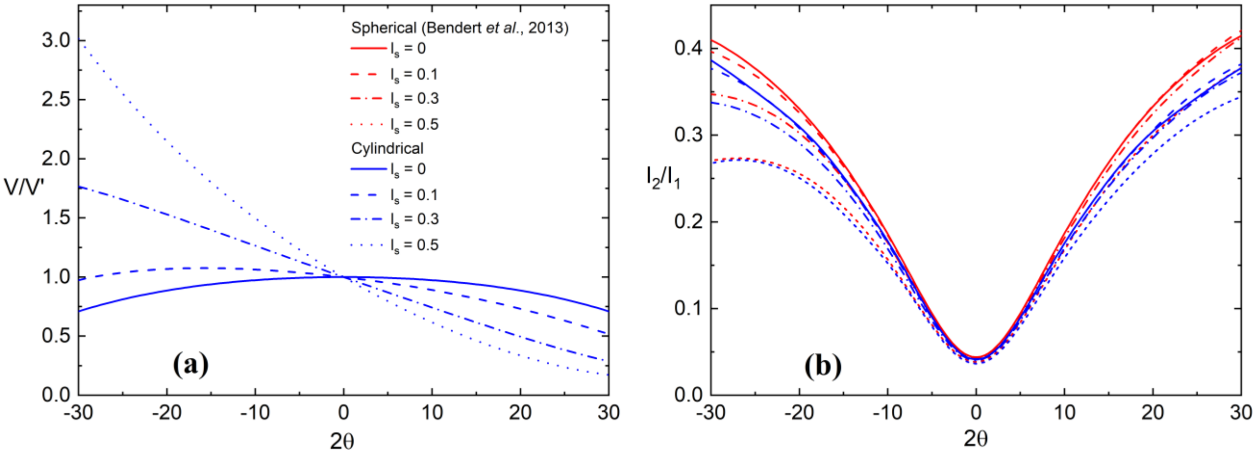

Figure 6.11 – Asymmetric (a) absorption and (b) multiple scattering corrections for a line profile across the $\phi = 0$ axis with offset distances $l_s = 0, 0.1, 0.3,$ and 0.5 for an Au test sample with $2\mu r_s = 10$ and $\lambda = 0.1$Å.

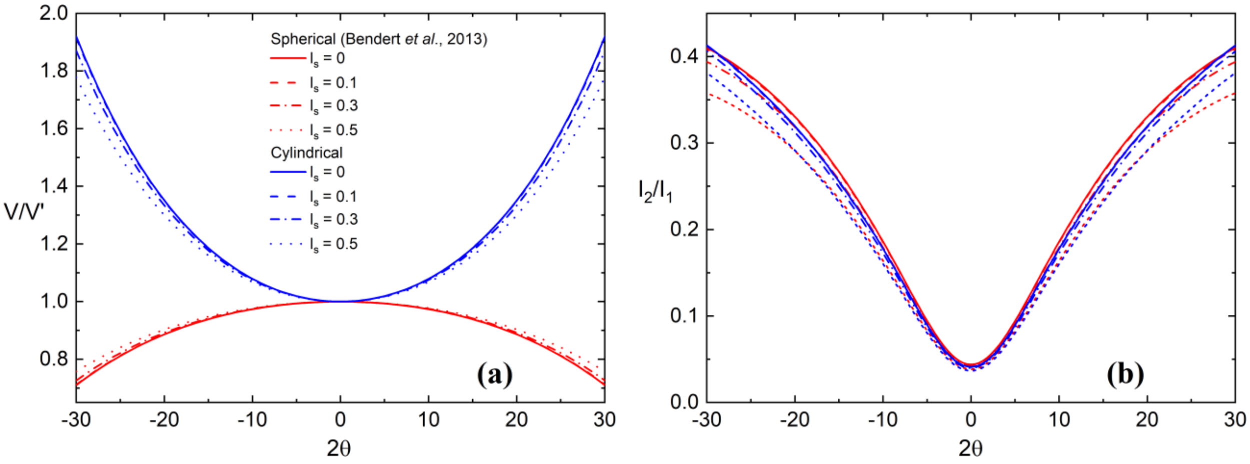

Figure 6.12 – Asymmetric (a) absorption and (b) multiple scattering corrections for a line profile across the $\phi = \pi/2$ axis with offset distances $l_s = 0, 0.1, 0.3,$ and 0.5 for an Au test sample with $2\mu r_s = 10$ and $\lambda = 0.1$Å.

6.4 Conclusions

Correctly accounting for absorption and secondary scattering is critical for obtaining accurate results from scattering data, particularly when the changes in structure that are investigated are small. Building on the work of others for absorption[12,16,23] and secondary scattering[10,11], corrections for scattering from samples with cylindrical geometries were developed. Accounting for the position of the beam on the sample is also important. For spherical samples, offsets in the position of the beam from the center of the sample produce significant asymmetries in the signal measured at the detector[15]. These effects were examined here for cylindrical samples.

The conditions for the corrections presented here go beyond the previous work for cases where the beam fully encompasses the sample[20] or for beam widths smaller than the cylinder diameter[18]. Soper and Egelstaff used a method of concentric rings to calculate the beam path length inside the sample, assuming that the beam height is the same as the sample height. Although the case of an off-axis beam with a beam height smaller than the sample height and associated beam path lengths for a cylindrical geometry were mentioned by Soper and Egelstaff, they were not computed. The work presented here develops a generalized, user-friendly, method for calculating the multiple scattering and absorption corrections, taking account of the beam profile and position on the sample. The solutions for absorption and multiple scattering are in terms of 2θ and ϕ the 2D detector coordinates, implying that the corrections may be useful for samples producing anisotropic scattering patterns in addition to isotropic scatterers. The exact expressions obtained, expressed in integral form, can be solved using current computer resources. Some approximations were also made to reduce the number of integrals, expressions that can be used to obtain results more quickly from simple numerical integration.

6.5 Acknowledgements

This research was partially funded by the National Science Foundation under grant DMR 17-20296 and Corning Inc.

6.6 References

1. Van Hoesen, D. C., Bendert, J. C. & Kelton, K. F. Absorption and secondary scattering of X-rays with an off-axis small beam for a cylindrical sample geometry. *Acta Crystallogr. Sect. A* **A75**, 362–369 (2019).

2. Kelton, K. F. *et al.* First X-Ray Scattering Studies on Electrostatically Levitated Metallic Liquids: Demonstrated Influence of Local Icosahedral Order on the Nucleation Barrier. *Phys. Rev. Lett.* **90**, 195504 (2003).

3. Kelton, K. F. & Greer, A. L. *Nucleation in Condensed Matter - Applications in Materials and Biology*. (Elsevier, 2010).

4. Iwashita, T., Nicholson, D. M. & Egami, T. Elementary excitations and crossover phenomenon in liquids. *Phys. Rev. Lett.* **110**, 1–5 (2013).

5. Soklaski, R., Tran, V., Nussinov, Z., Kelton, K. F. & Yang, L. A locally preferred structure characterises all dynamical regimes of a supercooled liquid. *Philos. Mag.* **96**, 1212–1227 (2016).

6. Mauro, N. A., Blodgett, M. E., Johnson, M. L., Vogt, A. J. & Kelton, K. F. A structural signature of liquid fragility. *Nat. Commun.* **5**, 4616 (2014).

7. Dai, R., Ashcraft, R. & Kelton, K. F. A possible structural signature of the onset of cooperativity in metallic liquids. *J. Chem. Phys.* **148**, 204502 (2018).

8. Egami, T. & Billinge, S. J. L. *Underneath the Bragg Peaks: Structural Analysis of Complex Materials*. *Pergamon Materials Series* **16**, (Pergamon, 2012).

9. Pauw, B. R. Corrigendum : Everything SAXS : small-angle scattering pattern collection. *J. Phys. Condens. Matter* **25**, 383201 (2014).

10. Warren, B. E. & Mozzi, R. L. Multiple scattering of X-rays by amorphous samples. *Acta Crystallogr.* **21**, 459–461 (1966).

11. Dwiggins, C. W. & Park, D. A. Calculation of the intensity of secondary scattering of X-rays by non-crystalline materials. *Acta Crystallogr. Sect. A* **27**, 264–272 (1971).

12. Dwiggins, C. W. Calculation of the intensity of secondary scattering of X-rays by non-crystalline materials. *Acta Crystallogr. Sect. A* **28**, 158–163 (1972).

13. Dwiggins, C. W. Rapid calculation of X-ray absorption correction factors for spheres to an accuracy of 0.05%. *Acta Crystallogr. Sect. A* **31**, 395–396 (1975).

14. Zeidler, A. X-ray and neutron attenuation correction factors for spherical samples. *J. Appl. Crystallogr.* **45**, 122–123 (2012).

15. Bendert, J. C., Blodgett, M. E. & Kelton, K. F. Calculation of absorption and secondary scattering of X-rays by spherical amorphous materials in an asymmetric transmission geometry. *Acta Crystallogr. Sect. A* **69**, 131–139 (2013).

16. Paalman, H. H. & Pings, C. J. Numerical evaluation of X-ray absorption factors for cylindrical samples and annular sample cells. *J. Appl. Phys.* **33**, 2635–2639 (1962).

17. Kendig, A. P. & Pings, C. J. X-ray absorption factors for cylindrical samples in annular sample cells exposed to incident beams of limited width. *J. Appl. Phys.* **36**, 1692–1698 (1965).

18. Soper, A. K. & Egelstaff, P. A. Multiple scattering and attenuation of neutrons in concentric cylinders: I. Isotropic first scattering. *Nucl. Instruments Methods* **178**, 415–425 (1980).

19. Sulyanov, S., Gogin, A. & Boysen, H. Spatial distribution of the absorption factor for an infinite cylindrical sample used with a two- dimensional area detector. *J. Appl. Crystallogr.* **45**, 93–97 (2012).

20. Blech, I. A. & Averbach, B. L. Multiple scattering of neutrons in vanadium and copper. *Phys. Rev.* **137**, 1–4 (1965).

21. Seeger, P. A. Scattering and multiple scattering in NISP. *Nucl. Instruments Methods Phys. Res. A* **510**, 290–299 (2003).

22. Malet, G., Cabos, C., Escande, a. & Delord, P. Double diffraction des rayons X par une substance amorphe. *J. Appl. Crystallogr.* **6**, 139–144 (1973).

23. Dwiggins, C. W. Rapid calculation of X-ray absorption correction factors for cylinders to

an accuracy of 0.1%. *Acta Crystallogr. Sect. A* **31**, 146–148 (1975).

Chapter 7: Summary and Future Work

The conclusions from chapters 3, 4, 5, and 6, which range from measurements of liquid metals on the ISS and studies of silicate glasses in collaboration with Corning Incorporated, are discussed in this chapter. Additional projects, including measurements and analysis of the crystal growth velocity of metallic alloys in an electrostatic levitator (ESL) on earth and in an electromagnetic levitator (EML) aboard the International Space Station (ISS), a geometry correction for the specific heat measured using modulation calorimetry on the ISS, remaining electrical resistivity questions, and remaining silicate glass modeling questions are also discussed.

Using EML and ESL techniques, thermophysical and dynamical properties of metallic liquids have been measured. This includes measurements of the electrical resistivity, specific heat, and viscosity. It is found that the structure and dynamics of metallic liquids are strongly related based on measurements of the electrical resistivity, which probes the local atomic structure and the viscosity measured in ESL, which is a measure of the liquid dynamics. Unfortunately, the specific heat of liquid metallic alloys, which could also provide atomic and chemical ordering information and is an essential parameter for determining the driving free energy for crystal nucleation and growth from the liquid, remains an elusive property to measure.

The nucleation and growth of $BaO\cdot 2SiO_2$ glass and $5BaO\cdot 8SiO_2$ glass were studied using numerical modeling techniques. It was found that the diffusion coefficient calculated from the measured macroscopic crystal growth velocity and the measured induction time gave a better indication of the diffusion coefficient controlling nucleation and growth than the diffusion coefficient calculated from the Stokes-Einstein relation in the region of significant nucleation. This is likely due to the breakdown of the Stokes-Einstein equation near $1.18T_g$.

7.1 Summary

7.1.1 Electrical Resistivity of Binary Metallic Alloys

The electrical resistivity of metallic binary alloys is very sensitive to local atomic order because the scattering length of an electron is approximately equal to the atomic spacing. As such, the electrical resistivity can be used to probe local structural changes with temperature. Using the EML aboard the ISS, metallic samples were levitated, eliminating container heterogeneous nucleation sites. The electrical resistivity of these samples was determined by measuring the additional impedance in the EML circuit provided by the sample[1,2].

The dynamics of the alloys are well characterized by their viscosity. At high temperatures the viscosity is Arrhenius. However, at temperatures below the onset of cooperative rearrangement temperature, T_A, the viscosity is super-Arrhenius, and the energy term in the exponential of the viscosity is temperature dependent. Above T_A, the Maxwell relaxation time, τ_M, and the time required to change the local coordination number around an atom by one, or the local cluster time, τ_{LC}, are equivalent. However, below T_A, τ_M/τ_{LC} increases rapidly as the viscosity becomes super-Arrhenius, changing by many order of magnitudes with a small change in temperature. In other words, the onset of cooperative rearrangement is the temperature at which local clusters begin to connect[3]. The crossover temperature has been discussed in detail elsewhere[3–12].

In electrical resistivity measurements of two binary metallic alloys, $Zr_{64}Ni_{36}$ and $Cu_{50}Zr_{50}$, we see a signal of the dynamical crossover temperature indicating that the structure and the dynamics of the alloys are strongly connected. For temperatures below T_A the electrical resistivity of the liquid and glass increases with decreasing temperature. However, above the crossover temperature, the electrical resistivity saturates and changes very little with increasing temperature. While no theory predicting the saturation of the electrical resistivity of metallic liquids exists, a qualitative explanation for the behavior above and below the crossover temperature is provided. The scattering time of the electrons is in the nano- to femtoseconds range, while the structural relaxation time varies drastically with temperature from approximately 100s near the glass transition temperature to approximately 10^{-13} seconds in the equilibrium liquid. For a large temperature range, the electron scatters much more quickly than the liquid is able to relax, giving rise to electron-phonon scattering. However, above some temperature the electron scattering time and the structural relaxation time become comparable, and electron-phonon scattering becomes ineffective. The phonon lifetime becomes shorter than the scattering time of the electron, so that the two processes cannot interact. It makes sense that the temperature at which the structural relaxation time and the electron scattering time become comparable is T_A, since at higher temperatures the local cluster lifetime is too short to communicate information to neighboring atoms and phonons are effectively localized.

7.1.2 Specific Heat of Metallic Alloys

The specific heat is a fundamental property that plays a central role in determining the driving free energy for crystallization. Nucleation of the crystal phase from the supercooled liquid occurs more easily if the magnitude of the driving free energy is large. The low temperature crystal or glass phase specific heat can typically be measured using differential scanning calorimetry (DSC). However, the specific heat of liquids, especially reactive liquids like many metallic alloys, is difficult to measure. Measuring properties of the liquid and supercooled liquid for these reactive metallic alloys requires levitation techniques so that there is no reaction with container walls and so that heterogeneous nucleation is minimized.

With electromagnetic levitation it is potentially possible to measure the specific heat using modulation calorimetry[13–16]. In modulation calorimetry, the power provided to the levitating sample by induction is modulated slowly by changing the homogeneous magnetic field strength. The specific heat is determined by measuring the sample temperature response as a function of temperature and modulation frequency. Unfortunately, the results of this method for ISS batch 1 and batch 2 samples were inconclusive. The specific heat measured in an inert gas atmosphere and in vacuum were different. Additionally, the method for determining the amount of power provided to the sample from the EML coils assumed that the sample is spherical. However, the amount of ellipsoidal elongation is appreciable in many samples and is a function of the heater and positioner magnetic field strength (i.e. a function of the current through the EML coils). The sample distortion with the magnetic field strength may be different in a gas atmosphere and in high vacuum causing the difference in the measured specific heats.

The external temperature time constant, τ_1, gives the timescale for radiative or convective cooling. It is possible to measure the specific heat of a spherical sample using the difference between τ_1 measured in a vacuum, where radiation dominates cooling, and τ_1 measured in a gas atmosphere, where convective cooling dominates. Measurements of τ_1 in vacuum were performed in ESL using step functions of the laser power to slowly decrease the temperature of the sample. The sample temperature changes exponentially when the power provided to the sample from an external source is changed by a small amount. Measurements of τ_1 in vacuum, helium, and argon were performed in the EML on the ISS by taking small sections of the time-temperature curve for free-cools (no power provided by an external source other than the power required to keep the sample stable) and fitting to exponential functions. Although the τ_1 data are interesting in their own right, in order to calculate the specific heat, the heat transfer coefficient between the sample and the conducting gas must be known. It was found that the external time constant does not change very much with composition and is not particularly sensitive to small changes in the sample mass. The external time constant measured in vacuum was larger than the time constant measured in argon, which is larger than the time constant measured in helium. This is because the thermal conductivity of helium is much larger than that of argon.

Another method to determine the specific heat involved calculating the emissivity of a sample as a function of temperature and combining it with the measured τ_1 data. This method was developed by Dr. Anup Gangopadhyay[17] and was used in this dissertation for batch 1, 2, and 3 ISS EML samples. In this ESL technique, the power absorbed by the sample from the heating laser was calibrated using a power balance equation during the melt plateau of the sample during heating and the final sample temperature after melting, reaching the equilibrium liquid temperature. The heat of fusion over the melt plateau time plus the radiative power term gave the power provided by the laser. The emissivity was calculated from the power balance equation. Combining these data with the measured τ_1 data in vacuum gave the specific heat. Unfortunately, the method was not viable for temperatures below the liquidus temperature, since the laser power could not be measured. The value for T_A is often close to the melting temperature, so little can be said about any change in emissivity or specific heat near the onset of cooperative rearrangement. Both the emissivity and the specific heat were found to increase with decreasing temperature in nearly all cases above the liquidus temperature. The technique was shown to give reasonable magnitudes of the emissivity and specific heat.

7.1.3 Modeling $BaO\cdot 2SiO_2$ and $5BaO\cdot 8SiO_2$ glasses

Using the classical nucleation theory (CNT) and, for the first time, the diffuse interface theory (DIT), numerical simulations of $BaO\cdot 2SiO_2$ glass and $5BaO\cdot 8SiO_2$ glass were performed. In these simulations the driving free energy, interfacial free energy, and the diffuse interface width (for DIT) were used as parameters to match the measured steady-state nucleation rate to the calculated rate. Transient nucleation and growth were then modeled using the kinetic solution to the classical theory, in which, a single monomer attaches to or detaches from a cluster at a time. After a cluster is sufficiently large, it preferentially grows according to the macroscopic growth velocity. The diffusion coefficient, which controls the forward and backward reactions rates, was calculated from either the induction time, growth velocity, or the viscosity using the Stokes-Einstein equation.

From these simulations, it was shown that the DTA method for determining the region of significant nucleation is valid and can be modeled with high accuracy[18]. In the $BaO\cdot 2SiO_2$ glass, the diffusion coefficient calculated from the induction time and the measured macroscopic growth velocity performed better at predicting the region of significant nucleation than when the Stokes-Einstein equation was used. This agrees with the fact that the Stokes-Einstein equation breaks down near $1.18T_g$ in this system. Additionally, it was clear from the diffusion coefficient curves with temperature that the Stokes-Einstein values deviate from the induction time and growth velocity values in the region of significant nucleation.

These simulations also probed the surface and volume crystallization differences for large particle sizes in the barium disilicate glass. No significant difference was found in the crystallization peak temperature when surface crystallization was taken into account, in addition to volume crystallization. This suggests that volume crystallization dominates over surface crystallization for large barium disilicate particles (average diameter of $526\ \mu m$). Additionally, the scan rate for the DTA simulations was explored to see if the region of significant nucleation predicted from the inverse crystallization peak temperature as a function of the nucleation treatment temperature changed. Using reasonable DTA scan rates, the region of significant nucleation remained unchanged, even as the scan rate changed.

For the $5BaO{\cdot}8SiO_2$ glass, neither the induction time nor the growth velocity alone work well for modeling nucleation and crystallization. The induction time is difficult to measure at high temperatures because it is very short. As such, the induction time at lower temperatures must be extrapolated to higher temperatures to get the full temperature range of the diffusion coefficient. This turns out to be a poor approximation of the diffusion coefficient at temperatures where the growth is appreciable. On the other hand, the relation derived by Kelton and Greer[19] for the diffusion coefficient calculated from the growth velocity does not work well in the $5BaO{\cdot}8SiO_2$ glass either. A monomer of the $5BaO{\cdot}8SiO_2$ glass is roughly five times larger than that of the $BaO{\cdot}2SiO_2$ glass, and attachment/detachment of this full monomer likely does not represent the actual nucleation process for small clusters. The diffusion coefficient in the nucleation temperature range is clearly too low. However, using the diffusion coefficient from the induction time to control the nucleation process and the measured macroscopic growth velocity to control the crystallization process works well. The inverse crystallization peak temperature as a function of the nucleation treatment temperature matches the measured results by Xia[20] in both temperature dependence and magnitude.

Nuclei grow spherically in the $5BaO{\cdot}8SiO_2$ glass. In the $BaO{\cdot}2SiO_2$ glass, however, nuclei are non-spherical likely leading to the offset in the calculated and measured inverse peak temperature curve. The simulation assumed the growth is spherical, and the offset did not exist for the $5BaO \cdot 8SiO_2$ glass. These simulations confirmed that the DTA method for determining the range of significant nucleation can be modeled and remains a robust technique.

7.1.4 X-ray Corrections for a Cylindrical Sample Geometry

X-ray scattering corrections for absorption and secondary scattering were developed for a cylindrical sample geometry. Correction methods for transmission and reflection geometries[21–23] as well as spherical geometries[24–26] already exist. However, cylindrical sample geometries are used frequently. The experiments looking at structural changes with time and temperature in glasses searched for very subtle differences in the measured scattering intensity, and as such required precise corrections for absorption and multiple scattering. In these corrections, the incident beam was assumed to be smaller than the sample, and in general, it was offset from the center of the sample. The results showed that the beam offset has a meaningful impact on the scattering corrections that must be applied to the measured scattering intensity. Both the full integral forms of the corrections and the small beam limit for easier computation were presented.

The corrections developed in chapter 6 of this dissertation provide a generalized method for calculating the absorption and multiple scattering, accounting for the beam profile as well as the position of the beam on the sample. In general, this procedure can be used for any sample geometry. In the cylindrical sample geometry, it was found that an offset of the beam from the center axis of the cylindrical sample produced significant asymmetries in the measured intensity. These asymmetries increase as the beam deviates further from the center of the cylinder.

7.2 Future Work

Remaining questions from the work presented in this dissertation are discussed in this section. The following work is unpublished and provides several ideas for future projects involving the NASA ISS EML data, the Washington University ESL, and understanding nucleation and crystallization in glasses with modeling.

7.2.1 Crystal Growth Velocity of Metallic Alloys

The crystal growth velocity of metallic alloys was measured in a ground-based electrostatic levitation facility using a high-speed camera capable of measuring up to 900,000 frames per second. It can also be measured in the electromagnetic levitator on the ISS. Comparing the results in ESL and the EML on the ISS could give some indication of the effect of diffusion on growth velocity. However, in the EML on the ISS the effects of diffusion are clouded by stirring caused from the positioner and heater magnetic fields. By controlling the magnitude of the magnetic fields, however, it may be possible to see an effect of diffusion on the macroscopic growth velocity. The conditions in ground-based ESL are more quiescent than those in the ISS EML, especially during free-cooling measurements when the sample heating laser is off. In this case, fluid flow from nonuniform sample heating, known as Marangoni flow, is not appreciable.

The growth velocity in metallic liquids has been studied in detail using the Lipton-Kurz-Trivedi[27] (LKT) and the Boettinger-Coriell-Trivedi[28] (BCT) theories for dendritic growth. In the combined theory, the supercooling is broken into five components: (1) the thermal supercooling, ΔT_T; (2) the constitutional supercooling, ΔT_C; (3) the supercooling due to the shift of the equilibrium liquidus line from its equilibrium position in the phase diagram due to concentration gradients at the solid/liquid interface, ΔT_N; (4) the curvature supercooling (Gibbs Thomson effect), ΔT_R; and (5) the kinetic supercooling, ΔT_K. The measured supercooling is given by the sum

$$\Delta T = \Delta T_T + \Delta T_C + \Delta T_N + \Delta T_R + \Delta T_K. \tag{7.1}$$

The thermal supercooling is found by solving the heat transport equation, which is found to be a function of the specific heat and the thermal Peclet number. The constitutional supercooling accounts for the solute redistribution at the crystal-liquid interface. This value is zero if the dendrite tip velocity is larger than the solute diffusion rate. When dendrites do not grow, the crystal growth velocity is dominated by the kinetic undercooling term and the growth velocity is given by

$$V = V_0\left(1 - \exp\left(\frac{-\Delta G}{k_B T}\right)\right), \tag{7.2}$$

where ΔG is the driving free energy encouraging crystallization, k_B is the Boltzmann constant, and T is the temperature in degrees Kelvin. V_0 is a prefactor term that depends on the type of growth. The speed of sound in the material is the upper limit of V_0. Equation 7.1 follows from the rate kinetic theory, also known as the theory of thermally activated growth[29]. The prefactor for collision limited growth was determined by Broughton, Gilmer, and Jackson[30] as

$$V_0 = \frac{a}{\lambda} f \sqrt{\frac{3k_B T}{m}}, \tag{7.3}$$

where λ is the atomic jump distance, a is the lattice parameter, f is the fraction of successful jumps of atoms in the liquid to the crystal, and m is the atomic mass. The prefactor for diffusion limited growth was determined by Wilson[31] and Frenkel[32] as

$$V_0 = \frac{Da}{\lambda^2} fexp\left(-\frac{\Delta H_f}{k_B T}\right), \tag{7.4}$$

where D is the diffusion coefficient and ΔH_f is the enthalpy of fusion. Assuming the Turnbull approximation and taking the first term in the Taylor series of eq. 7.2 gives a linear kinetic supercooling expression,

$$V = \left(\frac{V_0\,\Delta H_f}{k_B T\, T_m}\right)\Delta T_K, \tag{7.5}$$

where ΔT_K is the kinetic supercooling term from eq. 7.1.

A significant amount work has focused on measuring the crystal growth velocity of metallic samples, including $Cu_{50}Zr_{50}$[33–37], Fe-Co alloys[38], Zr and Zr-based alloys (Zr-Pd, Zr-Ni, and Zr-Ni-Cu)[36,39], $Ni_{50}Zr_{50}$[40], Zr-Si[41], Ni[42–44], Ni-C[45], Ni_2B[46], Ni-Si[47], Ni-Al[48–50], $Cu_{70}Ni_{30}$ and $Cu_{69}Ni_{30}B_1$[51], $Ti_{45}Al_{55}$[52], Si and Si-Ge[53–58], Si and Si-Co[59], Co-Mo[60], $Ni_{60}Nb_{40}$[61], and quasicrystalline and polytetrahedral phases (Al-Pd-Mn, Al-Co, and Al-Fe)[62]. Here, the Washington University BESL was used to measure the crystal growth velocities of NASA batch 2 and batch 3 samples, where the liquidus temperature is high and the color difference between the supercooled liquid and the crystal (due to the temperature difference) can be seen from a Nac Image Technology MEMRECAM HX-3 high-speed camera. Additional measurements were made using the EML on the ISS. The camera on the ISS is sensitive in the near infrared so that the crystal growth velocity of lower melting point samples can be determined. Figure 7.1 shows the crystal growth velocity of a $Zr_{64}Ni_{36}$ alloy (NASA batch 2 sample), measured in ESL and EML during free-cool cycles in vacuum as a function of the supercooling, $\Delta T = T_l - T_c$, where T_l is the liquidus temperature and T_c is the crystallization temperature. Figure 7.2 shows the crystal growth velocity of a $Zr_{80}Pt_{20}$ alloy (NASA batch 3 sample) measured in ESL during free-cool cycles. Figure 7.3 shows the crystal growth velocity of a $Ti_{45}Zr_{45}Ni_{10}$ alloy (NASA batch 3 sample) measured in ESL during free-cool cycles.

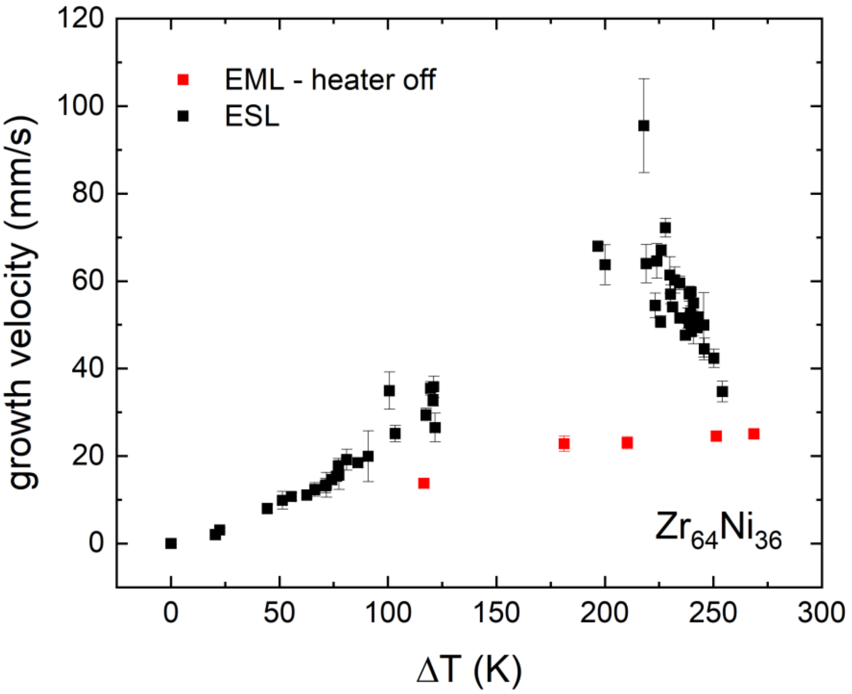

Figure 7.1 – The crystal growth velocity of a $Zr_{64}Ni_{36}$ alloy measured in ESL and EML in a high vacuum during free cooling cycles. For the measurements in EML, the heater magnetic field was turned off. Any power absorbed by the sample was from the positioner magnetic field.

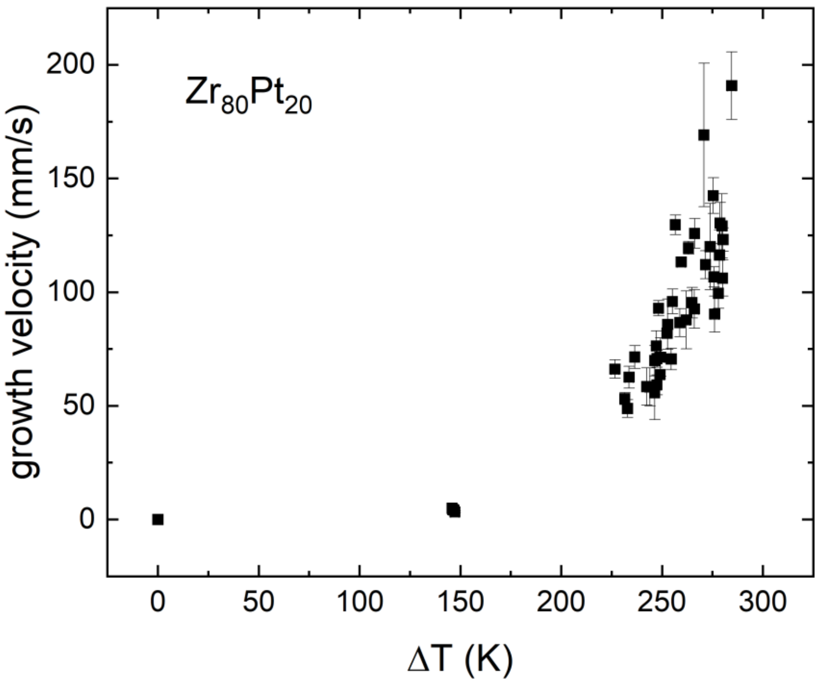

Figure 7.2 – The crystal growth velocity of a $Zr_{80}Pt_{20}$ alloy measured in ESL in a high vacuum during free cooling cycles.

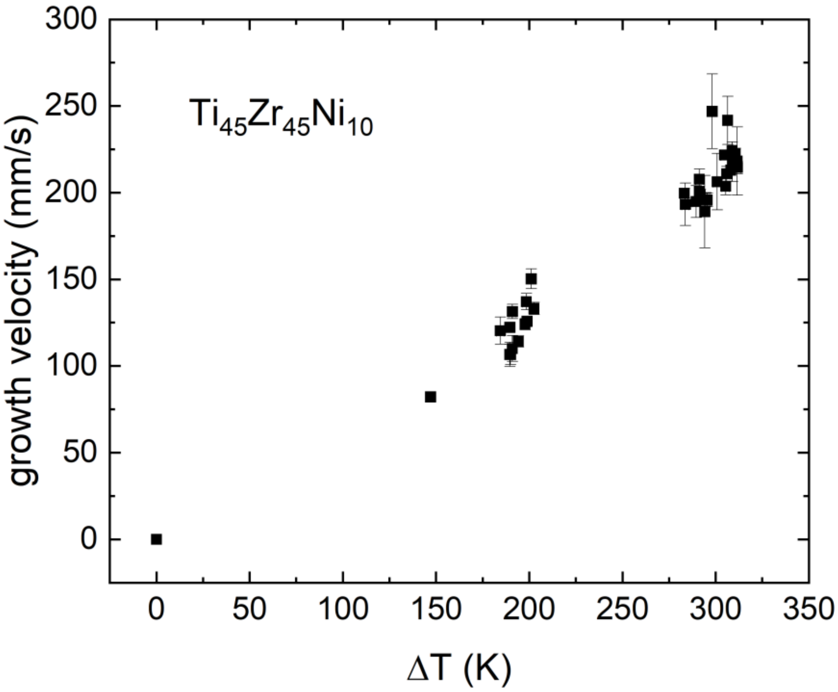

Figure 7.3 – The crystal growth velocity of a $Ti_{45}Zr_{45}Ni_{10}$ alloy measured in ESL in a high vacuum during free cooling cycles.

The crystal growth velocity of $Zr_{64}Ni_{36}$ has a maximum near $\Delta T = 220K$, likely due to diffusion limited growth. The growth velocity data from the EML are significantly lower than the growth velocity measured in the ESL. This has been seen before in the growth velocity of $Al_{50}Ni_{50}$ measured by Herlach[63], where the growth model without convection matches the ground-based measurements and the model with convection matches the microgravity measurements. When the growth velocity of both models equals the calculated fluid flow in the EML, the ground and microgravity measurements are equivalent. At the time of this dissertation, the $Zr_{80}Pt_{20}$ and $Ti_{45}Zr_{45}Ni_{10}$ growth velocity has not been measured using the EML on the ISS. In ESL, however, the $Zr_{80}Pt_{20}$ growth velocity is exponential with the supercooling temperature, whereas the $Ti_{45}Zr_{45}Ni_{10}$ growth is linear in the measured region. The difference is likely due to a different mechanism controlling the growth.

Large gaps exist in the growth velocity data where it is difficult to nucleate the crystal phase, either by homogeneous or heterogeneous nucleation, without a triggering mechanism. Additional measurements are needed to fill in the regions containing no data. The measured data should be fit with the diffusion limited, collision limited, and LKT/BCT theories of growth velocity in order to determine the growth mechanism. Scanning Electron Microscopy (SEM) and Transmission Electron Microscopy (TEM) may also be useful in determining if dendritic growth occurs during solidification. Additionally, by comparing the data to measurements made using the EML on the ISS, it may be possible to determine the role of diffusion and stirring on nucleation and growth. The heater current, producing the homogeneous magnetic field in the EML, can be used as a proxy for liquid stirring. As such, tracking the growth velocity as a function of heater current (or fluid flow velocity) would be an interesting study. Space station EML measurements of the crystal growth velocity of a $Ti_{39.5}Zr_{39.5}Ni_{21}$ alloy are shown in fig. 7.4. Unfortunately, the high-speed camera in the Washington University BESL cannot see the contrast between the liquid and crystal in this alloy.

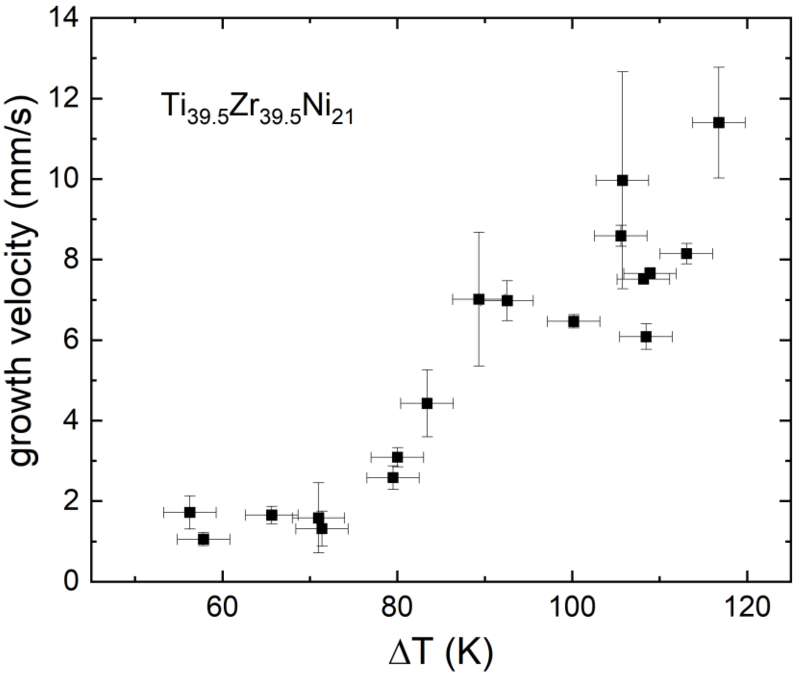

Figure 7.4 – The crystal growth velocity of a $Ti_{39.5}Zr_{39.5}Ni_{21}$ alloy measured in the EML on the ISS in vacuum during free cooling cycles. The heater magnetic field was off during these measurements.

7.2.2 Geometry Correction to Specific Heat Measured aboard the ISS

Measuring the specific heat of reactive metals in the liquid phase (supercooled or equilibrium) remains a difficult task. In 1965 Fromm and Jehn[64] derived the power absorbed by a sphere in a magnetic field (eq. 13 and eq. 14 from their paper) using the results of Smythe[65]. However, these results were derived for a spherical sample. Many of the samples in the EML aboard the space station (and likely in other EMLs) are not spherical. In fact, the ratio of the y-radius to the x-radius of the ellipsoidal $Ti_{39.5}Zr_{39.5}Ni_{21}$ NASA sample is near 1.2 (see fig. 7.5). Figure 7.6 shows that the deviation from sphericity is a function of the heater current. The scatter in the data is likely due to the positioner magnetic field strength, which is not considered. Additional scatter could be due to the data being taken during modulations of a modulation calorimetry cycle instead of an isothermal hold.

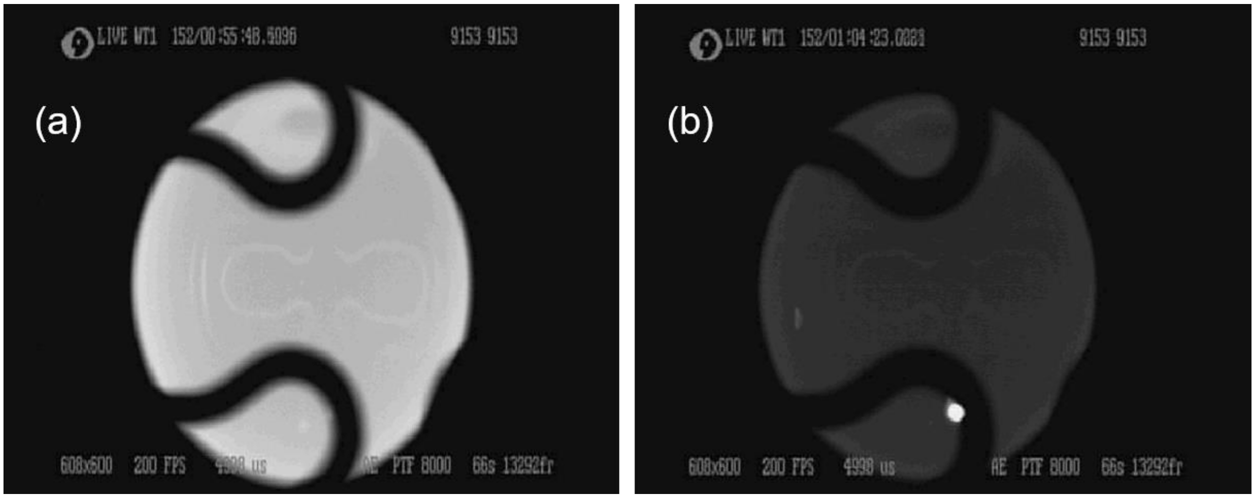

Figure 7.5 – Images of the non-spherical $Ti_{39.5}Zr_{39.5}Ni_{21}$ sample in the EML on the space station at a time when temperature was (a) high due to a high heater current and (b) low due to a low heater current. The sample is more spherical when the heater current is lower.

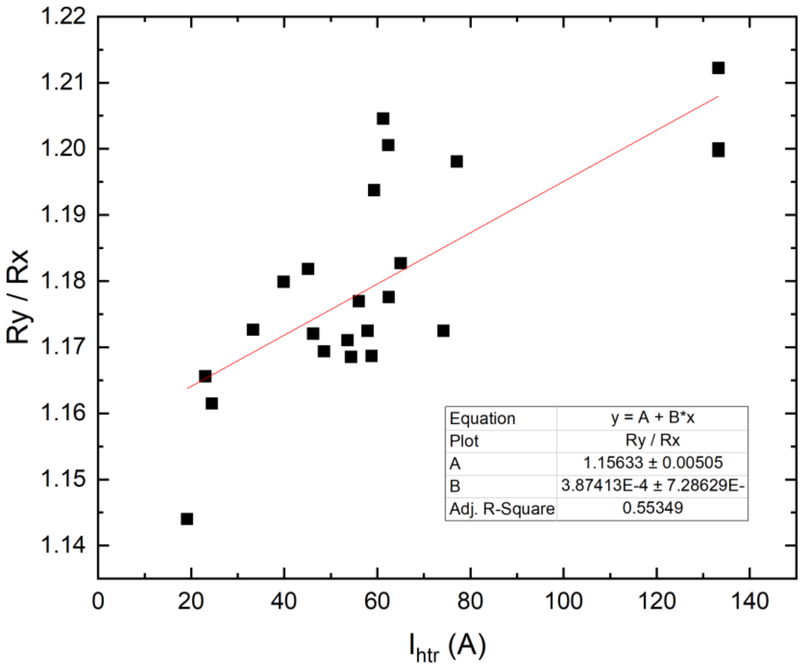

Figure 7.6 – The ratio of the y-radius, R_y, over the x-radius, R_x, as a function of the corrected heater current for the $Ti_{39.5}Zr_{39.5}Ni_{21}$ sample in the EML on the space station. The scatter in the data is likely due to the positioner magnetic field not being accounted for and the data being taken during modulations of a specific heat measurement cycle.

To correctly account for the sample geometry, eq. 13 in Fromm and Jenn's 1965 paper[64] must be built and solved with an ellipsoidal geometry. The chapter on eddy currents by Smythe[65], and in particular, section 10.06 *Conducting Sphere in Alternating Field* (pages 375-377) is likely a good starting point for this problem. Accounting for the correct geometry of the sample during modulation calorimetry may provide accurate specific heat data, solving the temperature-dependence and the data scatter problems discussed in chapter 4.

7.2.3 Remaining Electrical Resistivity Questions

New electrical resistivity findings are discussed in chapter 3 of this dissertation and published in Physical Review Letters[2]. However, several questions remain about the universality and interpretation of the data. Why does the electrical resistivity of the $Cu_{50}Zr_{50}$ alloy increase above the onset of cooperative rearrangement temperature, T_A? Is there a competing term that dominates whenever the electron-phonon scattering becomes ineffective? To explore the universality of the electrical resistivity saturation and to confirm its existence, further measurements are required. Ideal samples are those in which the evaporation rate is low so that the temperature can be increased sufficiently high above T_A before the measurement. When the heater magnetic field is changed from the value used to melt the sample to the value used to measure electrical resistivity, there is a transient time during which the electrical resistivity measurements are not accurate. During cooling, the transient regime should end well above T_A for accurate measurements of the electrical resistivity saturation.

Additional studies are required to determine the effect of a metal sample cage on the electrical resistivity measurements. It is speculated that the metal cage interferes with the magnetic fields of the EML, skewing the measurements. Until the effect is understood, all electrical resistivity measurements should be performed in ceramic cups instead of metal cages.

It would also be interesting to measure the electrical resistivity from the equilibrium liquid through the glass transition without any change in the heater or positioner magnetic field. Doing so would provide the first continuous electrical resistivity measurement of an alloy from the equilibrium liquid to the glass and allow for electrical resistivity measurements on earth in the glass state to be matched with the data from the EML on the space station. For this to be possible, measurements need to be made on a strong bulk metallic glass former.

7.2.4 Modeling Nucleation and Growth in Glasses using Advanced Theories

The modelling studies of nucleation and growth in lithium disilicate[66,67], barium disilicate[18], and $5BaO{\cdot}8SiO_2$ glasses (this work) have assumed the classical nucleation theory (CNT) and more recently the diffuse interface theory of nucleation (DIT). The CNT uses a temperature dependence of the interfacial free energy to account for the diffuseness at the interface. The interpretation of the interfacial free energy with temperature is not obvious. The DIT uses a more fundamental parameter, the interface width, to understand the nucleation rate. The DIT, to first order, accounts for the structural difference between the glass and the crystal. However, more complex structural considerations must be used to better model nucleation processes. Incorporating the semi-empirical density functional approach (SDFA), following the work of Bagdassarian, Oxtoby, and Kashchiev[68,69], into the differential thermal analysis (DTA) modelling code should be explored.

Since the paper by Gránásy and James[70] comparing the theories of nucleation, the steady-state nucleation rates of additional glasses, including $BaO{\cdot}2SiO_2$ and $5BaO{\cdot}8SiO_2$ glasses, have been measured. In the work by Gránásy and James, the logarithm of the steady-state nucleation rate divided by the nucleation rate prefactor, A^*, is shown as a function of a theory-dependent term. These curves should give intercepts close to the origin. Gránásy and James found that only the SDFA and the DIT gave reasonable results with the lithium disilicate nucleation rate data. Using the new steady-state nucleation rate data, these calculations should be performed again, and the nucleation theories should be reassessed.

7.3 Acknowledgements

This research was partially funded by NASA under Grant NNX16AB52G, the National Science Foundation under grant DMR 17-20296, and Corning Inc.

7.4 References

1. Lohöfer, G. High-resolution inductive measurement of electrical resistivity and density of electromagnetically levitated liquid metal droplets. *Rev. Sci. Instrum.* **89**, 4709 (2018).
2. Van Hoesen, D. C. *et al.* Resistivity Saturation in Metallic Liquids Above a Dynamical Crossover Temperature Observed in Measurements Aboard the International Space Station. *Phys. Rev. Lett.* **123**, 226601 (2019).
3. Soklaski, R., Tran, V., Nussinov, Z., Kelton, K. F. & Yang, L. A locally preferred structure characterises all dynamical regimes of a supercooled liquid. *Philos. Mag.* **96**, 1212–1227 (2016).
4. Jaiswal, A., Egami, T., Kelton, K. F., Schweizer, K. S. & Zhang, Y. Correlation between fragility and the Arrhenius crossover phenomenon in metallic, molecular, and network liquids. *Phys. Rev. Lett.* **117**, (2016).
5. Fan, Y., Iwashita, T. & Egami, T. Crossover from Localized to Cascade Relaxations in Metallic Glasses. *Phys. Rev. Lett.* **115**, 1–5 (2015).
6. Iwashita, T., Nicholson, D. M. & Egami, T. Elementary excitations and crossover phenomenon in liquids. *Phys. Rev. Lett.* **110**, 1–5 (2013).
7. Hu, Y. C., Li, F. X., Li, M. Z., Bai, H. Y. & Wang, W. H. Structural signatures evidenced in dynamic crossover phenomena in metallic glass-forming liquids. *J. Appl. Phys.* **119**, (2016).
8. Blodgett, M. E., Egami, T., Nussinov, Z. & Kelton, K. F. Proposal for universality in the viscosity of metallic liquids. *Sci. Rep.* **5**, 1–8 (2015).
9. Schmidtke, B., Petzold, N., Kahlau, R. & Rössler, E. A. Reorientational dynamics in molecular liquids as revealed by dynamic light scattering: From boiling point to glass transition temperature. *J. Chem. Phys.* **139**, (2013).
10. Mallamace, F. *et al.* Transport properties of glass-forming liquids suggest that dynamic crossover temperature is as important as the glass transition temperature. *Proc. Natl. Acad. Sci.* **107**, 22457–22462 (2010).

11. Garrahan, J. P. & Chandler, D. Coarse-grained microscopic model of glass formers. *Proc. Natl. Acad. Sci.* **100**, 9710–9714 (2003).

12. Sastry, S., Debenedetti, P. G. & Stillinger, F. H. Signatures of distinct dynamical regimes in the energy landscape of a glass-forming liquid. *Nature* **393**, 554–557 (1998).

13. Corbino, O. M. Oscillazioni termiche delle lampade a filamento sottile percorse da correnti alternate, e conseguente effetto raddrizzatore per la presenza di armonichi pari. *Nuovo Cim.* **19**, 75–84 (1910).

14. Fecht, H. J. & Johnson, W. L. A conceptual approach for noncontact calorimetry in space. *Rev. Sci. Instrum.* **62**, 1299–1303 (1991).

15. Wunderlich, R. K., Fecht, H.-J. & Willnecker, R. Power modulation technique for noncontact high-temperature calorimetry. *Appl. Phys. Lett.* **62**, 3111–3113 (1993).

16. Wunderlich, R. K. & Fecht, H. J. Modulated electromagnetic induction calorimetry of reactive metallic liquids. *Meas. Sci. Technol.* **16**, 402–416 (2005).

17. Gangopadhyay, A. K. & Kelton, K. F. Measurements of the Temperature-Dependent Total Hemispherical Emissivity Using an Electrostatic Levitation Facility. *Int. J. Thermophys.* **38**, 1–8 (2017).

18. Van Hoesen, D. C., Xia, X., McKenzie, M. E. & Kelton, K. F. Modeling nonisothermal crystallization in a BaO·2SiO 2 glass. *J. Am. Ceram. Soc.* (2020). doi:10.1111/jace.16979

19. Kelton, K. F. & Greer, A. L. Transient Nucleation Effects in Glass Formation. *J. Non. Cryst. Solids* **79**, 295–309 (1986).

20. Xia, X., Dutta, I., Mauro, J. C., Aitken, B. G. & Kelton, K. F. Temperature dependence of crystal nucleation in BaO.2SiO2 and 5BaO.8SiO2 glasses using differential thermal analysis. *J. Non. Cryst. Solids* **459**, 45–50 (2017).

21. Warren, B. E. & Mozzi, R. L. Multiple scattering of X-rays by amorphous samples. *Acta Crystallogr.* **21**, 459–461 (1966).

22. Dwiggins, C. W. & Park, D. A. Calculation of the intensity of secondary scattering of X-rays by non-crystalline materials. *Acta Crystallogr. Sect. A* **27**, 264–272 (1971).

23. Dwiggins, C. W. Calculation of the intensity of secondary scattering of X-rays by non-crystalline materials. *Acta Crystallogr. Sect. A* **28**, 158–163 (1972).

24. Dwiggins, C. W. Rapid calculation of X-ray absorption correction factors for spheres to an accuracy of 0.05%. *Acta Crystallogr. Sect. A* **31**, 395–396 (1975).

25. Zeidler, A. X-ray and neutron attenuation correction factors for spherical samples. *J. Appl. Crystallogr.* **45**, 122–123 (2012).

26. Bendert, J. C., Blodgett, M. E. & Kelton, K. F. Calculation of absorption and secondary scattering of X-rays by spherical amorphous materials in an asymmetric transmission

geometry. *Acta Crystallogr. Sect. A* **69**, 131–139 (2013).

27. Lipton, J., Kurz, W. & Trivedi, R. Rapid Dendrite Growth in Undercooled Alloys. *Acta Met.* **35**, 957–964 (1987).

28. Boettinger, W. J., Coriell, S. R. & Trivedi, R. Application of dendritic growth theory to the interpretation of rapid solidification microsctructures. *Rapid Solidif. Process. Princ. Technol. IV* **13**, (1988).

29. Christian, J. W. *The Theory of Transformations in Metals and Alloys*. (Pergamon, 1981).

30. Broughton, J. Q., Gilmer, G. H. & Jackson, K. A. Crystallization Rates of a Lennard-Jones Liquid. *Phys. Rev. Lett.* **49**, 1496–1500 (1982).

31. Wilson, H. A. On the velocity of solidification and viscosity of supercooled liquids. *Philos. Mag.* **50**, 238–250 (1900).

32. Frenkel, J. *Kinetic Theory of Liquids*. (Oxford University Press, 1947).

33. Galenko, P. K. *et al.* Thermodynamics of rapid solidification and crystal growth kinetics in glass-forming alloys. *Philos. Trans. R. Soc. A Math. Phys. Eng. Sci.* **377**, (2019).

34. Wang, Q. *et al.* Diffusion-controlled crystal growth in deeply undercooled melt on approaching the glass transition. *Phys. Rev. B - Condens. Matter Mater. Phys.* **83**, 1–5 (2011).

35. Wang, H., Herlach, D. M. & Liu, R. P. Dendrite growth in Cu $_{50}$ Zr $_{50}$ glass-forming melts, thermodynamics vs. kinetics. *EPL (Europhysics Lett.* **105**, 36001 (2014).

36. Galenko, P. K. *et al.* Solidification kinetics of a Cu-Zr alloy: Ground-based and microgravity experiments. *IOP Conf. Ser. Mater. Sci. Eng.* **192**, (2017).

37. Kobald, R. Crystal growth in undercooled melts of glass forming Zr-based alloys. PhD Thesis. (2016).

38. Rodriguez, J. E., Kreischer, C., Volkmann, T. & Matson, D. M. Solidification velocity of undercooled Fe-Co alloys. *Acta Mater.* **122**, 431–437 (2017).

39. Herlach, D. M. & Galenko, P. K. Rapid solidification: in situ diagnostics and theoretical modelling. *Mater. Sci. Eng. A* **448–451**, 34–41 (2007).

40. Kobold, R. *et al.* Dendrite growth velocity in the undercooled melt of glass forming Ni50Zr50 compound. *Philos. Mag. Lett.* **97**, 249–256 (2017).

41. Hu, L., Yang, S. J., Wang, L., Zhai, W. & Wei, B. Dendrite growth kinetics of βZr phase within highly undercooled liquid Zr−Si hypoeutectic alloys under electrostatic levitation condition. *Appl. Phys. Lett.* **110**, 1–5 (2017).

42. Willnecker, R., Herlach, D. M. & Feuerbacher, B. Evidence of nonequilibrium processes in rapid solidification of undercooled metals. *Phys. Rev. Lett.* **62**, 2707–2710 (1989).

43. Eckler, K. & Herlach, D. M. Measurements of dendrite growth velocities in undercooled pure Ni-melts-some new results. *Mater. Sci. Eng. A* **178**, 159–162 (1994).

44. Colligan, G. A. & Bayles, B. A. Dendrite growth in undercooled Ni melts. *Acta Met.* **10**, 895–897 (1962).

45. Eckler, K., Herlach, D. M., Hamerton, R. G. & Greer, A. L. Dendrite growth velocities in highly undercooled, dilute Ni-C melts. *Mater. Sci. Eng. A* **A133**, 730–733 (1991).

46. Binder, S., Galenko, P. K. & Herlach, D. M. The effect of fluid flow on the solidification of Ni2B from the undercooled mlet. *J. Appl. Phys.* **115**, (2014).

47. Lü, Y. J. Crystal growth velocity in deeply undercooled Ni – Si alloys. **92**, 37–41 (2012).

48. Hartmann, H., Holland-Moritz, D., Galenko, P. K. & Herlach, D. M. Evidence of the transition from ordered to disordered growth during rapid solidification of an intermetallic phase. *Epl* **87**, 2014–2016 (2009).

49. Herlach, D. M. *et al.* Non-equilibrium and near-equilibrium solidification of undercooled melts of Ni- and Al-based alloys. *Adv. Eng. Mater.* **10**, 444–452 (2008).

50. Herlach, D. M. *et al.* Solidification of Undercooled Melts of Al-Based Alloys on Earth and in Space. *Jom* **69**, 1303–1310 (2017).

51. Willnecker, R., Herlach, D. M. & Feuerbacher, B. Grain refinement induced by a critical crystal growth velocity in undercooled melts. *Appl. Phys. Lett.* **56**, 324–326 (1990).

52. Hartmann, H. *et al.* Nonequilibrium solidification in undercooled Ti45 Al55 melts. *J. Appl. Phys.* **103**, (2008).

53. Panofen, C. & Herlach, D. M. Solidification of highly undercooled Si and Si-Ge melts. *Mater. Sci. Eng. A* **449–451**, 699–703 (2007).

54. Li, D., Eckler, K. & Herlach, D. M. Evidence for transitions from lateral to continuous and to rapid growth in Ge-1at%Si solid solution. *Europhys. Lett.* **32**, 223–227 (1995).

55. Li, D. L., Volkmann, T., Eckler, K. & Herlach, D. M. Crystal growth in undercooled germanium. *J. Cryst. Growth* **152**, 101–104 (1995).

56. Li, D., Eckler, K. & Herlach, D. M. Undercooling, crystal growth and grain structure of levitation melted pure Ge and Ge-Sn alloys. *Acta Mater.* **44**, 2437–2443 (1996).

57. Li, D. & Herlach, D. M. Containerless solidification of germanium by electromagnetic levitation and in a drop-tube. *J. Mater. Sci.* **32**, 1437–1442 (1997).

58. Li, D. & Herlach, D. M. Direct Measurements of Free Crystal Growth in Deeply Undercooled Melts of Semiconducting Materials. *Phys. Rev. Lett.* **77**, 1801–1804 (1996).

59. Panofen, C. & Herlach, D. M. Rapid solidification of highly undercooled Si and Si-Co melts. *Appl. Phys. Lett.* **88**, 171913 (2006).

60. Wei, B., Herlach, D. M., Sommer, F. & Kurz, W. Rapid dendritic and eutectic solidification of undercooled Co-Mo alloys. *Mater. Sci. Eng. A* **181–82**, 1150–1155 (1994).

61. Rathz, T. J., Robinson, M. B., Hyers, R. W., Rogers, J. R. & Li, D. Triggered nucleation in Ni60 Nb40 using an electrostatic levitator. *J. Mater. Sci. Lett.* **21**, 301–303 (2002).

62. Schroers, J., Holland-Moritz, D., Herlach, D. M. & Urban, K. Growth kinetics of quasicrystalline and polytetrahedral phases of Al-Pd-Mn, Al-Co, and Al-Fe from the undercooled melt. *Phys. Rev. B - Condens. Matter Mater. Phys.* **61**, 14500–14506 (2000).

63. Herlach, D. M. Non-Equilibrium Solidification of Undercooled Metallic Melts. *Metals (Basel).* **4**, 196–234 (2014).

64. Fromm, E. & Jehn, H. Electromagnetic forces and power absorption in levitation melting. *Br. J. Appl. Phys.* **16**, 653–663 (1965).

65. Smythe, W. R. Eddy Currents. in *Static and Dynamic Electricity* 368–414 (McGraw-Hill, 1968).

66. Kelton, K. F., Narayan, K. L., Levine, L. E., Cull, T. S. & Ray, C. S. Computer modeling of non-isothermal crystallization. *J. Non. Cryst. Solids* **204**, 13–31 (1996).

67. Ray, C. S. *et al.* Non-isothermal calorimetric studies of the crystallization of lithium disilicate glass. *J. Non* **204**, 1–12 (1996).

68. Bagdassarian, C. K. & Oxtoby, D. W. Crystal nucleation and growth from the undercooled liquid: A nonclassical piecewise parabolic free-energy model. *J. Chem. Phys.* **100**, (1994).

69. Oxtoby, D. W. & Kashchiev, D. A general relation between the nucleation work and the size of the nucleus in multicomponent nucleation. *J. Chem. Phys.* **100**, 7665–7671 (1994).

70. Gránásy, L. & James, P. F. Nucleation in oxide glasses: comparison of theory and experiment. *Proc. R. Soc. London. Ser. A Math. Phys. Eng. Sci.* **454**, 1745–1766 (1998).

Appendix A: Cylindrical Corrections in the X-ray Scattering LabVIEW Software

James Bendert built the X-ray scattering analysis software (X-ray Batch) in LabVIEW that accounts for several common sample geometries including reflection, direct transmission, and symmetric transmission. Bendert also derived and implemented a spherical transmission geometry to be used with the beamline electrostatic levitator built at Washington University in St. Louis[1]. This geometry accounts for an off-center X-ray beam on a levitated spherical sample. A review of X-ray scattering corrections and the X-ray Batch LabVIEW software built to analyze the data can be found in Bendert's dissertation[2]. In chapter 6 of this dissertation, the X-ray scattering corrections for a cylindrical sample with an off-axis beam were calculated. The work is published in Van Hoesen, D. C. *et al.*, "*Absorption and secondary scattering of X-rays with an off-axis small beam for a cylindrical sample geometry*," Acta Crystallographica Section A. **75**, 362-369, (2019)[3]. Here we provide additional details on the analysis program used to correct the X-ray scattering data specific to the cylindrical sample geometry.

A.1 X-ray Batch with Cylindrical Corrections

The LabVIEW front panel of X-ray batch is shown in fig. A.1 with the cylindrical correction parameters on the left side of the image. Figure A.2 is a closeup image of the cylindrical correction parameters. The user inputs the beam properties including the beam height, beam width, and beam offset in the z-direction (i.e. along the axis of the cylinder) from the center. The user then inputs the sample height, radius, and packing fraction. The container parameters including the wall thickness and the attenuation factor are determined and placed in the appropriate boxes. In X-ray scattering experiments, it is common to include metal sheets between the sample and the detector in order to reduce fluorescence. If metal sheets are used (up to two sheets), the user places the sheet thickness and attenuation factor in the appropriate LabVIEW boxes. Additionally, the Argonne National Lab Advanced Photon Source uses a top-down beam intensity method, where the beam intensity slowly decreases until it is increased all at once back to full intensity. As such, it may be necessary to account for the beam intensity difference between samples. A multiplicative factor for the beam intensity correction exists to account for this X-ray intensity difference between measurements. The remaining X-ray batch files and parameters should be filled out according to Bendert's thesis.

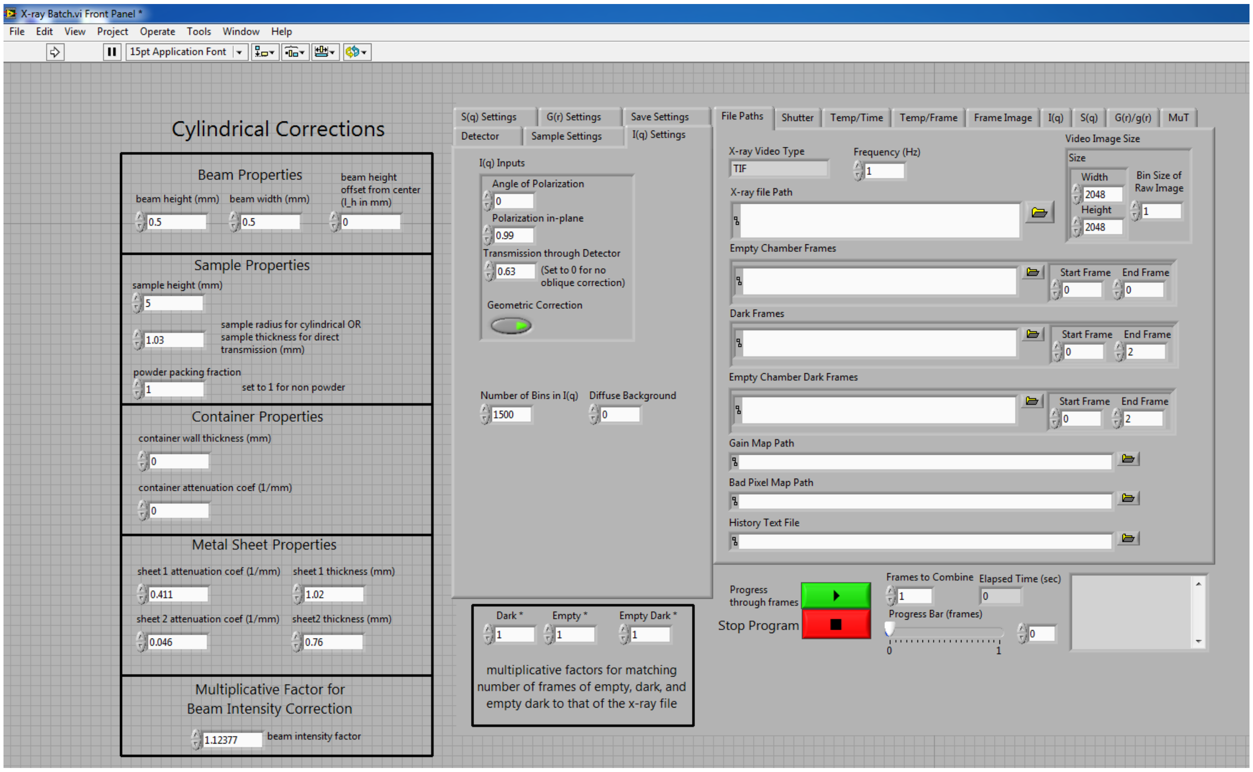

Cylindrical Corrections

Beam Properties
beam height (mm) 0.5
beam width (mm) 0.5
beam height offset from center (l_h in mm) 0

Sample Properties
sample height (mm) 5
1.03 sample radius for cylindrical OR sample thickness for direct transmission (mm)
powder packing fraction 1 set to 1 for non powder

Container Properties
container wall thickness (mm) 0
container attenuation coef (1/mm) 0

Metal Sheet Properties
sheet 1 attenuation coef (1/mm) 0.411
sheet 1 thickness (mm) 1.02
sheet 2 attenuation coef (1/mm) 0.046
sheet2 thickness (mm) 0.76

Multiplicative Factor for Beam Intensity Correction
1.12377 beam intensity factor

I(q) Inputs
Angle of Polarization 0
Polarization in-plane 0.99
Transmission through Detector 0.63 (Set to 0 for no oblique correction)
Geometric Correction
Number of Bins in I(q) 1500
Diffuse Background 0

Dark * 1
Empty * 1
Empty Dark * 1
multiplicative factors for matching number of frames of empty, dark, and empty dark to that of the x-ray file

X-ray Video Type TIF
Frequency (Hz) 1
Video Image Size
Size
Width 2048
Height 2048
Bin Size of Raw Image 1
X-ray file Path
Empty Chamber Frames Start Frame 0 End Frame 0
Dark Frames Start Frame 0 End Frame 2
Empty Chamber Dark Frames Start Frame 0 End Frame 2
Gain Map Path
Bad Pixel Map Path
History Text File

Frames to Combine 1
Elapsed Time (sec) 0
Progress Bar (frames) 0

Figure A.1 – The front panel of X-ray batch with cylindrical correction parameters on the left side of the image.

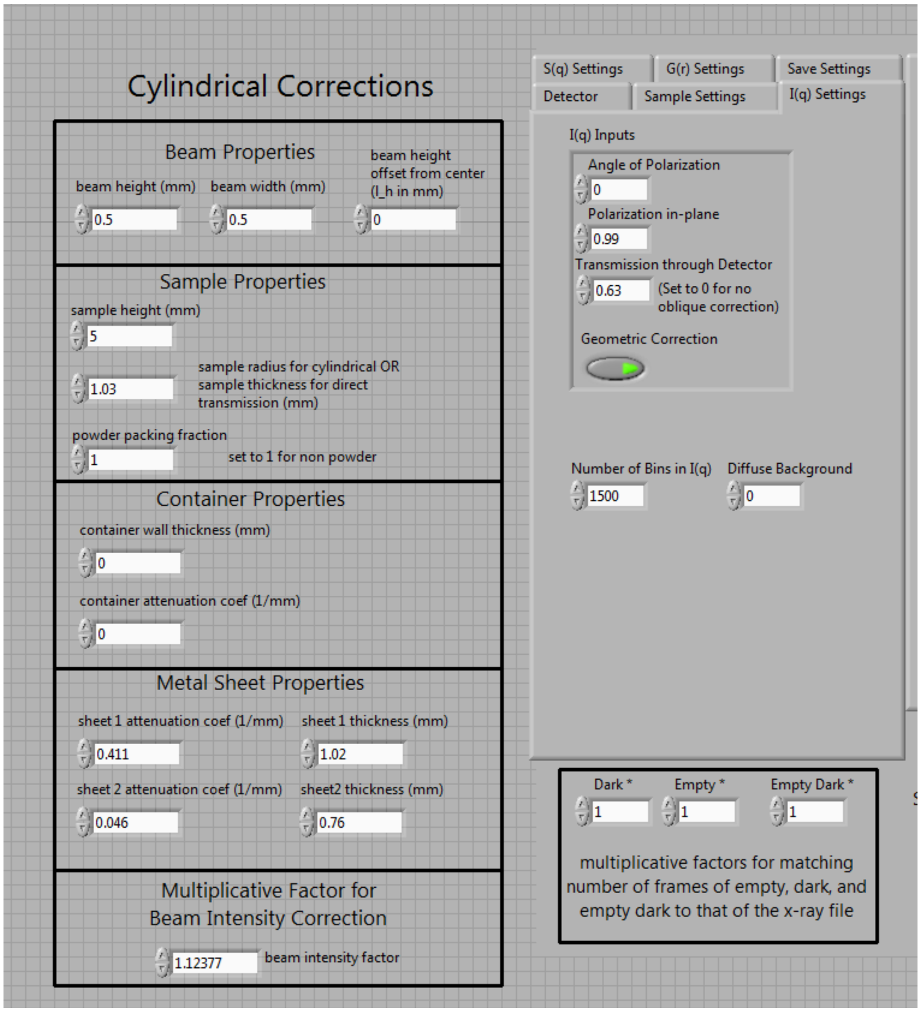

Cylindrical Corrections

Beam Properties

beam height (mm): 0.5
beam width (mm): 0.5
beam height offset from center (I_h in mm): 0

Sample Properties

sample height (mm): 5
sample radius for cylindrical OR sample thickness for direct transmission (mm): 1.03
powder packing fraction: 1 (set to 1 for non powder)

Container Properties

container wall thickness (mm): 0
container attenuation coef (1/mm): 0

Metal Sheet Properties

sheet 1 attenuation coef (1/mm): 0.411
sheet 1 thickness (mm): 1.02
sheet 2 attenuation coef (1/mm): 0.046
sheet2 thickness (mm): 0.76

Multiplicative Factor for Beam Intensity Correction

beam intensity factor: 1.12377

I(q) Inputs

Angle of Polarization: 0
Polarization in-plane: 0.99
Transmission through Detector: 0.63 (Set to 0 for no oblique correction)
Geometric Correction: ●

Number of Bins in I(q): 1500
Diffuse Background: 0

Dark *: 1
Empty *: 1
Empty Dark *: 1

multiplicative factors for matching number of frames of empty, dark, and empty dark to that of the x-ray file

Figure A.2 – The front panel of X-ray batch zoomed in on the cylindrical correction parameters.

It should be noted that the attenuation coefficients for the container and the metal sheets are specific to the wavelength used for scattering. These attenuation factors can be found on the NIST database (https://www.nist.gov/pml/x-ray-mass-attenuation-coefficients) or in Bendert's attenuation database text file, which is referenced by X-ray batch for several scattering calculations. Figure A.3 shows the location of the geometry selection. To use the cylindrical corrections, select the "Cylindrical" geometry in the S(q) Settings tab.

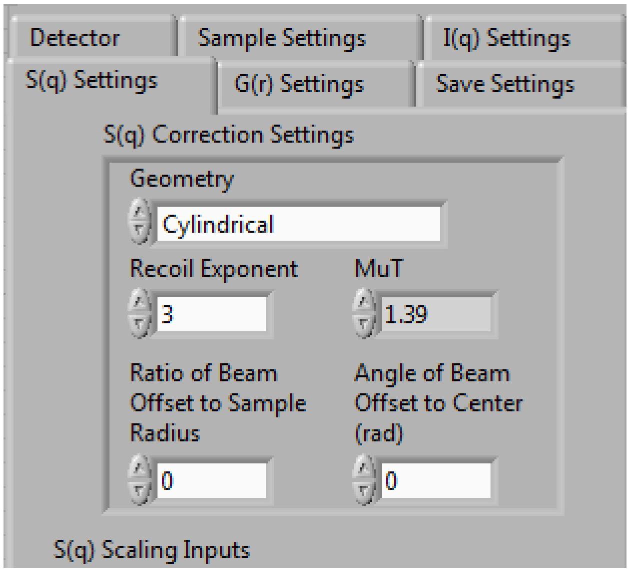

S(q) Correction Settings

Geometry: Cylindrical

Recoil Exponent: 3

MuT: 1.39

Ratio of Beam Offset to Sample Radius: 0

Angle of Beam Offset to Center (rad): 0

S(q) Scaling Inputs

Figure A.3 – The front panel of X-ray batch zoomed in on the S(q) correction settings showing how to select the cylindrical sample geometry.

Each of the cylindrical correction parameters is a global variable in the LabVIEW code, and used in the appropriate subprogram to calculate the absorption and multiple scattering corrections for the cylindrical geometry. Pressing “Ctrl-E” from the LabVIEW front panel brings up the block diagram, which shows the structure of the code. From here, it is possible to access the subprograms including the absorption and multiple scattering subprograms, which are in the “Calculate S(q) Corrections” selection box shown in fig. A.4. To access a subprogram in the block diagram, double click on the subprogram icon, which opens a new front panel for that specific program.

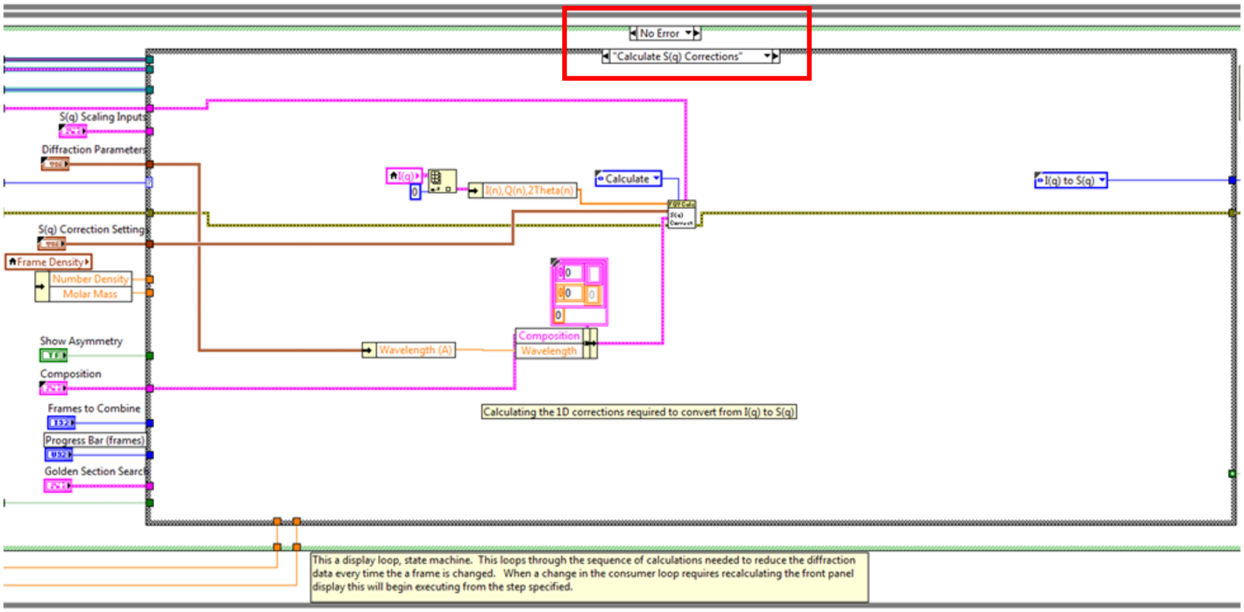

Calculating the 1D corrections required to convert from I(q) to S(q)

This a display loop, state machine. This loops through the sequence of calculations needed to reduce the diffraction data every time the a frame is changed. When a change in the consumer loop requires recalculating the front panel display this will begin executing from the step specified.

Figure A.4 – The block diagram of X-ray batch showing the location of the absorption and multiple scattering corrections.

A.2 References

1. Bendert, J. C., Blodgett, M. E. & Kelton, K. F. Calculation of absorption and secondary scattering of X-rays by spherical amorphous materials in an asymmetric transmission geometry. *Acta Crystallogr. Sect. A* **69**, 131–139 (2013).

2. Bendert, J. C. Thermophysical and Structural Measurements of Liquid Metallic Alloys Using Electrostatic Levitation. PhD Thesis. (Washington University in St. Louis, 2013).

3. Van Hoesen, D. C., Bendert, J. C. & Kelton, K. F. Absorption and secondary scattering of X-rays with an off-axis small beam for a cylindrical sample geometry. *Acta Crystallogr. Sect. A* **A75**, 362–369 (2019).

Appendix B: ESL High-Speed Camera Operation and the Analog to Digital Converter Box

Operation of the Nac Image Technology MEMRECAM HX-3 high-speed camera and updates made to the Analog-to-Digital (AD) and Digital-to-Analog (DA) cards are discussed in this appendix.

B.1 High-Speed Camera Operation

Figure B.1 shows the location and setup of the high-speed camera from three different angles on the Washington University Beamline Electrostatic Levitator (BESL). The high-speed camera views the sample from the same location that X-rays enter the chamber during X-ray scattering measurements at the Argonne National Lab Advanced Photon Source (APS). The high-speed camera is removed during scattering measurements.

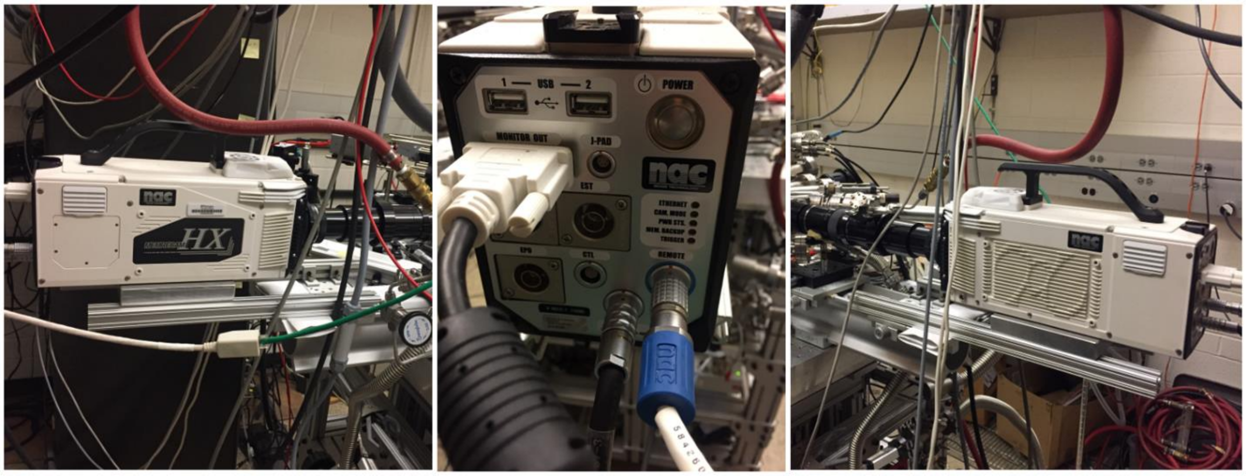

Figure B.1 – The high-speed camera from three different angles on the Washington University BESL.

To operate the high-speed camera, first the power supply (not shown in fig. B.1) must be turned on. Then the high-speed camera power button (middle of fig. B.1) is held until the power status indicator is green. The viscosity computer hosts the HX-Link software (located on the desktop) that controls the parameters of the camera. Starting the software opens the user interface, shown in fig. B.2. After the camera is powered on, selecting the icon indicated by the red arrow attaches the camera to the HX-Link software.

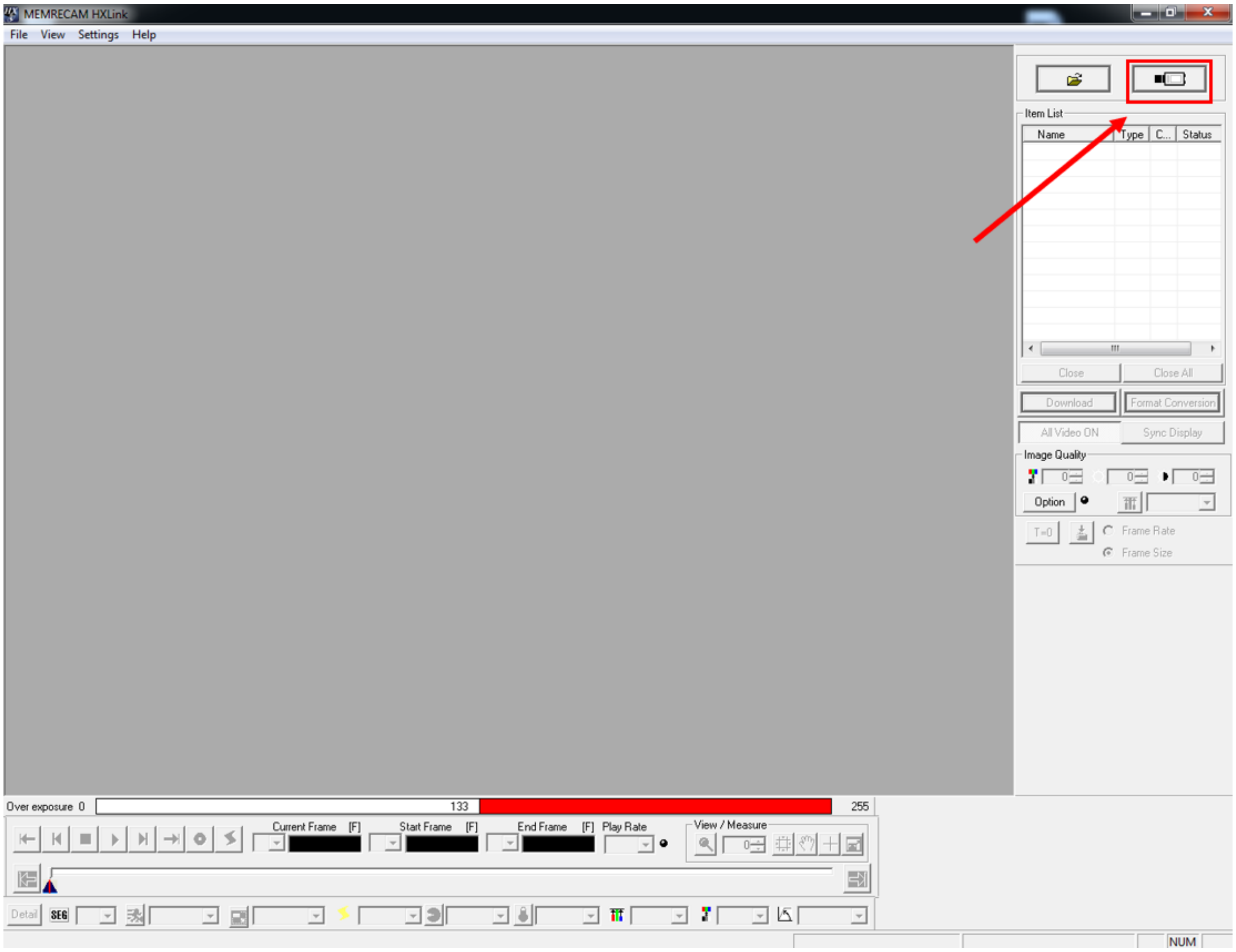

Figure B.2 – The HX-Link software used to control the high-speed camera. Attach the camera to the software by selecting the button indicated by the red arrow and the red box.

To view the camera live feed, press the view/arm button shown in the upper left image of fig. B.3 in the red box. After this, it is possible to change the frame rate and the frame size of the video (see fig. B.3 upper right image). Pressing the view/arm button again begins the recording process of the camera, which continuously stores new data up to a maximum allowable storage capacity of the camera. After the storage capacity is reached, only the most recent video is stored. Pressing the trigger button (see fig. B.3 lower left image) saves video data for a time interval that depends on the trigger type. It is convenient to have the trigger set to “end” (see fig. B.3 lower right image) for crystal growth velocity measurements because the nucleation and crystallization event must occur before the user knows to save the data (i.e. the nucleation event is the triggering mechanism for the user to save the data). Having the trigger set to “end” means that the video before the trigger is saved. The trigger icon is a yellow lightning bolt as shown in fig. B.3. The high-speed camera used with the electromagnetic levitator aboard the International Space Station is programmed to automatically trigger when a nucleation event occurs. It may be possible to do the same thing with the high-speed camera used with the BESL.

Figure B.3 – The arm/disarm and triggering buttons in the HX-Link software to view and record video data. After clicking the view button, the live camera feed appears, and the frame rate and frame size control boxes become active (upper right image). The triggering type can also be changed depending on the experiment to start, center, end, or custom (lower right image).

The video will populate in the software after the video save is triggered. The user can then fast-forward or rewind the video to locate the nucleation and crystallization event. The save bars (see fig. B.4 left image) should be placed around the crystallization event so only the important video is saved. The video files are inconveniently large without this step. Once the crystallization event is isolated, the user selects file and download to save the data as an avi video or other file type (see fig. B.4 right image). After creating the video file, the growth velocity of the front is measured using the procedure described in chapter 2 of this dissertation. The software for analysing the crystal growth velocity is also described in appendix B.2 of Chris Pueblo's dissertation[1].

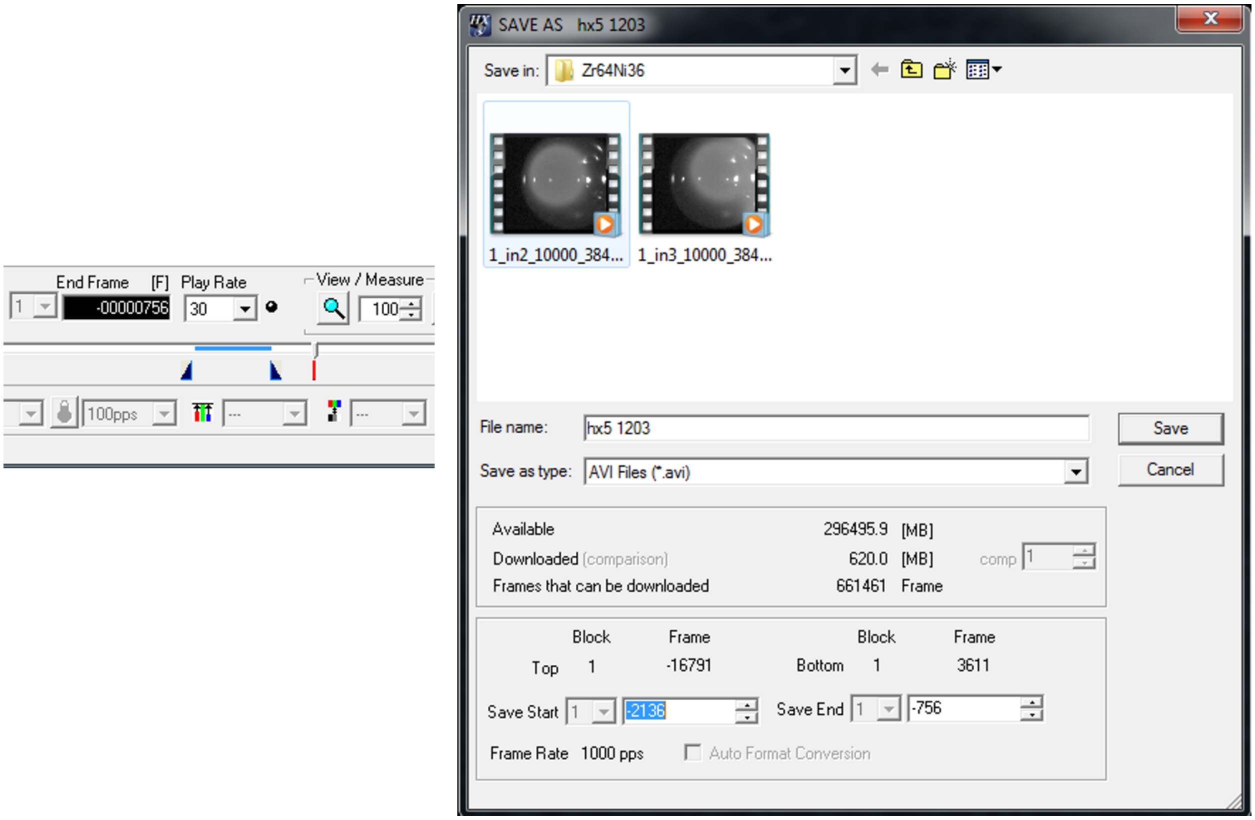

End Frame -00000756
Play Rate 30
View / Measure 100
100pps

Save in: Zr64Ni36
File name: hx5 1203
Save as type: AVI Files (*.avi)

Available 296495.9 [MB]
Downloaded (comparison) 620.0 [MB] comp 1
Frames that can be downloaded 661461 Frame

	Block	Frame		Block	Frame
Top	1	-16791	Bottom	1	3611

Save Start 1 -2136 Save End 1 -756

Frame Rate 1000 pps ☐ Auto Format Conversion

Figure B.4 – The left image shows isolation of the crystallization event using the save bars (the blue triangles indicating the timestamp locations in the video). The right image shows the save screen for a video file.

B.2 Analog to Digital Converter Box

The analog-to-digital and digital-to-analog cards of the Washington University BESL were updated in 2017 because the old versions of the cards were no longer available and required frequent calibration using an external computer. The new cards require a pin conversion box to take the signals from the position sensing detectors (PSDs) to the AD and DA cards. The National Instruments cards are inside the BESL TargetPC, which control the voltages applied to the electrodes to keep the samples levitated and stable during operation. Figure B.5 shows the configuration of the pin conversion box in relation to the PSD box and the TargetPC. Figure B.6 shows the pin conversions for the conversion box.

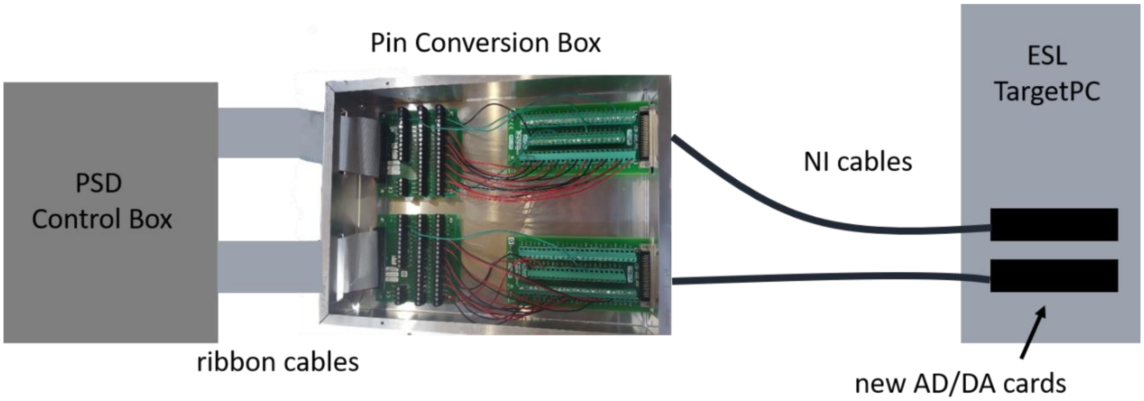

Figure B.5 – Schematic of the pin conversion box in relation to the PSD control box and the TargetPC.

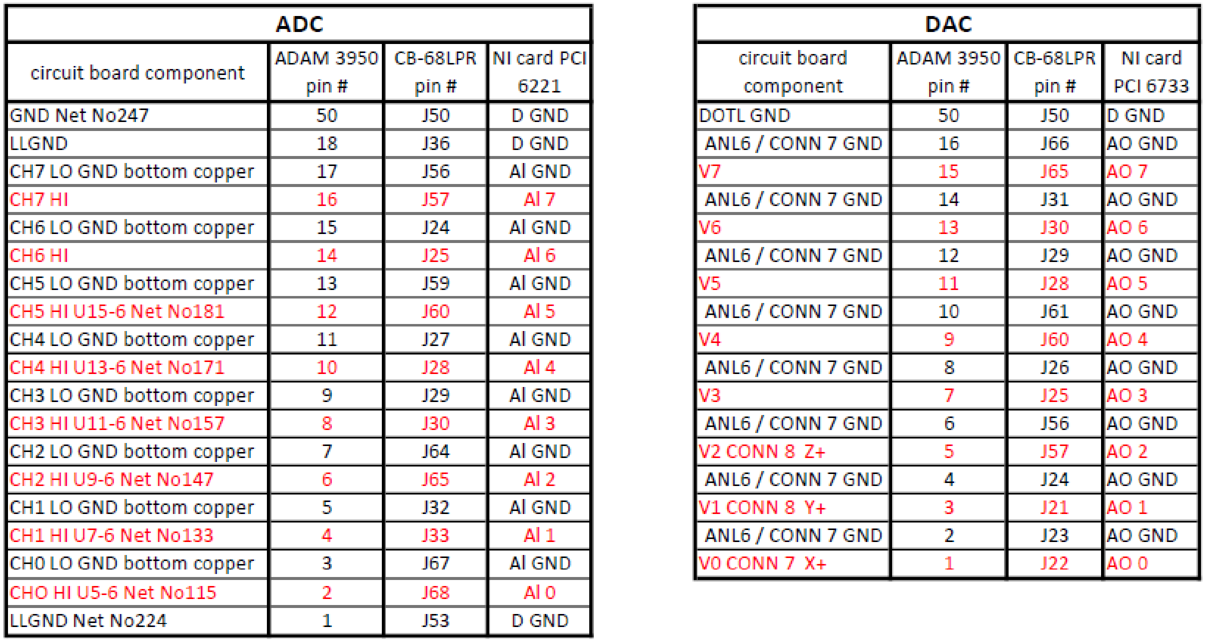

ADC			
circuit board component	ADAM 3950 pin #	CB-68LPR pin #	NI card PCI 6221
GND Net No247	50	J50	D GND
LLGND	18	J36	D GND
CH7 LO GND bottom copper	17	J56	AI GND
CH7 HI	16	J57	AI 7
CH6 LO GND bottom copper	15	J24	AI GND
CH6 HI	14	J25	AI 6
CH5 LO GND bottom copper	13	J59	AI GND
CH5 HI U15-6 Net No181	12	J60	AI 5
CH4 LO GND bottom copper	11	J27	AI GND
CH4 HI U13-6 Net No171	10	J28	AI 4
CH3 LO GND bottom copper	9	J29	AI GND
CH3 HI U11-6 Net No157	8	J30	AI 3
CH2 LO GND bottom copper	7	J64	AI GND
CH2 HI U9-6 Net No147	6	J65	AI 2
CH1 LO GND bottom copper	5	J32	AI GND
CH1 HI U7-6 Net No133	4	J33	AI 1
CH0 LO GND bottom copper	3	J67	AI GND
CHO HI U5-6 Net No115	2	J68	AI 0
LLGND Net No224	1	J53	D GND

DAC			
circuit board component	ADAM 3950 pin #	CB-68LPR pin #	NI card PCI 6733
DOTL GND	50	J50	D GND
ANL6 / CONN 7 GND	16	J66	AO GND
V7	15	J65	AO 7
ANL6 / CONN 7 GND	14	J31	AO GND
V6	13	J30	AO 6
ANL6 / CONN 7 GND	12	J29	AO GND
V5	11	J28	AO 5
ANL6 / CONN 7 GND	10	J61	AO GND
V4	9	J60	AO 4
ANL6 / CONN 7 GND	8	J26	AO GND
V3	7	J25	AO 3
ANL6 / CONN 7 GND	6	J56	AO GND
V2 CONN 8 Z+	5	J57	AO 2
ANL6 / CONN 7 GND	4	J24	AO GND
V1 CONN 8 Y+	3	J21	AO 1
ANL6 / CONN 7 GND	2	J23	AO GND
V0 CONN 7 X+	1	J22	AO 0

Figure B.6 – The pin conversion box mapping the PSD box to the new AD/DA cards. The colors distinguish lines of the figure and do not related to pin wiring colors.

The circuit board component in fig. B.6 is the item in the PSD box. The ADAM 3950 takes the ribbon cable from the PSD box and converts it to pin outputs. These are then transferred to the National Instruments board, CB-68LPR, which has the correct connection for the NI cables that attach to the new AD card (PCI 6221) and the new DA card (PCI 6733).

B.2 References

1. Pueblo, C. E. Ground and Flight Based Studies of Nucleation and Thermophysical Properties in Metallic Glass Forming Systems. PhD Thesis. (Washington Univeriesty in St. Louis, 2016).